



HAL
open science

Back to Single-Carrier for Beyond-5G Communications above 90GHz

Majed Saad

► **To cite this version:**

Majed Saad. Back to Single-Carrier for Beyond-5G Communications above 90GHz. Signal and Image processing. CentraleSupélec, 2020. English. NNT : 2020CSUP0009 . tel-03155646v1

HAL Id: tel-03155646

<https://theses.hal.science/tel-03155646v1>

Submitted on 1 Mar 2021 (v1), last revised 9 Feb 2022 (v3)

HAL is a multi-disciplinary open access archive for the deposit and dissemination of scientific research documents, whether they are published or not. The documents may come from teaching and research institutions in France or abroad, or from public or private research centers.

L'archive ouverte pluridisciplinaire **HAL**, est destinée au dépôt et à la diffusion de documents scientifiques de niveau recherche, publiés ou non, émanant des établissements d'enseignement et de recherche français ou étrangers, des laboratoires publics ou privés.

Copyright

THESE DE DOCTORAT DE

CENTRALESUPELEC

ECOLE DOCTORALE N° 601
*Mathématiques et Sciences et Technologies
de l'Information et de la Communication*
Spécialité : *Télécommunications*

Par

« Majed SAAD »

« Back to Single-Carrier for Beyond-5G Communications above 90GHz »

« Novel Index Modulation techniques for low-power Wireless Terabits system in sub-THz bands »

Thèse présentée et soutenue à Rennes, le 15 décembre 2020
Unité de recherche : UMR 6164 – IETR (Équipe SCEE)
Thèse N° : 2020CSUP0009

Composition du Jury :

Président :

Didier LE RUYET

Professeur des universités, CNAM Paris, France

Rapporteurs :

Marco DI RENZO

Directeur de Recherche CNRS, CentraleSupélec, Université Paris-Saclay, France

Ana I. PEREZ-NEIRA

Professeur des universités, UPC Universitat Politècnica de Catalunya, Espagne

Examineurs :

Didier LE RUYET

Professeur des universités, CNAM Paris, France

Kostas BERBERIDIS

Professeur des universités, University of Patras, Grèce

Ali CHAMAS AL GHOUWAYEL

Encadrant, Professeur Associé, Lebanese International University, Liban

Hussein HIJAZI

Encadrant, Professeur Associé, Lebanese International University, Liban

Directeur de thèse :

Carlos Faouzi BADER

Professeur Associé, CentraleSupélec-Campus de Rennes, France

Co-directeur de thèse :

Jacques PALICOT

Professeur Émérite, CentraleSupélec-Campus de Rennes, France

Invitée :

Catherine DOUILLARD

Professeur, IMT Atlantique/LabSTICC, France

Abstract

Wireless Terabits per second (Tbps) link is needed for the new emerging data-hungry applications in Beyond 5G (B5G) (e.g., high capacity broadband, enhanced hotspot, three Dimensional (3D) extended reality, etc.). Besides, the sub-THz/THz bands are the next frontier for B5G due to scarce sub-GHz spectrum, and insufficient bandwidth for wireless Tbps link in 5G millimeter Wave (mmWave) bands. Even though a wider bandwidth and large-scale Multiple-Input Multiple-Output (MIMO) are envisioned at sub-THz bands, but the system and waveform design should consider the channel characteristics, technological limitations, and high Radio Frequency (RF) impairments. Based on these challenges, we proposed to use an energy-efficient low order single carrier modulation accompanied by spectral-efficient Index Modulation (IM) with MIMO. Firstly, MIMO Spatial Multiplexing (SMX) and spatial IM domain (e.g. Generalized Spatial Modulation (GSM)) are explored, where we reduced their optimal detection complexity by 99% and the high-spatial correlation effect on GSM. Besides, we proposed Dual-Polarized Generalized Spatial Modulation (DP-GSM) that provides higher Spectral Efficiency (SE) via multi-dimensional IM and helps with the latter problem. We derived the theoretical performance of DP-GSM, and all these potential candidates are assessed in sub-THz environment. We also proposed a novel IM domain, called filter IM domain, that generalizes most existing Single-Input Single-Output (SISO)-IM schemes. Within the filter IM domain, we proposed two novel schemes: Filter Shapes Index Modulation (FSIM) and In-phase and Quadrature Filter Shape Index Modulation (IQ-FSIM) to enhance system SE and Energy Efficiency (EE) through indexation of the filters in the bank. In addition, their optimal low complexity detectors and their specialized equalization techniques are designed. Starving for further SE and EE improvement, this filter IM domain is exploited in MIMO. Besides, we theoretically characterized the performance of FSIM, IQ-FSIM, and Spatial Multiplexing with Filter Shape Index Modulation (SMX-FSIM) systems. To conclude, the proposed SMX-FSIM is compared in sub-THz environment to the previously considered candidates. The results confirm that SMX-FSIM is the most promising solution for low-power wireless Tbps B5G system due to its high SE/EE, robustness to RF impairments, low power consumption, feasible complexity, and low-cost with a simple linear receiver. Finally, the challenging filter bank design problem imposed by the filter IM domain is tackled by optimization to achieve better results.

Résumé

Pour les futures applications de l'après 5G, qui seront très gourmandes en données, des communications sans fils de l'ordre du Terabits/s sont envisagées. Pour atteindre ce niveau de débit, il faudra disposer d'une grande largeur de bande. Comme le spectre est déjà saturé autour de 6 GHz, il est envisagé d'utiliser la bande sous-THz (90-200GHz). Les formes d'ondes doivent être étudiées en prenant en compte les caractéristiques des canaux à ces fréquences, les limitations technologiques, la sensibilité aux défauts RF (bruit de phase, par exemple). Nous avons donc proposé d'étudier une modulation monoporteuse très efficace énergétiquement, puis d'accroître son efficacité spectrale par des techniques d'indexation et des techniques MIMO.

Dans un premier temps les techniques MIMO multiplex spatial et spatial Index Modulation (GSM) sont étudiées. En particulier des détecteurs réduisant la complexité de 99% sont proposés. La très forte corrélation spatiale du GSM est aussi étudiée et des solutions pour en diminuer l'effet sont proposées. Une modulation d'index dans le domaine de la polarisation est aussi proposé pour augmenter l'efficacité spectrale.

Dans un second temps, nous proposons un nouveau domaine pour l'indexation : le domaine filtre. Ce domaine généralise la plupart des schémas de modulation d'Index existants. Dans ce domaine filtre, nous avons proposé deux nouvelles modulations d'index : la modulation d'index de filtre de mise en forme (FSIM) et sa version en phase et en quadrature (IQ-FSIM). Une version MIMO de ces modulations est aussi proposée. Différents détecteurs sont proposés, ainsi que des techniques d'égalisation. Les performances théoriques de ces modulations sont développées et validées par des simulations. Ces modulations nécessitent de définir des bancs de filtres avec de fortes contraintes. Deux solutions sont proposées pour résoudre ce challenge, qui font partie des perspectives de cette thèse. Tous nos résultats confirment que la modulation FSIM MIMO offre un gain considérable par rapport aux modulations de l'état de l'art et permet d'atteindre le Terabits/s dans les canaux sous-THz.

Résumé Etendu en Français

Contexte et Motivation

Cette thèse se situe dans le contexte des communications numériques à très haut débit. C'est-à-dire dans le contexte de l'après 5G, voire de l'après 6G. Les applications/services visés dans ce contexte sont détaillés au chapitre 1 section 1.1 (état de l'art) [1–5]. L'application la plus représentative est appelée « Le Kiosque ». Elle consiste à transmettre en un temps très court, une très grosse quantité de données, à très courte distance entre l'émetteur et le récepteur. Il s'agit d'un scénario « Indoor », par exemple télécharger lors de l'entrée dans un train ou un avion de très gros fichiers (vidéo de très haute définition). Dans ce scénario l'émetteur est fixe et est relié au courant électrique et a donc peu de contraintes du point de vue consommation électrique. Le récepteur est soit fixe soit mobile (à très faible vitesse).



Figure 1 – Scénario Kiosque [4].

Pour atteindre de tels débits, même avec des modulations spectralement efficaces, il sera nécessaire d'utiliser une largeur spectrale importante. Cette largeur sera obtenue soit par une agrégation de plusieurs bandes spectrales soit par une bande suffisamment large en elle-même. Se pose alors la question de la bande de fréquences visée. En dessous de 6 GHz le spectre est totalement alloué, saturé. Il est donc nécessaire, pour avoir des bandes libres suffisamment larges, de s'intéresser aux bandes de fréquences plus hautes telles que la bande « sub-THZ » 90-200 GHz [5, 6]. Un intérêt secondaire dans ces bandes de fréquences est que la longueur d'onde est telle qu'elle rend possible l'intégration de réseaux d'antennes de petites dimensions compatibles avec un équipement utilisateur.

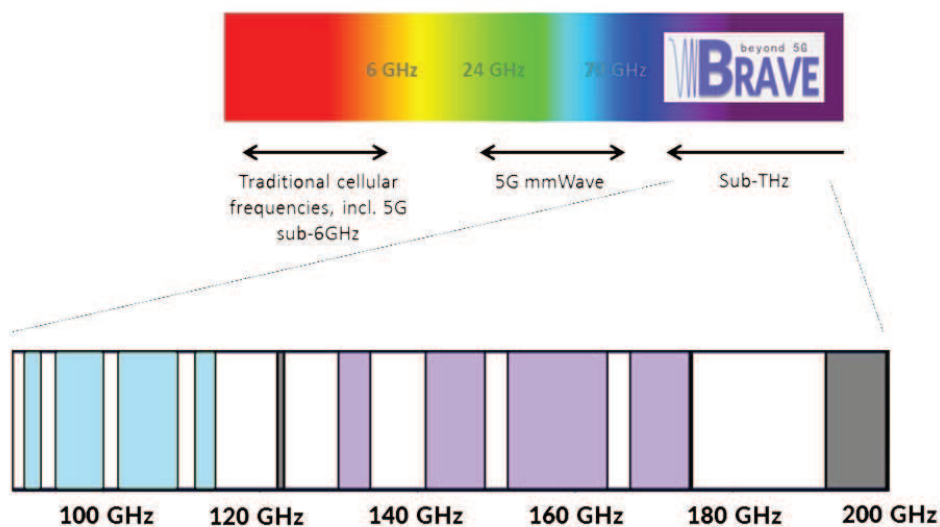


Figure 2 – Bande “sub-THz” considérée dans le projet ANR BRAVE [4].

Cette bande est actuellement réservée pour des applications d’observation astronomique passive et de météorologie, et n’a pas encore été utilisée pour des applications de télécommunications. Bien entendu, l’utilisation de cette bande doit se faire en respectant les utilisateurs primaires et en ne perturbant pas les observations astronomiques. Un autre aspect fondamental des futurs systèmes de communications qui doit nécessairement être pris en compte est la consommation d’énergie et donc l’efficacité énergétique. De fait, aujourd’hui les TIC (Technologies de l’Information et de la Communication) sont une des activités humaines qui voit son empreinte carbone croître de l’ordre de 10% par an [7]. Cette contrainte d’efficacité énergétique nous aura guidés sur tous les choix techniques, notamment en ce qui concerne la modulation proposée. A ces fréquences et pour des applications de type « Kiosque », les canaux entre l’émetteur et le récepteur seront majoritairement Line-of-Sight (LoS) et seront quasi stationnaires. Il en découle qu’une modulation de type multiporteuses, résistante aux canaux sélectifs en fréquence, ne sera pas nécessaire. De plus, la contrainte énergétique disqualifie ces modulations multiporteuses car leurs variations de puissance (PAPR) sont très élevées. Pour toutes ces raisons, nous proposons dans cette thèse de revenir à des modulations de type monoporteuse [8–10]. Deux approches sont alors possibles pour trouver le meilleur compromis efficacité spectrale pour atteindre le Terabits/s et efficacité énergétique pour diminuer l’empreinte carbone.

- Choisir une modulation très efficace spectralement et diminuer son PAPR.
- Choisir une modulation très efficace énergétiquement et augmenter son efficacité spectrale.

C’est cette seconde approche que nous avons choisi de suivre. En effet un premier bilan de liaison nous prouve que pour s’approcher du Terabits/s avec une puissance réaliste une solution à base de modulation QPSK est tout à fait envisageable (voir Tableau 3.3 du chapitre 3 et l’Annexe A).

L'accroissement de l'efficacité spectrale est obtenu par l'intermédiaire de modulations d'Index, ce qui est le cœur de cette thèse. Dans la partie I, les modulations classiques d'index sont présentées et des améliorations proposées. Dans la seconde partie, un nouveau domaine d'indexation (le domaine filtre de mise en forme) est proposé et étudié en détail. Les résultats obtenus offrent des gains considérables (de plusieurs db) par rapport aux modulations à même efficacité spectrale. Cette thèse a été réalisée dans le cadre d'un projet de recherche de l'Agence Nationale de Recherche (ANR) intitulé BRAVE "Back to single-carrier for beyond-5G communications above 90 GHz-(BRAVE)," [8]. Ce projet comporte 4 partenaires, un industriel SIRADEL, un centre de recherche CEA-LETI, l'agence Française des fréquences ANFR et un académique CentraleSupélec. Il se propose d'étudier les différentes facettes de ces transmissions à très haut débit dans les bandes « sub-THZ ». Cette thèse a contribué à l'étude de plusieurs aspects en particulier ceux traitant de la couche physique et des modulations les mieux adaptées au problème. De plus plusieurs résultats obtenus par les autres partenaires ont été intégrés dans nos développements et ont permis de valider notre approche, en particulier les modèles de canaux fournis par SIRADEL et les modèles de bruit de phase fournis par le CEA.

Plan de la thèse et contributions principales

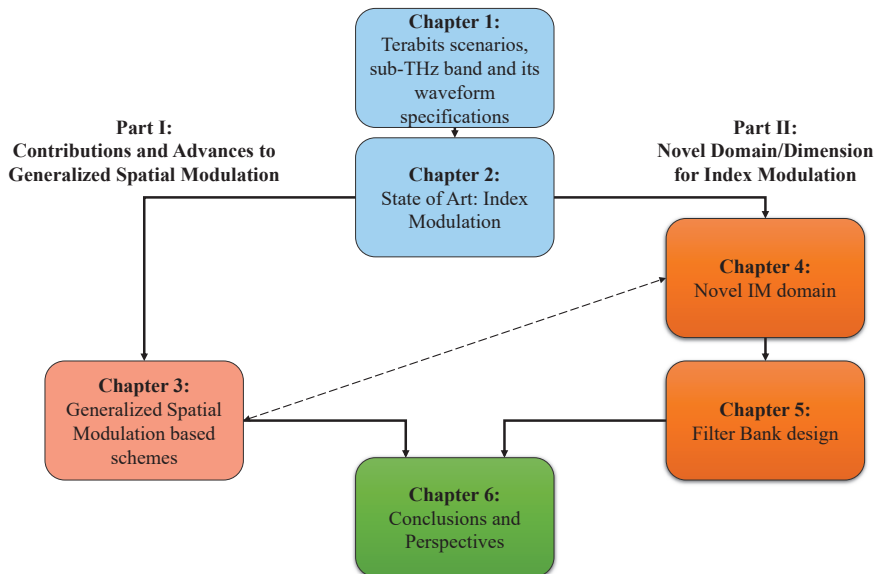


Figure 3 – Résume le plan de la thèse.

Dans le chapitre 1, les scénarios envisagés pour des applications à très haut débit dans les bandes THZ sont détaillés, tout particulièrement le scénario Kiosque qui est notre cas d'école pour cette thèse. Ensuite, les caractéristiques et la propagation des canaux sub-THZ (voir Figure ci-dessous) sont présentées, ce qui permet de présenter toutes les contraintes matérielles notamment celles liées au bruit de phase à ces hautes fréquences [11]. Enfin, basée sur tous les précédents éléments, une discussion

approfondie sur le choix entre multi et mono porteuse est effectuée et le choix d'une modulation monoporteuse avec modulation d'index est effectué.

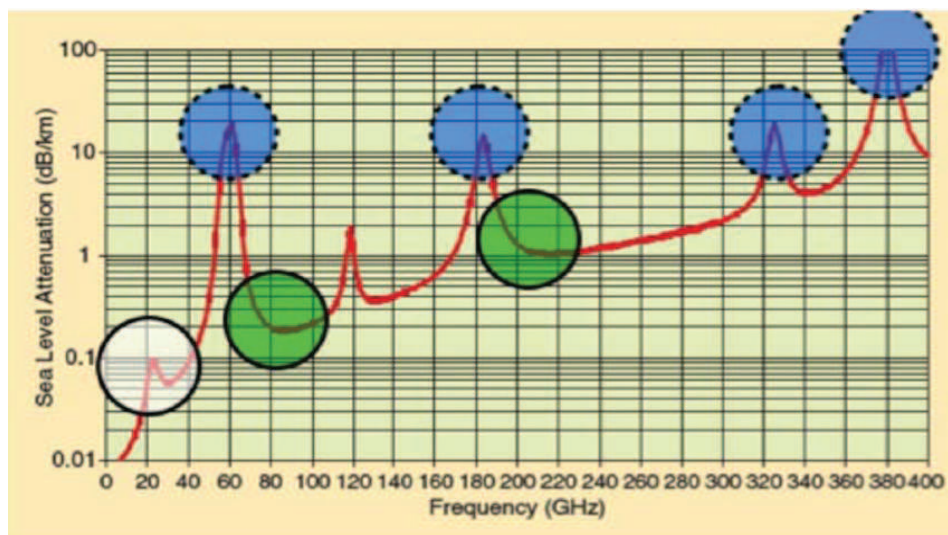


Figure 4 – Exemple d'atténuation en fonction de la bande de fréquence [12, 13].

Dans le chapitre 2, un état de l'art, le plus exhaustif possible sur l'ensemble des modulations d'index est réalisé. L'idée principale des modulations d'index est de transporter des bits supplémentaires (des bits virtuels) dans des caractéristiques du signal qui peuvent être détectées à la réception. En particulier les modulations d'index dans tous les domaines dans la Fig. 5 sont listées et comparées en termes d'avantages/inconvénients pour une application visée.

Dans le chapitre 3 de la partie I la modulation classique multiplexage MIMO et la modulation d'index spatial le GSM sont étudiées et comparées dans ce contexte de très haut débit dans la bande sub-THZ. Plusieurs contributions sont proposées, étudiées dans le but de résoudre quelques limitations du GSM.

- Un bilan de liaison pour une modulation monoporteuse avec indexation est effectué dans des canaux de Rayleigh et de Rice [10, 14].
- Une sélection du groupe d'antennes utilisé, ne nécessitant pas d'information sur le canal est proposée, afin de réduire la dégradation avec des canaux corrélés [15].
- Une nouvelle allocation des groupes d'antennes basée sur un codage de Gray est proposée pour améliorer le taux d'erreur [15].
- Une étude complète pour BLAST et GSM est réalisé sous des canaux sub-THz avec bruit de phase [16, 17].
- Des techniques de détection sous-optimales (perte entre 0.1 et 1 dB) permettant un gain de complexité de l'ordre de 99% sont proposées, pour les systèmes GSM et BLAST [18, 19].

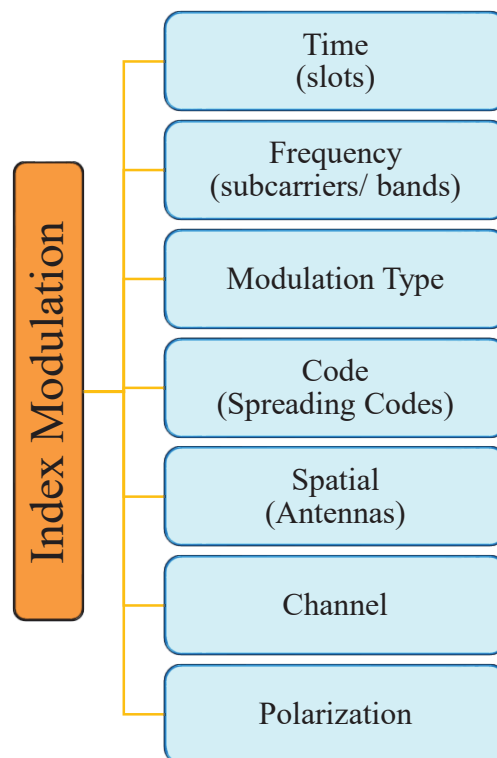


Figure 5 – Les différents domaines pour les modulations d’Index.

- Un second niveau d’indexation, basé sur une indexation de la polarisation de la modulation GSM est proposé. Ses performances, dont le gain en efficacité spectrale, sont détaillées [20,21].

Dans la seconde partie de cette thèse, en particulier dans le chapitre 4, un nouveau domaine d’indexation est proposé, il s’agit du domaine filtre, qui offre un nouveau degré de liberté pour transporter des bits “virtuels”. Les différentes possibilités, versions, d’indexation dans ce domaine sont discutées.

- Il est démontré que l’indexation dans ce domaine généralise la plupart des techniques d’indexation dans les domaines fréquentiel et temporel [22].
- Un nouveau schéma d’indexation est proposé le FSIM, qui consiste à coder par des bits virtuels la forme du filtre de mise en forme utilisé pour le symbole reçu. Etant donné que ce filtre peut changer à chaque symbole, le gain en efficacité spectrale est évident et considérable. Bien sûr cela se fait au prix d’une complexité au niveau du récepteur pour trouver le filtre adapté adéquat et corriger toute l’interférence entre symboles générée par l’utilisation de ces filtres. Cette modulation fait l’hypothèse qu’il existe un banc de filtres tel qu’il est possible, à la réception, de retrouver le filtre qui a été utilisé pour le symbole considéré [22,23].

Parameters	Temperature (degree C)	20		Carrier Frequency (GHz)	150		Distance (m)	5	
	99% of Channel Bandwidth (GHz)	1		Number of Channel Aggregation/bounding	44		Total Bandwidth (GHz) [8]	44	
	Modulation	CPM	$\pi/4$-QPSK	$\pi/4$-DQPSK	16-QAM	64-QAM	256-QAM	Units	
	GSM (Nt,Na)	(22,6)	(17,6)	(17,6)	(13,6)	(11,3)	(4,3)		
	Bits per GSM symbol	28.00	25.00	25.00	25.00	25.00	26.00	bits	
	Symbol Rate (R)	0.80	0.92	0.91	0.91	0.92	0.91	GSym/s	
Rate	APM Spectral Efficiency	1.59	1.83	1.82	3.65	5.49	7.3	bps/Hz	
	GSM Spectral Efficiency	22.26	22.90	22.80	22.83	22.88	23.71	bps/Hz	
Receiver	Total Throughput	979.4	1007.6	1003.2	1004.3	1006.5	1043.328	Gbps	
	SNR with Rayleigh	13.00	12.00	15.00	20.00	29.00	31.00	dB	
	RX Noise Figure (NF)	10.00						dB	
	Thermal Noise (Nthermal)	-83.93						dBm	
	Noise floor	-73.93						dBm	
	Rx Signal Level	-60.93	-61.93	-58.93	-53.93	-44.93	-42.93	dBm	
	RX Cable Loss (Lcrx)	1						dB	
	RX Antenna Gain (Gr)	3						dBi	
	Free space path loss (fspl)	89.94						dB	
	Vapour attenuation	1.28						dB/Km	
O2 attenuation	0.01						dB/Km		
Rain attenuaton	11.78						dB/Km		
Total Path loss	90.01						dB		
Transmitter	Required Tx EIRP	27.08	26.08	29.08	34.08	43.08	45.08	dBm	
	Cable Loss (Lctx)	1						dB	
	TX Antenna Gain (Gt)	24						dBi	
	Required Pt	4.08	3.08	6.08	11.08	20.08	22.08	dBm	
PAPR	PAPR for ($\alpha=0.2$)	0	3.8	4.86	7.5	8.2	8.35	dB	
	Theoretical PA Efficiency	0.8	0.52	0.44	0.34	0.3	0.28		
Uncorrelated	Power per Channel	3.20	3.91	9.21	37.70	339.40	576.34	mW	
	Total Power Consumption	0.14	0.17	0.41	1.66	14.93	25.36	W	
		21.48	22.35	26.08	32.20	41.74	44.04	dBm	
	SNR with Rician K=3	23.00	17.00	21.00	24.00	29.00	31.00	dB	
	Total Power Consumption	31.48	27.35	32.08	36.20	41.74	44.04	dBm	
Correlated	SNR with Rayleigh $\beta=0.8$	21.00	17.00	18.00				dB	
	Total Power Consumption	29.48	27.35	29.08				dBm	
	SNR with Rician $\beta=0.8$	29.00	22.00	27.00				dB	
	Total Power Consumption	37.48	32.35	38.08				dBm	

Figure 6 – Bilan de liaison de différentes configurations pour atteindre le Terabits/s avec une puissance réaliste. Où l'on constate que seules les configurations configurations Continuous Phase Modulation (CPM)-GSM et QPSK-GSM permettent de prendre en compte les contraintes

- Une version en phase et en quadrature de FSIM. Sur chaque composante les filtres peuvent être différents, ce qui multiplie par deux l'efficacité spectrale. [24]
- Une version MIMO de ces modulations est finalement proposée pour atteindre l'ensemble de nos objectifs en termes d'efficacité spectrale et d'efficacité énergétique. [25]
- Une analyse théorique des performances de ces modulations qui permet d'obtenir des bornes inférieures de taux d'erreur. Cette analyse théorique est validée par de nombreuses simulations [22, 24, 25].

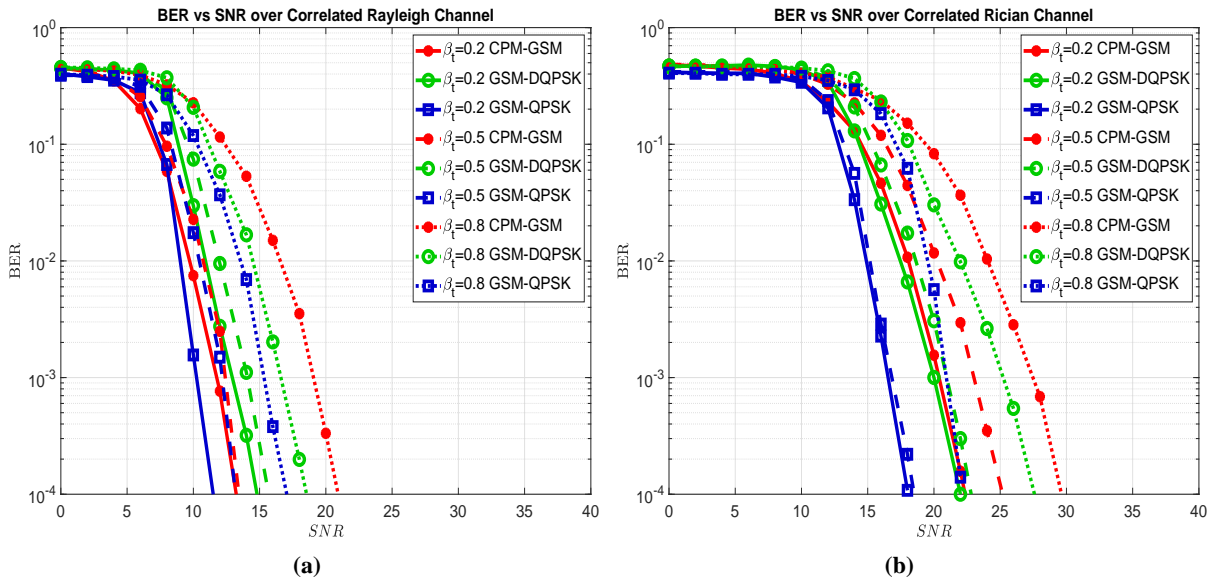


Figure 7 – Taux d’erreur pour différentes configurations dans des canaux de: (a) Rayleigh, (b) Rice.

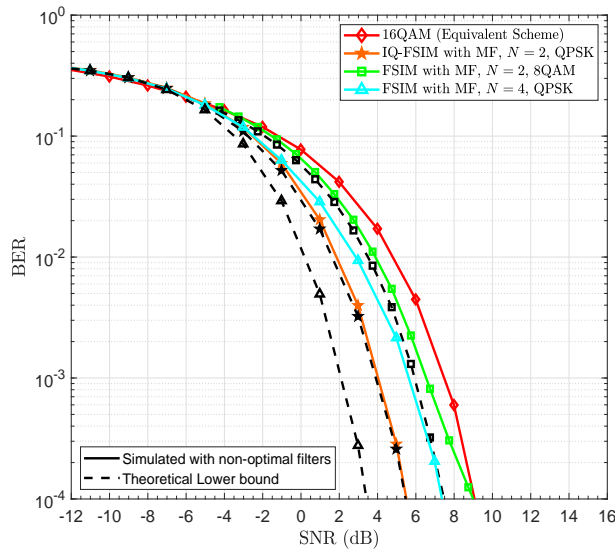


Figure 8 – Taux d’erreur pour les modulations FSIM, IQ-FSIM, leur équivalent MAQ 16, et comparaison avec leur bornes théoriques.

Dans le chapitre 5 de la partie II, est étudié le difficile problème d’obtention du banc de filtres pour la modulation FSIM. En effet comme dit précédemment, la modulation FSIM suppose l’existence d’un banc de filtres permettant de retrouver le filtre utilisé à l’émission. Ce banc de filtres doit obéir à un certain nombre de contraintes très fortes et parfois antagonistes. Parmi ces contraintes, nous trouvons : une IES la plus faible possible, une intercorrélacion entre les filtres la plus faible possible également, réjection dans les bandes adjacentes la plus faible, une bande passante la plus plate possible, etc. Le problème posé avec toutes ces contraintes devient un problème non convexe très difficile à résoudre.

Pour le résoudre un algorithme itératif est proposé qui fonctionne très bien pour deux et quatre filtres mais qui montre ses limites pour un plus grand nombre de filtres. La figure ci-dessous montre les performances de FSIM avec deux filtres optimisés.

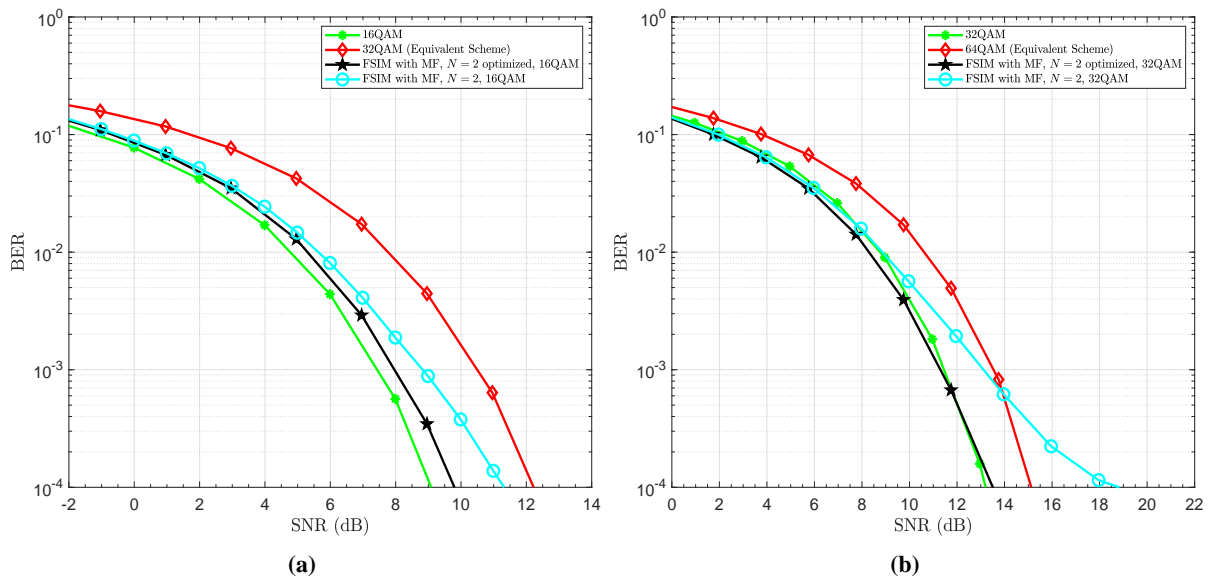


Figure 9 – Taux d’erreur de 2-FSIM avec les filtres optimisés: (a) 5 bits/symbole avec $M = 16$, (b) 6 bits/symbole avec $M = 32$.

Il reste très clairement un grand espace de recherche dans ce problème d’obtention du banc de filtres pour un plus grand nombre de filtres.

Finalement le chapitre 6 conclut ce travail de thèse en résumant les contributions principales et en soulignant l’ensemble des problèmes qui restent ouverts pour ce nouveau domaine d’indexation et cette nouvelle modulation FSIM.

Contents

Abstract	iii
Résumé étendu en français	v
List of Figures	xxi
List of Tables	xxvii
List of Algorithms	xxix
Acronyms	xxxii
Notations	xxxvii
General Introduction	1
1 Terabits scenarios, sub-THz band and its waveform specifications	3
1.1 Terabits Scenarios	4
1.2 sub-THz Background	7
1.2.1 Channel and propagation characteristics	7
1.2.2 THz challenges & limitations: Hardware technology, design and RF impairments	8
1.3 Candidate Waveform for sub-THz (Single carrier vs Multicarrier)	11
1.4 Major Contributions and Thesis Outline	14
1.4.1 Summary of the major contributions	17
1.5 List of Publications and R&D involvement	20
1.6 Summary	23
2 State of Art: Index Modulation	25
2.1 Introduction	26

2.2	SISO systems with/without Index Modulation	27
2.2.1	SISO time, frequency and modulation IM domains	28
2.2.2	Code IM- Spreading spectrum	32
2.3	MIMO systems with/without Index Modulation	32
2.3.1	Spatial Multiplexing	33
2.3.2	Spatial IM domain	34
2.3.2.1	Transmit Spatial IM	34
2.3.2.2	Receive Spatial IM	35
2.3.2.3	Summary	36
2.4	Channel/polarization IM domains	39
2.4.1	IM using polarized/Reconfigurable antennas	39
2.4.2	Scattering and Beam based IM	39
2.4.3	Media-Based Modulation using RF mirrors	39
2.5	Multidimensional IM	40
2.5.1	Channel/polarization IM with spatial and time IM domains	40
2.5.2	Modulation Type-based IM with spatial IM domain	41
2.5.3	Spatial IM with time and/or frequency IM	41
2.6	IM advantages/disadvantages and applications	42
2.7	Conclusions/Discussions	43
I	Contributions and Advances to Generalized Spatial Modulation	47
3	Generalized Spatial Modulation based schemes	49
3.1	Introduction	51
3.2	GSM for low power Terabits systems	52
3.2.1	System Model	52
3.2.2	GSM joint ML Detector	53
3.2.3	GSM OB-MMSE Detector	53
3.2.4	Channel Model: Rayleigh and Rician channels with\without correlation	54
3.2.5	Performance assessment and discussions	55
3.2.6	Link Budget	58
3.2.7	GSM Challenges	61
3.2.7.1	RF switching transmitter architecture	61

3.2.7.2	Peak-to-Average Power Ratio	62
3.2.7.3	Spatial Correlation	65
3.3	GSM in highly correlated channel	65
3.3.1	Efficient Legitimate TAC Selection	66
3.3.1.1	GSM System Relying on Channel Side Information at the transmitter side (EGSM)	66
3.3.1.2	Simplified Enhanced GSM S-EGSM	67
3.3.2	Efficient Spatial bit mapping	68
3.3.3	Results for proposed Simplified Enhanced Generalized Spatial Modulation (S-EGSM) and best-effort spatial bit mapping	70
3.4	GSM with RF impairments	73
3.4.1	Sub-THz MIMO Channel	74
3.4.2	Sub-THz Phase noise model	75
3.4.3	System comparison: GSM vs SMX	76
3.4.3.1	Performance in sub-THz environment	76
3.4.3.2	Optimal Detection Complexity	80
3.4.3.3	PAPR Discussion	80
3.4.3.4	Link budget for systems in sub-THz environment	81
3.5	Near-Optimal Performance with Low Complexity ML-based detector for SMX	83
3.5.1	Proposed OSIC-ML Detector	84
3.5.1.1	Detection algorithm	84
3.5.1.2	Complexity Analysis	87
3.5.2	Proposed SMX detector OSIC-ML results and discussions	89
3.6	Near-Optimal Performance with Low Complexity ML-based detector for GSM	93
3.6.1	Proposed GSM Detector: O ² SIC-ML	93
3.6.1.1	Detection algorithm	93
3.6.1.2	Complexity Analysis	97
3.6.2	Proposed GSM detector O ² SIC-ML results and discussions	97
3.7	Dual Polarized GSM	101
3.7.1	DP-GSM System model	102
3.7.2	DP-GSM Joint-ML Detector	104
3.7.3	Modified OB-MMSE Detector for DP-GSM	104
3.7.4	MIMO Channel models with Dual-Polarized antennas	105
3.7.4.1	Channel model with spatial and cross-polarization correlation	105

3.7.4.2	Sub-Terahertz MIMO channel	107
3.7.5	sub-THz PN model for DP MIMO systems	107
3.7.6	Analytical Performance: Average error probability bound	108
3.7.7	DP-GSM results and discussions	110
3.8	Conclusions and Discussions	116

II Novel Domain/Dimension for Index Modulation 119

4 Novel IM domain 121

4.1	Introduction	123
4.2	Filter IM domain	125
4.3	Filter Shape Index Modulation (FSIM)	127
4.3.1	FSIM Transmitter System model	127
4.3.2	FSIM Receiver System model	129
4.3.2.1	Joint ML Detector	130
4.3.2.2	Matched Filter-based Detector	130
4.3.2.3	ISI Estimation and Cancellation	132
4.3.3	Filter Bank Design requirements	133
4.3.4	Theoretical performance analysis	134
4.3.5	Numerical results analysis and discussions	137
4.3.5.1	FSIM vs Media-Based Modulation (MBM)	144
4.3.6	Conclusions	146
4.4	Quadrature Filter Shape Index Modulation (IQ-FSIM)	146
4.4.1	Introduction	146
4.4.2	IQ-FSIM Transmitter System model	147
4.4.3	IQ-FSIM Receiver System model	149
4.4.3.1	Joint ML Detector	149
4.4.3.2	Matched Filter-based Detector	150
4.4.3.3	ISI Estimation and Cancellation	151
4.4.4	Theoretical Performance Analysis	153
4.4.5	Numerical Results Analysis and Discussions	156
4.4.5.1	Performance Analysis based on Theoretical Lower Bound	157
4.4.5.2	Comparison to Equivalent M -ary QAM	158

4.4.5.3	Comparison to Equivalent FSIM System	161
4.4.6	Conclusions	162
4.5	MIMO Spatial Multiplexing with FSIM	163
4.5.1	System Model: MIMO Spatial Multiplexing with FSIM	164
4.5.1.1	SMX FSIM Transmitter	164
4.5.1.2	SMX-FSIM Receiver	166
4.5.2	Theoretical Performance	168
4.5.3	Results and Discussions	171
4.5.3.1	Theoretical and simulated performance comparison of SMX-FSIM to equivalent SMX-QAM system	171
4.5.3.2	Spectral Efficiency Analysis: SMX-FSIM vs existing MIMO techniques	172
4.5.3.3	Comparison of SMX-FSIM, conventional SMX and GSM in sub- THz environment	175
4.5.4	Conclusion	180
4.6	Summary	181
5	Filter Bank design	185
5.1	Introduction	186
5.2	Filter Design problem formulation	188
5.2.1	Filter Design $N = 2$	194
5.2.2	N -filter shapes design	197
5.3	Results	199
5.3.1	Filter bank of 2 filter shapes	199
5.3.2	Filter bank of N filter shapes	203
5.4	Conclusion	204
6	General Conclusions and Perspectives	207
6.1	Conclusion on our contributions	207
6.2	Perspectives for future works	211
A	Appendix A	215
B	Appendix B	219

C Appendix C	221
D Appendix D	223
List of Publications and R&D involvement	225
Bibliography	229

List of Figures

1	Frequency allocation for wireless communications in BRAVE considered spectrum [4].	2
1.1	Beyond 5G scenarios with Tbps data rate requirements [4].	5
1.2	Air attenuation at microwave, mmWave frequency bands [12, 13].	8
1.3	Transmit output power as function of frequency, [38] in 2011.	9
1.4	Saturated Transmit output power as function of high frequencies, [37] in 2020.	10
1.5	Map of the thesis organization. Any top-down path can be followed to read the thesis, or one of the two parts.	15
2.1	3D representation for Time, frequency and spatial division.	26
2.2	Index modulation domains presented in this chapter.	27
2.3	General SISO wireless communication system.	28
2.4	MIMO transceiver System Model with N_t transmit antennas and N_r receive antennas.	33
2.5	General system model for MIMO system with/without spatial IM.	36
2.6	Presented IM Domains and their sub-categories.	45
3.1	GSM System Model	52
3.2	GSM Derivatives	54
3.3	Bit-Error Rate (BER) vs SNR for various Amplitude-Phase Modulation (APM)-GSM systems over uncorrelated: (a) Rayleigh channel, (b) Rician channel.	57
3.4	BER vs SNR for (D)QPSK-GSM and Continuous phase modulation (CPM)-GSM over correlated: (a) Rayleigh channel, (b) Rician channel.	57
3.5	System comparison between different SC modulations with GSM.	61
3.6	Summary of GSM transmitter RF architecture.	64
3.7	System model of GSM with TAC selection	66
3.8	BER vs E_b/N_0 for various TAC selection with: (a) $\beta_t = 0$, (b) $\beta_t = 0.4$.	71
3.9	BER vs E_b/N_0 for various TAC selection with $\beta_t = 0.8$	71
3.10	BER vs E_b/N_0 for different TAC spatial mapping with $\beta_t = \{0.2, 0.6\}$	72

3.11	Spatial BER vs E_b/N_0 for binary and gray coding for spatial bits	73
3.12	Flowchart decision for the most suitable GSM TAC selection.	74
3.13	In-office scenario environment studied by our “Agence Nationale de la Recherche” (ANR) BRAVE partner SIRADEL [36]	75
3.14	BER performance of different APM-GSM systems in sub-THz channels and with different Phase Noise (PN) levels in Distributed Oscillators (DO) setup. The spectral efficiency is 12bpcu. The concerned sub-THz indoor MIMO channels are generated using Uniform Linear Array (ULA) array geometry with 4λ antenna separation. (a) $N_r = 6$, (b) $N_r = 10$	77
3.15	BER performance of different APM-GSM systems in sub-THz channels and with different PN levels in DO setup. The spectral efficiency is 12bpcu. The concerned sub-THz indoor MIMO channels are generated using URA array geometry with 4λ antenna separation and $N_r = 10$	78
3.16	Average BER performance of 12bpcu MIMO SMX and GSM systems subjected to different phase noise levels in DO setup. AP-UE mean distance is $d_{mean} = 5m$. ULA array geometry with 4λ antenna separation is used with (a) $N_r = 6$, (b) $N_r = 10$	79
3.17	Average BER performance of 12bpcu MIMO SMX and GSM systems subjected to different phase noise levels in DO setup. AP-User Equipment (UE) mean distance is $d_{mean} = 5m$. Uniform Rectangular Array (URA) array geometry with 4λ antenna separation is used with $N_r = 10$	79
3.18	ML detector computational complexity for GSM and SMX with same spectral efficiency 12bpcu.	81
3.19	OSIC-ML model with/without ordering. ‘EN’ is a boolean variable to activate the ordering technique prior to detection and interference cancellation. The stream estimator in the N_t receive circuits is based on a linear symbol detection.	85
3.20	The tree search for the Ordered Successive Interference Cancellation with ML verification (OSIC-ML) MIMO detectors of N_t height and N_{ei} branching factor. The corresponding branches of each node in the tree are numbered from 1 to N_{ei}	86
3.21	Uncoded BER performance of SMX-MIMO system using different detectors. The system parameters are: $N_t = 4$, $N_r = 5$, $N_{ei} = 2$ and 3: (a) QPSK (SE=8 bpcu), (b) 16-QAM (SE=16 bpcu).	89
3.22	Uncoded BER performance of SMX-MIMO system using different detectors. The system parameters are: 64-QAM, $N_t = 4$, $N_r = 5$, $N_{ei} = 2, 3$ and 4 that has a spectral efficiency of 24 bpcu.	90
3.23	Uncoded BER performance of SMX-MIMO system using different detectors with different number of TAs. The system parameters are: 16-QAM, $N_t = [4, 6, 8]$, $N_r = N_t + 2$, $N_{ei} = 4$. The SE is [16, 24, 32] bpcu.	91
3.24	Uncoded BER performance of SMX-MIMO system using different detectors with perfect and imperfect channel estimation. The system parameters are: QPSK, $N_t = 6$, $N_r = 10$, $N_{ei} = 2$ and $\sigma_e^2 = [0, 10^{-2}, 10^{-3}]$. The SE is 12 bpcu.	91

3.25	Uncoded GSM performance with $N_t = N_r = 5$ and $N_a = [2, 3]$ and different linear and non-linear detectors: (a) 16QAM, (b) 32QAM	98
3.26	Uncoded GSM performance with $N_t = 8$, $N_r = 6$, $N_a = 4$, $N_{ei} = 2$ and $M = [8, 16]$ QAM compared to linear and non-linear detectors.	99
3.27	Relative complexity reduction compared to ML of different optimal GSM detectors with $N_t = N_r = 5$: (a) $N_a = 2$ and $M = [16, 32]$ QAM, (b) $N_a = [2, 3]$ and 32QAM. . .	100
3.28	$N_r \times N_t$ DP-GSM system model.	102
3.29	BER performance of $N_r \times N_t$ DP-GSM system with spatial correlation $\beta \in \{0.2, 0.8\}$ and power leakage parameter $\mu = 0.2$ for QPSK over: (a) correlated Rayleigh channel and (b) correlated Rician channel ($K = 3$) using both MOB-MMSE and ML detectors. The spectral efficiency is 12 bpcu.	111
3.30	BER performance comparison of DP-GSM , DP-SMX, and UP-GSM systems with spatial correlation $\beta \in \{0.2, 0.8\}$ and power leakage $\mu = 0.2$ over: (a) correlated Rayleigh channel and (b) correlated Rician channel ($K = 3$) for QPSK using ML detector. The spectral efficiency is 12 bpcu.	112
3.31	BER performance of DP-GSM and DP-SMX systems for QPSK over correlated Rayleigh channel with spatial correlation: (a) $\beta = 0.2$ and (b) $\beta = 0.8$ using ML detector. Both systems are affected by PN with different levels (low, medium and strong noise). The power leakage parameter is $\mu = 0.2$ and the spectral efficiency is 12 bpcu.	113
3.32	BER performance of DP-GSM and DP-SMX systems for QPSK over correlated Rician channel ($K = 3$) with spatial correlation: (a) $\beta = 0.2$ and (b) $\beta = 0.8$ using ML detector. Both systems are affected by PN with different levels (low, medium and strong noise). The power leakage parameter is $\mu = 0.2$ and the spectral efficiency is 12 bpcu.	114
3.33	BER performance of DP-GSM , DP-SMX and Uni-polarized Generalized Spatial Modulation (Conventional GSM) (UP-GSM) systems with sub-THz channels and QPSK using ML detector.	115
3.34	BER performance of DP-GSM and DP-SMX systems with sub-THz channels and different PN levels. The spectral efficiency is 12 bpcu.(a) $N_r = 3$ and (b) $N_r = 5$	115
3.35	Comparison of MIMO Systems in sub-THz channels. Axes are normalized by the best achieved value among the 3 systems of same spectral efficiency.	117
4.1	System model of the FSIM-based transmitter and receiver with MF-based detector using N filters of length L and M -ary APM. Note that the detector can be replaced by the joint ML detector.	128
4.2	An example for the Overlap-Add block in the proposed scheme assuming $\eta = 6$ symbols. 129	
4.3	ISI estimation and cancellation using feedback decisions $\{\hat{i}, \hat{c}\}$ for past symbols and tentative decisions $\{\tilde{i}, \tilde{c}\}$ for future symbols.	131
4.4	Impulse Response for the two filters used in our simulations compared to RRC pulse shaping filter, where $\eta = 10$ and $\lambda = 8$	138

4.5	Magnitude and phase response of the filter f_1 depicted in Fig. 4.4.	138
4.6	Magnitude and phase response of the filter f_2 depicted in Fig. 4.4.	138
4.7	Complete responses of the 2 filters obtained after correct matched filtering at the receiver side, where $\eta = 10$ and $\lambda = 8$	138
4.8	The error probabilities of filter index detection with ISI estimation and cancellation, perfect Inter-Symbol Interference (ISI) cancellation, and the derived theoretical lower bound, $N = 2$ (2-FSIM-MQAM). The SE is: (a) [3, 4] bits/symbol using $M = [4, 8]$, (b) [5, 6] bits/symbol using $M = [16, 32]$	140
4.9	Uncoded BER performance of 2-FSIM-MQAM, its analytical lower bound and its equivalent scheme 2MQAM of the same SE: (a) 3 bits/symbol using $M = 4$, (b) 4 bits/symbol using $M = 8$	141
4.10	Uncoded BER performance of 2-FSIM-MQAM, its analytical lower bound and its equivalent scheme 2MQAM of the same SE: (a) 5 bits/symbol using $M = 16$, (b) 6 and 7 bits/symbol using $M = 32$ and $M = 64$ respectively.	142
4.11	Spectrum comparison between the proposed FSIM system with 2 non-optimal filters and the conventional transceivers with QAM and Root Raised Cosine (RRC) filters.	143
4.12	Complete responses of the 4 filters obtained after correct matched filtering at the receiver side, where $\eta = 10$ and $\lambda = 8$	143
4.13	Uncoded BER performance of 4-FSIM-MQAM, its analytical lower bound and its equivalent scheme 4MQAM of the same SE: (a) 4 bits/symbol using $M = 4$, (b) 6 bits/symbol using $M = 16$	143
4.14	Average BER comparison of different SC schemes with IM in a frequency selective Rayleigh fading: (a) $J = 2$, (b) $J = 4$	144
4.15	System model of the IQ-FSIM based transceiver with Matched Filter (MF)-based detector using N filters of length L and M -ary APM. Note that the joint ML detector can replace the IQ-FSIM detector.	148
4.16	Matched filter detector with input either \hat{s}^I or \hat{s}^Q to detect the index of the used filter shape \hat{i} or \hat{j} respectively.	150
4.17	ISI estimation and cancellation using feedback decisions $\{\hat{i}, \hat{j}, \hat{c}\}$ for past symbols and tentative decisions $\{\tilde{i}, \tilde{j}, \tilde{c}\}$ for future symbols.	152
4.18	Impulse Response for the two filters used in our simulations compared to RRC pulse shaping filter, where $\eta = 10$ and $\lambda = 8$	157
4.19	Magnitude and phase response of the filter f_1 depicted in Fig. 4.18.	157
4.20	Magnitude and phase response of the filter f_2 depicted in Fig. 4.18.	157
4.21	Complete responses of the 2 filters obtained after correct matched filtering at the receiver side, where $\eta = 10$ and $\lambda = 8$	157

4.22	The error probabilities of filter index detection on I and Q with ISI estimation and cancellation, perfect ISI cancellation, and the derived theoretical lower bound, $N = 2$ (2-IQ-FSIM-MQAM). The SE is: (a) [4, 5] bits/symbol using $M = [4, 8]$, (b) [6, 7] bits/symbol using $M = [16, 32]$	158
4.23	Uncoded BER performance of 2-IQ-FSIM-MQAM, its theoretical lower bound and its equivalent scheme 4MQAM of the same SE: (a) 4 bits/symbol using $M = 4$, (b) 5 bits/symbol using $M = 8$	159
4.24	Uncoded BER performance of 2-IQ-FSIM-MQAM, its theoretical lower bound and its equivalent scheme 4MQAM of the same SE: (a) 6 bits/symbol using $M = 16$, (b) 7 and 8 bits/symbol using $M = 32$ and $M = 64$ respectively.	160
4.25	Spectrum of the proposed IQ-FSIM system with 2 non-optimal filters compared to the traditional transceivers with QAM and RRC filters.	160
4.26	Uncoded BER performance of 4-IQ-FSIM-MQAM, its theoretical lower bound and its equivalent scheme 16MQAM of the same SE: (a) 6 bits/symbol using $M = 4$, (b) 8 bits/symbol using $M = 16$	161
4.27	BER performance comparison between FSIM, IQ-FSIM and their equivalent scheme 16QAM of the same SE 4 bits/symbol.	162
4.28	System model of $N_t \times N_r$ SMX-FSIM transceiver.	165
4.29	System model of FSIM Modulator with M -ary APM mapping and a filter bank of N filters.	166
4.30	System model of FSIM demodulator with the controlled-ISI cancellation and detection.	167
4.31	SER performance of the proposed SMX 2-FSIM-QPSK system and its equivalent SMX-QAM systems of the same SE: (a) SE= 12 bpcu with $N_r = 8$, (b) SE= 24 bpcu with $N_r = 12$	172
4.32	SER performance of the proposed SMX 2-FSIM-QPSK system and its equivalent SMX-QAM systems of same SE= 30 bpcu and $N_r = 16$	173
4.33	Maximum SE for different MIMO techniques: $N_a = [1, \dots, N_t - 1]$ for fixed N_a schemes, $N = 2$ for FSIM, and different M for systems with APM: (a) $M = 4$, (b) $M = 16$	174
4.34	Uncoded BER performance of the proposed non-coherent SMX FSIM compared to SMX-QAM and GSM in sub-THz channels. The SE for all systems is 12 bits/symbol (bcpu) and they are subjected to different PN levels: (a) low PN ($\sigma_g^2 = 10^{-1}$), (b) medium PN ($\sigma_g^2 = 10^{-2}$).	176
4.35	Comparison of CCDF of PAPR for the SMX FSIM, the SMX QAM and the GSM systems with pulse shaping having SE= 12 bpcu. SMX FSIM uses the filter shapes presented in [22], while SMX QAM and GSM use RRC filter.	179
4.36	Filter IM domain and its special cases.	181
5.1	Low pass filter magnitude response.	189
5.2	A transmit spectral mask template.	190

5.3	Magnitude response of the optimized filter f_2 using the iterative ISI minimization in Algorithm 4 compared to the previously designed filter by intuition depicted in Fig. 5.4a.	200
5.4	Comparison of the previous intuitive filters and the optimized filter f_2 using the iterative ISI minimization in Algorithm 4: (a) impulse responses, (b) complete responses after correct matched filtering at the receiver side.	201
5.5	Uncoded BER performance of 2-FSIM- M QAM with optimized filter shapes, and its equivalent scheme $2M$ QAM of the same SE: (a) 3 bits/symbol using $M = 4$, (b) 4 bits/symbol using $M = 8$	202
5.6	Uncoded BER performance of 2-FSIM- M QAM with optimized filter shapes, and its equivalent scheme $2M$ QAM of the same SE: (a) 5 bits/symbol using $M = 16$, (b) 6 bits/symbol using $M = 32$	202
5.7	Uncoded BER performance of 2-FSIM-64QAM with optimized filter shapes, and its equivalent scheme 128QAM of the same SE=5 bits/symbol.	203
A.1	Excel Sheet for achievable SNR estimator.	216
A.2	Excel Sheet for data rate estimation with channel bonding and/or aggregation.	216
A.3	Excel Sheet for link budget and power comparison estimation.	217

List of Tables

1.1	General comparison of single carrier and multi-carrier waveforms.	13
2.1	SE summary of most existing SISO schemes with/without IM.	31
2.2	Summary of existing MIMO schemes in the spatial IM domain.	38
3.1	Simulation parameters for different APM-GSM systems	56
3.2	Link Budget equations to estimate the required transmit power P_t	58
3.3	Link Budget and Power Consumption for different GSM parameters achieving Tbps	59
3.4	HD matrix for Spatial Mapping example with $N_t = 5$ and $N_a = 2$	69
3.5	Link budget of SMX and GSM systems over sub-THz channels and subjected to medium PN.	82
3.6	Relative Complexity reduction vs SNR for different system configurations at BER= 10^{-4}	91
3.7	Complexity of the proposed GSM detector $O^2SIC-ML$ and its complexity saving for different system configurations with $N_r = N_t$	100
3.8	Simulation parameters for DP-GSM sub-THz system example.	111
3.9	Our proposed solutions for the main challenges of GSM and SMX MIMO systems.	118
4.1	Simulation parameters	139
4.2	Simulation parameters	171
4.3	Spectral efficiency of different $N_t \times N_r$ MIMO techniques (Selected from Table 2.2).	174
4.4	System configuration for sub-THz candidates with 12 bpcu.	175
4.5	Average computational complexity in terms of real multiplications for SMX-FSIM, SMX-APM, and GSM equalizers/detectors.	178
4.6	Link budget and power consumption of SMX FSIM, SMX QAM and GSM systems with ZF based detection over sub-THz channels subjected to low PN.	180
4.7	Summary of different MIMO techniques for low-power wireless ultra-high data rates systems in sub-THz bands.	183

List of Algorithms

1	Proposed OSIC-ML detector for MIMO SMX systems.	87
2	Proposed O ² SIC-ML detector for GSM that generalizes several transmit spatial IM schemes as shown in Fig. 3.2.	96
3	MOB-MMSE detection algorithm for DP-GSM	106
4	Proposed filter design procedure for linear-phase filter shape f_2	197
5	Proposed joint design procedure for N filter shapes.	199

Acronyms

B5G	Beyond 5G.
3D	three Dimensional.
mmWave	millimeter Wave.
MIMO	Multiple-Input Multiple-Output.
RF	Radio Frequency.
IM	Index Modulation.
SMX	Spatial Multiplexing.
GSM	Generalized Spatial Modulation.
DP-GSM	Dual-Polarized Generalized Spatial Modulation.
SE	Spectral Efficiency.
SISO	Single-Input Single-Output.
FSIM	Filter Shapes Index Modulation.
IQ-FSIM	In-phase and Quadrature Filter Shape Index Modulation.
EE	Energy Efficiency.
SMX-FSIM	Spatial Multiplexing with Filter Shape Index Modulation.
S-EGSM	Simplified Enhanced Generalized Spatial Modulation.
O²SIC-ML	Ordered TAC- Ordered Successive Interference Cancellation with ML verification.
PN	Phase Noise.
DP	Dual Polarized antenna.
ISI	Inter-Symbol Interference.
BER	Bit-Error Rate.
APM	Amplitude-Phase Modulation.
CPM	Continuous phase modulation.
ANR	“Agence Nationale de la Recherche”.
DO	Distributed Oscillators.
ULA	Uniform Linear Array.
URA	Uniform Rectangular Array.
UE	User Equipment.
OSIC-ML	Ordered Successive Interference Cancellation with ML verification.
UP	Uni-Polarized antenna.
UP-GSM	Uni-polarized Generalized Spatial Modulation (Conventional GSM).
MF	Matched Filter.
RRC	Root Raised Cosine.
CCDF	Complementary Cumulative Distribution Function.

PAPR	Peak-to-Average Power Ratio.
AP	Access Point.
O²SIC-ML	Ordered TAC-Ordered Successive Interference Cancellation with ML verification.
CMOS	Complementary Metal Oxide Semiconductor.
ZP	Zero-Prefix.
EGSM	Enhanced Generalized Spatial Modulation.
FCC	Federal Communications Commission.
5G NR	5G New Radio.
ABEP	Average Bit-Error Probability.
ADC	Analog-to-Digital Converter.
APEP	Average Pairwise Error Probability.
AWGN	Additive White Gaussian Noise.
Bi-SSK	Bi-Space Shift Keying.
BLAST	Bell Laboratories Layered Space-Time.
BPSK	Binary-Phase Shift Keying.
CEPT	European Conference of Postal and Telecommunications Administrations.
CFO	Carrier Frequency Offset.
CIM-SS	Code Index Modulation-Spread Spectrum.
GCIM-SS	Generalized Code Index Modulation-Spread Spectrum.
CDMA	Code Division Multiple Access.
CM	Complex Multiplication.
FDM	Frequency Division Multiplexing.
FDMA	Frequency Division Multiple Access.
DSL	Digital Subscriber Line.
eMBB	enhanced Mobile Broadband.
ERASK	Extended Receive Antenna Shift Keying.
ERSM	Extended Receive Spatial Modulation.
ExSSK	Extended Space Shift Keying.
QCQP	Quadratically Constrained Quadratic Program.
i.i.d.	independent and identically distributed.
mMTC	massive Machine Type Communication.
FTTH	Fiber To The Home.
LTE	Long-Term Evolution.
LPWA	Low-Power Wide Area.
KPI	Key Performance Indicator.
DAC	Digital-to-Analog Converter.
FBMC	Filter Bank Multi-Carrier modulation.
MRT	Maximum Ratio Transmission Pre-coding.
RASK	Receive Antenna Shift Keying.
PLL	Phase-Locked Loop.
PEP	Pairwise Error Probability.
DCSK	Differential Chaos Shift Keying.
IEEE	Institute of Electrical and Electronics Engineers.
STBC	Space-Time Block Code.
DSP	Digital Signal Processor.

TDM	Time Division Multiplexing.
TDMA	Time Division Multiple Access.
uRLLC	ultra-Reliable Low Latency Communication.
VLC	Visible Light Communication.
WiGig	Gigabits WiFi at 60 GHz frequency.
WLAN	Wireless Local Area Network.
WPAN	Wireless Personal Area Network.
XPD	Cross-Polarization Discrimination.
CVX	Matlab Software for Disciplined Convex Programming.
InP	Indium Phosphide.
SDMA	Space Division Multiple Access.
CO	Centralized or Common Oscillator.
CP	Cyclic Prefix.
CSI	Channel Side Information.
CSIT	Channel Side Information at the transmitter side.
DMBM	Differential Media-Based Modulation.
DM-OFDM-VSIM	Dual Mode-Orthogonal Frequency-Division Multiplexing with Variable Subcarrier Index Modulation.
DPSK	Differential Phase Shift Keying.
DQPSK	Differential Quadrature Phase Shift Keying.
DQSM	Differential Quadrature Spatial Modulation.
DSM	Differential Spatial Modulation.
ED	Euclidean Distance.
EIRP	Effective Isotropic Radiated Power.
ExSM	Extended Spatial Modulation.
FDE	Frequency Domain Equalization.
FD-MM-SM	Frequency Domain Multi-Mode Spatial Modulation.
FTN	Faster Than Nyquist.
FTN-TIM	Faster-Than-Nyquist with Time Index Modulation.
GBMM	Generalized Beamspace Modulation using Multiplexing.
GFDM-IM	Generalized Frequency Division Multiplexing with Index Modulation.
GMM-OFDM-IM	Generalized Multi-Mode Orthogonal Frequency-Division Multiplexing with Index Modulation.
GPPM	Generalized Pulse Position Modulation.
GPQSM	Generalized Pre-coding-Aided Quadrature Spatial Modulation.
GPSM	Generalized Pre-coding Aided Spatial Modulation.
G-QSM	Generalized-Quadrature Spatial Modulation.
GSFIM	Generalized Spatial-Frequency Index Modulation.
GSSK	Generalized Space Shift Keying.
HD	Hamming Distance.
IAI	Inter-Antenna Interference.
ICI	Inter-Carrier Interference.
IMMA	Index Modulation Multiple Access.
IoT	Internet of Things.
LO	Local Oscillator.
LoS	Line of Sight.
MBM	Media-Based Modulation.

MC	Multi-Carrier.
MM-GSM	Multi-Mode Generalized Spatial Modulation.
MM-OFDM-IM	Multi-Mode Orthogonal Frequency-Division Multiplexing with Index Modulation.
MMSE	Minimum Mean-Squared Error.
MS	Mobile Station.
MS-STSK	Multi-Set Space-Time Shift Keying.
NLoS	Non-Line of Sight.
OB-MMSE	Ordered Block Minimum Mean-Squared Error.
OFDM	Orthogonal Frequency-Division Multiplexing.
OFDMA	Orthogonal Frequency-Division Multiple Access.
OFDM-HIQ-SIM	Orthogonal Frequency-Division Multiplexing with Hybrid In-phase Quadrature Sub-carrier Index Modulation.
OFDM-QSIM	Orthogonal Frequency-Division Multiplexing with Quadrature Sub-carrier Index Modulation.
OFDM-SIM	Orthogonal Frequency-Division Multiplexing with Sub-carrier Index Modulation.
OFDM-SNM	Orthogonal Frequency-Division Multiplexing with Sub-carrier Number Modulation.
OLA	Overlap and Add.
OOB	Out-of-Band.
OOK	On-Off Keying.
OSIC	Ordered Successive Interference Cancellation.
OSM	Offset Spatial Modulation.
PA	Power Amplifier.
PAM	Pulse Amplitude Modulation.
PDF	Probability Density Function.
PDSM	Transmit Pre-coding Aided Differential Spatial Modulation.
PPM	Pulse Position Modulation.
PSD	Power Spectral Density.
P-SD	Path-based Sphere Decoder.
PSK	Phase Shift Keying.
PWM	Pulse-Width Modulation.
QSM	Quadrature Spatial Modulation.
RA	Receive Antenna.
Rc-SD	Reduced complexity Sphere Decoder.
RM	Real Multiplication.
RP	Radiation Pattern.
Rx-SD	Receive-based Sphere Decoder.
SC-FDE	Single Carrier Frequency Domain Equalization.
SC-TIM	Single Carrier with Time Index Modulation.
RC-SC-TIM	Reduced Correlation Single Carrier with Time Index Modulation.
SD	Sphere Decoder.
SeFDM	Spectral efficient Frequency Division Multiplexing.
SFSK	Space-Frequency Shift Keying.
SINR	Signal-to-Interference-plus-Noise Ratio.
SSK	Space Shift Keying.
SSM	Spatial Scattering Modulation.
STFSK	Space-Time-Frequency Shift Keying.
STSK	Space-Time Shift Keying.

TAPC	Transmit antenna and polarization combination.
TPC	Transmit Polarization Combination.
TPSM	Transmit Pre-coding aided Spatial Modulation.
T-SD	Tree search Sphere Decoder.
Tx-SD	Transmit-based Sphere Decoder.
VB	Virtual Bit.
VGSM	Variable N_a Generalized Spatial Modulation.
NOMA	Non-Orthogonal Multiple Access.
QIMMA	Quadrature Index Modulation Multiple Access.
IM-OFDMA	Index Modulation with Orthogonal Frequency Division Multiple Access.
SC-FDMA-IM	Single carrier Frequency Division Multiple Access with Index Modulation.
\mathcal{L}-OFDM-SIM	Layered-Orthogonal Frequency-Division Multiplexing with Subcarrier Index Modulation.
DM-FTN-IM	Dual Mode-Faster Than Nyquist with Index Modulation.
DM-OFDM-IM	Dual Mode-Orthogonal Frequency-Division Multiplexing with Index Modulation.
MM-OFDM-QIM	Multi-Mode-Orthogonal Frequency-Division Multiplexing with Quadrature Index Modulation.
DM-SC-IM	Dual Mode-Single Carrier with Index Modulation.
DP-SM	Dual Polarized Spatial Modulation.
DP-SM-MBM	Dual Polarized Spatial Modulation with Media-Based Modulation.
DP-SMX	Dual Polarized Spatial Multiplexing.
FBE-SM	Fractional Bit Encoded Spatial Modulation.
MM-SM	Multi-Mode Spatial Modulation.
FTN-IM	Faster-Than-Nyquist with Index Modulation.
SM-ATA	Spatial Modulation with an Arbitrary number of Transmit Antennas.
TMMSE	Transmit Minimum Mean-Squared Error pre-coding.
TZF	Transmit Zero-Forcing pre-coding.
STBC-SM	Space-Time Block Coded Spatial Modulation.
I	In-phase.
Q	Quadrature.
ML	Maximum Likelihood.
QAM	Quadrature Amplitude Modulation.
QPSK	Quadrature Phase Shift Keying.
SER	Symbol-Error Rate.
Rx	Receiver.
SC	Single Carrier.
SM	Spatial Modulation.
SNR	Signal-to-Noise Ratio.
TA	Transmit Antenna.
TAC	Transmit Antenna Combination.
Tx	Transmitter.
THz	TeraHertz.

Notations

Constants

c	Speed Of Light
k	Boltzman Constant

Font convention

X	Capital bold letter for matrix
x	Small bold letter for vector
x or X	Small or Capital non-bold typeface for a scalar value

Number sets

$\mathbb{C}^{U \times V}$	Vector or Matrix of complex numbers of size $U \times V$
\mathbb{N}	Set of Natural numbers: All positive integers between 0 and $+\infty$
\mathbb{R}	Set of Real Numbers: All real numbers between $-\infty$ and $+\infty$
\mathbb{Z}	Set of Integer numbers: All positive and negative integers between $-\infty$ and $+\infty$

Mathematical operators

$\arg \max(\cdot)$	Return the index of maximum value
$\arg \min(\cdot)$	Return the index of minimum value
$\arg \text{sort}(\mathbf{x}, \text{order})$	Return the indices of sorted elements according to the order parameter (ascending ,descending)
$\ x\ $	Frobenius norm
$\{\cdot\}$	Complex conjugate
\cap	Intersection of two sets/events
$\Im\{\cdot\}$	Imaginary value of a complex number
\int	Indefinite integral

\int_a^b	Definite integral from a to b
$\langle \mathbf{x}, \mathbf{y} \rangle$	Vector dot-product
$\lceil x \rceil$	Ceil function that means the smallest integer larger than or equal to x
$\lfloor x \rfloor$	Floor function that means the largest integer smaller than or equal to x
\log_n	logarithmic function of base n
$\mathcal{I}_0(\cdot)$	Zero-order modified Bessel function of 1 st kind
$\mathcal{Q}(\cdot)$	Symbol quantization/slicing operation that gives the nearest sliced APM constellation point to the raw APM symbol estimate
$\mathcal{Q}_{N_{ei}}(\cdot)$	Symbol quantization/slicing operation that gives the N_{ei} nearest sliced neighbors to the raw APM symbol estimate
$\mathbb{E}\{x\}$	Expectation (mean) is the weighted average of the possible values that x can take, each value being weighted according to the probability of that event occurring
\odot	Element-by-element Hadamard multiplication
\otimes	Kronecker product
$\prod(\cdot)$	Product: multiplication of a set of elements
$\Re\{\cdot\}$	Real value of a complex number
$\sqrt{\cdot}$	Square root of a number
Σ	Summation: addition of a set of elements
$\mathbf{x} \star \mathbf{y}$	Cross-correlation between 2 vectors
$\mathbf{x} * \mathbf{x}$	Convolution
$\text{sort}(\mathbf{x}, \text{order})$	Sorting vector according to order parameter {ascending, descending}
$\{\cdot\}^\dagger$	Pseudo inverse of a matrix
$\text{diag}(\cdot)$	Return the diagonal elements of matrix
$\exp(\cdot)$ or $e^{(\cdot)}$	Exponential function
$\text{flip}(\mathbf{x})$	Reverse the order of elements of a vector
$\text{length}(\mathbf{x})$	Return the number of elements in a vector (length)
$\ln(\cdot)$	Natural logarithms (logarithm base e)
$\text{Pr}(\cdot)$ and $P(\cdot)$	Probability of an event
$Q(\cdot)$	Gaussian Q-function defined by: $Q(x) = \frac{1}{\sqrt{2\pi}} \int_x^\infty \exp(-\frac{u^2}{2}) du$

$\sin(\cdot)$	Sine function
$Tr(\mathbf{X})$	Trace: sum of diagonal elements of a matrix
$var(\cdot)$	Variance operator
$vec(\mathbf{X})$	Transform a matrix into vector by taking column by column
$x \ll y$	x is several orders of magnitude smaller than y
$\{\cdot\}^H$	Hermitian of matrix
$\{\cdot\}^{-1}$	Matrix inverse
$\{\cdot\}^T$	Matrix transpose

List of Symbols

α	Rolloff factor of the pulse shaping filter
\mathbf{I}^n	ISI vector from previous/future n^{th} symbols overlapping with the desired symbols
Γ	Leakage matrix between polarized antennas
μ_z	Mean vector for a multivariate distribution
$\mathbf{\Pi}_r$	Polarization correlation matrix at the receiver
$\mathbf{\Pi}_t$	Polarization correlation matrix at the transmitter
$\mathbf{\Psi}_r$	Composite receive correlation matrices combining spatial and polarization correlations
$\mathbf{\Psi}_t$	Composite transmit correlation matrices combining spatial and polarization correlations
$\mathbf{\Sigma}_r$	Receive correlation matrix
$\mathbf{\Sigma}_t$	Transmit correlation matrix
$\mathbf{\Sigma}_{t,r}$	Overall Transmit-Receive Correlation matrix
$\mathbf{\Sigma}$	Covariance matrix
$CN(0, \sigma^2)$	Complex Gaussian distribution where the elements are independent and identically distributed with zero-mean and variance σ^2
\mathcal{L}_{GSM}	Number of bits per GSM MIMO vector symbol
\mathcal{L}_{SMX}	Number of bits per conventional SMX MIMO vector symbol
\mathcal{L}_1	Number of bits conveyed in the spatial IM domain with DP-GSM
\mathcal{L}_2	Number of bits conveyed in the polarization IM domain with DP-GSM
\mathcal{L}_3	Number of bits conveyed in the conventional signal domain using APM symbols with DP-GSM

\mathcal{L}_{DP-GSM}	Number of bits per DP-GSM MIMO vector symbol
$\mathcal{N}(0, \sigma^2)$	Normal Gaussian distribution where the elements are independent and identically distributed with zero-mean and variance σ^2
μ	Percentage of power leakage from one polarization to the other: $0 < \mu \leq 1$
\bar{P}_e	Average error probability (APEP)
ϕ_g	Set of possible number of activated elements with a group : $\{1, 2, 3, \dots, N_g\}$
σ_g	Phase noise variance
$\mathbf{0}^{U \times V}$	All zero matrix of size $U \times V$
$\mathbf{1}^{U \times V}$	All one matrix of size $U \times V$
\mathbf{H}_{LoS}	MIMO LoS Channel matrix of size $N_r \times N_t$
\mathbf{H}_{NLoS}	MIMO NLoS Channel matrix of size $N_r \times N_t$
$\mathbf{I}^{U \times V}$	Identity Matrix of size $U \times V$
$f(\cdot)$ and $p(\cdot)$	Probability density function
f_c	Carrier frequency
f_{spl}	Free space path loss
G	Number of time slots or frequency bands/subcarriers groups
G_r	Receive antenna gain
G_t	Transmit antenna gain
L	Length of filter shape or pulse shaping
L_{crx}/L_{ctx}	Receiver/transmitter cable loss
M	Modulation order
M_A	Modulation order for the APM 'A' used with primary activated indexed elements in dual-mode modulation type IM
M_B	Modulation order for the APM 'B' used with secondary activated indexed elements in dual-mode modulation type IM
N	Number of filters
N_e	Number of bits error
N_g	Number of time slots or frequency bands/subcarrier elements within a group
N_T	Total Number of data time slots or frequency bands/subcarriers
N_{at}	Number of activated indexed elements for the in-phase components

N_{aQ}	Number of activated indexed elements for the quadrature components
N_a	Number of activated indexed element (antenna, time slot, sub-carrier, etc.)
N_{cl}	Number of clusters
N_{CP}	Number of cyclic prefix symbols
N_{ei}	Number of symbol neighbors
N_{Figure}	Receiver Noise figure
N_{rem}	Number of remained undetected symbols
N_{re}	Number of unused TACs that are not considered as legitimate TACs
N_{RP}	Number of radiation patterns
N_r	Number of receive antennas
$N_{Thermal}$	Thermal noise
N_t	Number of transmit antennas
N_u	Number of users
P_b	Bit error probability
P_e	Symbol error Probability or PEP
SE_{GSM}	GSM spectral efficiency
V_{th}	Threshold value used for early termination in the detection

Units

b/s/Hz	bit per second per Hertz
bpcu	bit per channel per use
dB	decibel unit
dB _i	decibel-isotropic unit
dB _m	decibel-milliwatts unit
Gbps	Gigabits per second
GHz	GegaHertz
Hz	Hertz
Km	Kilometer
m	meter

MHz	MegaHertz
s	Second
Tbps	Terabits per second
THz	TeraHertz

General Introduction

Wireless communication systems have undergone a real revolution, where the recent 5G communication standard targets to support three main use cases: massive Machine Type Communication (mMTC), ultra-Reliable Low Latency Communication (uRLLC), and enhanced Mobile Broadband (eMBB). These use cases have several constraints, such as the demands of a higher data rate that allow data-hungry application, the increasing traffic capacity from subscribers/devices, the involvement of applications with more latency, power consumption, and/or cost constraints.

The wireless data rates have doubled every 18 months over the last three decades, and it is projected to increase continuously to reach wireless Tbps in the next decade [1], according to Edholm's law. Such an ultra-high throughput is needed to support the new emerging applications of B5G [2–5] that will be presented in Section 1.1. Besides, the unsatisfied 5G requirements and applications will be pushed to B5G, and many future applications and technologies will be integrated. It is worth mentioning that B5G scenarios consider more stringent application requirements such as ultra-high data rate, a higher number of devices, and less energy consumption. The effort for achieving these requirements must be considered at the same pace on the user access and backhauling segments to avoid any bottleneck effect [26]. Thus, the ever-increasing data rate will rise in the near future towards new limits in order of Tbps.

The sub-6 GHz spectrum is almost fully allocated, overused and scarce. Hence, in order to accommodate for the high throughput requirements and according to Shannon-Hartley theorem, more spectrum is acquired in the mmWave bands for 5G New Radio (5G NR), mainly between 24.25 GHz to 52.6 GHz, where a larger bandwidth can be allocated for each UE [27]. In addition, the higher spectrum in the mmWave and TeraHertz (THz) bands are getting more attention as a solution of ultra-high data rate wireless communication for B5G (6G,...) and it is the next frontier immediately after the 5G mmWave bands [28–30]. Fortunately, these higher frequencies are advantageous for exploiting large-scale MIMO technology, because it allows integrating a large number of antennas in a compact area due to the small wavelength.

In the context of the BRAVE project [8] funded by ANR, this thesis aims at exploiting the mmWave/sub-THz bands mainly in the 90-200 GHz spectrum, where up to 58.1 GHz bandwidth could be made available for B5G wireless communication services [26, 31] as depicted in Fig. 1.

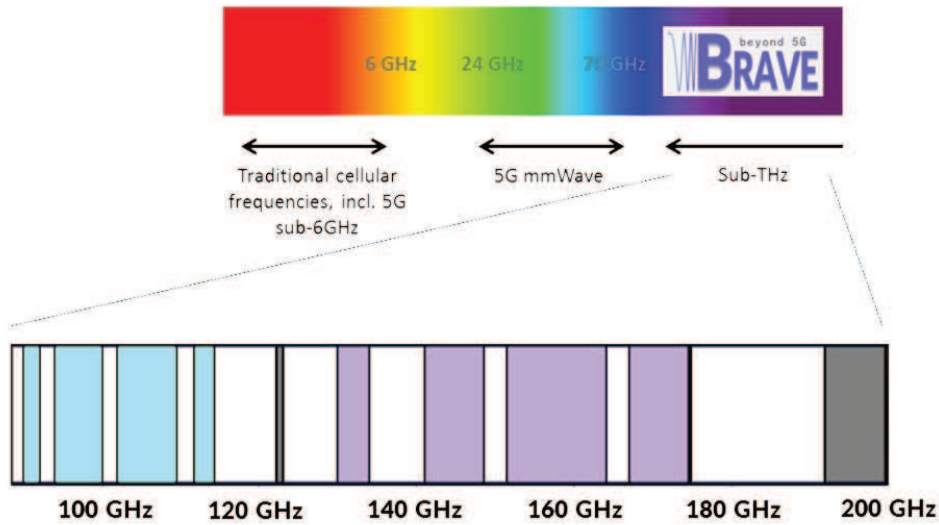


Figure 1 – Frequency allocation for wireless communications in BRAVE considered spectrum [4].

In addition, we are particularly interested in this band since electronic technology is more mature even though several challenges and limitations still exist, as it will be highlighted in Section 1.2. It can also be noted that there is some ongoing work within the European Conference of Postal and Telecommunications Administrations (CEPT) aiming to facilitate the deployment of fixed and mobile services in the frequency ranges 92-115 GHz and 130-175 GHz, similarly Federal Communications Commission (FCC) takes in 2019 steps to open spectrum horizons between 95 GHz and 3 THz for new services and technologies [32]. In addition, many standardization activities are currently in progress for the contiguous spectrum between 250 and 325 GHz (Institute of Electrical and Electronics Engineers (IEEE) 802.15.3d) [29]. The radio spectrum above 90 GHz is today essentially known for being used by scientific services (e.g., astronomy observation, earth exploration, satellite services, meteorology, etc.) and has never been used effectively for radio wireless communications purposes. However, it is expected that the coexistence with these scientific applications can be managed with a reasonable effort and few constraints, as those applications are precisely localized [5].

This dissertation aims at proposing innovative solutions for low-power wireless ultra-high data rates communications in sub-THz bands, where the system and waveform design are the core of B5G framework. In order to design such a system, it is crucial to develop a new wireless communication technique that helps to survive with the sub-THz limitations and severe RF impairments, and achieve a high SE with a given power expenditure.

Chapter 1

Terabits scenarios, sub-THz band and its waveform specifications

Contents

1.1	Terabits Scenarios	4
1.2	sub-THz Background	7
1.2.1	Channel and propagation characteristics	7
1.2.2	THz challenges & limitations: Hardware technology, design and RF impairments	8
1.3	Candidate Waveform for sub-THz (Single carrier vs Multicarrier)	11
1.4	Major Contributions and Thesis Outline	14
1.4.1	Summary of the major contributions	17
1.5	List of Publications and R&D involvement	20
1.6	Summary	23

This Chapter firstly discusses the emerging B5G scenarios and gives a general background about the sub-THz bands including its channel characteristics, challenges, and limitations. Afterward, the possible waveform for sub-THz bands are discussed, then the main waveform/modulation requirements are defined. Finally, the main contributions and the thesis outline are presented.

1.1 Terabits Scenarios

The wireless data rate demand is increasing over time, and the foreseen required rate is extending towards Tbps to support the new emerging applications. This subsection will focus on the B5G applications with wireless ultra-high data rates over 100 Gbps up to 1 Tbps. This is mainly driven by the need for having to move files of ever-increasing size and downloading and streaming/podcast services, enhancing the network capacities, and reducing the latency. These scenarios include applications with transmission distances ranging from the extremely-short (few centimeters or less) to relatively long distances of several kilometers [3–5]. Some of these use cases are described or considered by the IEEE 802.15.3d Standards Association in the band between 250-325 GHz [3, 29], IEEE 802.11ad also known as Gigabits WiFi at 60 GHz frequency (WiGig) [33], and IEEE 802.15.3e [28] in the 60GHz band. In the following, some of the wireless ultra-high data rate scenarios depicted in Fig. 1.1 are presented:

1. **Data kiosk application, Enhanced Wireless Local Area Network (WLAN) or Wireless Personal Area Network (WPAN):** These use-cases are indoor scenarios of short-range up to few meters with ultra-high-throughput to download large files instantaneously, enable streaming 8K-16K videos with high frame rate and pixel resolution, and replacing the wired multi-connection to personal UE. For example, the user can automatically download a file from his wish-list using a data kiosk machine, served by the data showers at the train station/airports' entrance ports, or in the crowded waiting area. This data offloading using the data kiosk reduces the burden of networks. In these applications, the transmitter Access Point (AP) or data kiosk machine have more relaxed constraints than the handheld UE as phones/tablets, since the former is directly connected to a power outlet and can support higher complexity/cost. In these applications, the transceivers are stationary in most cases or with a very low receiver mobility (pedestrian).
2. **Extended Reality (e.g., Virtual/augmented/mixed reality):** These applications are small range applications where a high data-speed is required to capture multi-sensory inputs, provide real-time user interaction and enable remote connectivity with 3D hologram technology. The specifications of the use cases are similar to the data kiosk.
3. **Datacenter/Server farm network:** This connection is needed to facilitate infrastructure setup and solve the network congestion issues that reduce connection latencies for real-time services. The servers are well localized in the data center that permits to establish different wireless links simultaneously, and it can also be an add-on to complement the fiber optics connectivity.

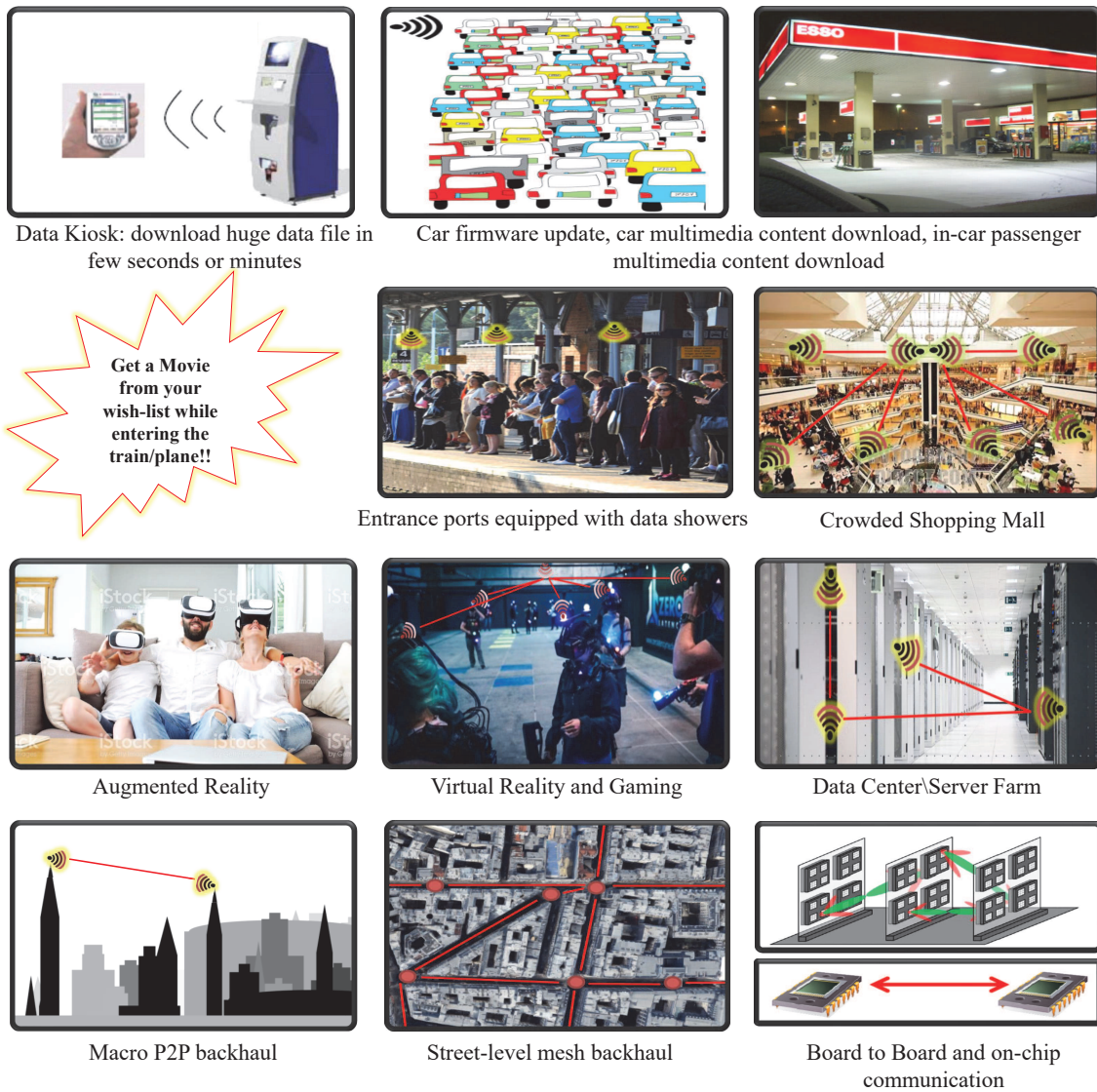


Figure 1.1 – Beyond 5G scenarios with Tbps data rate requirements [4].

4. **Inter/Intra-chip communication:** It needs an ultra-high data rate, and the available copper wires connection nowadays cannot reach Tbps. Hence, soon it will be the bottleneck and will limit the development of a faster system. For example, 200 Gbps is needed to transfer within device chips an 8K video with 48-pixel resolution and 120 Hz frame rate [3], and 765 Gbps for a 16K video with the same format. Similarly, the parallelization to enhance the performance necessitates chips collaboration as nowadays multi-core computers. However, the copper routing and congestion will lead to important losses due to longer paths in the future computers with highly parallel architecture. The wireless Tbps connection overcomes these limitations with limited power requirements due to extremely short-distance links up to a few centimeters and enables the massive wireless network/system-on-chip.
5. **High capacity Backhaul and enhanced broadband fixed wireless access:** The Tbps wireless infrastructure can be as an alternative/complement to optical fiber deployment to provide high capacity while reducing the cost and network repair time. Similarly, the fixed wireless access can replace the wireline xDigital Subscriber Line (DSL) technology and the Fiber To The Home (FTTH) that reached the limits for viable deployment costs because of the last mile complexity. Moreover, ultra-high-speed is required to serve the dense areas and smart city devices (e.g., video-surveillance as part of the internet of objects) or public internet access. In addition, this scenario allows deploying a smart connected city, houses/offices, and hotspots with high-data rates to avoid any bottleneck in the connection. The envisioned ultra-dense network topology in urban areas with the extreme data rate, capacity, and latency requirements makes the fiber-based backhauling highly desirable but sometimes complicated due to current fiber network penetration (variable from one country to the other) and related extension cost. Therefore, high data rate wireless backhauling is a valuable competitive technology, which benefits from lower deployment costs and constraints.

Furthermore, Tbps wireless communications will open new (partly unexpected) services/application opportunities and other market perspectives in the future. For more details about these scenarios and their Key Performance Indicators (KPIs), the readers are referred to IEEE 802.15.3d application requirements document [3] and our deliverable “D1.0” in the BRAVE project [4]. Finally, it is worth mentioning that sub-THz and real THz bands are being investigated for other types of applications in addition to the communication due to the small-wavelength characteristics, the ultra-wide bandwidth, and narrow-beamwidths at THz frequencies. For instance, the THz wireless systems are also promising for novel sensing, smart healthcare, imaging, and positioning capabilities to enhance automated machinery, autonomous cars, intra-body THz communications with nanotechnology THz transceivers, and new human interfaces [6, 34].

1.2 sub-THz Background

The mmWave bandwidth is getting tremendous attention from researchers and industries for 5G communication and beyond, mainly due to the significant unused spectrum and its business market perspectives. The overall mmWave spectrum is ranging between 30-300 GHz, where the wavelength is in order of a millimeter, while the THz spectrum is defined between 0.3 THz and 3 THz. The mmWave spectrum being investigated for 5G communication is below 71 GHz since the large mmWave spectrum has different characteristics and electronics technology maturity. These higher frequencies, mainly between 100-300 GHz, are so-called sub-THz since they share more properties with true THz bands. After presenting the sub-THz opportunities and possible scenarios, it is essential to highlight such system feasibility with current technology, the main challenges and limitations, then deduce the critical modulation aspects that should be considered for sub-THz wireless communication.

1.2.1 Channel and propagation characteristics

In the sub-THz bands, the channel propagation is characterized by very strong obstruction losses and blockage (from walls, vegetation, urban furniture, etc.), atmospheric, and rainfall attenuation. The atmospheric attenuation of mmWave and sub-THz is much higher than sub-GHz bands, as shown in Fig. 1.2 [13], and some mmWave/sub-THz windows in the BRAVE considered spectrum are affected by severe attenuation up to 11 dB/Km. However, the other windows between the peaks are of special interest for B5G wireless communication. In addition, the sub-THz bands suffer from important attenuation due to the rain, which is almost constant above 100 GHz with a loss of 0.8 dB/Km up to 50 dB/Km depending on rain density per ITU-R P.838-3 [12].

Thus, the long-distance true THz wireless communication is a real challenge with these high propagation losses, and the low sub-THz bands below 200 GHz have more opportunities for these applications. However, a high-gain directional antenna is necessary to deal with the overall propagation losses for outdoor long-distance scenarios such as backhaul and fixed wireless access. Besides, MIMO technology with beamforming can help to counteract these losses and achieve ultra-high data rates. Note that these propagation losses are negligible and irrelevant for the short-range indoor sub-THz/THz communication. Nevertheless, these scenarios are still facing important losses from the surrounding environment and furniture details. Besides, the sub-THz/THz wireless communication is more vulnerable to severe blockage and penetration losses than the 60 GHz mmWave losses, as shown in [6, 35] and references therein. But it is worth mentioning that these attenuations, molecular/gas absorption, propagation losses as well as reflections, scattering, and diffraction phenomena, have much more contribution at the true THz bands. Thus, the efficient communication link will be most likely in Line of Sight (LoS) and/or with possible few survival Non-Line of Sight (NLoS) paths. Hence, the sub-THz channel is expected to be composed of only a few dominant paths, typically the LoS contribution

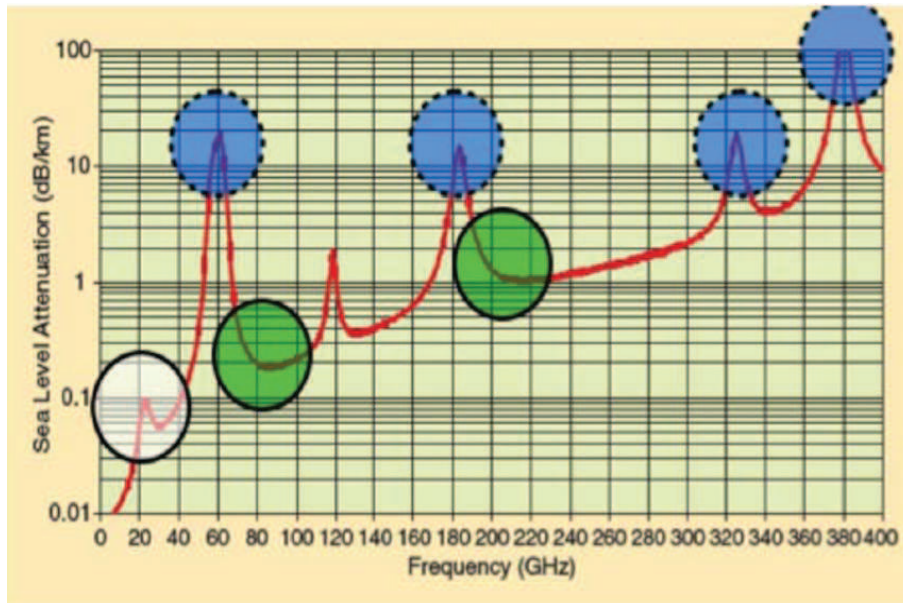


Figure 1.2 – Air attenuation at microwave, mmWave frequency bands [12, 13].

with the highest power, one-bounce specular reflections (from electrically-large surfaces), and possible scattering (from objects with small electrical size) [36].

1.2.2 THz challenges & limitations: Hardware technology, design and RF impairments

In this section, the major sub-THz band hardware challenges and limitations are presented. The RF front-end is all the components between the antenna and the digital baseband system of a transceiver, namely mixer or modulator, phase shifter, filters, data converters, and Power Amplifier (PA). Note that the THz hardware components exist from decades for radio astronomy and satellite applications, but the off-the-shelf components do not suit the emerging sub-THz communication scenarios since the latter has more stringent hardware constraints and requirements such as transceiver dimension, heat dissipation, processing power, operating temperature, and cost. Thus, nowadays, technology is still not mature enough for sub-THz frequencies, even though significant efforts have been made in the last years. For instance, the electronics technology is the most convenient for massive low-cost production and business interest for such Tbps scenarios, but the electronics components at the sub-THz frequencies are working at the edge of the maximum theoretical operating frequency with very low efficiency.

The RF challenges at sub-THz bands, especially for low-cost electronics components, can be summarized as follows :

1. The efficiency and achievable transmit output power of the power amplifier and power/signal generation are low compared to sub-GHz bands, where the maximum achievable output power

today is less than 20 dBm for Complementary Metal Oxide Semiconductor (CMOS) and 30 dBm for Indium Phosphide (InP) technology as shown in Fig. 1.4. For information, the optical technology provides high transmit output-power at THz optical frequencies, and similarly, the electronics technology at sub-GHz bands. However, the mobile wireless communication systems were not possible at the sub-THz and low THz bands for decades due to the so-called THz-gap in the transmit-output power, as shown in Fig. 1.3. Today's technology starts filling the THz-gap but with low output power, as shown in Fig. 1.4 [37].

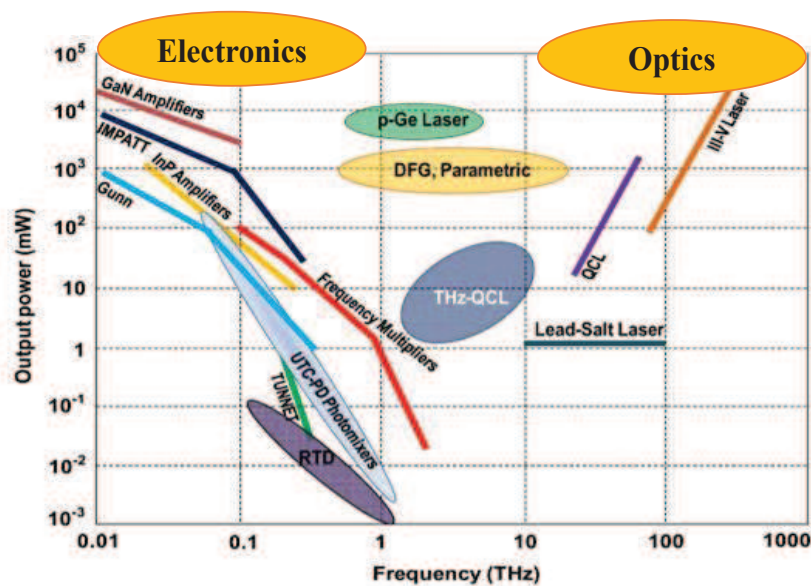


Figure 1.3 – Transmit output power as function of frequency, [38] in 2011.

2. Sub-THz systems suffer from Carrier Frequency Offset (CFO) and medium to high PN impairments due to the poor performance of high-frequency Local Oscillators (LOs). This impairment is negligible at sub-GHz, but at higher frequencies becomes more significant and leads to system performance degradation that can limit the achievable throughput rate. However, many research efforts are investigating new technologies and circuits design topologies to achieve a lower PN level.
3. The high sampling rate for Analog-to-Digital Converters (ADCs) is needed to digitize a wide-band received signal, and the sampling frequency should obey the Nyquist theorem. However, the ultra-high sampling rate ADC suffers from high power dissipation that increases exponentially with the sampling frequencies [39]. Note that the total bandwidth available at sub-THz is recommended to be divided into sub-bands (250 MHz or its multiple [40], 2.16 GHz [29]), where a channel aggregation and bonding is suggested to use a larger bandwidth. Thus, such a channel arrangement limits the ADC power consumption at the price of more parallelization.

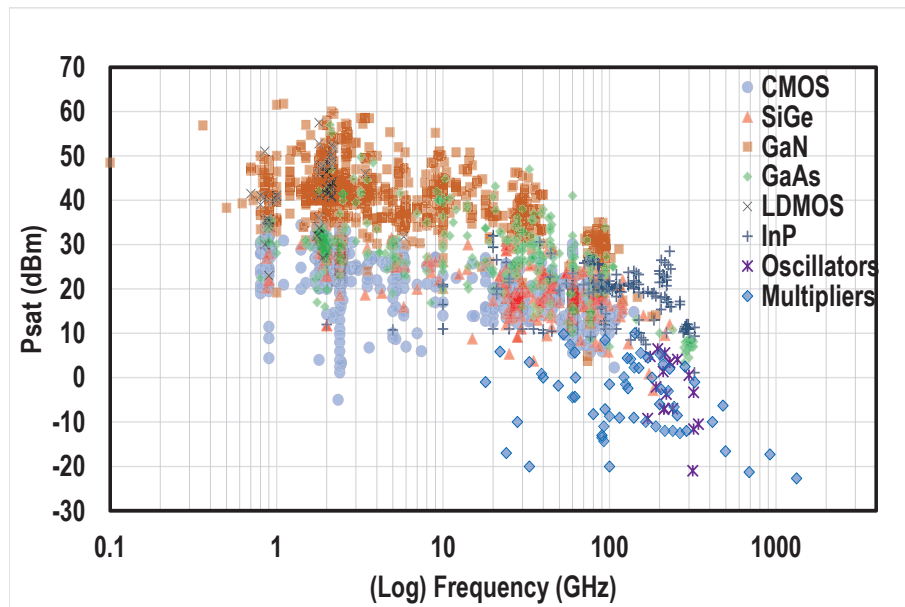


Figure 1.4 – Saturated Transmit output power as function of high frequencies, [37] in 2020.

4. Another limitation for ADCs is the lack of efficient design with large resolution, and thus most low-cost ADCs have few bits resolution or quantization levels.
5. For high-frequency wide-band systems, the non-linearity of analog components used in RF front ends and mainly the PA imposes more challenges in modeling circuits and in anticipating the compensation measures required for performance improvements.

The sub-THz wireless communication also has challenges at the digital side, especially for real-time applications like mixed reality scenarios with a Tbps data rate. These applications necessitate ultra-fast decoding because the offline processing cannot be accepted like with the other applications. In practice, the current energy-efficient Digital Signal Processors (DSPs) have a small clock frequency, and thus a Tbps decoding speed can only be achieved by means of parallel architecture [41, 42], i.e., at the expense of higher complexity and larger chip area. It is worth mentioning also that the clock distribution network of integrated circuits consumes a significant portion of the energy, area, and metal resources, all of which scale with the clock frequency [43].

Last but not least, the efficient antenna array with the tiny wavelength is difficult to design, especially with Silicon-based electronic technology at true THz frequencies. However, significant works for the true THz bands mainly (1-1.5 THz) are proposed based on the new Graphene technology, where a Graphene-based complete transceiver design is developed [44–48].

1.3 Candidate Waveform for sub-THz (Single carrier vs Multicarrier)

After presenting the THz challenges and limitations, it is crucial to briefly review Single Carrier (SC) and Multi-Carrier (MC) waveforms because it is a crucial design stage to enable the Tbps wireless communication in sub-THz bands. Indeed, both waveforms have several advantages and disadvantages, and based on their strong/weak features, we can conclude which waveform is more suitable for sub-THz bands and then proceed forward in communication system design.

Different MC waveforms have been widely investigated for 5G mobile communication, but all of them share to some extent similar properties compared to SC. The MC popularity is widely used in wireless communication at sub-GHz frequencies and even at the lower mmWave bands below 71GHz. For example, Orthogonal Frequency-Division Multiplexing (OFDM) based modulation is adopted by different standards such as Long-Term Evolution (LTE) downlink mobile communication, digital audio/video broadcasting, different Wifi versions, and also supported in IEEE 802.11ad/ay known as WiGig [33]. Recalling that MC waveform is mainly designed to overcome the channel frequency selectivity due to multipath by dividing the allocated bandwidth into narrow subchannels/subcarriers exposed to almost frequency flat channels (subcarrier band smaller than channel coherence bandwidth). For instance, the frequency-selective fading is more difficult to compensate, and in such a channel, the SC waveforms require more sophisticated equalization techniques. In contrast, the MC basic idea aided by a Cyclic Prefix (CP) helped CP-OFDM modulation to combat deep fading effect and mitigate the performance degradation due to interference with a simple equalization. It is worth mentioning that SC's complex equalization methods were a real challenge few decades ago, especially when the end-users are low-cost devices (e.g., handheld UE in downlink mobile communication). However, the development of the low-cost digital signal processors and the introduction of the Frequency Domain Equalization (FDE) concept of lower complexity enabled the SC implementation even in the frequency-selective channel. Thus, the SC waveform suits well the applications in a frequency-flat fading channel and can be used in frequency-selective fading when the receiver supports the increased complexity of time-domain equalization or can use a simple FDE technique to mitigate the interference. However, MC's reduced equalization complexity comes with more stringent synchronization requirements since any inaccurate frequency synchronization and/or PN deteriorates the system performance due to Inter-Carrier Interference (ICI). For information, the CFO in practical systems is a natural phenomenon due to the local oscillators' frequency mismatch and the Doppler effect when the transmitter and/or the receiver are in mobility. Hence, it is clear that SC waveforms, especially the amplitude modulation (e.g., Pulse Amplitude Modulation (PAM)), and the low order Quadrature Amplitude Modulation (QAM) are more robust to inaccurate CFO synchronization and PN, which is more significant at higher carrier frequency as previously mentioned in Section 1.2.

Another essential aspect to consider when selecting a convenient waveform is its EE, which is directly related to the waveform Peak-to-Average Power Ratio (PAPR) [9]. For clarification, the PAs' efficiency decreases with the PAPR increase to maintain the linear amplification by increasing the power

backoff and operating the PA farther from its saturation point of the maximum efficiency. Hence, the MC waveforms of inherent high PAPR (high amplitude variations with an important difference between its peak and average value) lead to lower PAs efficiency and thus suffer from high power consumption [49]. In contrast, the SC waveform, in general, has much lower PAPR and thus less power consumption. It is worth mentioning that constant-envelope modulations (e.g., CPM) are the only schemes that permit the PAs to operate at maximum efficiency in the saturation region due to their 0 dB PAPR. In addition, the PAPR of SC with amplitude modulations (e.g., QAM or PAM) and their power consumption increase with the modulation order. But the PAM scheme is the worst SC in terms of power efficiency because its PAPR increases rapidly with the modulation order, but it provides the maximum robustness to CFO and PN since no information is transmitted in the phase. In addition, the SC modulation is also more robust to PA non-linearity than MC waveforms [50]. Another advantage of MC that enabled the OFDM widespread is its simple extension to support a multi-access technique (Orthogonal Frequency-Division Multiple Access (OFDMA)) for multi-user scenarios. However, the latter MC advantage is not critical for sub-THz bands, where the thin beamwidth of directive antennas in sub-THz bands enables frequency reuse and allows efficient use of spatial division multiple access (Space Division Multiple Access (SDMA)), and even for some scenarios, Time/Frequency Division Multiple Access (Time Division Multiple Access (TDMA)/Frequency Division Multiple Access (FDMA)) could be possible when the ultra-high data rate is not needed continuously for a single user.

Moreover, some other special requirements can help in judging which SC or MC based scheme is more suitable for a specific scenario/application. For example, the simple MIMO compatibility is crucial for high data rate application, the low latency for uRLLC, and the low power consumption for uplink mobile communication, Low-Power Wide Area (LPWA) network, and Internet of Things (IoT) applications. A lower level of analysis should be considered for these requirements since these properties are more modulation and system dependent. For example, OFDM is more compatible with MIMO than the MC Filter Bank Multi-Carrier modulation (FBMC), constant envelope modulations are preferred over other SC modulations (e.g., QAM, PAM, or Phase Shift Keying (PSK)) for low power IoT [51]. Therefore, it is clear that a particular SC/MC scheme can afford some of these properties, but it is not a general rule for the waveform type (SC or MC).

The main advantages and disadvantages of SC and MC are summarized in Table 1.1. Hence, the sub-THz challenges and limitations in Section 1.2 make the SC waveform, as opposed to the popular MC schemes, more favorable and appropriate for wireless communication systems operating in sub-THz bands. This conclusion is based mainly on the following reasons:

1. In contrast to MC, SC is more robust to RF impairments that increase in sub-THz bands, like PA non-linearity, CFO, and PN [52].
2. SC is more power/energy efficient than MC due to lower PAPR of the former, and mainly SC with constant or near-constant envelope has very low PAPR that leads to low power consumption [9]. This aspect is crucial for sub-THz to permits the PAs to operate at higher efficiency and deliver

Table 1.1 – General comparison of single carrier and multi-carrier waveforms.

Performance indicator	SC	MC
High Spectral efficiency	- to +++	- to +++
High Power efficiency (low PAPR)	+ to +++	-
Robustness to CFO and PN [52, 53]	+ to +++	-
Robustness to PA non-linearity [50, 54, 55]	+++	-
Low equalization complexity	- to ++	++ to +++
Robustness to frequency selective fading	- to ++	+++
Robustness to time selective fading [56]	+ to +++	- to +
MIMO compatibility	+ to +++	- to +++

more transmit power (better Signal-to-Noise Ratio (SNR)) with the limited power sources of current electronics technology.

- Both SC and MC can achieve high SE depending on system configuration, adopted modulation and its order. Similarly, both suffer from a SE penalty when a Zero-Prefix (ZP) or CP is used.
- The considered scenarios in the sub-THz channels have fewer survival multipaths, and thus less frequency selectivity (almost flat) than in the lower bands since the communication is LoS or nearly LoS. Also, the high propagation loss for sub-THz signals and their weak penetration capability leads to receiving the reflected/scattered signals (if any) with very low power. Hence, the SC waveform, especially with FDE, can still operate satisfactorily with low system complexity and affordable cost even if the channel is not perfectly flat. This leads to adopting the Single Carrier Frequency Domain Equalization (SC-FDE) recently in IEEE 802.11ad/ay WiGig standard [33], after its previous adoption in LTE-Advanced (4G) uplink for a better UE power efficiency, 2G global system for mobile communications, 3G Universal Mobile Telecommunications System, IEEE 802.15.4 standard and Bluetooth, etc.

In conclusion, the SC waveform is more suitable for wireless ultra-high data rate up to Tbps with low power consumption for B5G communication at sub-THz bands, and the modulation should provide the following: (1) high robustness to RF impairments (PN, CFO, non-linearity of analog components), (2) high SE, (3) high EE, (4) limited PAPR to operate the PA more efficiently and thus ensure that an acceptable SNR can be achieved with the limited transmit output power, and (5) compatibility with MIMO system such as spatial multiplexing to increase the data rates. In addition, the modulation should be able to cope with few-bits low cost-power data converters, especially in a large-scale MIMO to keep an affordable system cost and power consumption. Besides, a flexible/scalable and adaptive system is an advantage to permit the system adaptation according to channel conditions and received signal power.

It is worth mentioning that our SC waveform conclusion is strongly dependent on the sub-THz scenarios and the current technology maturity. Thus, this analysis and waveform selection should

be revisited for future potential applications, higher frequency bands (true THz or higher), or after a technological breakthrough.

In the true THz context (above 1 THz), a wider bandwidth (in order of THz) is available that can simplify the transceiver design. For instance, the wireless Tbps rate at true THz bands can be achieved with a simple transceiver using On-Off Keying (OOK) based modulations [57, 58], which is not the case for sub-THz bands of smaller available contiguous bandwidth. However, the true THz bands above the BRAVE considered spectrum have more stringent technological limitations, and the signal propagation is limited to extremely short distances with a very low output-power using current electronic technology. Hence, they are more suited nowadays for nano-scale communication paradigms, such as nanotechnology applications for industrial and military fields, nano-bio-sensing, and even intra/inter-chip communication [59, 60]. But, more research is required at the technology level to enable the macro-scale Tbps wireless communication at true THz. For instance, Graphene-based plasmonic technology can be a potential key enabler for wireless communication at these true THz frequencies [47, 61].

Finally, it is obvious that the sub-THz bands are the first stop for B5G communication system, where the low-cost electronic technology can operate but with several critical challenges, limitations, and RF impairments. This thesis aims to create and evaluate new radio technologies that would operate in the sub-THz spectrum and offer the desired B5G performance. The ultimate goal is to define a solution that would reach 1 Tbps (100x peak data rate defined in IMT-2020 for 5G). More insights are given in the next section about our adopted approach to enable and promote the wireless Tbps at sub-THz bands.

1.4 Major Contributions and Thesis Outline

As described earlier, the main challenge to exploit the sub-THz bands for ultra-high data rates wireless applications is its technological limitations, intrinsic RF impairments, and channel characteristics. Even though larger spectrum and MIMO are envisaged [62], but additional breakthroughs are necessary to exploit the sub-THz bands and reach the B5G throughput requirements. Recently, the IEEE 802.11ax standard in sub-GHz band enhanced the data rates using higher-order modulation up to 1024 QAM, wider channels, and the adoption of MIMO technologies. However, the sub-THz systems suffer from more severe RF challenges and technological limitations such as low transmit power, PN, PA non-linearity, and limited resolution for low power/cost ADC as summarized in Section 1.2. Considering these limitations and RF impairments, the usage of high-order APMs becomes not a suitable solution in current sub-THz technology. In addition, the sub-THz channel characteristics impose the replacement of the MC waveform with high PAPR in IEEE 802.11ax by SC modulations, as discussed in Section 1.3. The existing high data rate system uses a spectral-efficient modulation with high PAPR and then seeks for PAPR reduction to limit the power consumption. In contrast to the previous traditional approach,

our approach insists on benefiting from a power-efficient SC waveform that can survive with sub-THz challenges and then enhances its spectral efficiency through IM and advanced MIMO techniques. This thesis is divided into two parts, as shown in Fig. 1.5, and outlined as follows.

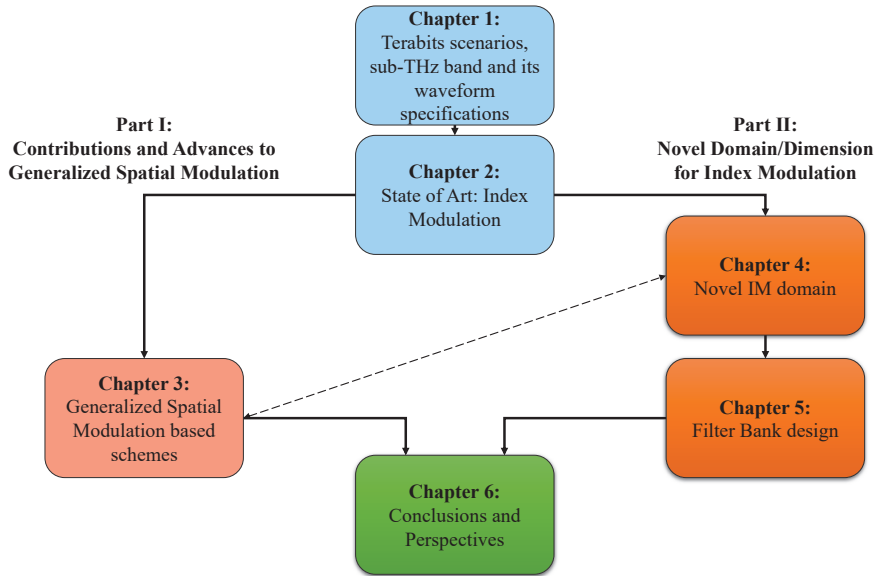


Figure 1.5 – Map of the thesis organization. Any top-down path can be followed to read the thesis, or one of the two parts.

In Chapter 2, the different existing IM domains and techniques are reviewed to converge towards the most spectral-efficient technique suitable for sub-THz. The basic idea of IM is to convey additional information bits contained implicitly in the index of an element among several possible combinations that can be detected at the receiver side. It is worth mentioning that IM has attracted tremendous attention in the last decade, mainly due to its potential spectral and/or energy efficiency enhancement that can help to suit the different B5G requirements from high-data-rate applications to low-power IoT systems. Firstly, the SISO systems based on time, frequency, code IM domains are presented with a focus on their achievable SE, and the combination of the modulation type IM with either time or frequency domains is also provided. Afterward, the MIMO SMX that allows increasing the SE is presented, followed by the investigation of the spatial IM domain. The existing transmit spatial IM and the receive spatial IM schemes that convey information by indexing the activated/targeted transmit/receive antennas respectively, are explored, then their SEs are compared. After presenting these IM techniques, a brief comparison of their advantages and disadvantages is given, and their convenient application is deduced.

In Chapter 3 of the first part I in this thesis, the MIMO SMX and the spatial IM domain, mainly GSM based scheme, are studied in the context of ultra-high data rate systems in sub-THz bands. Besides, several contributions are proposed in order to overcome the main GSM limitations related to sub-THz channel characteristics, MIMO SMX and GSM detection complexity. Then, a scheme is

proposed allowing the increase of MIMO system SE through multidimensional IM. More precisely, in the first section, the potential of the proposed approach of using power-efficient SC accompanied by a spectral-efficient IM technique is investigated in Rayleigh and Rician channels, followed by a link budget and power consumption estimation. Then, a **S-EGSM** is proposed where a selection technique of the indexed antennas' groups is developed, without instantaneous channel side information at the transmitter. The proposed S-EGSM aims to reduce the transmit spatial IM's performance degradation in highly correlated channels without a feedback channel overhead. Also, a **best-effort spatial bit mapping based on gray coding** is proposed to minimize the system BER. After these enhancements, the GSM system with power-efficient SC and its equivalent MIMO SMX of the same SE are compared in sub-THz channel with RF impairments from different perspectives: performance, PAPR, energy efficiency, robustness to PN, optimal detection complexity, cost, and compatibility with low-resolution ADC. Consequently, low-complexity near-optimal detection techniques, called **OSIC-ML** and **O²SIC-ML**, are proposed for MIMO SMX and GSM respectively to enable the extension to large-scale MIMO systems. The results with the proposed detectors show that the optimal performance is achieved with 99% complexity reduction. In the last section, another layer of indexation based on the polarization IM domain is proposed to obtain **DP-GSM** scheme that enhances GSM SE while maintaining its advantages. The theoretical performance assessment of this indexation scheme along with its study in sub-THz scenario are provided to highlight that the advantages of GSM based schemes.

In the second part II, mainly in Chapter 4, a novel IM domain, named **Filter IM domain**, is proposed where another degree of freedom is given to convey information bits by a filter's index. In addition, the derivatives of this domain and its different potential indexation techniques are discussed to highlight that this domain generalizes most existing SISO-IM techniques, especially the time and frequency IM domains. Following our approach and within the filter IM domain, two novel schemes **FSIM, and its two-layers indexation on the in-phase (I)/quadrature (Q) components ("IQ-FSIM")** are proposed to enhance the SE/EE of the power-efficient SC modulation. The study of the proposed systems is completed by proposing optimal detection techniques with low complexity and an appropriate equalization scheme. In order to better assess the performance of the proposed techniques, the lower-bound performance is derived, and a comparative study with the equivalent conventional SC systems and SISO-IM schemes of the same SE is provided. Finally, the filter IM domain is exploited in MIMO system by proposing **SMX-FSIM** to achieve the target rate with low power consumption while respecting the existing sub-THz challenges and limitations. The proposition of MIMO SMX-FSIM system is accompanied by a development of low complexity transceiver, theoretical performance derivation, an assessment from different perspectives, and a comparison with the previously investigated solutions of Chapter 3.

In Chapter 5, the challenges introduced by the proposed filter IM domain to maximize its associated SE/EE are discussed. These challenges lie in the filter bank design that should respect the proposed filter IM schemes' requirements and constraints. In order to tackle the filter bank design of N filter shapes, the problem to be solved by optimization techniques is formulated. But, the addressed

multivariate optimization problem to jointly design the N filter shapes of length L is a non-convex jointly constrained problem with: (1) multimodal quartic objective, (2) quadratic equality, and (3) several multimodal quartic non-convex constraints. In order to solve it, a relaxation and restriction approach is followed, then an algorithm to design 2 filter shapes is proposed and extended to jointly design N filter shapes. Finally, the obtained results are used to evaluate the FSIM scheme and prove that a higher SE and EE can be attained by tackling this challenging problem.

Finally, chapter 6 concludes the thesis and summarizes the main contribution. It also points out the open research problems and provides a discussion about the perspective directions for future works.

1.4.1 Summary of the major contributions

In the following, the main contributions of this thesis are listed briefly:

1. We proposed a new approach based on constant or near-constant envelope SC modulation with IM to reach Tbps with low power consumption. In addition, its feasibility is evaluated depending on error performance, power consumption, complexity, and cost. The performance analysis of the proposed approach SC with spectral-efficient IM is addressed over spatially correlated/uncorrelated Rician and Rayleigh channels as a starting point. Moreover, the link budget is calculated, and the power consumption is estimated based on the waveform PAPR to emphasize the importance of SC-IM for Tbps. Finally, the advantage of power-efficient SC enhanced by spectral-efficient IM scheme for mmWave and sub-THz bands is presented. The details are presented in Section 3.2 and [10, 14].
2. GSM conveys information by the index of the activated Transmit Antenna Combination (TAC) and by the M -ary APM symbols. In conventional GSM, the legitimate TACs are randomly selected, where their number should be a power of 2. An Enhanced Generalized Spatial Modulation (EGSM) based on adaptive legitimate TAC selection is previously proposed in [63] to provide the optimal performance, but EGSM requires the full knowledge of Channel Side Information at the transmitter side (CSIT). In order to avoid the overhead of feedback channel and effective data loss, a S-EGSM without instantaneous CSIT is proposed for highly correlated channels. Moreover, the spatial bit-mapping for conventional GSM is based on binary bit-mapping that can lead to errors in all spatial-bits when the activated TAC is misdetected. In order to reduce the BER, an efficient best-effort spatial bit-mapping (Index-to-Bit) is proposed to reduce the BER degradation in correlated channels. The two proposed techniques are detailed in Section 3.3 and [15].
3. We provided a complete analysis for MIMO SMX and GSM subjected to major sub-THz limitations and RF impairments. This study considers the performance analysis of different power-efficient APM with GSM systems subjected to PN effects over sub-THz channels, then the best APM candidate with GSM is compared to SMX. The proposed approach is assessed

in a realistic sub-THz environment by considering the system performance, robustness to PN, computational complexity, cost, PAPR, link budget, and power consumption. This study is discussed in Section 3.4 and [16, 17].

4. We proposed a novel quasi-linear detector for MIMO SMX, called OSIC-ML. The proposed detector combines the linear Ordered Successive Interference Cancellation (OSIC) technique with the non-linear optimal Maximum Likelihood (ML) technique to enable an important performance enhancement while providing a prominent complexity reduction of non-linear optimal detectors like sphere decoder. The system performance with perfect/imperfect channel estimation and the proposed detector's computational complexity are evaluated with different configurations to highlight its advantages. In addition, the proposed detector is reconfigurable to provide the best performance-complexity tradeoff. This detection scheme is provided in Section 3.5 and [19].
5. We extended the proposed OSIC-ML detector for SMX to GSM system and all its special cases. The proposed detector denoted by Ordered TAC-Ordered Successive Interference Cancellation with ML verification (O^2 SIC-ML) is designed to achieve the optimal performance with a controllable complexity-performance tradeoff even for a large-scale MIMO system. The proposed O^2 SIC-ML detector is accompanied by ordering techniques for the TACs and APM symbols to further reduce the complexity and improve the performance, respectively. The results reveal that O^2 SIC-ML allows reaching the optimal performance of non-linear detector with a complexity reduction in order of 99% as shown in Section 3.6 and [18].
6. We proposed a DP-GSM scheme where we incorporate DP antennas with GSM to reduce the spatial correlation impact and also to enhance the system SE by adding another layer of polarization indexation. Furthermore, we proposed a low complexity detector and joint ML detector for this scheme that estimates jointly all bits conveyed by APM symbols, indexation of TACs and polarization dimension. Moreover, the theoretical performance of DP-GSM is derived and validated by Monte Carlo simulations, then a comparison with uni-polarized GSM and SMX in sub-THz channel with RF impairments is provided. The details of the proposed DP-GSM can be found in Section 3.7 and [20, 21].
7. We explored a novel IM domain named "Filter Domain" that generalizes many existing modulations and SISO-IM domains. In addition, the proposed domain allows attaining higher SE and EE by exploring all available time and frequency resources. This domain's special cases are discussed, and their achievable SEs are presented in Section 4.2 and [22].
8. We proposed a novel scheme within the filter IM domain denoted FSIM. The proposed scheme conveys additional information bits by the index of the selected filter shape at the transmitter side. This indexation can be changed at symbol rate and exploits all available time-frequency resources, and thus permits to achieve higher SE and EE gain in SISO system. However, the

proposed technique allows using non-Nyquist filters to achieve low filters' cross-correlation even if a controllable ISI is introduced. Hence, we developed an ISI estimation and cancellation technique to compensate the added ISI and reach the optimal performance with low-order power-efficient APM schemes. Moreover, the joint ML detector for this scheme is presented, and an optimal detector with low complexity is proposed. The theoretical lower bound of the probability of filter error, total BER and Symbol-Error Rate (SER) are derived and validated by Monte Carlo simulations to truly characterize the proposed scheme. Then, the performance and EE gain of FSIM is shown by comparing to the equivalent SISO systems with/without IM in Additive White Gaussian Noise (AWGN) channel and frequency selective fading channel. The proposed novel FSIM scheme and its study is detailed in Section 4.3 and [22].

9. We developed another scheme in the filter IM domain, called IQ-FSIM, to double the SE gain of FSIM. This technique performs a parallel indexation of the filter shapes on the in-phase and quadrature components. Then, the joint ML and a low complexity detector are designed to estimate the additional information bits, and the previous ISI estimation and cancellation technique is adapted to deal with the separate filter shapes' indexation on I and Q. Finally, the theoretical performance lower bound is deduced and validated, then compared to the previously proposed FSIM scheme.
10. We extended the FSIM to MIMO SMX system in order to deliver the highest SE and EE gain among the existing MIMO systems with/without IM. This superiority is guaranteed by exploiting all the available time, frequency, and spatial resources in contrast to most IM techniques that sacrifice in some resources to enable the indexation. The proposed MIMO FSIM with low complexity linear receiver is evaluated theoretically by using its derived analytical lower bound and Monte Carlo simulations to confirm the achieved enhancements. Then, it is compared in sub-THz with RF impairments from different perspectives to the previously investigated technique in Chapter 3. The proposed approach leads to this end by designing power and spectral-efficient SC waveform using IM and MIMO techniques to achieve B5G rate requirements. The results also show that the proposed MIMO transceiver with a linear low complexity detector is a promising solution for ultra-high data rates system in sub-THz bands due to its high robustness to RF impairments, high SE/EE, and low power consumption. This conclusive research study is presented and discussed in Section 4.5 and [25].
11. We completed this thesis by formulating the challenging problem for filter bank design that respects the proposed filter IM schemes' requirements. This non-convex problem is not addressed previously in the literature, and its multi-non-convexity levels necessitate the simplification by relaxation and restriction. Firstly, an optimization algorithm for designing a filter bank of size two is proposed to search for the filter shape iteratively. Afterward, this algorithm is extended to design a larger number of filter shapes jointly. The problem analysis and discussion reveal that the global optimum can be achieved only when the used initialization

lies in the vicinity of its global optimum. Consequently, the obtained filter bank is used to evaluate FSIM system and compare it to the previous results with non-optimal filters, where we showed that a significant performance gain is achieved. Finally, we discussed the limitations of the proposed filter bank design, and we highlighted at the end of Chapter 5 that there is still room for enhancements in our future work.

1.5 List of Publications and R&D involvement

Publication related to the thesis

The contributions related to the works presented in this manuscript are listed in the following, and ordered historically from the most recent to the oldest:

Accepted Journal articles:

- [J6] N. Bouhlef, M. Saad, F. Bader, "Sub-Terahertz Wireless System using Dual-Polarized Generalized Spatial Modulation with RF Impairments," *IEEE Journal on Selected Areas in Communications*- Special issue on THz Communications and Networking, 2021, In press.
- [J5] M. Saad, N. Al Akkad, H. Hijazi, A. C. Al Ghouwayel, F. Bader and J. Palicot, "Novel MIMO Technique for Wireless Terabits Systems in sub-THz Band," *IEEE Open Journal of Vehicular Technology*, vol. 2, pp. 125-139, Jan. 2021, doi: 10.1109/OJVT.2021.3054737.
- [J4] M. Saad, J. Palicot, F. Bader, A. C. Al Ghouwayel and H. Hijazi, "A Novel Index Modulation Dimension based on Filter Domain: Filter Shapes Index Modulation," *IEEE Transactions on Communications*, *IEEE Transactions on Communications*, Nov. 2020, In press, doi: 10.1109/TCOMM.2020.3039842.
- [J3] H. Hijazi, A. Haroun, M. Saad, A. C. Al Ghouwayel and A. Dhayni, "Near-Optimal Performance with Low Complexity ML-based detector for MIMO Spatial Multiplexing," *IEEE Communications Letters*, vol. 25, no. 1, pp. 122-126, Jan. 2021, doi: 10.1109/LCOMM.2020.3024107.

Journal articles under review:

- [J2] M. Saad, H. Hijazi, A. C. Al Ghouwayel, F. Bader and J. Palicot, "Quadrature Filter Shapes Index Modulation", submitted to *IEEE Transactions on Communications*.
- [J1] M. Saad, H. Hijazi, A. C. Al Ghouwayel, F. Bader and J. Palicot, "Low Complexity Quasi-Optimal Detector for Generalized Spatial Modulation," submitted to *IEEE Communications letters*.

International conferences

- [C7] M. Saad, J. Palicot, F. Bader, A. C. Al Ghouwayel and H. Hijazi, “Filter Shape Index Modulation,” *IEEE International Conference on Communications (ICC)*, Montreal, Canada, June 2021.
- [C6] N. Bouhlef, M. Saad, F. Bader and J. Palicot “Dual-Polarized Generalized Spatial Modulation for Wireless Terabit System,” *2020 IEEE International Symposium on Personal, Indoor and Mobile Radio Communications (PIMRC)*, London, United Kingdom, Sept 2020, pp. 1-7.
- [C5] M. Saad, A. C. Al Ghouwayel, H. Hijazi, F. Bader and J. Palicot, “MIMO Techniques for Wireless Terabits Systems under sub-THz Channel with RF Impairments,” in *IEEE International Conference on Communications (ICC)*, Dublin, Ireland, June 2020, pp. 1-6.
- [C4] M. Saad, F. Bader, A. C. Al Ghouwayel, H. Hijazi, N. Bouhel and J. Palicot, “Generalized Spatial Modulation for Wireless Terabits Systems Under Sub-THz Channel With RF Impairments,” *2020 IEEE International Conference on Acoustics, Speech and Signal Processing (ICASSP)*, Barcelona, Spain, 2020, pp. 5135-5139.
- [C3] M. Saad, F. C. Lteif, A. C. Al Ghouwayel, H. Hijazi, J. Palicot and F. Bader, “Generalized Spatial Modulation in Highly Correlated Channels,” *2019 IEEE 30th International Symposium on Personal, Indoor and Mobile Radio Communications (PIMRC Workshops)*, Istanbul, Turkey, 2019, pp. 1-6.
- [C2] Y. Corre, G. Gougeon, J. Doré, S. Bicaïs, B. Miscopein, M. Saad, J. Palicot, F. Bader, “Sub-THz Spectrum as Enabler for 6G Wireless Communications up to 1 Tbit/s”, *2019 6G wireless summit*, Levi Lapland, Finland, Marc 2019.
- [C1] M. Saad, F. Bader, J. Palicot, A. Chamas Al Ghouwayel and H. Hijazi, “Single Carrier with Index Modulation for Low Power Terabit Systems,” *2019 IEEE Wireless Communications and Networking Conference (WCNC)*, Marrakech, Morocco, Apr. 2019, pp. 1–7.

French National Conference

- [NC1] M. Saad, F. Bader, J. Palicot, A. C. Al Ghouwayel and H. Hijazi, “Nouvelle Approche pour les Systèmes Térabit à Faible Puissance,” *XXVIIème Colloque francophone de traitement du signal et des images-GRETSI*, Lille, France, Aug. 2019.

Poster

- [P1] M. Saad, “Back to single carrier for beyond 5G communications above 90GHz”, IETR PhD student Day, University of South Brittany (UBS)- Campus Tohannic, Vannes, France, June 2018.

Technical deliverable of the French funded project-ANR-17-CE25-0013 BRAVE

- [TR2] M. Saad, F. Bader, J. Palicot, Y. Corre, G. Gougeon, J-B Doré, “Beyond-5G wireless Tbps Scenarios and Requirements,” French funded project-ANR-17-CE25-0013 BRAVE, Tech. Report BRAVE D1.0, 2018. [Online]. Available: <https://hal.archives-ouvertes.fr/hal-01947363/document>.
- [TR1] M. Saad, N. Bouhlef, F. Bader, S. Bicaïis, J-B Doré, Y. Corre, M. Z. Aslam, “Propagation channel model and RF impairments definition and waveform design,” French funded project-ANR-17-CE25-0013 BRAVE, Tech. Report BRAVE D2.1, 2020.

Talks without proceedings

- [T1] M. Saad, “New Methodology for Low Power Terabit Systems/ Nouvelle Méthodologie pour les Systèmes Térabit à Faible Puissance”, IETR/CentraleSupélec seminar, Rennes, France, 21th Feb. 2019.

Work in progress for soon submission

- [1] M. Saad, K. Berberidis, C. Mavrokefalidis, F. Bader, J. Palicot, A. C. Al Ghouwayel and H. Hijazi, “Filter bank design for filter index modulation domain”

Publications indirectly related to this thesis

During my earlier research in PhD, I have had the opportunity to work on broader research aspects indirectly related to this dissertation, in the fields of 5G waveform candidates and the transceiver complexity reduction. The relevant published works are listed here.

International conferences

- [C9] M. Saad, A. Al-Ghouwayel and H. Hijazi, “UFMC Transceiver Complexity Reduction,” *2018 25th IEEE International Conference on Telecommunications (ICT)*, St. Malo, Jun. 2018, pp. 295-301.
- [C8] M. Saad, M. Alawieh, A. C. Al Ghouwayel, H. Hijazi and S. Omar, “On the Hardware Implementation of a Reduced Complexity UFMC Chain,” *2018 IEEE International Conference on Computer and Applications (ICCA)*, Beirut, Aug. 2018, pp. 162-167.

R&D ANR Project Involvement

BRAVE

BRAVE (**B**ack to single-carrier for beyond-5G communications **A**bove 90GHz) is a collaborative research project funded by the French Research Agency ANR started in January 2018 and ends in September 2021. BRAVE aims at creating new physical-layer (PHY) techniques devoted to beyond-5G wireless communications. The partners (Siradel, CentraleSupélec, CEA-Leti and ANFR) are designing new high-data-rate and energy-efficient waveforms that operate in frequencies above 90 GHz. Application to scenarios such as kiosks, backhauling, hotspots are assessed to evaluate the benefit of the proposed technology [8].

The consortium is combining skills from an industry (SIRADEL), an academic laboratory (Centrale-Supélec), a research institute (CEA-Leti) and a regulator (ANFR), which are all familiar with collaborative research and recognized in the field of wireless innovation. The partners bring complementary skills to efficiently tackle the project's different challenges: regulation, signal processing, realistic modeling of the PHY-layer, and software-based evaluation.

My role as a member of CentraleSupélec in this project has been related mainly to ultra-high data rates scenarios' definition, waveform design, and its performance assessment in sub-THz bands with RF impairments. Almost all the publications related to this thesis contribute to this project.

Others

- Participating in the organizing committee of the 2018 25th IEEE International Conference on Telecommunication (ICT) held at Saint-Malo, France, June 2018.
- Earning a mobility grant for research collaboration between IETR-CentralSupélec and University of Patras-Greece from the French National Centre for Scientific Research (CNRS) jointly with "Le Groupement de Recherche Information, Signal, Images et ViSion" (GdR-ISIS) organization in 2019.

1.6 Summary

In this chapter, an overview of the thesis motivation is provided by highlighting B5G communication goals and the sub-THz bands as a key enabler for ultra-high data rates applications. Besides, a brief introduction of the sub-THz bands, its use cases, and its main challenges were given. Afterward, the existing potential waveforms for sub-THz bands are discussed, where it is highlighted that a breakthrough in waveform design is required to achieve B5G target rate in sub-THz environments. Finally, the thesis outline and its main contributions are presented.

Chapter 2

State of Art: Index Modulation

Contents

2.1	Introduction	26
2.2	SISO systems with/without Index Modulation	27
2.2.1	SISO time, frequency and modulation IM domains	28
2.2.2	Code IM- Spreading spectrum	32
2.3	MIMO systems with/without Index Modulation	32
2.3.1	Spatial Multiplexing	33
2.3.2	Spatial IM domain	34
2.3.2.1	Transmit Spatial IM	34
2.3.2.2	Receive Spatial IM	35
2.3.2.3	Summary	36
2.4	Channel/polarization IM domains	39
2.4.1	IM using polarized/Reconfigurable antennas	39
2.4.2	Scattering and Beam based IM	39
2.4.3	Media-Based Modulation using RF mirrors	39
2.5	Multidimensional IM	40
2.5.1	Channel/polarization IM with spatial and time IM domains	40
2.5.2	Modulation Type-based IM with spatial IM domain	41
2.5.3	Spatial IM with time and/or frequency IM	41
2.6	IM advantages/disadvantages and applications	42
2.7	Conclusions/Discussions	43

2.1 Introduction

Future wireless communications systems seek to achieve higher data rates and/or lower energy consumption, and thus they require schemes with enhanced SE/or EE. Nowadays, MIMO technology is integrated into different standards due to its impressive system improvements. However, the traditional modes of MIMO wireless systems (spatial multiplexing, space diversity) are not enough to achieve the wireless Terabits system with low power consumption. The transmitted signal spans mainly a 3D representation, as depicted in Fig. 2.1, where the time/frequency and space are the basis of this representation, and the signal can contain complex symbols that map the information bits to the in-phase and quadrature components. These three domains are previously considered for data multiplexing/diversity or multiple access transmission (TDMA, FDMA, SDMA).

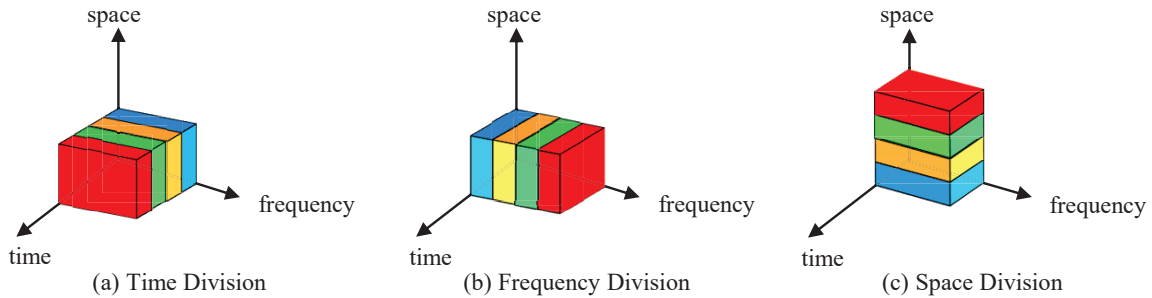


Figure 2.1 – 3D representation for Time, frequency and spatial division.

Recently, Index Modulation has attracted tremendous attention due to its important potential enhancement in the system SE and/or EE achieved by the intelligent exploitation of the signal aspects and its surrounding environment. Firstly, IM is well explored separately and jointly in the spatial, frequency, and temporal domains, and also other dimensions are investigated, as shown in Fig. 2.2. The IM principle is to convey additional information bits implicitly (as Virtual Bits (VBs)) in the selected element index among several possibilities. Note that using an IM strategy, the receiver should be able to correctly detect the indexed element before deducing the associated VBs. For example, in the spatial IM domain, the indexed element is the antenna while it is the time slot, the frequency band/subcarrier in time and frequency IM domain, respectively. The IM immense advantages encouraged the researchers to investigate this concept in many other dimensions based on spreading code, channel medium, radiation patterns of reconfigurable or polarized antennas, and modulation type. Consequently, different multidimensional IM schemes are proposed by combining several existing IM domains.

In this chapter, the traditional SISO system and its combination with time, frequency, and code IM domains are presented in Section 2.2. However, the MIMO systems with/without spatial IM domain are reviewed in Section 2.3. Section 2.4 discusses the different strategies to convey additional information bits by indexing the scattering clusters in a real channel, and the generated radiation patterns/beam with the help of reconfigurable antennas/beamforming or RF mirrors. Finally, the multidimensional IM

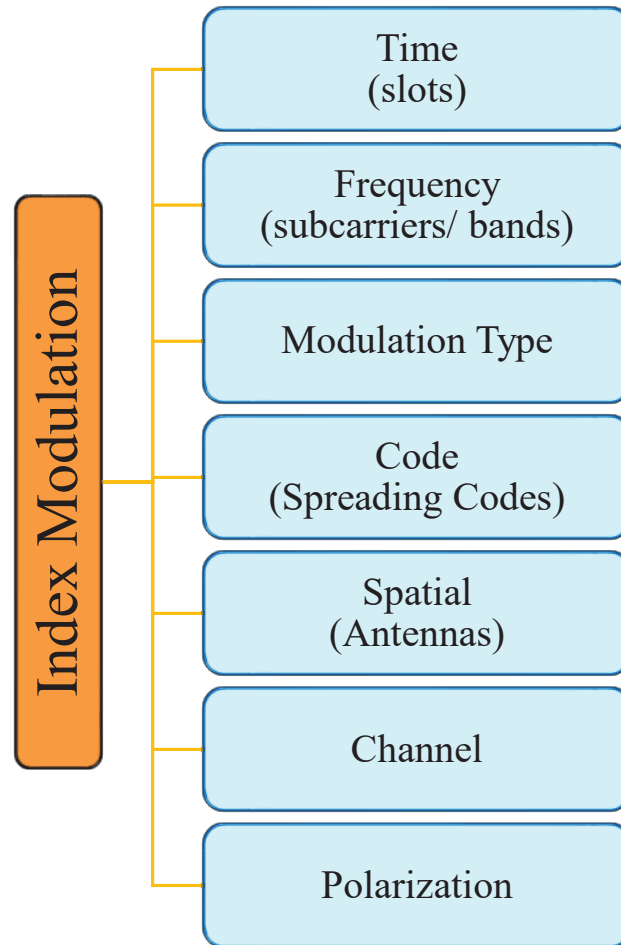


Figure 2.2 – Index modulation domains presented in this chapter.

schemes are introduced in Section 2.5. Finally, the advantages/disadvantages of these IM domains are highlighted in Section 2.6, while Section 2.7 concludes this chapter.

2.2 SISO systems with/without Index Modulation

SISO wireless communication system is the most straightforward antenna technology, where the transmitter and receiver are equipped with one antenna, as depicted in Fig. 2.3. The data is transmitted in a dedicated time-frequency block, where this block can be divided in time to smaller slots, and in frequency to sub-bands to allow data diversity and/or multiplexing. The Time Division Multiplexing (TDM) and Frequency Division Multiplexing (FDM) multiplexing techniques are extended to TDMA and FDMA multiple-access techniques, respectively, to allow simultaneous multi-user communication. Afterward, these domains are explored by IM, where a single or a set of slots/sub-bands are selected

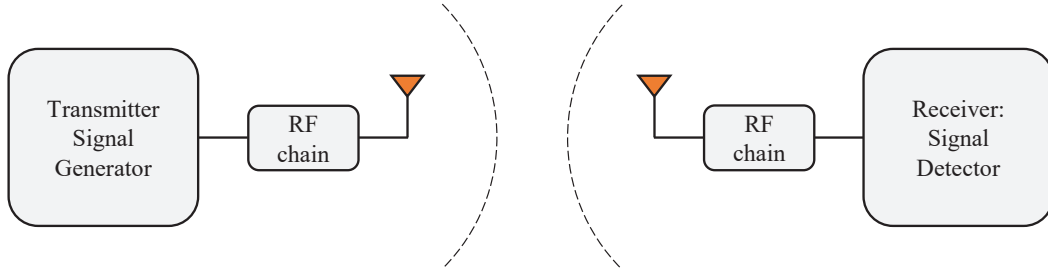


Figure 2.3 – General SISO wireless communication system.

for transmission based on the input bit-stream, and the Rx detects the activated resource to deduce the VBs.

2.2.1 SISO time, frequency and modulation IM domains

In general, the time and frequency domain IMs have limited SE enhancement for high data rate applications, as we will highlight in this sub-section. This limitation is due to the discarding of some available time and frequency resources. The time domain-IM, which activates a single time slot to convey information bits, appeared from many decades in several schemes as OOK, Pulse Position Modulation (PPM) without APM [64], and Generalized Pulse Position Modulation (GPPM) with APM [65]. Then, the SE is enhanced by activating a fixed number of time slots in Single Carrier with Time Index Modulation (SC-TIM) [66], which is proposed with frequency domain equalization (FDE) inspired by the frequency IM domain counterpart Orthogonal Frequency-Division Multiplexing with Sub-carrier Index Modulation (OFDM-SIM) [67] [68]. Similarly, the Generalized Frequency Division Multiplexing with Index Modulation (GFDM-IM) [69] uses the index of activated frequency bands for the same purpose. Their SEs are expressed in Table 2.1 without considering the pulse shaping roll-off factor SE penalty that has similar impact on all schemes. Hence, the unit bit per channel use (bpcu) is used for SE, and the SE in b/s/Hz can be deduced by multiplying the SE in bpcu by the roll-off SE penalty (i.e., $\frac{\text{Symbol Rate}}{\text{Occupied Bandwidth}}$). In this table, we used the following notations: N_T denotes time slots or sub-carriers/frequency bands without the cyclic prefix elements of length N_{CP} , N_T is divided into G groups of N_g elements ($N_T = N_g G$), and N_a elements ($N_a \leq N_g$) within each group are activated to convey information bits in IM. The indexation is performed using an acceptable group size N_g to avoid the high detection complexity with a large N_T . Inspired by OFDM-SIM, the MC Differential Chaos Shift Keying (DCSK) modulation is combined with IM by conveying bits using the activated carrier index and transmitting zero symbols on non-activated ones [70]. Other IM idea is also investigated in OFDM with Orthogonal Frequency-Division Multiplexing with Sub-carrier Number Modulation (OFDM-SNM) [71] [72], where only the number of activated sub-carriers (N_a value) conveys the VBs. The allowed N_a values for a certain OFDM-SNM system is represented in the set ϕ_g , which can contain

all possible values in the extreme case ($\phi_g = \{1, 2, \dots, N_g\}$ where its SE remains lower than that of conventional M -ary APM in most cases, according to their SE equations in Table 2.1).

Moreover, the time and frequency IM domains are adopted with non-orthogonal (overlapped) resources in Faster-Than-Nyquist with Time Index Modulation (FTN-TIM) and Spectral efficient Frequency Division Multiplexing (SeFDM), respectively as shown in Fig. 2.6. These systems suffer from inherited interference, but they can compensate for some of the SE loss or limited gain of their orthogonal version, depending on the compression factor ν at the price of performance degradation.

Similarly, the Index Modulation Multiple Access (IMMA) [73] and Index Modulation with Orthogonal Frequency Division Multiple Access (IM-OFDMA) [74] exploit the appealing advantage of IM in proposing a new Non-Orthogonal Multiple Access (NOMA) in time and frequency, respectively. Note that IMMA is similar to GPPM, whereas it allows resource sharing among N_u users. However, the frequency domain counterpart IM-OFDMA allows activating N_a subcarriers in contrast to IMMA that uses a single time slot. The SE enhancement of IMMA is doubled in Quadrature Index Modulation Multiple Access (QIMMA) [75] by performing separate indexation on the In-phase (I) and Quadrature (Q) components. In other words, QIMMA transmits the real and imaginary parts of the complex symbol through different resources unless the VBs for I and Q are the same. Consequently, these non-orthogonal schemes with a convenient configuration achieve a performance gain that can vanish due to collisions when many users transmit during the same time/frequency resources. Thus, they provide a tradeoff between the SE system enhancement and the collision probability that are affected by the maximum number of users in each time/frequency chunk.

Furthermore, several SE enhancements for these SISO-IM are enabled by allowing the activation of a variable number of sub-carriers in Dual Mode-Orthogonal Frequency-Division Multiplexing with Variable Subcarrier Index Modulation (DM-OFDM-VSIM) [76] and/or independent sub-carriers activation with the same N_a between the I and Q components in Orthogonal Frequency-Division Multiplexing with Quadrature Sub-carrier Index Modulation (OFDM-QSIM) [76] or different N_a between them in Orthogonal Frequency-Division Multiplexing with Hybrid In-phase Quadrature Sub-carrier Index Modulation (OFDM-HIQ-SIM) [77]. For the same reason, the Layered-Orthogonal Frequency-Division Multiplexing with Subcarrier Index Modulation (\mathcal{L} -OFDM-SIM) is proposed in [78] while taking advantage of modulation type IM domain that uses distinguishable modulations between different layers. In each group of N_g subcarriers, the \mathcal{L} -OFDM-SIM scheme activates N_a subcarriers per layer of $N_g - N_a(\mathcal{L} - 1)$ elements. This \mathcal{L} -OFDM-SIM activates more subcarriers in total ($G\mathcal{L}N_a$) compared to OFDM-SIM ($G N_a$), and the former performs another SIM on the remaining non-activated subcarriers successively on the subsequent $\mathcal{L} - 1$ layers within each group that help to enhance the SE of OFDM-SIM.

However, the previous techniques do not use all available time/frequency resources that limit the SE enhancement. Hence, the modulation type IM domain is explored to convey information bits in the selected modulation type while using all available time/frequency resources. For instance, the

dual-mode (DM) IM is introduced to better compensate for the SE loss or limited gain. Indeed, the non-activated slots/bands are exploited to send different and distinguishable APM symbols by means of modulation type IM, so M_A and M_B -ary APM schemes are used respectively during the primary and secondary activated time slots in Dual Mode-Single Carrier with Index Modulation (DM-SC-IM) [79] and Dual Mode-Faster Than Nyquist with Index Modulation (DM-FTN-IM) [80], sub-carriers in Dual Mode-Orthogonal Frequency-Division Multiplexing with Index Modulation (DM-OFDM-IM) as discussed in [81] and its generalized version with a variable number of N_a DM-OFDM-VSIM [82]. These DM-IM techniques convey information by the used modulation type, and this idea is extended to Multi-Mode Orthogonal Frequency-Division Multiplexing with Index Modulation (MM-OFDM-IM) [83], where each subcarrier within a group of N_g elements transmits a symbol from different distinguishable constellation sets, and the permutation of these modulation conveys the VBs, similarly for Multi-Mode-Orthogonal Frequency-Division Multiplexing with Quadrature Index Modulation (MM-OFDM-QIM) but with different indexation on I and Q components. Afterward, a generalized version of Generalized Multi-Mode Orthogonal Frequency-Division Multiplexing with Index Modulation (GMM-OFDM-IM) is proposed in [84] to provide a more flexible choice for SE compared to MM-OFDM-IM, by adjusting the number of subcarriers n_k that use the same modulation order M_k (the special case MM-OFDM-IM is obtained when all M_k are equal to M as shown in Table 2.1).

It is clear from Table 2.1 that most SISO-IM schemes, mainly the time and the frequency IM domains that do not fully use the time and frequency resources, suffer from SE reduction in most configurations. Whereas the modulation type IM domain (DM or MM) that uses all resources can achieve some SE enhancement using distinguishable APMs. Although the SE for single-mode IM schemes is limited, they are promising for low data rate applications, such as the LPWA IoT devices and machine-to-machine communications, because better EE can be achieved with appropriate configurations compared to conventional APM schemes. Indeed, a theoretical EE can be enhanced with low data rate applications to reach 50% as a rough estimation for the same SE with $M = 2$ Binary-Phase Shift Keying (BPSK), $N_g = 4$, $N_a = 2$ as presented in Single carrier Frequency Division Multiple Access with Index Modulation (SC-FDMA-IM) [85]. However, their EE is dramatically reduced compared to conventional APM schemes (QAM) for high data rate applications. This lower EE is due to the need for higher power (SNR) to maintain the same SE, by using either higher M -ary APM when not all resources are used according to Table 2.1, or non-orthogonal schemes with inherited interference.

Table 2.1 – SE summary of most existing SISO schemes with/without IM.

IM Domain	SC/ MC	System Name	Spectral Efficiency (bpcu)	Inherited Interference
-	SC	Linear APM: QAM, PSK,...	$\log_2 M$	No
	SC	SC-FDE	$\frac{N_T \log_2 M}{N_T + N_{CP}}$	No
	MC	OFDM		
Time	SC	OOK	1	No
Time	SC	PPM [64]	$\frac{\lfloor \log_2 N_g \rfloor}{N_g}$	No
Time	SC	GPPM [65]	$\frac{\lfloor \log_2 N_g \rfloor + \log_2 M}{N_g}$	No
Time	SC	NOMA : IMMA [73]	$\frac{N_u (\lfloor \log_2 N_g \rfloor + \log_2 M)}{N_g}$	YES
Time	SC	NOMA : QIMMA [75]	$\frac{N_u (2 \lfloor \log_2 N_g \rfloor + \log_2 M)}{N_g}$	YES
Frequency	SC	NOMA : IM-OFDMA [74]	$\frac{N_u (\log_2 M + \lfloor \log_2 C_{N_g}^{N_a} \rfloor)}{N_g}$	YES
Time	SC	FDE SC-TIM [66] SC-FDMA-IM [85]	$\frac{G(N_a \log_2 M + \lfloor \log_2 C_{N_g}^{N_a} \rfloor)}{N_T + N_{CP}}$	No
Frequency	MC	OFDM-SIM [67] [68] GFDM-IM [69]		
Frequency	MC	OFDM-VSIM [76]	$\frac{G(\lfloor \log_2 (\sum_{N_a \in \phi_g} M^{N_a} C_{N_g}^{N_a}) \rfloor)}{N_T + N_{CP}}$ Extreme case: $\frac{G(\lfloor \log_2 (M+1)^{N_g} \rfloor)}{N_T + N_{CP}}$	No
Frequency	MC	OFDM-QSIM [76]	$\frac{G(N_a \log_2 M + 2 \lfloor \log_2 C_{N_g}^{N_a} \rfloor)}{N_T + N_{CP}}$	No
Frequency	MC	OFDM-HIQ-SIM [77]	$\frac{G((N_{a_I} + N_{a_Q}) \log_2 \sqrt{M} + \lfloor \log_2 C_{N_g}^{N_{a_I}} C_{N_g}^{N_{a_Q}} \rfloor)}{N_T + N_{CP}}$	No
Frequency	MC	OFDM-SNM [71] [72]	$\frac{G(N_a \log_2 M + \lfloor \log_2 N_g \rfloor)}{N_T + N_{CP}}, 1 \leq N_a \leq N_g$ Average: $\frac{G(0.5(1+N_g) \log_2 M + \lfloor \log_2 N_g \rfloor)}{N_T + N_{CP}}$	No
Time Frequency	SC	FTN-TIM [86] SeFDM-IM [87]	$\frac{1}{\nu} \frac{G(N_a \log_2 M + \lfloor \log_2 C_{N_g}^{N_a} \rfloor)}{N_T + N_{CP}}$	YES
Modulation	SC	DM-FTN-IM [80]	$\frac{1}{\nu} \frac{G(N_a \log_2 M_A + (N_g - N_a) \log_2 M_B + \lfloor \log_2 C_{N_g}^{N_a} \rfloor)}{N_T + N_{CP}}$	YES
Modulation Modulation	SC MC	DM-SC-IM [79] DM-OFDM-IM [81]	$\frac{G(N_a \log_2 M_A + (N_g - N_a) \log_2 M_B + \lfloor \log_2 C_{N_g}^{N_a} \rfloor)}{N_T + N_{CP}}$	No
Frequency	MC	DM-OFDM-VSIM [82]	$\frac{G(\lfloor \log_2 (\sum_{N_a \in \phi_g} M_A^{N_a} M_B^{N_g - N_a} C_{N_g}^{N_a}) \rfloor)}{N_T + N_{CP}}$	No
Modulation	MC	MM-OFDM-IM [83]	$\frac{G(\lfloor \log_2 N_g \rfloor + N_g \log_2 M)}{N_T + N_{CP}}$	No
Modulation	MC	MM-OFDM-QIM [83]	$\frac{G(2 \lfloor \log_2 N_g \rfloor + N_g \log_2 M)}{N_T + N_{CP}}$	No
Modulation	MC	GMM-OFDM-IM [84]	$\frac{G(\lfloor \log_2 N_g \rfloor + \sum_{k=1}^K n_k \log_2 M_k)}{N_T + N_{CP}}$ where $\sum_{k=1}^K n_k = N_g$ and $M_1 > M_2 > \dots M_K$	No
Frequency	MC	\mathcal{L} -OFDM-SIM [78]	$\frac{G \mathcal{L}(\lfloor \log_2 C_{N_g - N_a}^{N_a} \rfloor + N_a \log_2 M)}{N_T + N_{CP}}$	No

In conclusion, all orthogonal/non-orthogonal time and frequency SISO-IM schemes in Table 2.1 achieves a fraction of bit SE gain on average in their best-case scenario compared to a linear APM without IM (e.g., QAM). In contrast, the modulation type IM domain (DM/MM) is more spectrally efficient among these SISO-IM domains only when distinguishable APM constellations' sets can be guaranteed. Similarly, the NOMA schemes enhance the SE only when the number of users is near the number of allocated time/frequency resources ($N_u \approx N_g$), but this will lead to a larger collision probability between users' data (25% for $N_u = N_g$ [73]) and thus causes overall performance degradation.

Finally, it is worth mentioning that some schemes are investigated with spatial multiplexing to compensate the SE loss or limited gain by benefiting from the multiplexing gain as in MIMO OFDM-SIM [88].

2.2.2 Code IM- Spreading spectrum

The appealing SE/EE advantages of IM have inspired the combination of IM also with the spreading spectrum techniques, where a Code Index Modulation-Spread Spectrum (CIM-SS) and its generalization Generalized Code Index Modulation-Spread Spectrum (GCIM-SS) are proposed in [89,90]. The code IM domain principle is to convey bits by selecting one of the predefined spreading codes (e.g., Walsh code). In contrast to the traditional SS scheme, the used code at the Transmitters (Tx) side is not known for the Receiver (Rx), so it should estimate the selected code to recover the VBs and use it for de-spreading before APM detection. The GCIM ameliorates more the SE by using different spreading codes for the in-phase and quadrature components. Note that the CIM-SS scheme is also investigated with differential chaos shift keying in [91].

However, it is worth mentioning that the indexation in this domain for multiple-access purpose leads to user interference due to data collision when different users use the same code. Hence, this IM domain loses the advantage of code orthogonal multiple access techniques (e.g., Code Division Multiple Access (CDMA)) that dedicates a single code for each user.

2.3 MIMO systems with/without Index Modulation

MIMO wireless system is composed of multiple antennas at the transmitter and receiver side, as depicted in Fig. 2.4, and it gives another degree of freedom to allow simultaneous data transmission on the same allocated time slot and frequency band. However, the emitted symbol from the Transmit Antennas (TAs) can be either the same to achieve only diversity gain (transmit diversity) or different to introduce multiplexing gain (Spatial Multiplexing). In general, a spatial diversity in MIMO systems can be achieved when various replicas of the same transmitted symbols are received from independent path fading that allows enhancing the performance. Hence, the multiplexing adds SE gain while the

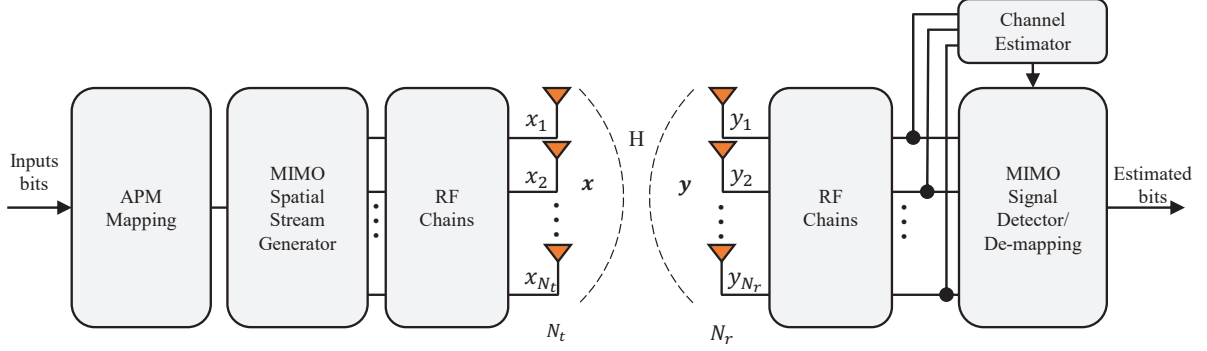


Figure 2.4 – MIMO transceiver System Model with N_t transmit antennas and N_r receive antennas.

diversity enables the increase in EE. For example, a full-diversity over flat-fading channels is obtained by Space-Time Block Code (STBC) [92] with two TAs, but a capacity loss will occur with a larger number of TAs [93]. Hence, the MIMO system has a fundamental tradeoff between the multiplexing and the diversity gain [94]. Since our ultimate goal is to achieve high SE using MIMO and IM techniques, we will focus in sub-section 2.3.1 on MIMO SMX, and in sub-section 2.3.2 on different spatial IM schemes, where a SE improvement could be achieved. Whereas, the other techniques that aim for diversity enhancement only (e.g., transmit/receive diversity, STBC, etc.) are not presented.

2.3.1 Spatial Multiplexing

A MIMO-SMX system (also known as Bell Laboratories Layered Space-Time (BLAST)) using N_t TAs and N_r Receive Antennas (RAs) with $N_r \geq N_t$ is considered as depicted in Fig. 2.4, where all TAs transmit simultaneously different symbols of modulation order M [95, 96]. Thus, the number of bits per SMX symbol is expressed as:

$$\mathcal{L}_{SMX} = N_t \log_2 M. \quad (2.1)$$

The received signal vector \mathbf{y} is expressed as:

$$\mathbf{y} = \mathbf{H}\mathbf{x} + \mathbf{v}, \quad (2.2)$$

where $\mathbf{H} = [\mathbf{h}_1, \dots, \mathbf{h}_{N_t}]$ is the $N_r \times N_t$ MIMO channel matrix with \mathbf{h}_i is the column vector of N_r elements, $\mathbf{x} = [x_1, \dots, x_{N_t}]^T$ is the transmitted vector, \mathbf{v} is $N_r \times 1$ channel noise vector and its elements v_r obeys the independent and identically distributed (i.i.d.) AWGN with zero-mean and variance of σ_v^2 , i.e., $\mathcal{CN}(0, \sigma_v^2)$ for $r = 1, \dots, N_r$. The power of the transmit symbols is normalized.

At the receiver side, the ML detector for estimating \mathbf{x} performs an exhaustive search over all the possible transmit vector as described by:

$$\hat{\mathbf{x}}_{\text{ML}} = \arg \min_{\mathbf{x} \in \mathcal{X}'} \|\mathbf{y} - \hat{\mathbf{H}}\mathbf{x}\|^2, \quad (2.3)$$

where \mathcal{X}' denotes the set of all possible transmit vectors of size M^{N_t} , $\hat{\mathbf{x}}$ is the estimated transmit vectors, and $\hat{\mathbf{H}}$ is the estimated channel.

2.3.2 Spatial IM domain

Spatial IM uses the indices of the different combinations for transmitter or receiver antennas to convey additional information bits by activating some transmit antennas and/or targeting some receive antennas. The former is a Transmit Spatial Modulation, whereas the latter is a Receive Spatial Modulation as shown in Fig. 2.6. In the following, both sub-categories of the spatial IM domain are presented.

2.3.2.1 Transmit Spatial IM

The transmit Spatial Modulation (SM) activates a single antenna at the transmitter side to send an M -ary APM symbol [97, 98]. The detection of the index of the activated antenna among the N_t TAs conveys additional $\lfloor \log_2(N_t) \rfloor$ VBs (spatial bits) to $\log_2(M)$ real bits. In addition, an arbitrary number of TAs is allowed in Fractional Bit Encoded Spatial Modulation (FBE-SM) [99] to facilitate fractional bit rates over time, and in Spatial Modulation (SM) conceived for an arbitrary number of TAs (Spatial Modulation with an Arbitrary number of Transmit Antennas (SM-ATA)) [100]. However, another variant is proposed in [101] to combat the error propagation effect of FBE-SM, due to unequal bit mapping for the transmitted symbols in [99], by changing the constellation order M of APM symbol to keep the same number of total bits at each time slot.

Moreover, a simplified version of SM named Space Shift Keying (SSK) is introduced. All the information bits of SSK are transmitted through IM without any APM symbol [102] to reduce the receiver complexity, but at the price of lower SE for the same number of TAs. Later on, these IM methods (SSK and SM) are generalized to allow the activation of a fixed number of transmit antennas N_a at the same time to increase the number of virtual bits in Generalized Space Shift Keying (GSSK) [103] and GSM respectively. The latter can transmit the same APM symbol on all activated TAs to add a transmit diversity [104], or different APM symbols on activated TAs to have a higher SE by benefiting from the multiplexing gain [105]. In addition, SSK and GSSK are studied over multiple access independent fading channels [106]. The authors proved that these modulations with a multi-user detector are more robust to multi-user interference compared to conventional APM schemes. Moreover, GSSK has SE higher than SSK for the same number of transmit antennas at the price of performance degradation. Another SE enhancement method is added in Bi-Space Shift Keying

(Bi-SSK) [107], Quadrature Spatial Modulation (QSM) [108], to double the number of virtual bits of SSK and SM respectively by activating different TAs for in-phase and quadrature components of the signal. Afterward, Generalized-Quadrature Spatial Modulation (G-QSM) [109] extended QSM concept by dividing the N_t TAs into N_g subgroups of size N_{t_i} then performs parallel QSM with same/different M_i -ary APM. Note that SM and QSM are combined with Space-Time coding in Space-Time Block Coded Spatial Modulation (STBC-SM) and ST-QSM respectively [110, 111], to provide also a diversity gain.

Furthermore, Extended Space Shift Keying (ExSSK) is proposed in [112] that allows the activation of variable number of transmit antennas varying between 1 and $N_t - 1$ to have $\lfloor \log_2(2^{N_t} - 2) \rfloor$ as virtual bits, and another version of ExSSK is introduced later in [113] that conveys information bits even when no antenna or all antennas are activated to have N_t virtual bits. Similarly, the variable number of active TAs is introduced in [114, 115] with SM (called Extended SM (Extended Spatial Modulation (ExSM))) and Variable N_a Generalized Spatial Modulation (VGSM) scheme with single APM symbol to have $\lfloor \log_2(2^{N_t} - 2) \rfloor$ and $\log_2(2^{N_t} - 1)$ virtual bits respectively, because at least one TA is needed to transmit the APM symbol. The latter permits the usage of an arbitrary number of TAs with the help of the FBE-SM concept. These transmit spatial IM schemes are summarized in Table 2.2 to highlight their SE and the adopted methods to conveying the spatial information bits.

Additionally, the differential counterpart of SM (Differential Spatial Modulation (DSM)) [116, 117], and QSM (Differential Quadrature Spatial Modulation (DQSM)) [118] are proposed to eliminate the requirement of Channel Side Information (CSI) at the receiver side. However, DSM has 3dB SNR penalty like most differential-based modulations compared to coherent SM [119], and it was enhanced in [120] to achieve full diversity with two TAs.

2.3.2.2 Receive Spatial IM

A similar analogy for transmit spatial IM schemes (SM, GSM, QSM, SSK, and ExSSK) is considered at the receiver side to convey bits by the index of RA(s). For instance, the Transmit Pre-coding aided Spatial Modulation (TPSM) and Generalized Pre-coding Aided Spatial Modulation (GPSM) target a single RA [121] and multiple RAs [122] while transmitting a single and multiple APM symbol(s) respectively. Inspired by QSM concept, a Generalized Pre-coding-Aided Quadrature Spatial Modulation (GPQSM) is explored in [123] to double the VBs of GPSM. Also, different schemes without APM symbols are considered to reduce more the Rx complexity like Receive Antenna Shift Keying (RASK) and Extended Receive Antenna Shift Keying (ERASK) that target a single RA [124] and a variable number of RAs [125] respectively. Moreover, the authors of [125] upgraded the ERASK technique by incorporating an APM symbol to achieve higher SE, as shown in Table 2.2, and this scheme is called Extended Receive Spatial Modulation (ERSM) [126]. For instance, ERSM uses two different power levels for primary/secondary targeted RAs to allow APM symbol detection, especially when no RAs are targeted. Inspired by DSM, the Transmit Pre-coding Aided Differential

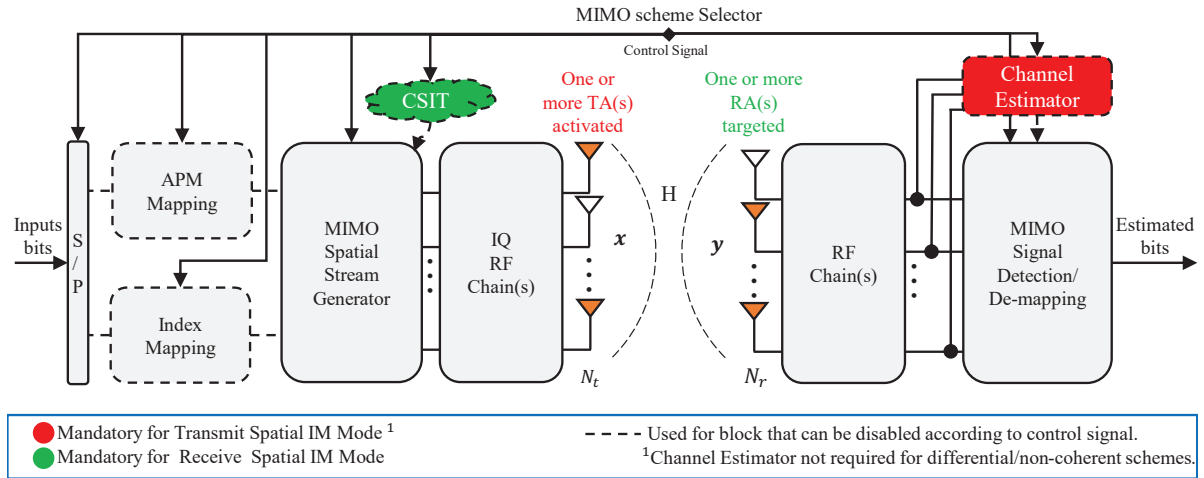


Figure 2.5 – General system model for MIMO system with/without spatial IM.

Spatial Modulation (PDSM) is proposed to eliminate the requirements of the power normalization factor in TPCM detection [127]. Note that the receive spatial IM schemes require the full knowledge of CSIT to enable the pre-coding for focusing the emitted power on selected RA(s), as depicted in Fig. 2.5. For instance, the linear pre-coding such as Transmit ZF/MMSE (Transmit Zero-Forcing pre-coding (TZF)/Transmit Minimum Mean-Squared Error pre-coding (TMMSE)) and Maximum Ratio Transmission Pre-coding (MRT) pre-coding techniques are mostly used to keep a low transmitter complexity, where TZF cancels the interference on non-target RAs by using the pseudo-inverse of the channel matrix and requires more antennas at Tx side ($N_t \geq N_r$), while the latter allows increasing the spatial gain on target RAs by using the Hermitian of the channel matrix. Therefore, a sufficiently large number of TAs is necessary for a better beam-focusing to allow correct detection of targeted RA(s).

2.3.2.3 Summary

A general system model for MIMO schemes with/without spatial IM is represented in Fig. 2.5. The control signal 'MIMO scheme selector' in Fig. 2.5 allows to: enable/disable the APM symbol(s) transmission, adapt the number of bits associated with APM symbol(s) and the indexed element, instruct the signal detection/de-mapping and the MIMO spatial stream generator. According to the control signal, the latter block adapts to the selected MIMO schemes by the following: (1) enable/disable the transmit precoding layer; (2) distribute the real and imaginary parts of APM symbol(s) if any; (3) create the transmit vector with 0 up to N_t activated TA(s) to target 0 up to N_r RA(s). In the transmit spatial IM context, the channel estimator at the Rx side is required with all schemes except the differential schemes like DSM [116]. Besides, not all TAs are activated together during all the transmission time unless SMX without Transmit Spatial IM is selected. In the receive spatial IM context, the CSIT is exploited to target the RA(s) by using all TAs, and the coherent/non-coherent detection can be performed with/without the estimated channel. Note that the full or partial

CSIT is not necessary with Transmit Spatial IM, but it can be used at the Tx side to enhance the system performance [15, 63, 128–130]. Furthermore, the authors in [131] proposed a Joint transmitter-receiver SM (JSM) that uses the indices of TAs, RAs, and the APM symbols for data transmission. Hence, JSM is able to provide simultaneously transmit/receive diversity and multiplexing gain.

Finally, the presented MIMO schemes with spatial IM domain are summarized in Table 2.2 with their SEs. Although not all schemes are able to reach high SE, which is needed to reach ultra-high data rates, these low SE systems can be suitable for different applications that target different advantages such as lower Tx and/or Rx cost, less Inter-Antenna Interference (IAI), less detection complexity, higher EE compared to traditional MIMO systems, etc. These advantages/disadvantages will be discussed more in Section 2.6.

Table 2.2 – Summary of existing MIMO schemes in the spatial IM domain.

	System Name	Spectral Efficiency (bpcu)	1	2	3	Number of activated/targeted antenna(s)
Transmit Spatial IM	SSK [102]	$\lfloor \log_2 N_t \rfloor$				1
	GSSK [103]	$\lfloor \log_2 C_{N_t}^{N_a} \rfloor$				N_a
	Bi-SSK [107]	$2\lfloor \log_2 N_t \rfloor$		✓		$N_a = 1$ for I/Q: {1, 2}
	ExSSK [112]	$\lfloor \log_2(2^{N_t} - 2) \rfloor$			✓	$\{1, \dots, N_t - 1\}$
	ExSSK [113]	N_t			✓	$\{0, \dots, N_t\}$
	SM [97, 98]	$\log_2 M + \lfloor \log_2 N_t \rfloor$	✓			1
	DSM [116]	$\log_2 M + \frac{1}{N_t} \lfloor \log_2(N_t!) \rfloor$	✓			1
	FBE-SM [99]	$\approx \log_2 M + \log_2 N_t$	✓			1
	SM-ATA [100]	$\log_2 M + \lfloor \log_2 N_t \rfloor$	✓			1
	GSM using diversity [104]	$\log_2 M + \lfloor \log_2 C_{N_t}^{N_a} \rfloor$	✓			N_a
	GSM [105]	$N_a \log_2 M + \lfloor \log_2 C_{N_t}^{N_a} \rfloor$	✓			N_a
	QSM [108]	$\log_2 M + 2\lfloor \log_2 N_t \rfloor$	✓	✓		$N_a = 1$ for I/Q: {1, 2}
	DQSM [118]	$\log_2 M + \frac{2}{N_t} \lfloor \log_2 N_t! \rfloor$	✓	✓		$N_a = 1$ for I/Q: {1, 2}
	G-QSM [109]	$\sum_{i=1}^{N_g} \log_2 M_i + 2\lfloor \log_2 N_{t_i} \rfloor$	✓	✓		$N_a = 1$ for I/Q in each subgroup: $\{N_g, 2N_g\}$
	ExSM [114]	$\log_2 M + \lfloor \log_2(2^{N_t} - 2) \rfloor$	✓		✓	$\{1, \dots, N_t - 1\}$
FBE-VGSM using diversity [115]	$\approx \log_2 M + \log_2(2^{N_t} - 1)$	✓		✓	$\{1, \dots, N_t\}$	
Receive Spatial IM	RASK [124]	$\lfloor \log_2 N_r \rfloor$				1
	ERASK [125]	N_r			✓	$\{0, \dots, N_r\}$
	TPSM [121]	$\log_2 M + \lfloor \log_2 N_r \rfloor$	✓			1
	GPSM [122]	$N_a \log_2 M + \lfloor \log_2 C_{N_r}^{N_a} \rfloor$	✓			N_a
	GPQSM [123]	$N_a \log_2 M + 2\lfloor \log_2 C_{N_r}^{N_a} \rfloor$	✓	✓		Fixed N_a for I/Q: $\{N_a, \dots, \min(2N_a, N_r)\}$
	ERSM [126]	$\log_2 M + N_r$	✓			$\{0, \dots, N_r\}$
	PDSM [127]	$\log_2 M + \frac{1}{N_r} \lfloor \log_2(N_r!) \rfloor$	✓			1

¹ with APM symbol(s).² using separate indexation for I and Q.³ with variable N_a .

2.4 Channel/polarization IM domains

More IM schemes are investigated by exploiting the channel and antenna characteristics. For instance, the latter take advantage of the different radiation patterns/planes generated using reconfigurable/polarized antennas for example. However, the channel-based IM domain can convey information by indexing the different real scattering clusters or emitted beams, as shown in Fig. 2.6.

2.4.1 IM using polarized/Reconfigurable antennas

The reconfigurable antenna characteristics attracted the researchers also to apply the IM concept, and thus it allows the SE enhancement by exploiting the multiple possible Radiation Patterns (RPs). For instance, SM with reconfigurable antennas creates N_{RP} different RPs that can be indexed to transmit $\log_2 N_{RP}$ bpcu in addition to M -ary APM symbol [132]. Similarly, the scheme based on SSK is studied in [133] to achieve lower transceiver complexity. However, another architecture based on the polarization IM dimension is proposed in [134] and called Polarization Modulation. This modulation bears the VBs by the different RPs possibility emitted from the polarized TA, and it allows to transmit 1 extra bit by each dual-polarized TA.

2.4.2 Scattering and Beam based IM

In addition, Spatial Scattering Modulation (SSM) is proposed for mmWave uplink scenario in [135], and it uses the analog and hybrid beamforming with a large antenna array to exploit through IM the existing scattering clusters N_{cl} in real channel. SSM transmits $\log_2 N_{cl} + \log_2 M$ bits with a single stream steered towards the selected cluster. However, SSM restricts its design to an orthogonal beam and only at the Tx side by exciting the designated beam port at the transmitter beamforming network's input. Consequently, a Beam IM scheme is proposed later to relax this condition and make such a system more practical and feasible [136]. Moreover, a generalized version like GSM called Generalized Beam-space Modulation using Multiplexing (GBMM) with more RF chains at the Tx side is introduced in [137] to transmits multiple data streams simultaneously and achieves higher SE. In comparison to Receive Spatial IM schemes, the emitted beam of these channel IM schemes targets the selected scattering cluster and not the RAs.

2.4.3 Media-Based Modulation using RF mirrors

Media-Based Modulation (MBM) is one of the newest members of the IM family that can be implemented by intentionally altering the far-field radiation pattern of a reconfigurable antenna by adjusting the On/Off status of the added RF mirrors according to the information bits. This scheme is based on parasitic reconfigurable antenna elements that contain PIN diodes to allow changing its status.

In this sense, MBM offers an entirely new dimension for the transmission of digital information: the realizations of wireless channels themselves by deliberate perturbation of the transmission environment [138, 139]. Note that MBM scheme is investigated in different transmission modes SISO, SIMO, and MIMO where the results show that it has important SE and performance gain only when more than one RA is available [140].

MBM based schemes use $N_{RF\ mirrors}$ RF mirrors around each TAs to generate different channel states and convey $N_{RF\ mirrors}$ additional information bits as long as the independence of the generated RPs is guaranteed. However, a channel sounding is required prior to data transmission to estimate the different fades realizations. A differential MBM (Differential Media-Based Modulation (DMBM)) scheme is proposed in [141] to combat the channel sounding burden, but it leads to performance degradation. Besides, MBM is also considered with MIMO SMX (SMX-MBM) and STBC. The former allows reducing the transmitter cost by decreasing the number of required RF mirrors for higher SE [142], whereas the latter adds a diversity gain for a better system performance [143].

2.5 Multidimensional IM

The different IM domains shown in Fig. 2.2 are also investigated jointly as multidimensional IM schemes in order to combine various advantages. In the following, we present a few combinations of IM domains that have more SE advantages, and for a wider survey, the readers are referred to the most recent survey about multidimensional IM [144].

2.5.1 Channel/polarization IM with spatial and time IM domains

The polarization dimension can be integrated with all MIMO-IM schemes, and it allows achieving higher SE, lower antenna array space occupancy, and/or better system performance in severe channel conditions. The polarization domain's appealing advantage is that it can be easily distinguished at the receiver side even with a realistic cross-polarization correlation level. For this reason, the dual-polarized TAs are used with different spatial IM schemes (e.g., Dual Polarized Spatial Modulation (DP-SM) [145, 146], DP-TPSM [147] and DP-GSM [20, 21]).

Moreover, MBM based on RF mirrors was also combined with the different spatial IM schemes (SM, GSM, DP-SM), e.g., SM-MBM [148], Dual Polarized Spatial Modulation with Media-Based Modulation (DP-SM-MBM) [149], or GSM-MBM [139] techniques. These combined systems enhance the SE progressively but at the price of larger acceptable detection complexity and transmitter cost (for more details check [140, Table 1]).

Furthermore, the time IM domain is merged with MBM and SM-MBM to obtain their time-indexed version TI-MBM and TI-SM-MBM, respectively [148], where the virtual bits are encapsulated on the activated time slots and RPs for both schemes, and also by the selected TA with the latter. It is clear

that the inherent SE drawback of the time IM domain will be reflected on these multidimensional schemes TI-MBM and TI-SM-MBM, and thus leads to lower SE compared to MBM and SM-MBM, respectively.

2.5.2 Modulation Type-based IM with spatial IM domain

The modulation type is also considered as another dimension for IM, where the selected modulation scheme APM conveys some information bits. However, the different APM constellations should be distinguishable to allow correct VBs recovery. For instance, the dual-mode and multi-mode schemes presented in Section 2.2 take advantage of the modulation type IM to convey information bits by using different APM.

This domain is incorporated with the spatial IM domain and mainly with SM and GSM (Multi-Mode Spatial Modulation (MM-SM) and Multi-Mode Generalized Spatial Modulation (MM-GSM)) to achieve higher SE and/or performance gain [150, 151]. The idea of MM-GSM is to transmit symbols from a primary APM set when N_a TAs are activated (similar to GSM) and to use one or more secondary APM sets with all available TAs, inspired from modulation type IM domain. This strategy increases the number of possible combinations, and thus more VBs are induced in addition to APM bits. Note that the secondary APM sets size is half of the primary APM order $\frac{M}{2}$ to keep the same number of bits for all transmitted symbols [150]. Besides, its counterpart in the Frequency Domain Multi-Mode Spatial Modulation (FD-MM-SM) is presented in [152] to provide mainly the same advantages by exploiting the spatial and modulation type IM, but the full-RF Tx architecture is always required in the frequency domain based indexation.

2.5.3 Spatial IM with time and/or frequency IM

In addition to the previous domain combinations, Generalized Spatial-Frequency Index Modulation (GSFIM) exploits both spatial and frequency (subcarrier) IM domains to convey additional information bits by combining GSM with OFDM-SIM concept [153]. Thus, GSFIM tries to overcome the SE limitation of OFDM-SIM. Similarly, the space-time IM (STIM) is considered by using SM and SC-TIM principle, where the VBs are conveyed by the index of activated time slots and the selected TA during these time slots [154].

Moreover, dispersion matrix-based IM schemes are adopted to exploit different IM domains simultaneously, where the spatial IM dimension is used with time IM and/or frequency IM. These joint-IM schemes provide a good tradeoff between multiplexing and diversity gains for a better performance in dispersive channel as shown in: coherent Space-Time Shift Keying (STSK) [155–159], differential STSK [155], Multi-Set Space-Time Shift Keying (MS-STSK) [159], Space-Frequency Shift Keying (SFSK) and Space-Time-Frequency Shift Keying (STFSK) [160].

2.6 IM advantages/disadvantages and applications

After summarizing most of the existing IM schemes in this Chapter, it is interesting to highlight their potential advantages and challenges. In the SISO context, all systems in the time and frequency IM domains have a low SE gain and even a significant SE loss in most cases compared to the original schemes without IM. This drawback is a consequence of discarding some available time/frequency resources to enable IM technology. However, they still provide SE gain with low modulation APM order (e.g., BPSK). Thus, they are suitable for LPWA IoT devices due to their essential EE gain at low data rates, as shown in [85]. Whereas, their SE/EE advantages vanish at higher data rates due to the usage of higher M -ary APM order compared to conventional systems without IM. Note the non-orthogonal schemes (Faster-Than-Nyquist with Index Modulation (FTN-IM) and SEFDM-IM based schemes) and/or their combination with Modulation type IM as in dual-mode/multi-mode IM overcome the SE limitation at the price of performance degradation. Similarly, the achievable SE of spatial IM schemes without APM symbols is constrained by the antenna array size because only IM is used for data transmission.

Hence, these systems are also more appropriate for LPWA IoT devices with low-power and cost constraints. More precisely, the receive spatial IM (RASK based schemes) is investigated for downlink IoT applications since it permits the use of simple un-coherent IoT receivers for the detection of the targeted RAs with low computational complexity [113]. Whereas, the transmit spatial IM without APM (SSK based schemes) is investigated for the uplink IoT scenario to keep the compatibility with its downlink transceiver system design [113]. Moreover, the GSSK system is also suggested for indoor Visible Light Communication (VLC) systems in [161] to exploit IM advantages.

In contrast to SMX, the transmit spatial IM with single activated TA with/without APM symbol eliminates the requirement of TAs synchronization and the IAI at the Rx. Furthermore, the spatial IM schemes with APM symbol show an important SE/EE gain. Thus they are more suitable for ultra-high data rates applications, especially when multiple APM symbols are transmitted to benefit from multiplexing gain (e.g., GSM). Consequently, GSM system is studied in the mmWave [130, 162, 163] and sub-THz bands [14, 17].

Concerning the quadrature based IM schemes in SISO and MIMO are able to enhance more the SE and keep some EE gain, but mainly at the price of more considerable detection complexity compared to their original IM system. Moreover, QSM, DQSM, and G-QSM have higher transmitter cost and power consumption than SM, DSM, and GSM; since more RF chains are required to use different TAs for I/Q components. Whereas, the GPQSM uses already more RF chains and all TAs with GPSM to target the selected RAs. However, in general, the receive spatial IM schemes can reduce the number of RF chains when combined with the analog or hybrid beamforming.

It worth mentioning that the spatial IM domain, like any MIMO system in general, requires a rich scattering environment to allow correct detection of indexed elements and the recovery of APM

symbol(s), if any. Similarly, the schemes of channel IM domain are more channel-dependent, especially SSM for example, which tries to apply IM concept on real channel details (scattering clusters). Note that the other channel IM schemes (based on polarized/reconfigurable antennas, beamforming, or RF mirrors) can control more the indexed element by the transceiver system design, and thus reduce the dependency on the channel conditions. However, all channel IM schemes' success and the maximum SE gain are limited by the independence and number of the generated RPs. For instance, those IM systems based on polarized/reconfigurable antennas have a limited number of RPs.

In contrast, the usage of RF mirrors in MBM system helps to achieve higher SE gain in bpcu and a significant EE improvement only when more than one RA is used. Note that these advantages of schemes that switch RPs at symbol rate (e.g., MBM) come with a critical disadvantage related to the spectral regrowth due to discontinuity in their signals. This disadvantage is crucial for the band-limited communication system and will deteriorate its effective spectral efficiency in b/s/Hz. In reality, MBM comes with challenging design and implementation difficulties from the number of RF mirrors that can be supported around each TA to the generated RPs's characteristics and their interdependency. Therefore, the future of these systems in channel IM domains is based on the hardware components' research and development in the next years.

Finally, multidimensional IM uses different indexation criteria jointly. Thus, such a system is very appealing for SE enhancement, especially when the time/frequency IM dimensions are not involved. Note that the joint IM systems try to take advantage of the different indexation techniques, but they have a detection complexity penalty, especially with a joint ML detector. A lower complexity detection is possible by detecting each indexed element separately and successively before the APM symbol(s). However, such detectors are more prone to error. The erroneous detection of the information on the top indexed layer will propagate to the subsequent layer(s) and can highly degrade the system performance. Thus, for a good performance, the top IM layers mainly should be very robust to channel conditions with the minimum possible ambiguity between the indexed elements on each layer to minimize the error propagation when using a successive detection strategy. Therefore, the multidimensional IM schemes are more beneficial when the last condition is satisfied to enable simple detection or when the joint detection remains feasible.

2.7 Conclusions/Discussions

This chapter presented conventional SISO/MIMO wireless communications systems and their different possible extensions to apply IM concept. The various existing IM domains are also thoroughly reviewed while highlighting the different strategies to convey additional information bits in each domain. The reviewed dimensions in this chapter are summarized in Fig. 2.6, where each dimension introduces another degree of freedom to convey information bits implicitly. It is worth mentioning that IM can be applied to any property/element in the transceiver and even in the channel or surrounding environment,

as long as the receiver can detect the indexed elements. Our comparison focused on the SE of these systems to highlight their appropriate scenario and applications for B5G communication. In particular, the SE of the different systems in the time/frequency, modulation type, and spatial IM domains are investigated and summarized in Table 2.1 and 2.2. Then, the potential advantages/disadvantages and challenges of all IM dimensions are discussed, and their suitable applications are highlighted. Note that all IM schemes with appropriate configurations can provide SE/EE gain and a significant performance enhancement compared to conventional communication systems without IM. For example, of an inadvisable setting, the single-mode time/frequency IM schemes (e.g., SC-TIM, OFDM-IM, etc.) may induce a huge SE/EE and performance penalty when trying to reach the same SE as the original system using APM order $M > 4$ without IM. This degradation (in order of 9 dB [164]) appears in this case since a higher M -ary APM order is required to compensate for the SE loss resulting from discarding some available resources. While the dual/multi-mode with these SISO IM domains allows achieving SE/EE gain even with high M -ary schemes, thanks to its combination with Modulation type IM, but these systems suffer from higher detection complexity. Similarly, the channel IM domain provides the same advantages, mainly when applied in SIMO/MIMO systems or with spatial IM domain but not in SISO. However, the main drawback of MBM in the channel IM domain is the spectral regrowth that can deteriorate the SE in b/s/Hz, and the limited number of uncorrelated radiations patterns in practical implementation that limits the feasible SE.

The transmit and receive spatial IM schemes showed a significant SE improvement, especially when incorporated with APM symbols multiplexing. According to the adopted scheme and its configuration, the spatial IM can allow having some of the following advantages: higher SE, lower transmitter and/or receiver cost, less IAI, better system performance, higher EE, and lower detection complexity. Therefore, it is clear that the spatial IM domain has a flexible design that can be configured to meet different specific requirements and tradeoffs among the spectral efficiency, energy efficiency, deployment cost, and system performance.

In brief, the spatial-domain IM can enhance the SE/EE, depending on the spatial IM scheme being adopted, while the time/frequency domain IM strategies in SISO have a limited SE enhancement (in most cases a SE loss) but with a better EE for low data rate applications and performance especially in a dispersive channel. Therefore, spatial IM is the most promising and practical existing IM dimension for beyond 5G that targets ultra-high data rates. In the next chapter of Part I, the transmit spatial IM domain is considered due to its appealing advantages on SE and EE, while in Part II a novel IM domain is proposed to avoid the limitation of the former and achieve our ultimate goal of low-power wireless ultra-high data rates.

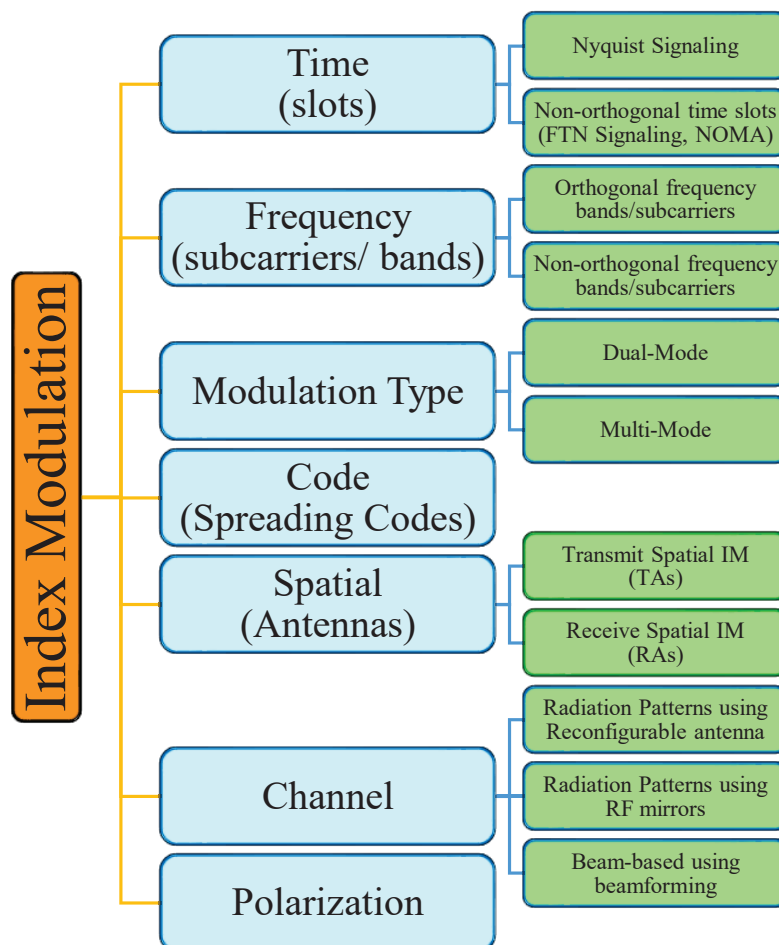


Figure 2.6 – Presented IM Domains and their sub-categories.

Part I

Contributions and Advances to Generalized Spatial Modulation

Chapter 3

Generalized Spatial Modulation based schemes

Contents

3.1	Introduction	51
3.2	GSM for low power Terabits systems	52
3.2.1	System Model	52
3.2.2	GSM joint ML Detector	53
3.2.3	GSM OB-MMSE Detector	53
3.2.4	Channel Model: Rayleigh and Rician channels with\without correlation	54
3.2.5	Performance assessment and discussions	55
3.2.6	Link Budget	58
3.2.7	GSM Challenges	61
3.2.7.1	RF switching transmitter architecture	61
3.2.7.2	Peak-to-Average Power Ratio	62
3.2.7.3	Spatial Correlation	65
3.3	GSM in highly correlated channel	65
3.3.1	Efficient Legitimate TAC Selection	66
3.3.1.1	GSM System Relying on Channel Side Information at the transmitter side (EGSM)	66
3.3.1.2	Simplified Enhanced GSM S-EGSM	67
3.3.2	Efficient Spatial bit mapping	68
3.3.3	Results for proposed S-EGSM and best-effort spatial bit mapping	70
3.4	GSM with RF impairments	73
3.4.1	Sub-THz MIMO Channel	74
3.4.2	Sub-THz Phase noise model	75

3.4.3	System comparison: GSM vs SMX	76
3.4.3.1	Performance in sub-THz environment	76
3.4.3.2	Optimal Detection Complexity	80
3.4.3.3	PAPR Discussion	80
3.4.3.4	Link budget for systems in sub-THz environment	81
3.5	Near-Optimal Performance with Low Complexity ML-based detector for SMX .	83
3.5.1	Proposed OSIC-ML Detector	84
3.5.1.1	Detection algorithm	84
3.5.1.2	Complexity Analysis	87
3.5.2	Proposed SMX detector OSIC-ML results and discussions	89
3.6	Near-Optimal Performance with Low Complexity ML-based detector for GSM .	93
3.6.1	Proposed GSM Detector: O ² SIC-ML	93
3.6.1.1	Detection algorithm	93
3.6.1.2	Complexity Analysis	97
3.6.2	Proposed GSM detector O ² SIC-ML results and discussions	97
3.7	Dual Polarized GSM	101
3.7.1	DP-GSM System model	102
3.7.2	DP-GSM Joint-ML Detector	104
3.7.3	Modified OB-MMSE Detector for DP-GSM	104
3.7.4	MIMO Channel models with Dual-Polarized antennas	105
3.7.4.1	Channel model with spatial and cross-polarization correlation	105
3.7.4.2	Sub-Terahertz MIMO channel	107
3.7.5	sub-THz PN model for DP MIMO systems	107
3.7.6	Analytical Performance: Average error probability bound	108
3.7.7	DP-GSM results and discussions	110
3.8	Conclusions and Discussions	116

3.1 Introduction

The wireless ultra-high data rate is required for many emerging scenarios as highlighted in Section 1.1, and in the following, we will focus on short-range indoor scenarios such as a kiosk, indoor hot-spot (high throughput WLAN), server farm, etc..., where the distance between transceiver is limited to few meters.

In the previous chapter, a comparison between the different IM domains is presented, and the main advantages/disadvantages of each scheme are pointed out. In this chapter, our approach insists on benefiting from IM and advanced MIMO schemes to enhance the SE of the power-efficient SC modulation. For instance, the GSM system generalizes different IM techniques in the spatial IM domain and shows an important improvement of SE, and thus it is a key enabler for wireless ultra-high data rates systems. This chapter aims to provide a more in-depth study of the GSM system with single carrier modulations in the sub-THz environment and discuss and tackle its main challenges.

Towards this end, first, GSM performance is analyzed with several APM in different channel conditions, then the most appropriate APM candidates that can reach Tbps with low power consumption are selected. The results show that exploiting IM to transmit most of the information bits with low order M -ary APM schemes to reach a high system SE is more power-efficient than GSM of same SE that uses higher-order modulation and/or less virtual bits through spatial IM (like SMX in the extreme case). However, the GSM system is sensitive to channel correlation. Since highly correlated channels as in sub-THz bands can lead to erroneous detection of activated TAC and the carried APM symbols. This performance degradation is reduced in this chapter firstly by adequately selecting the legitimate TAC set without instantaneous CSIT, using efficient spatial bit mapping.

Further, GSM and SMX systems are evaluated in sub-THz indoor channels with RF impairments, where the results reveal that GSM is a promising candidate for wireless ultra-high data rate systems. Then, we proposed the DP-GSM system to enhance more the SE and EE by exploiting the polarization dimension, and its analytical average BER is derived to truly characterize the system performance. After these enhancements of GSM-based systems, it is essential to achieve the optimal GSM performance with low detection complexity. Hence, we proposed a low complexity ML-based detector to SMX, and then we extended this technique for the GSM system that generalizes many other IM schemes while also considering the detection of the virtual bits. Our proposed detection algorithm provides an excellent controllable performance-complexity tradeoff, where a prominent complexity reduction in order of 99% can be obtained while achieving the optimal performance.

The remainder of this chapter is organized as follows. Section 3.2 analyzes the GSM system in different channel conditions. Section 3.3 presents the proposed techniques for GSM performance enhancement in highly correlated channels. Section 3.4 provides the comparison of GSM and SMX from different perspectives in sub-THz channels with RF impairments. In Sections 3.5 and 3.6, near optimal detectors with low complexity are proposed for SMX and GSM systems respectively. Finally,

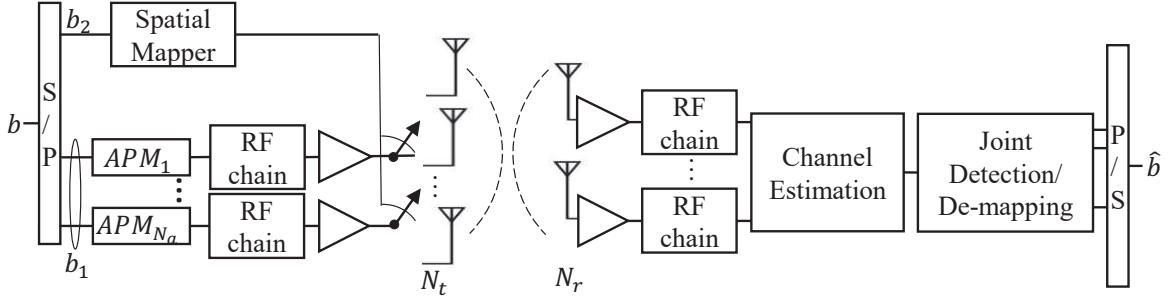


Figure 3.1 – GSM System Model

we present the proposed DP-GSM scheme with its analytical performance and sub-THz evaluation in Section 3.7.

3.2 GSM for low power Terabits systems

In this section, we propose a new approach based on constant or near-constant envelope SC modulation with IM to reach Tbps with low power consumption. In addition, its feasibility is evaluated depending on error performance, power consumption, complexity, and cost. The performance analysis of the proposed approach with GSM scheme is addressed over spatially correlated/uncorrelated Rician and Rayleigh channels. Moreover, the link budget is calculated, and the power consumption is estimated to emphasize its importance for low power wireless Tbps. Finally, the advantages and challenges of GSM system are discussed.

3.2.1 System Model

The GSM system model is a MIMO system with N_t TAs and N_r RAs. In this system, the source binary information sequence b is divided into two streams b_1 and b_2 as shown in Fig. 3.1. The bit-stream b_1 is mapped by the M -ary APM such as QAM, PSK, CPM, etc. The bit-stream b_2 is encapsulated in the index of the selected TAC at each symbol period, where each TAC is formed of N_a activated TA out of N_t .

The possible number of TAC with N_a activated antennas is the combination $N_{all} = C_{N_t}^{N_a}$. However, only $N_{TAC} = 2^{\lfloor \log_2(N_{all}) \rfloor}$ are used to keep the length of the VBs an integer number, and the other possibilities are marked as illegal combinations. Note that the appropriate TACs should be carefully selected from the N_{all} possibilities to minimize the interference and the effect of spatial correlation between antennas as it will be shown in Section 3.3. Accordingly, the number of bits per GSM symbol

can be expressed as:

$$\mathcal{L}_{GSM} = \log_2(N_{TAC}) + N_a \cdot \log_2(M) \quad (3.1)$$

The GSM transmitted symbol vector $\mathbf{x} = [x_1, \dots, x_{N_t}]^T$ contains only ' N_a ' APM symbols (s_1, s_2, \dots, s_{N_a}) at the positions of activated TAs according to the selected TAC based on b_2 . Note that the inter-antenna synchronization at the transmitter is required to make sure that the receiver can detect the activated antenna from each received vector y . The received signal y is expressed as:

$$\mathbf{y} = \mathbf{H}\mathbf{x} + \mathbf{v} = \sum_{n=1}^{N_a} \mathbf{h}_k s_k + \mathbf{v} \quad (3.2)$$

where $\mathbf{H} = [\mathbf{h}_1, \dots, \mathbf{h}_{N_t}]$ is the $N_r \times N_t$ MIMO channel matrix with \mathbf{h}_k is the column vector of N_r elements, the power of transmit symbols is normalized, \mathbf{v} is $N_r \times 1$ channel noise vector and its elements v_r obeys the i.i.d. AWGN with the variance of σ_v^2 , i.e., $CN(0, \sigma_v^2)$ for $r = 1, \dots, N_r$.

3.2.2 GSM joint ML Detector

At the receiver side, the selected TAC index and the modulated symbols on all activated TAs can be jointly estimated using the ML detector that performs an exhaustive search over all the possible transmit vector described as:

$$(\widehat{\mathbf{s}}_{ML}, \widehat{\mathbb{I}}) : \widehat{\mathbf{x}} = \arg \min_{\mathbf{x} \in \Omega} \|\mathbf{y} - \mathbf{H}\mathbf{x}\|^2 = \arg \min_{\mathbf{s} \in \chi, \mathbb{I} \in \mathcal{I}} \|\mathbf{y} - \mathbf{H}_{\mathbb{I}}\mathbf{s}\|^2 \quad (3.3)$$

where Ω denotes the set of all possible GSM transmit vectors in both the spatial and signal constellation domains and $\widehat{\mathbf{x}}$ is the estimated transmit vector with N_a non-zero elements in the position of the activated TAs, χ contains the vectors of all possible APM symbols combinations (M^{N_a}), $\mathcal{I} = \{\mathbb{I}_1, \mathbb{I}_2, \dots, \mathbb{I}_{N_{TAC}}\}$ is the set of all legitimate TACs where each \mathbb{I} contains the indices of activated TAs, and $\mathbf{H}_{\mathbb{I}}$ is the sub-matrix of \mathbf{H} with N_a columns corresponding to activated TAs in \mathbb{I} .

3.2.3 GSM OB-MMSE Detector

However, a GSM symbol detection with lower complexity is possible by Ordered Block Minimum Mean-Squared Error (OB-MMSE) [165]. The OB-MMSE detector reduces the iterations of search algorithm by ordering the appropriate TAC and stop the search when $\|\mathbf{y} - \mathbf{H}_{\mathbb{I}}\widehat{\mathbf{s}}\|^2$ becomes less than a predefined threshold $V_{th} = N_r \sigma_v^2$, where $\widehat{\mathbf{s}}$ is the Minimum Mean-Squared Error (MMSE) equalized symbol and quantized to an APM symbol. The descending order sorting of the TACs is based on their weighting factor w_i that measures the reliability of each TAC \mathbb{I} defined as:

$$z_p = (\mathbf{h}_p)^\dagger \mathbf{y} \quad (3.4)$$

$$w_i = \sum_{n=1}^{N_a} z_{i_n}^2 \quad (3.5)$$

where $(\mathbf{h}_p)^\dagger = \frac{\mathbf{h}_p^H}{\mathbf{h}_p^H \mathbf{h}_p}$ is the pseudo inverse of the p^{th} column of channel matrix \mathbf{H} with $p \in \{1, \dots, N_t\}$. Thus z_{i_n} represents the element from $\mathbf{z} = [z_1, z_2, \dots, z_{N_t}]$ at the n^{th} activated TA according to TAC I_i where $i \in \{1, \dots, N_{TAC}\}$.

Then, the symbol vector is estimated by a simplified block based MMSE equalizer

$$\widehat{\mathbf{s}}_i = Q \left(\left((\mathbf{H}_{I_i})^H (\mathbf{H}_{I_i}) + \sigma_v^2 \mathbf{I}^{N_a \times N_a} \right)^{-1} (\mathbf{H}_{I_i})^H \mathbf{y} \right) \quad (3.6)$$

where Q represents the quantization operation that restricts $\widehat{\mathbf{s}}_i$ to be a value from the APM constellation set \mathcal{S} and the $N_r \times N_a$ matrix \mathbf{H}_{I_i} is a sub-matrix with all columns of \mathbf{H} corresponding to the antenna indices in TAC I_i .

The adopted notation for this system is $\text{GSM}(N_t, N_a, M)$ where the parameter M is the APM M -ary size, $M = 2^p$ with $p \geq 0$. Note that $p = 0$ means that the transmitted symbols are just a constant power value to simplify the receiver detection at the expense of a lower data rate. Furthermore, it worth recalling that GSM includes other spatial modulation techniques such as the SM $\text{GSM}(N_t, 1, M)$ [98], SSK $\text{GSM}(N_t, 1, 1)$ [166], GSSK $\text{GSM}(N_t, N_a, 1)$ [103] and conventional MIMO SMX or BLAST $\text{GSM}(N_t, N_t, M)$ as shown in Fig. 3.2. This feature can be utilized to have a reconfigurable system with different data rates.

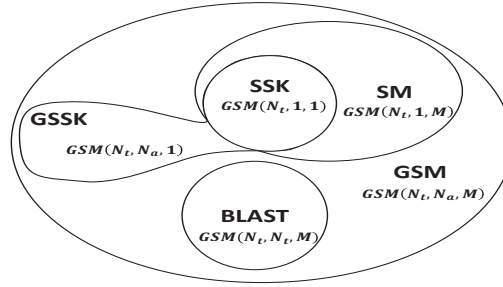


Figure 3.2 – GSM Derivatives

3.2.4 Channel Model: Rayleigh and Rician channels with\without correlation

In this section, we consider a slow fading MIMO channel matrix \mathbf{H} as a Rayleigh or Rician multipath fading channel with/without spatial correlation [167] defined as:

$$\mathbf{H} = \sqrt{\frac{K}{K+1}} \mathbf{H}_{LoS} + \sqrt{\frac{1}{K+1}} \boldsymbol{\Sigma}_r^{\frac{1}{2}} \mathbf{H}_{NLoS} \boldsymbol{\Sigma}_t^{\frac{1}{2}T} \quad (3.7)$$

where K is the Rician factor, \mathbf{H}_{LoS} and \mathbf{H}_{NLoS} are the $N_r \times N_t$ LoS and the non-LoS channel matrix respectively. The \mathbf{H}_{NLoS} can be considered as a Rayleigh channel whose elements satisfies $CN(0, 1)$. In addition, the NLoS part exhibits a spatial correlation described by Kronecker model that assumes the spatial correlations at the transmit and receive sides are separable. This model approximates the correlation matrix $\Sigma_{t,r}$ as the Kronecker product of the correlation matrices at transmitter and receiver, denoted as Σ_t , and Σ_r , respectively:

$$\Sigma_{t,r} = \Sigma_t \otimes \Sigma_r \quad (3.8)$$

Thus, (3.7) includes the uncorrelated/correlated Rayleigh and Rician fading channel as a special case depending on the value of K and the correlation matrices.

3.2.5 Performance assessment and discussions

In this section, firstly, we compare MIMO SMX with GSM using RF-switching Tx architecture to prove that the latter is able to reduce the number of required RF chains at both sides, but it is maintained only at the receiver when using full-RF Tx architecture. However, these advantages of GSM are at the price of a higher number of TAs, which is feasible for example with downlink scenarios as Kiosk downloading at mmWave and sub-THz bands. Note that the RF-switching Tx architecture has some drawbacks that will be discussed in sub-section 3.2.7.1 and Fig. 3.6.

In the following, we present the numerical comparison between several APM-GSM systems that employ different APM schemes: PSK, Differential Phase Shift Keying (DPSK), CPM, and QAM. The BER of these systems in function of the average SNR was evaluated using Monte Carlo Simulations. In order to conduct a fair comparison, the same transmission rate has been used without restriction on the constellation size and the number of antennas.

In fact, the GSM(N_t, N_a, M) parameters for Tbps are chosen, such that the required number of RF chains is minimized to reduce the cost with a maximum allowed $N_t \leq 22$ and a given M -ary APM. The adopted GSM detector in these systems is OB-MMSE that can detect the TAC and the APM constellations with low complexity. The simulations are performed over correlated/uncorrelated Rayleigh and Rician channels with different correlation levels. The correlation matrices in the Kronecker model are formed according to the exponential model of [168] where the elements of transmit Σ_t and receive Σ_r correlation matrices are affected by fixed correlation factor β : $[\Sigma_t]_{m,n} = \beta_t^{|m-n|}$. We used $\Sigma_r = I_{N_r}$ to concentrate on the impact of correlation at the transmitter side where a larger antenna array is used to convey the data in the spatial domain of index modulation.

The simulation parameters for the different systems that can achieve Tbps are summarized in Table 3.1. The CPM parameters used with CPM-GSM system are: modulation index $h = \frac{1}{3}$, raised cosine as frequency pulse with length $L = 3$ symbol intervals.

Table 3.1 – Simulation parameters for different APM-GSM systems

Parameters	Value
CPM-GSM	GSM(22, 6, 4)
QPSK-GSM	GSM(17, 6, 4)
DQPSK-GSM	GSM(17, 6, 4)
16QAM-GSM	GSM(13, 4, 16)
64QAM-GSM	GSM(11, 3, 64)
256QAM-GSM	GSM(24, 2, 256)
N_r	$2N_a$
Rician factor K	[0, 3]
Oversampling factor	2
Raised Cosine Rolloff α	0.2
Correlation factor β_t	[0, 0.2, 0.5, 0.8]
Number of GSM symbols	10^4

Fig. 3.3a shows the performance of different systems over uncorrelated Rayleigh channel. As we remark, the systems with more data conveyed by IM with small M -ary size as (D)QPSK-GSM and CPM-GSM have better performance than those with a lower number of antennas but with higher M -ary size $M \geq 16$. Therefore, the total BER is affected by the modulation order of APM being used more than the order of index modulation. In other words, the larger N_{TAC} and the lower M -ary APM are, the better the performance is.

The same systems are evaluated over the uncorrelated Rician channel, and the simulation results are shown in Fig. 3.3b. However, the required SNR in this channel is higher than that in Rayleigh channel for the same BER. It is worth mentioning that CPM-GSM has a notable degradation in the Rician channel about 10 dB, and this system requires an additional 2 dB compared to Differential Quadrature Phase Shift Keying (DQPSK)-GSM while it was completely the inverse in Rayleigh channel.

The best APM candidates (CPM-GSM and (D)QPSK-GSM) are compared in Fig. 3.4a and 3.4b with different correlation levels $\beta_t = [0.2, 0.5, 0.8]$ over Rayleigh and Rician channels respectively. These results show that these systems conserve their good performance with low spatial correlation while they start to degrade at high correlation levels. In particular, (D)QPSK-GSM performance is reduced by less than 1 dB at un-coded BER = 10^{-4} when the correlation increases to $\beta_t = 0.5$ as shown in Fig. 3.4a and 3.4b. Also, their performance degrades by approximately 5 dB at a high correlation level $\beta_t = 0.8$, while CPM-GSM is more sensitive to correlation and degrades by 6 – 8 dB.

Furthermore, the spatial correlation that is larger at high frequencies with uniform planar array [169] affects any spatial modulation performance with multiple active TAs. However, its effect can be reduced by carefully choosing the appropriate TAC and their elements, as it will be shown in Section 3.3.1.

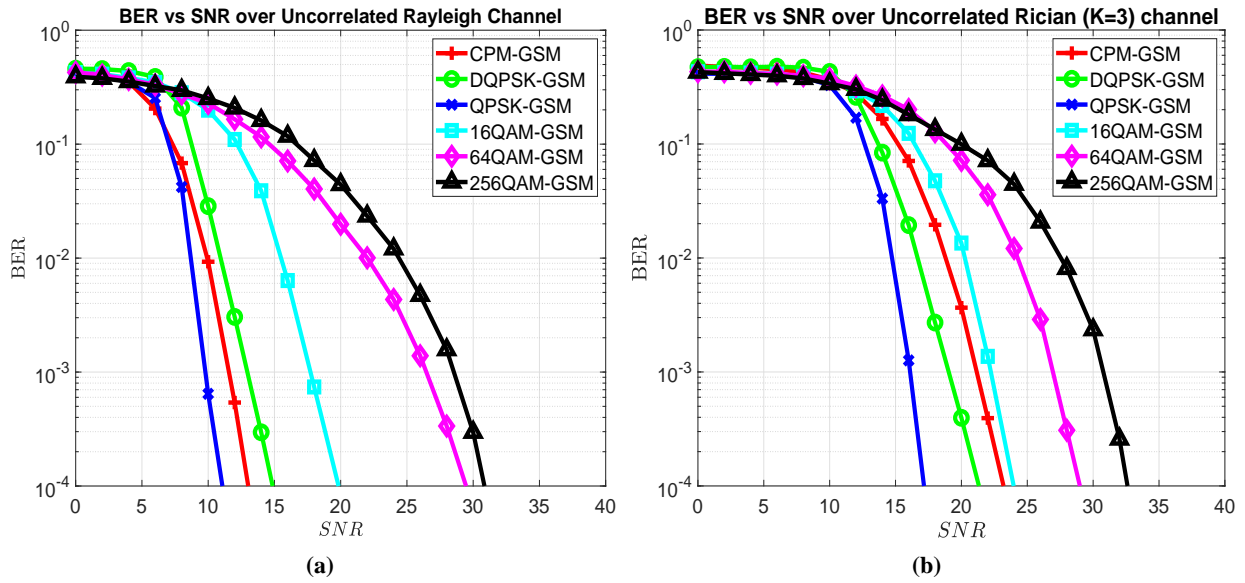


Figure 3.3 – BER vs SNR for various APM-GSM systems over uncorrelated: (a) Rayleigh channel, (b) Rician channel.

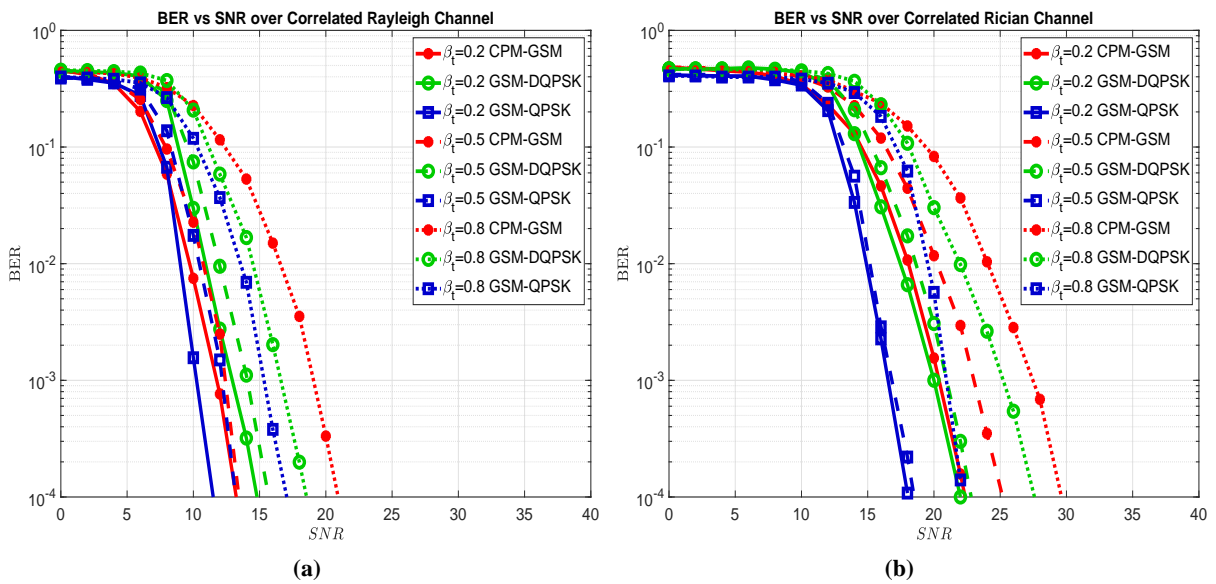


Figure 3.4 – BER vs SNR for (D)QPSK-GSM and CPM-GSM over correlated: (a) Rayleigh channel, (b) Rician channel.

In reality, perfect channel estimation can not be guaranteed, and the results in [170] show that the channel estimation error degrades the performance of large M -ary QAM ($M = 16$) rapidly and creates an error floor at $\text{BER} = 10^{-5}$ or higher while its effect on low M -ary as Quadrature Phase Shift Keying (QPSK) is less important and the error floor is as low as $\text{BER} = 10^{-7}$. Thus, these low M -ary APM, which have a near-constant or constant envelope, are more robust to channel estimation errors.

3.2.6 Link Budget

In this section, the link budget is calculated for all systems for the same un-coded BER 10^{-4} with correlated/uncorrelated Rayleigh and Rician channels. Then, their power consumption for an ultra-high data rate is deduced. For a fair comparison, these systems are configured for the same SE that is defined as:

$$SE_{GSM} = \frac{BitRate_{(bits/s)}}{W_{(Hz)}} = \frac{R_{(Symbol/s)} * \mathcal{L}_{GSM}(bits/symbol)}{W_{(Hz)}} \quad (3.9)$$

where R is the symbol rate, and W is the allocated bandwidth. Since the non-linear modulation as CPM requires a larger bandwidth, its symbol rate is adjusted accordingly to keep the same occupied bandwidth among all systems. Thus, the number of bits per GSM symbol must be higher with CPM, as shown in Table 3.3.

Henceforth, we consider close proximity scenarios (as Downlink kiosk) with distance $d=5m$ and channel bandwidth $W = 1$ GHz with channel aggregation/bonding. Note that the available spectrum is in order of 50 GHz in the frequency range between 90GHz and 200GHz according to [26] and 50GHz contiguous spectrum between 275-325GHz [3].

Note that the receivers in this scenario are the mobile devices that have small antenna gain, power, and cost constraints. However, the antenna gains are higher when considering other scenarios with longer distances as Wireless Backhaul, where the transceivers have less stringent cost/complexity constraints.

In Table 3.3, the required transmit power P_t with small distance communication is calculated from the required SNR according to the following parameters summarized in Table 3.2:

Table 3.2 – Link Budget equations to estimate the required transmit power P_t

$N_{Thermal}$	$= 10 \log_{10}(k.T.W) + 30$	dBm
N_{Floor}	$= N_{Figure} + N_{Thermal}$	dBm
Rx_{Level}	$= SNR + N_{Floor}$	dBm
$fspl$	$= 20 \log_{10}(\frac{4\pi d f_c}{c})$	dB
$T_{PathLoss}$	$= fspl + Attenuation$	dB
$EIRP$	$= T_{PathLoss} - G_r + L_{crx} + Rx_{Level}$	dBm
P_t	$= EIRP - G_t + L_{ctx}$	dBm

where k , T , N_{Figure} , $fspl$, f_c , c , G_r/G_t , L_{crx}/L_{ctx} and $EIRP$ are Boltzmann constant, the temperature in kelvin, the noise figure, the free space path loss, the carrier frequency, the speed of light in vacuum ($c = 3 \times 10^8 m/s$), receive/transmit antenna gain, receiver/transmitter cable loss, the effective isotropic radiated power respectively.

Furthermore, the power consumption is deduced based on the power amplifier efficiency, which is affected by the APM PAPR. Note that in this section, an RF switching is considered after the PA, as depicted in Fig. 3.1. Consequently, the constant and near-constant envelope modulations combined

Table 3.3 – Link Budget and Power Consumption for different GSM parameters achieving Tbps

Parameters	Temperature (degree C)	20	Carrier Frequency (GHz)		150	Distance (m)		5
	99% of Channel Bandwidth (GHz)	1	Number of Channel Aggregation/bounding		44	Total Bandwidth (GHz) [8]		44
	Modulation	CPM	$\pi/4$-QPSK	$\pi/4$-DQPSK	16-QAM	64-QAM	256-QAM	Units
	GSM (Nt,Na)	(22,6)	(17,6)	(17,6)	(13,6)	(11,3)	(4,3)	
	Bits per GSM symbol	28.00	25.00	25.00	25.00	25.00	26.00	bits
Symbol Rate (R)	0.80	0.92	0.91	0.91	0.92	0.91	GSym/s	
Rate	APM Spectral Efficiency	1.59	1.83	1.82	3.65	5.49	7.3	bps/Hz
	GSM Spectral Efficiency	22.26	22.90	22.80	22.83	22.88	23.71	bps/Hz
	Total Throughput	979.4	1007.6	1003.2	1004.3	1006.5	1043.328	Gbps
Receiver	SNR with Rayleigh	13.00	12.00	15.00	20.00	29.00	31.00	dB
	RX Noise Figure (NF)	10.00						dB
	Thermal Noise (Nthermal)	-83.93						dBm
	Noise floor	-73.93						dBm
	Rx Signal Level	-60.93	-61.93	-58.93	-53.93	-44.93	-42.93	dBm
	RX Cable Loss (Lcrx)	1						dB
	RX Antenna Gain (Gr)	3						dBi
Channel	Free space path loss (fspl)	89.94						dB
	Vapour attenuation	1.28						dB/Km
	O2 attenuation	0.01						dB/Km
	Rain attenuaton	11.78						dB/Km
	Total Path loss	90.01						dB
Transmitter	Required Tx EIRP	27.08	26.08	29.08	34.08	43.08	45.08	dBm
	Cable Loss (Lctx)	1						dB
	TX Antenna Gain (Gt)	24						dBi
	Required Pt	4.08	3.08	6.08	11.08	20.08	22.08	dBm
PAPR	PAPR for ($\alpha=0.2$)	0	3.8	4.86	7.5	8.2	8.35	dB
	Theoretical PA Efficiency	0.8	0.52	0.44	0.34	0.3	0.28	
Uncorrelated	Power per Channel	3.20	3.91	9.21	37.70	339.40	576.34	mW
	Total Power Consumption	0.14	0.17	0.41	1.66	14.93	25.36	W
		21.48	22.35	26.08	32.20	41.74	44.04	dBm
	SNR with Rician K=3	23.00	17.00	21.00	24.00	29.00	31.00	dB
Total Power Consumption	31.48	27.35	32.08	36.20	41.74	44.04	dBm	
Correlated	SNR with Rayleigh $\beta=0.8$	21.00	17.00	18.00				dB
	Total Power Consumption	29.48	27.35	29.08				dBm
	SNR with Rician $\beta=0.8$	29.00	22.00	27.00				dB
	Total Power Consumption	37.48	32.35	38.08				dBm

with GSM prove their ability to reach a high throughput of 1 Tbps. Also, they conserve their low power consumption as shown in Table 3.3 that is limited to few Watts while large M -ary APM-GSM requires 15 to 20 dB more. In addition, it is worth mentioning that CPM-GSM has the lowest power consumption in Rayleigh channel, but this behavior changes with the spatial correlation effect or in Rician channel due to its performance degradation. Therefore, QPSK-GSM system becomes the least power consuming system due to its better performance. Whereas the DQPSK-GSM system requires more power compared to CPM-GSM and QPSK-GSM, but it is more robust to cumulative phase noise.

The high M -ary APM-GSM systems exceed the maximum allowed Effective Isotropic Radiated Power (EIRP) limitations 40 dBm; even the 16QAM requires 11 dBm as transmit power which is greater than the actual transmit power (P_t is in order of 10 dBm) at the sub-THz frequencies with current technologies. For this reason, the power consumption for large M -ary schemes ($M \geq 16$) are omitted with correlated Rayleigh and Rician channel.

These power estimations prove that with the proposed approach for Tbps throughput, less than 1 Watt (21 – 26 dBm) is sufficient for (D)QPSK-GSM and CPM-GSM in Rayleigh channel, and few Watts (32 – 38 dBm) are more than enough even in highly correlated Rician channel ($\beta_t = 0.8$).

Moreover, a high M -ary schemes also require a power-hungry ADC/Digital-to-Analog Converter (DAC) with a large resolution. In comparison, the low order modulation schemes allow the usage of few bits (1 – 3 bits ADC), which is a critical requirement to use higher speed ADC for a larger bandwidth at a low cost. Therefore, the high M -ary APM-GSM systems are not suitable for an ultra-high data rate in the order of Tbps with a given power expenditure.

However, the advantages of the CPM-GSM and (D)QPSK-GSM systems suffer from high optimal detection complexity that will be tackled in Section 3.6. Another advantage of QPSK system is the ability to perform the demodulation in the analog domain that reduces the required converter's resolution [171], where they implement a multi-Gbps analog synchronous QPSK demodulator with phase-noise suppression.

Finally, any system requires a higher SNR in more severe channels, but the analog or hybrid beamforming gain can keep the systems shown in Fig. 3.5 feasible in terms of energy consumption. This feature is enabled by massive MIMO where the number of TAs can be increased by replacing each antenna element by a small antenna array that performs analog beamforming as proposed in [130] without increasing the number of RF chains at transmitter nor at the receiver side. Therefore, these constant and near-constant envelope modulations with beamforming aided GSM are very appealing for ultra-high data rates, especially for a Tbps downlink Kiosk scenario, where the power consumption and cost of the receiver of the mobile devices are the most critical constraints.

In brief, the comparison of these APM-GSM systems from different points of view is illustrated in Fig. 3.5, and it shows that the power-efficient (D)QPSK-GSM systems are a balanced tradeoff between system performance, power efficiency, hardware cost, and detector computational complexity.

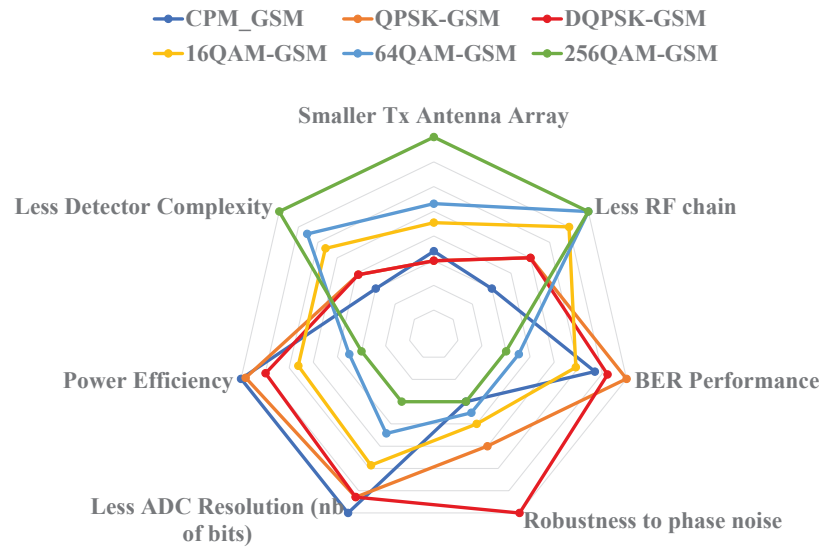


Figure 3.5 – System comparison between different SC modulations with GSM.

In conclusion, the recent approach for high data rate wireless communication as used in IEEE 802.11ax is based on increasing the MIMO spatial multiplexing order and M -ary schemes, but it requires a great effort to reduce the PAPR for limiting the power consumption. This approach is not a convenient solution for the ultra-high data rate in the order of Tbps in the 90GHz-200GHz band, especially for low-cost implementation where the efficiency and the achievable output power decreases at higher frequencies with current technology. For this reason, we proposed a different approach that insists on using power-efficient modulation like constant or near-constant envelope modulation (CPM and (D)QPSK), and then enhance its SE with the aid of any IM techniques that can increase the system SE and conserve the power efficiency. Furthermore, this approach allows the usage of low-resolution ADC with low power and cost as required for sub-THz communication.

This section proved the feasibility of the proposed approach from different points of view as performance, spectral\power efficiency, complexity, and cost. Therefore, our approach is more suitable for reaching the ultra-high data rates in the order of Tbps with low power consumption. In the next sub-section, the main challenges of the GSM system are discussed.

3.2.7 GSM Challenges

3.2.7.1 RF switching transmitter architecture

One of the advantages of GSM systems and transmit spatial IM schemes is that it allows reducing the number of RF-chains at the Tx and Rx sides because only one or a few TAs are activated at each symbol period. However, the in-depth investigation of subcarrier-based SM showed that the MC waveform like

OFDM requires more RF-chains at the Tx side since multiple TAs will be activated over the entire OFDM frame [172, 173]. Afterward, the researchers noticed that the transmit spatial IM using SC modulations with the minimum number of RF-chains (equal to the number of activated TAs) has a spectral regrowth due to limiting the time duration of the pulse shaping filter to a single symbol period [174]. In other words, the use of the minimum number of RF chains at the transmitter leads to pulse shaping time truncation at the symbol rate since the activated TAs are changed. Hence, the transmitted signal from each antenna becomes a signal windowed by a rectangular time-domain pulse. Thus, the occupied spectrum increases, leading to SE in (b/s/Hz) degradation due to spectral regrowth, when the spatial IM domain scheme requires an antenna transition at every symbol period. Moreover, the RF switching time spent to change the activated TAs also induces some SE degradation, as shown in [175] where they developed the effective SE for SM based schemes.

A possible solution for this problem is to use full-RF Tx architecture (Number of RF chains= N_t) with SC and MC modulations. This allows transmitting a band-limited pulse (of longer pulse duration like conventional pulse shaping) on all TAs, even on non-active ones, and avoids RF switching time issue. Another possible solution named Offset Spatial Modulation (OSM) [176], can reduce the RF-switching time between the TAs with the aid of the instantaneous CSIT. Thus, for band-limited communication systems, the minimum number of RF-chains with the different spatial IM schemes cannot be guaranteed without an impact on SE.

In addition, the transmission rate is affected by the maximum switching rate between RF chains that current hardware technology can support. Therefore, the usage of a transmitter with full-RF chains (number of RF chains equals the number of transmit antenna) remains the obvious solution to avoid RF switching drawbacks.

Finally, it is worth mentioning that this solution avoids any limitation in the achievable data rates and conserves the low number of RF-chains at the Mobile Station (MS) receiver with cost constraints in our considered scenarios.

3.2.7.2 Peak-to-Average Power Ratio

When RF-switching is considered after the PA, the PAPR of GSM signal measured at PA inputs is maintained equal to that of the used APM schemes. However, there is an increase of PAPR with full-RF GSM due to transmitting a pulse shaped signal generated from a sequence of APM/zero symbols when the TA is/isn't activated. Hence, the average power at the PA input is reduced, and the PAPR of GSM signal with full-RF architecture is increased. This PAPR increase depends on the number of zero-symbols added for each TA during a specific time duration. Hence, increasing the number of activated TAs in GSM systems keeps the low PAPR advantage of SC modulations in contrast to SM system that has an important PAPR increase [173]. Thus, the GSM with full-RF Tx architecture can have a balanced PAPR-performance tradeoff when the number of activated TAs is increased while conveying most of the information bits in the IM domain.

To summarize, Fig. 3.6 shows both GSM transmitter RF architectures with SC modulation and compares their operation along with advantages/disadvantages. Recalling that the full-RF transmitter architecture is needed for subcarrier-based MC (e.g., OFDM) with any transmit spatial IM, because different TAs are selected for each subcarrier to maintain its SE gain [172].




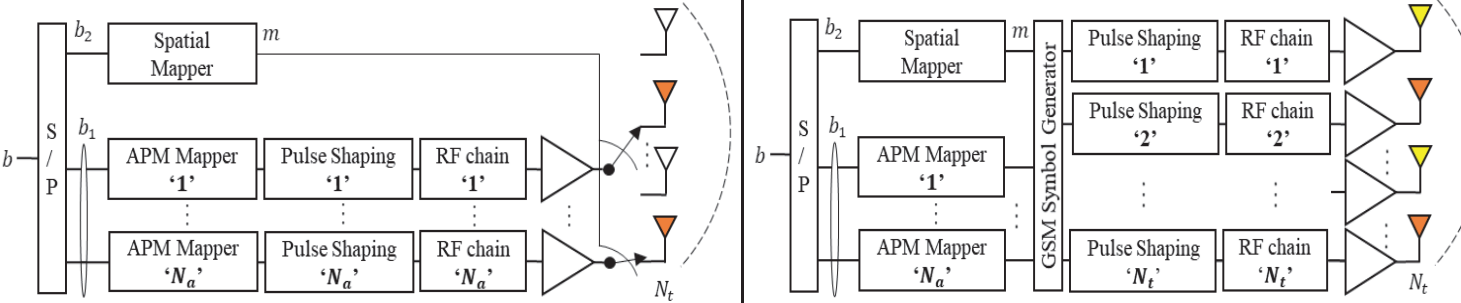
	RF-switching GSM Transmitter Architecture	Full-RF GSM Transmitter Architecture
<p>System Model</p> <ul style="list-style-type: none">  Transmitting pulse with current APM-symbol  Transmitting pulse tails with current zero-symbol  Completely off 	<p>Operation Mode</p> <p>N_a RF-chains and antennas are activated to transmit only pulses of APM symbols, where each pulse is truncated to one symbol period.</p>	<p>Operation Mode</p> <p>N_t RF-chains and antennas are activated to transmit pulses of APM and zero symbols in GSM MIMO vector that contains only N_a non-zero APM symbols. In this setup, each pulse can span multiple symbol periods.</p>
<p>Advantages</p> <ul style="list-style-type: none"> • Lower-cost transmitter due to less number of RF chains (N_a). • Lower PAPR which is affected only by APM PAPR, PAs inputs are the pulses of non-zero APM symbols only. • Lower power consumption due to less RF chains and higher PA efficiency (lower PAPR) 	<ul style="list-style-type: none"> • Maintain the GSM spectral efficiency because this architecture allows using longer pulse shaping filters that leads to: <ul style="list-style-type: none"> ➢ Efficient band-limitation. ➢ Lower OOB radiations. • No hardware limitation on maximum data rates compared to traditional MIMO systems (e.g., SMX). 	
<p>Disadvantages</p> <ul style="list-style-type: none"> • Spectral regrowth due to pulse shaping truncation at symbol rate that leads to: <ul style="list-style-type: none"> ➢ GSM system spectral degradation due to larger bandwidth occupation and RF-switching time. ➢ Higher OOB radiations. • Data rate limited by the RF hardware switching speed. 	<ul style="list-style-type: none"> • Higher-cost transmitter due to more number of RF chains (N_t). • Higher PAPR which is affected by APM PAPR and the number N_t and N_a. PAs inputs are the pulses of APM and zero symbols. (zero symbol contains the tails of future/past APM symbols if filter length is greater than 1). • Higher power consumption due to more RF chains and lower PA efficiency (higher PAPR). 	

Figure 3.6 – Summary of GSM transmitter RF architecture.

3.2.7.3 Spatial Correlation

One of the most significant limitations of transmit spatial IM systems is its performance degradation in highly correlated channels as shown in the previous results with GSM, where the wrong detection of activated TAC will consequently lead to an error in the detection of the symbols due to the attempt of symbols estimation on non-activated TAs. As a result, the total BER will increase tremendously. To combat the Rician Fading and the latter problem, a precoding technique that uses the TAs correlation matrix and the channel statistics is proposed for SM in [129]. Similarly, another precoding method for GSM in [128] is designed by the real-time optimization of maximum-minimum Euclidean Distance (ED) that shows substantial performance gain with extremely fast convergence and low computational complexity.

In this regard, the following section will introduce other approaches for GSM that be incorporated with precoding based enhancement methods. Our techniques are based on an efficient TAC selection method and a spatial bit mapper (Index-to-Bit mapping) to minimize the overall BER in highly correlated channels.

3.3 GSM in highly correlated channel

In conventional GSM, the cardinality of the legitimate TAC set N_{TAC} is a power of 2 ($2^{\lfloor \log_2(N_{all}) \rfloor}$), where the TACs are randomly selected among the possible TACs N_{all} . Also, the mapping of the spatial bits was just a binary coding for the selected TAC index.

Unlike the redesigned spatial modulation in [177] where they try to enhance the performance of SM in a correlated channel by activating a second antenna to benefit from transmit diversity when the most correlated TA is selected. In this section, we focus on the performance enhancement of GSM systems in highly correlated channels by proposing general methods for efficient TAC selection and Index-to-Bit mapping. In this context, we designed a TAC selection method based only on the transmit spatial correlation, which is quasi-constant for a specific Tx and does not require the instantaneous CSIT estimation or its feedback. The TAC selection aims to reduce the errors in TAC detection because these errors will propagate to APM symbols. In such a case, the erroneous detection of APM symbols is due to the fact that the Rx is trying to detect the symbols on the non-activated TAs since the TAC is wrongly detected. Moreover, we proposed a spatial bit mapping based on Gray coding to reduce the spatial BER. This mapping tries to reduce the number of different bits between the neighbor TACs that are most susceptible to be interchanged in highly correlated channels.

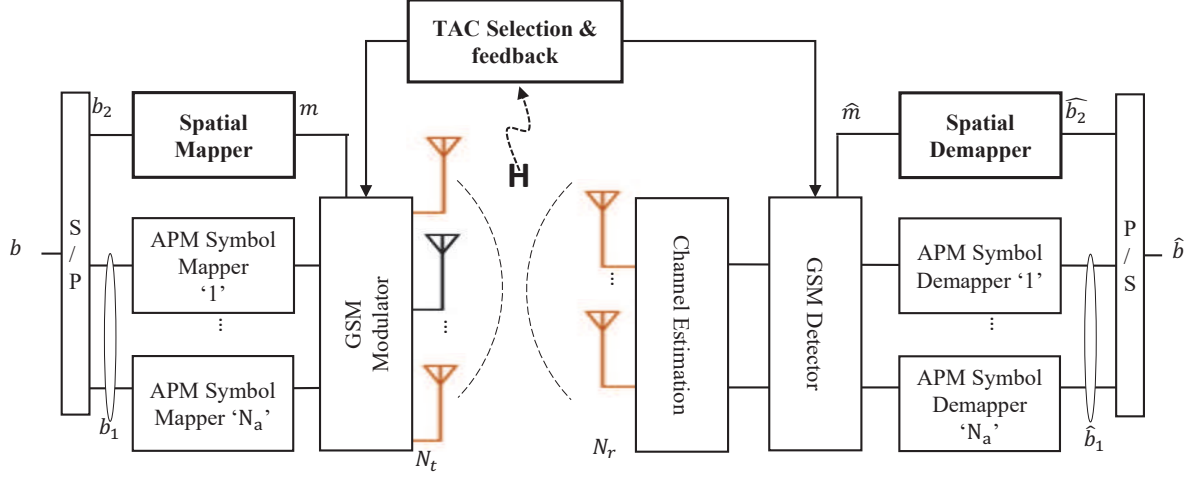


Figure 3.7 – System model of GSM with TAC selection

3.3.1 Efficient Legitimate TAC Selection

The GSM system has N_a TAs activated out of N_t TAs, and only $N_{TAC} = 2^{\lceil \log_2 N_{all} \rceil}$ TACs among N_{all} possible TACs will be used to encode the spatial bits. Firstly, the conventional GSM system was used with a random selection of N_{TAC} out of N_{all} , then TAC selections with/without CSIT were introduced in [63]. TAC selection's objective is to select the optimal legitimate TAC set that permits to reduce the TAC detection errors.

In this sub-section, we will propose a TAC selection method without instantaneous CSIT for highly correlated channels, and a comparative study with the existing methods will be provided.

3.3.1.1 GSM System Relying on Channel Side Information at the transmitter side (EGSM)

The Enhanced GSM system (EGSM) is an adaptive technique proposed in [63] where it uses the instantaneous CSIT, as shown in Fig. 3.7 to select the optimal legitimate TAC set instead of random TAC selection.

This selection is updated continuously in real-time to consider the channel variation. Then, the transceiver shares the legitimate TAC set through a feedback channel. This method is based on computing the Euclidian Distance (ED) matrix w between the N_{all} TACs ($\mathbb{I}_1, \dots, \mathbb{I}_{N_{TAC}}$) with all possible M -ary APM symbols according to (3.10), then eliminating $N_{re} = N_{all} - N_{TAC}$ TACs having the minimum ED.

$$w_{m,n} = \min_{\forall s_m, s_n} \|\mathbf{H}_{\mathbb{I}_m} \mathbf{s}_m - \mathbf{H}_{\mathbb{I}_n} \mathbf{s}_n\|^2, \quad (3.10)$$

where \mathbb{I}_m and \mathbb{I}_n are the TACs of index m and n respectively and they contain the indices of the activated TAs within a TAC, and \mathbf{s} represents the M -ary symbol vector of N_a elements with M^{N_a} possibilities.

The number of ED estimations to generate the matrix \mathbf{W} can be reduced from $N_{all}^2 (M^{N_a})^2$ to $N_{all} \frac{(N_{all}+1)}{2} \cdot (M^{N_a} \frac{(M^{N_a}+1)}{2})$ by removing the repeated estimations due to symmetry in each $w_{m,n}$ and \mathbf{W} .

Despite the optimal TAC selection of this method, it still has a large complexity for real-time estimation of these EDs, especially with large values M -ary and N_{all} . The useful data rate will also be highly reduced in a fast time-variant channel due to the overhead of the feedback channel. Moreover, for obtaining full CSIT, an infinite rate feedback channel, is required, which is practically infeasible for a band-limited channel.

3.3.1.2 Simplified Enhanced GSM S-EGSM

In this method, we target the mmWave/sub-THz bands where the antenna size and separation are very small, which leads to a high spatial correlation. Thus, the spatial correlation matrices in (3.7) are the dominant terms that will highly affect the detection of the activated TAC. For this reason, we propose a S-EGSM that considers only the Tx spatial correlation matrix instead of the complete channel matrix \mathbf{H} , where there is a larger number of antennas compared to the Rx side. In addition, the Tx spatial correlation matrix has very low variations (quasi-constant) for a specific Tx because it depends mainly on the antenna characteristics, separation, and array geometry. Therefore, S-EGSM is a TAC selection method without instantaneous CSIT, where the feedback channel is no more required as in EGSM because the transceivers agree on the TAC set only once at the setup phase and they can update them accordingly when the transmit spatial correlation is changed. The S-EGSM system can be described, as shown in Fig. 3.7 but without using the CSI feedback (\mathbf{H}).

The algorithm can be summarized as follows:

Step 1: Generate all possible TACs according to N_t and N_a .

Step 2: Using only the transmit spatial correlation, compute the lower or upper part of ED matrix \mathbf{W}' since by symmetry $w'_{m,n} = w'_{n,m}$:

$$w'_{m,n} = \min_{\forall \mathbf{s}_m, \mathbf{s}_n} \left\| \mathbf{H}_{\mathbb{I}_m} \mathbf{s}_m - \hat{\mathbf{H}}_{\mathbb{I}_n} \mathbf{s}_n \right\|^2, \quad (3.11)$$

where \mathbf{H} is calculated according to (3.7) with $\mathbf{H}_{LoS} = \mathbf{0}^{N_r \times N_t}$, $\mathbf{H}_{NLoS} = \mathbf{I}^{N_r \times N_t}$, and $\mathbf{\Sigma}_r = \mathbf{I}^{N_r \times N_r}$.

Step 3: Sort the ED values in ascending order

$$[v_1, v_2, \dots] = \text{sort}(w', \text{'ascending'}) \quad (3.12)$$

Step 4: Obtain the TAC set by removing N_{re} TAC starting with those that generate the smallest EDs (v_1, v_2, \dots) .

Note that another TAC selection method without CSIT was proposed in [63]. In the following, we will compare our proposed method (S-EGSM) to both methods with/without CSIT in [63].

3.3.2 Efficient Spatial bit mapping

After reducing the TAC error probabilities in the TAC selection methods, an efficient spatial mapping (Index-to-Bit Mapping) is proposed to reduce the spatial BER further and thus the total BER. In conventional GSM, the spatial mapping was simply the standard binary representation of the index $(m - 1)$ of the TAC \mathbb{I}_m , e.g., when $N_{TAC} = 4$, the spatial bits for \mathbb{I}_1 to \mathbb{I}_4 are coded as 00, 01, 10, 11 respectively.

In this section, we propose a spatial bit mapping method that considers the effect of spatial correlation. Note that the spatial correlation will lead to the high similarity between the channels of neighbor TACs, so when the Rx mis-detects the activated TAC, it will most probably be confusing by one of its neighbors.

Therefore, a Gray coding for spatial bits among each group of neighbor TACs can reduce the total BER. The spatial correlation is the highest between the adjacent antennas, so the order of correlation between any pair of TACs can be deduced from the Hamming distance between their antenna indices. The algorithm for the proposed mapping is summarized in the following:

Step 1: Compute the Hamming Distance (HD) matrix using the indices of activated antennas between the N_{TAC} possible legitimate TACs according to the following equation:

$$\mathbf{HD}_{m,n} = \sum_{i=1}^{N_a} |m_i - n_i|, \quad (3.13)$$

where $\mathbb{I}_m = \{m_1, \dots, m_{N_a}\}$ and $\mathbb{I}_n = \{n_1, \dots, n_{N_a}\}$ and the activated antennas indices m_i and n_i on each TAC are sorted in ascending order. In addition, the number of $\mathbf{HD}_{m,n}$ can be reduced from N_{TAC}^2 to $(N_{TAC} - 1) \frac{N_{TAC}}{2}$ by benefiting from the symmetry ($\mathbf{HD}_{m,n} = \mathbf{HD}_{n,m}$) and skipping the distance calculation between the same TACs.

Step 2: Compute the frequency of $\mathbf{HD} = 1$ for all TACs $\lambda_m^{HD=1} : \lambda_1^1, \dots, \lambda_{N_{TAC}}^1$ that represents the number of nearest neighbors for each TAC.

Step 3: Sort the N_{TAC} in descending order according to their λ_m^1 :

$$[p_1, p_2, \dots, p_{N_{TAC}}] = \text{sort}(\lambda_m^1, \text{'descending'}). \quad (3.14)$$

Table 3.4 – HD matrix for Spatial Mapping example with $N_t = 5$ and $N_a = 2$

$\mathbb{I}_m \setminus \mathbb{I}_n$	\mathbb{I}_1	\mathbb{I}_2	\mathbb{I}_3	\mathbb{I}_4	\mathbb{I}_5	\mathbb{I}_6	\mathbb{I}_7	\mathbb{I}_8
$\mathbb{I}_1 = \{1, 4\}$	0	1	1	2	2	1	2	3
$\mathbb{I}_2 = \{1, 5\}$	1	0	2	1	3	2	3	2
$\mathbb{I}_3 = \{2, 4\}$	1	2	0	1	1	2	1	2
$\mathbb{I}_4 = \{2, 5\}$	2	1	1	0	2	3	2	1
$\mathbb{I}_5 = \{2, 3\}$	2	3	1	2	0	1	2	3
$\mathbb{I}_6 = \{1, 3\}$	1	2	2	3	1	0	3	4
$\mathbb{I}_7 = \{3, 4\}$	2	3	1	2	2	3	0	1
$\mathbb{I}_8 = \{3, 5\}$	3	2	2	1	3	4	1	0
λ_m^1	3	2	4	3	2	2	2	2

Step 4: Start the Gray coding by assigning an unused bit mapping for the TAC that have the highest number of nearest neighbors (p_1, p_2, \dots). If this TAC has a previously assigned bit mapping skip this step.

Step 5: Generate the Gray code set for this TAC where any bit mapping in the set differs only by a single bit.

Step 6: Get the allowed Gray set for this TAC by removing the used bit mapping.

Step 7: Assign a bit mapping from its allowed Gray set to its neighbor TACs ($HD = 1$) if it is not previously assigned.

Step 8: Repeat from Step 4 until a bit mapping is assigned for all TACs.

In the following, we will illustrate an example for Gray coded spatial mapping with $N_t = 5$ and $N_a = 2$. Thus, the legitimate TACs ($\mathbb{I}_1, \dots, \mathbb{I}_8$) shown in Table 3.4 are obtained from the TAC selection, and each TAC index will be mapped to $\log_2(8) = 3$ spatial bits.

Consider a uniform linear antenna array, the HDs between indices of activated antennas are generated using (3.13), i.e. $HD_{1,2} = |1 - 1| + |4 - 5| = 1$. Note that the HD matrix for these TACs and the λ_m^1 are represented in Table 3.4 (Step 1, 2). Firstly, the Gray coding algorithm starts with the TAC \mathbb{I}_3 that has the highest number ($\lambda_3^1 = 4$) of nearest neighbors ($\mathbb{I}_1, \mathbb{I}_4, \mathbb{I}_5, \mathbb{I}_7$) as shown in Table 3.4. According to Step 3 to 6, \mathbb{I}_3 is initialized with '000', then its Gray Set is generated $\{001, 100, 010\}$, and nothing is removed because not all bit mappings have yet been used. Then, the bit mapping for $\mathbb{I}_1, \mathbb{I}_4, \mathbb{I}_5$ are assigned respectively from its Gray set, and \mathbb{I}_7 is left for future assignment by another TAC. Next, the neighbors for $\mathbb{I}_1 = 001$ (previously assigned) with $\lambda_1^1 = 3$ will be assigned from its allowed Gray set $\{101, 011, 000\}$. Finally, these steps are continuously repeated until a bit mapping is assigned for all TACs.

This best-effort Gray coding for spatial bits reduces the effect of spatial correlation that causes confusion in the detector at Rx between neighbor TACs. Note that this method enhances the spatial

BER up to 2 dB, as shown in the next section because it limits the number of different bits between neighbors TAC to the minimum possible.

3.3.3 Results for proposed S-EGSM and best-effort spatial bit mapping

In this sub-section, firstly, we compare our proposed technique for TAC selection S-EGSM to the existing methods EGSM and No CSI method in [63]. Note that both methods without instantaneous CSIT (S-EGSM and No CSI from [63]) estimate offline the best legitimate TAC set once in the setup phase, and they will keep using this set all the time while the Tx configuration (N_t and N_a) and antenna array characteristics are unchanged. However, the EGSM method is an adaptive TAC selection that keeps tracking the channel variation and updates the TAC set accordingly. Hence, this method requires a feedback channel to share the selected TAC set between the transceiver. For a fair comparison, we set the same GSM configuration with the same channels and transmitted bit-stream for all TAC selection methods. These TAC selection methods are compared under different transmit correlation factors to highlight the importance of the proposed method S-EGSM in highly correlated channels.

The correlation matrices in the Kronecker model are formed according to the exponential model of [168] where the elements of the transmit Σ_t and the receive Σ_r correlation matrices are affected by a correlation factor β : $[\Sigma_t]_{i,j} = \beta_t^{|i-j|}$. We used $\Sigma_r = I_{N_r}$ to concentrate on the impact of correlation at the Tx side where a larger antenna array is used to convey the data in the spatial domain of index modulation.

The following parameters are adopted with all TAC selection methods: $GSM(N_t, N_a, M) = GSM(6, 2, 2)$, $N_r = 4$, $\beta_t = \{0, 0.4, 0.8\}$, the number of GSM symbols is 10^4 simulated under 100 channel realizations. In addition, S-EGSM takes into consideration only the transmit spatial correlation matrix, which is the dominant term in highly correlated channels. For this reason, Rician channel is used with $K = 5$ to prove that the S-EGSM will not be affected by the LoS component even when neglecting the Rician K factor in Step 2 of the S-EGSM algorithm. Moreover, the adopted GSM detector in these systems is OB-MMSE that can detect the TAC and the APM constellations with a balanced tradeoff between system performance and complexity.

The results in Fig. 3.8a to Fig. 3.9 show that the adaptive method EGSM with CSIT has the best performance in all correlation levels because it keeps updating the legitimate TAC set instantaneously according to channel variations. However, we notice in Fig. 3.8a to Fig. 3.9 that the No CSIT method from [63] has a slightly better performance at low SNR compared to S-EGSM, but as transmit correlation level increases the S-EGSM performance at high SNR becomes the best TAC selection without instantaneous CSIT. Moreover, the advantage of No CSIT method [63] at low SNR disappears in highly correlated channel $\beta_t = 0.8$, and the performance of proposed S-EGSM becomes better by 1.4 dB at BER= 10^{-4} compared to the other method without CSIT.

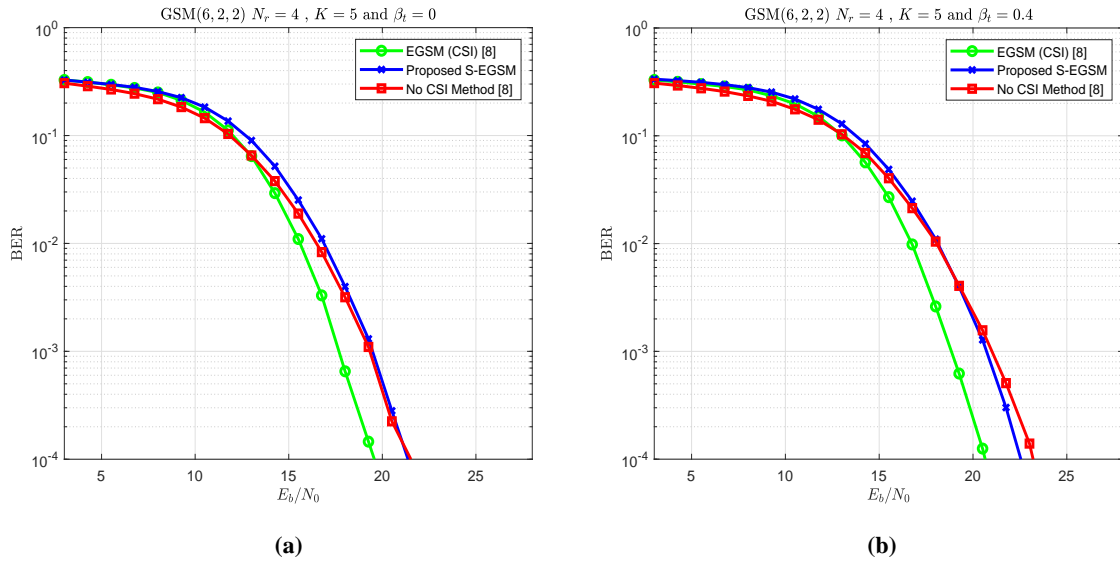


Figure 3.8 – BER vs E_b/N_0 for various TAC selection with: (a) $\beta_t = 0$, (b) $\beta_t = 0.4$.

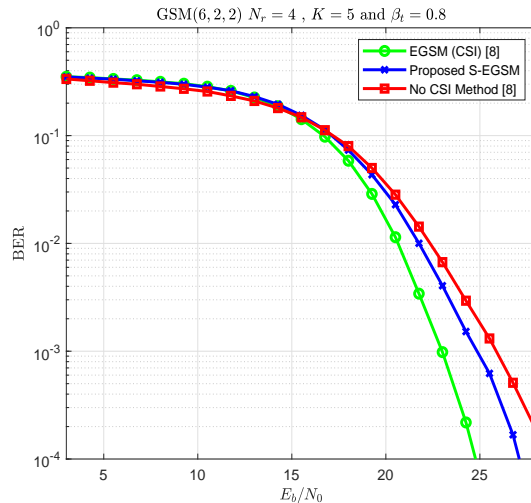


Figure 3.9 – BER vs E_b/N_0 for various TAC selection with $\beta_t = 0.8$

Therefore, the S-EGSM is an efficient TAC selection method without instantaneous CSIT in highly correlated channels, which is the case in mmWave and THz bands where the correlation factor is in the order of $\beta_t = 0.8$ according to [169]. However, the TAC selection with CSIT EGSM can be used in the slow time-variant channel (small Doppler) to achieve the optimal performance, while in fast variant channels TAC selection methods without instantaneous CSIT is preferred to avoid the increased complexity due to real-time TAC selection and to limit the overhead of the feedback channel. Finally, the usage of S-EGSM technique in a fast variant channel environment depends on the correlation level, where it will be highly recommended for highly correlated channels.

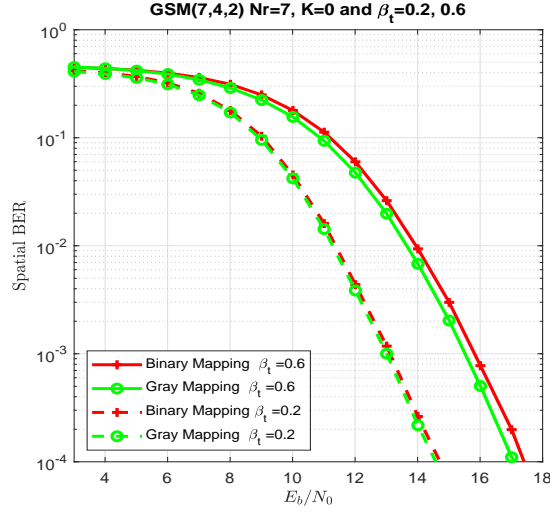


Figure 3.10 – BER vs E_b/N_0 for different TAC spatial mapping with $\beta_t = \{0.2, 0.6\}$

In the following, the spatial mapping with binary and gray coding is compared under the same conditions with different correlation levels. For this comparison, we used $GSM(7, 4, 2)$ where we have $\lceil \log_2(C_7^4) \rceil = 5$ spatial bits. As shown in Fig. 3.10, as the correlation factor increases, the Gray coding gain increases from 0.15 dB to 0.4 dB. Note that the gray coding gain is higher when TAC selection is not used because it reduces the number of neighbor TACs.

Consequently, the gray coding gain appears when the detector at the Rx is confused between the activated TAC and one of its neighbor TACs ($HD=1$). This misdetection of the activated TAC can cause a single bit error only if this TAC and its neighbors are Gray coded. Thus, the gray coding advantages appear more in a highly correlated channel, as shown in Fig. 3.10 where the neighbor TACs cannot be distinguishable at the Rx side to correctly detect the activated TAC.

Moreover, this gain does not always appear because the gray coding for spatial bits is a best-effort algorithm to reduce the number of bits difference between neighbor TACs. However, the gray coding for all neighbor TACs is not always guaranteed, so this gain in some cases might vanish, and the performances for both the gray and normal binary coding become similar. Note that the Gray coding for spatial bits is prepared offline once for a given GSM configuration. Therefore, the gray coding should be used in spatial mapping because in all cases it will have some gain, but it will never have a loss compared to normal binary coding for spatial bits.

In the following, we show that the gray coding gain is larger when all the neighbor TACs are gray coded. For example, the gray coding for all neighbors can be satisfied when SM is taken into consideration because it has a single active antenna instead of N_a ($SM(N_t, M) = GSM(N_t, 1, M)$). The gray coding gain increases with SNR for $SM(16, 2)$ and $N_r = 2$ in a highly correlated Rician channel ($K = 5$), as shown in Fig. 3.11 where it reaches 1.5 dB at $BER=5 \cdot 10^{-4}$.

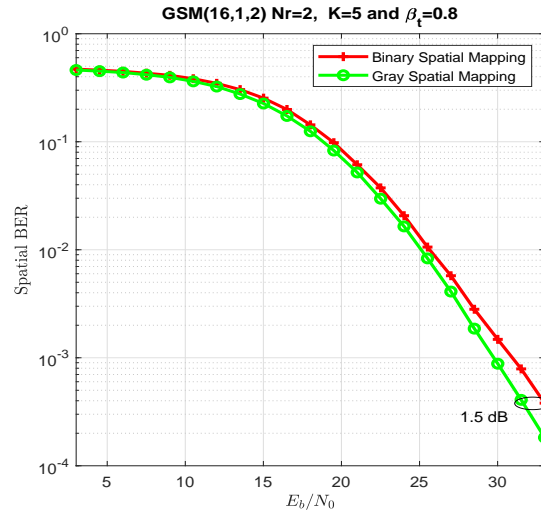


Figure 3.11 – Spatial BER vs E_b/N_0 for binary and gray coding for spatial bits

To conclude this section, we proposed a TAC selection method without instantaneous CSIT (S-EGSM) for highly correlated channels, where we consider only the transmit spatial correlation. Hence, the proposed S-EGSM without instantaneous CSIT is more suitable for time-varying channels since it permits to avoid the overhead of the feedback channel and the increased complexity in real-time TAC selection. However, the adaptive TAC selection with full CSIT (EGSM) can be adopted in time-invariant or slow-time varying channels to reach the optimal performance. Hence, the decision of GSM TAC selection can be summarized in the flowchart shown in Fig. 3.12.

Moreover, we developed an algorithm that uses gray spatial bit-mapping in GSM (applicable for GSM sub-systems) to minimize the number of bit errors between neighbor TACs. Finally, it is worth mentioning that the authors of [178] proposed to use signature constellations with an inter-constellation minimum ED for different TAs to combat the Rician Fading channels and to reduce more the channel correlation effect, where it also provides an important performance gain, and it can be incorporated with our proposed techniques.

3.4 GSM with RF impairments

MIMO system with IM as GSM [105] is a promising technique for wireless ultra-high data rates system where it achieves the best performance and lowest power consumption when using low order modulation schemes in correlated/uncorrelated Rayleigh and Rician channels [14] as discussed in Section 3.2. However, GSM performance degrades in highly correlated channels and many enhancement techniques are proposed in [63] and [15] to reduce this degradation as shown in Section 3.3. Moreover, mmWave and sub-THz bands are considered for beyond 5G ultra-high data rate scenarios [4] as highlighted in Section 1.1. However, these bands especially the sub-THz suffer from

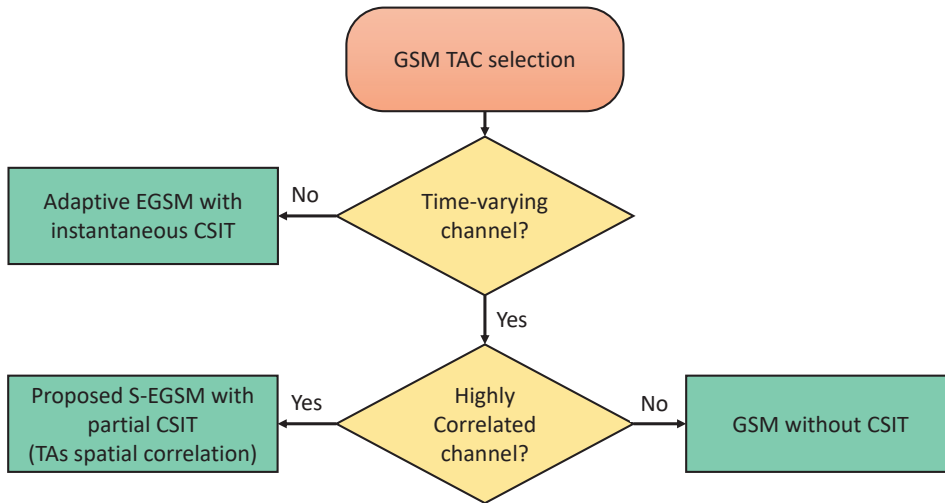


Figure 3.12 – Flowchart decision for the most suitable GSM TAC selection.

higher channel attenuation and sensitivity to small environment details [36] [6], severe RF-impairments and many technological limitations such as low output power, limited resolution of high-speed low-power ADCs [39], important PN introduced by the LO [11].

In this section, different modulations schemes with GSM are compared from different perspectives while considering the sub-THz impairments mentioned in Section 1.2. The effect of PN has been investigated for these modulation schemes in sub-THz channels using uniform linear and rectangular antenna arrays. Moreover, SMX and GSM are compared from different perspectives while considering these impairments. The comparison is also performed in terms of PAPR, power consumption, optimal detection complexity, and transmitter/receiver cost. In addition, the link budget and the system power consumption is estimated for both systems.

3.4.1 Sub-THz MIMO Channel

A ray-based deterministic channel modeling developed by our BRAVE partner SIRADEL for sub-THz Band (mainly between 90-200 GHz) is presented in [36]. It is worth mentioning that the propagation channel model in [36] considers the material properties, gas attenuation, and the impact of furniture that leads to more obstructions along the propagation paths and new scattered paths. It also characterizes the main channel properties such as path loss and delay spread for LOS, NLOS with vegetation, and NLOS cases for indoor in-office and outdoor in-street scenarios. In the following, we will focus on the downlink hotspot (or kiosk) indoor scenario where the AP, acting as transmitters, and the MSs, acting as receivers, are equipped with N_t and N_r isotropic antennas. Therefore, the MIMO propagation channels are obtained using the simulator for ray-based deterministic channel modeling. The MIMO channels are obtained with different array geometry, such as ULA and URA. Note that an antenna element separation

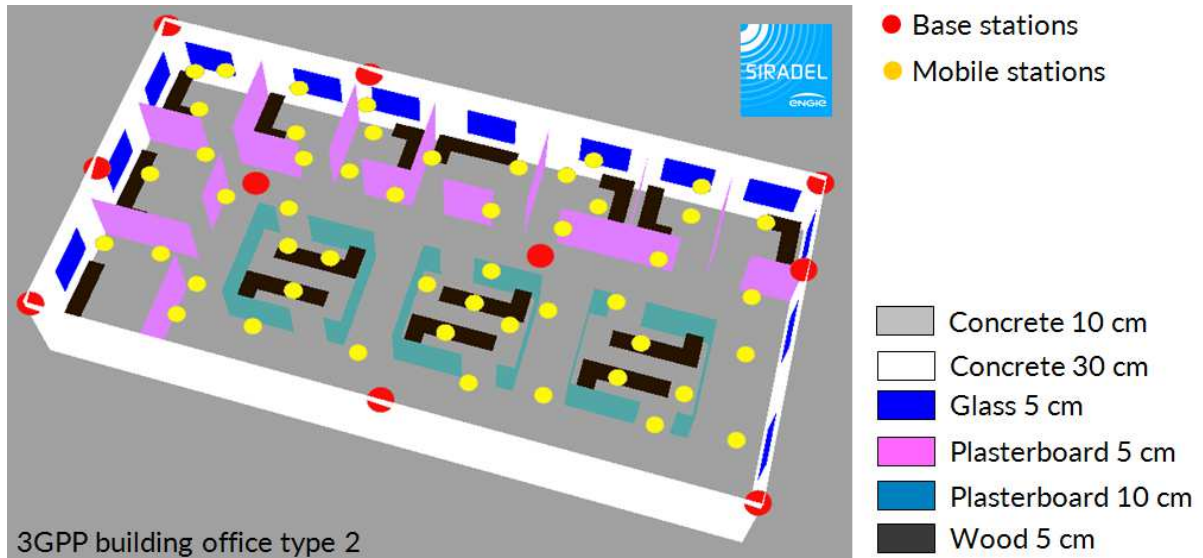


Figure 3.13 – In-office scenario environment studied by our ANR BRAVE partner SIRADEL [36]

of 4λ , where λ is the wavelength, is considered to reduce the effect of spatial correlation [169], and thus enhance MIMO communication.

3.4.2 Sub-THz Phase noise model

It is well known that a practical oscillator can never generate a pure sinusoid, and the PN increases with the carrier frequency. Thus, the sub-THz communication system should be analyzed under this impairment since neglecting its impact is no more tolerable as in sub-GHz systems.

In general, the analysis of PN impact on MIMO systems is dependent on the RF architecture, where there are mainly two LO setups: Distributed Oscillators (DO), Centralized or Common Oscillator (CO). The main difference is that each antenna in the DO setup has its own LO, while in the CO setup, all antennas at the transmitter/receiver are connected to a common LO. Consequently, all parallel streams in CO have the same PN while the DO suffers from different phase and amplitude distortions.

The PN model is widely investigated where the PN, in general, is modeled by two main models: Gaussian PN (uncorrelated PN) and Wiener PN (correlated PN). The Wiener model is more accurate since it includes the cumulative PN (correlated term) due to the integration step of the Phase-Locked Loop (PLL). However, for high-rate communications, the effect of Wiener PN on the system performance is negligible compared to the Gaussian PN [179]. Besides, the Wiener PN process becomes negligible compared to the Gaussian for wide-band systems where the oscillator corner frequency f_c is small compared to the system bandwidth [11]. Thus uncorrelated Gaussian PN model is appropriate for sub-THz bands. Note that the uncorrelated model remains valid when the following condition is

satisfied [11]:

$$N_s f_c^2 T^2 \leq \frac{\ln(2)}{2\pi^2}, \quad (3.15)$$

where N_s is the number of symbols per frame, f_c is the corner frequency of the oscillator and T is the symbol period. It is clear that a careful communication system design can limit the wiener effect by selecting the appropriate N_s and T .

The received baseband vector of an equivalent $N_r \times N_t$ MIMO system with phase noise can be expressed as:

$$\tilde{\mathbf{y}} = \Phi_r \mathbf{H} \Phi_t \mathbf{x} + \mathbf{n}, \quad (3.16)$$

where Φ_t and Φ_r are the $N_t \times N_t$ and $N_r \times N_r$ diagonal matrices of phase noise from the transmitter and receiver oscillators respectively. These phase noise matrices can be represented as follows:

$$\Phi_t = \text{diag}\left([e^{j\theta_1^{Tx}}, \dots, e^{j\theta_{N_t}^{Tx}}]^T\right) \quad (3.17)$$

$$\Phi_r = \text{diag}\left([e^{j\theta_1^{Rx}}, \dots, e^{j\theta_{N_r}^{Rx}}]^T\right), \quad (3.18)$$

where θ_i^{Tx} and θ_j^{Rx} are the phase noise at the i^{th} TA and j^{th} RA respectively that can be described in sub-THz band by a truncated Gaussian distribution $\mathcal{N}(0, \sigma_g^2)$ with zero-mean and variance σ_g^2 similar to SISO PN model described by our BRAVE partner CEA-Leti in [11]. In the DO setup, $\theta_i^{Tx} \neq \theta_j^{Tx}$ and $\theta_i^{Rx} \neq \theta_j^{Rx}$ for all $i \neq j$. However, in the CO setup, with different oscillators at Tx and Rx sides, $\theta_i^{Tx} = \theta^{Tx}$ for all $i = 1, \dots, N_t$ and $\theta_j^{Rx} = \theta^{Rx}$ for all $j = 1, \dots, N_r$. Thus, the received signal in the CO setup can be simplified to:

$$\tilde{\mathbf{y}} = e^{j\theta^{Tx}} e^{j\theta^{Rx}} \mathbf{H} \mathbf{x} + \mathbf{n} \quad (3.19)$$

3.4.3 System comparison: GSM vs SMX

3.4.3.1 Performance in sub-THz environment

In this section, the performance of the GSM subjected to sub-THz impairments will be studied using the sub-THz channel generated from the ray-based model. Firstly, we will show the impact of PN in DO setup over MIMO sub-THz channels on GSM systems with different modulation schemes for an indoor ultra-high data rate scenario. The system comparison is performed with different PN levels (low $\sigma_g^2 = 0.001$, medium $\sigma_g^2 = 0.01$, strong $\sigma_g^2 = 0.1$) without applying any phase noise mitigation technique. In our comparison, we consider the sub-THz indoor MIMO channels with a separation distance between MS and AP going from 2 to 8 meter (m), i.e., an average distance of 5m. For a fair comparison, the different GSM systems are compared under the same SE, which requires the same number of activated TAs N_a and the same total number of TAs N_t when using linear modulation schemes as PSK, QAM, DPSK, PAM. The optimal ML detection is used along with the same number of RAs N_r . In the following, we will consider different GSM systems with 12 bits per channel use (bpcu)

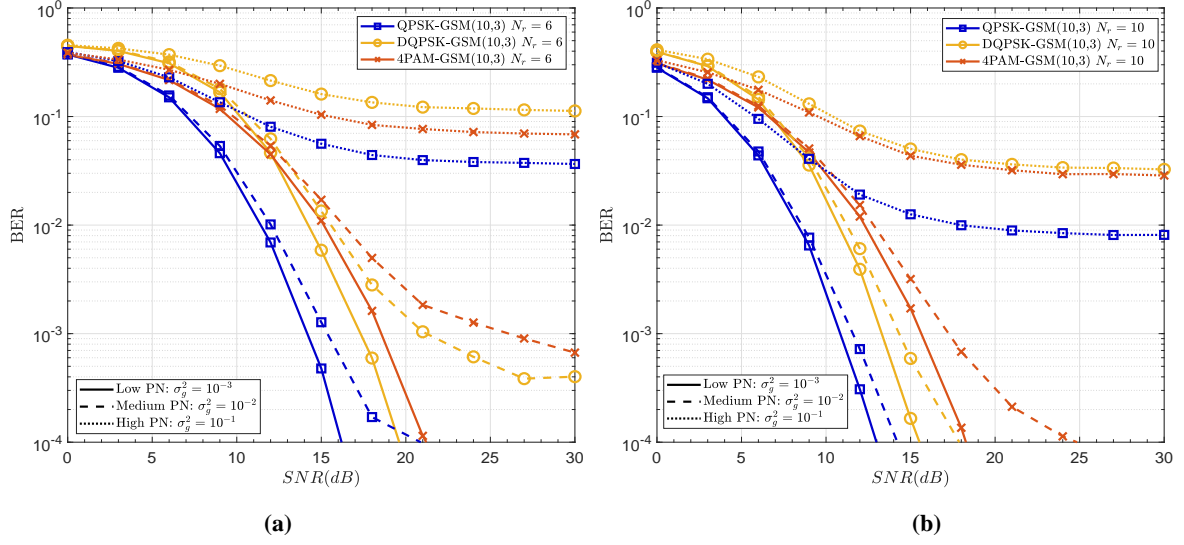


Figure 3.14 – BER performance of different APM-GSM systems in sub-THz channels and with different PN levels in DO setup. The spectral efficiency is 12bpcu. The concerned sub-THz indoor MIMO channels are generated using ULA array geometry with 4λ antenna separation. (a) $N_r = 6$, (b) $N_r = 10$.

with $N_t = 10$ and $N_a = 3$ and one of the following modulations: QPSK, DQPSK, 4PAM. Note DPSK and PAM schemes are considered in our study with MIMO GSM because they show some robustness to PN in SISO channels.

Fig. 3.14 shows clearly that QPSK-GSM outperforms DQPSK-GSM and 4PAM-GSM subjected to any PN level. For example, a gain of 3.4 and 5 dB is obtained using QPSK-GSM as compared to DQPSK-GSM and 4PAM-GSM systems, respectively with $N_r = 6$ at low PN, as shown in Fig. 3.14a. However, these values of gain become respectively 2.5 and 5.2 dB when $N_r = 10$, as shown in Fig. 3.14b. Moreover, the performance gain of QPSK-GSM is much higher at medium PN compared to DQPSK-GSM and 4PAM-GSM. Thus, MIMO QPSK-GSM is more robust to PN even when compared to PAM modulation, which is not sensitive to PN in SISO mode. Note that these systems, without phase noise mitigation techniques, suffer from a high error floor when subjected to strong PN in sub-THz channels. The simulation results with URA geometry are shown in Fig. 3.15, where similar conclusions on the obtained gain can be drawn for low PN with the difference that all systems require a slightly larger SNR due to the higher spatial correlation between antennas. However, only QPSK-GSM maintains the small degradation at medium PN when using URA geometry.

Therefore, GSM can survive at low to medium PN in the sub-THz channel, but more research is required to enhance GSM performance with a strong PN channel. We would like to highlight that the performance could be improved in the PN channel by using PN robust modulations (e.g., spiral QAM [180]), powerful channel coding technique and special detector/equalizer designed specifically for PN channel.

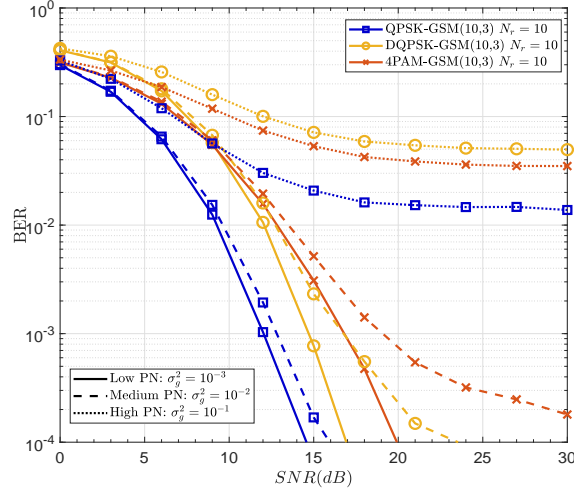


Figure 3.15 – BER performance of different APM-GSM systems in sub-THz channels and with different PN levels in DO setup. The spectral efficiency is 12bpcu. The concerned sub-THz indoor MIMO channels are generated using URA array geometry with 4λ antenna separation and $N_r = 10$.

It is worth mentioning that low order modulation schemes are only considered with GSM because they have lower PAPR, lower power consumption, and lower sensitivity to PN compared to higher M -ary APM schemes, and they can be accompanied with low-power high-speed ADCs of few bits resolution. Among the compared low order modulations, QPSK-GSM achieves the lowest power consumption due to the lowest SNR requirements and PAPR. Note that another drawback for M -ary PAM is that higher M -ary PAM suffers from higher PAPR increase and require larger resolution bits for ADCs due to using only the amplitude dimension in the signal domain. Finally, these GSM systems with low order modulation 4-ary APM have similar computational complexity in terms of real multiplication/additions and cost in terms of the number of RF chains.

In the following, the average BER performance of SMX and QPSK-GSM are compared over different sub-THz channel realizations, while varying PN levels and antenna array geometries. Fig. 3.16 shows clearly that QPSK-GSM outperforms SMX subjected to any PN level. For example, a gain of 4 dB is obtained using QPSK-GSM as compared to QPSK-SMX system, and which goes to 6.8 dB when compared to 16QAM-SMX with $N_r = 6$ at low PN as shown in Fig. 3.16a. However, these values of gain are respectively reduced to 2 and 4.2 dB when $N_r = 10$, as shown in Fig. 3.16b. Note that QPSK-SMX in sub-THz channels performs better than 16QAM-SMX for the same SE in all cases.

Moreover, the performance gain of QPSK-GSM is much higher at medium PN when compared with QPSK-SMX, and becomes more advantageous when compared to 16QAM-SMX, where the results prove that the high M -ary QAM schemes are very sensitive to PN. Thus, GSM is more robust to PN since the amount of information being conveyed and contained in the phase of the complex symbols (QPSK or QAM) is less as compared to SMX, while a part of this information is conveyed through the virtual bits (less sensitive to the PN effect). Note that both systems, without phase noise

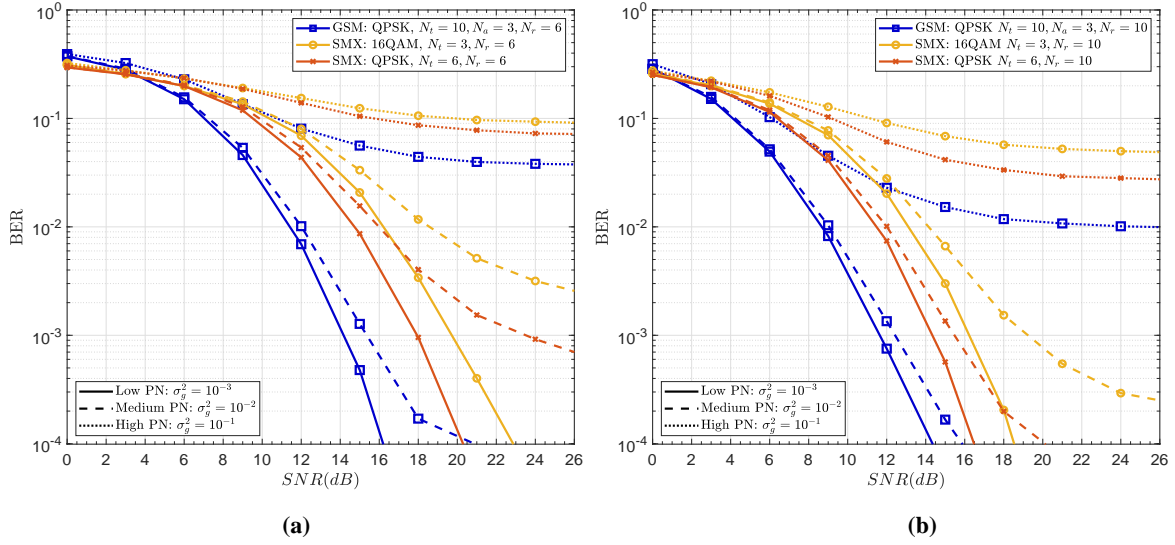


Figure 3.16 – Average BER performance of 12bpcu MIMO SMX and GSM systems subjected to different phase noise levels in DO setup. AP-UE mean distance is $d_{mean} = 5m$. ULA array geometry with 4λ antenna separation is used with (a) $N_r = 6$, (b) $N_r = 10$.

mitigation techniques, suffer from a high error floor when subjected to high PN in sub-THz channels. The simulation results with URA geometry are shown in Fig. 3.17, where similar conclusion on the obtained gain can be drawn with the difference that all systems require a slightly larger SNR due to the higher spatial correlation between antennas.

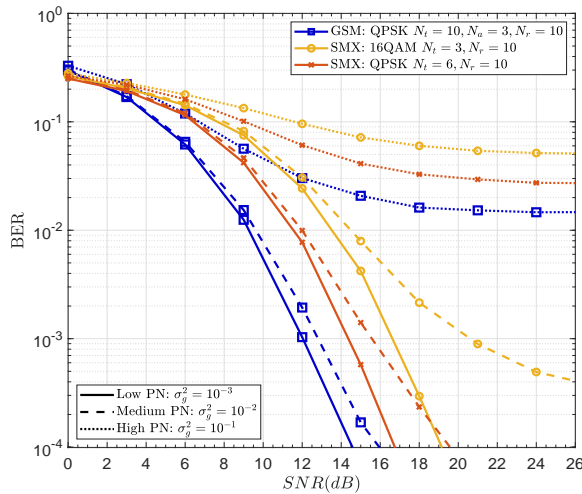


Figure 3.17 – Average BER performance of 12bpcu MIMO SMX and GSM systems subjected to different phase noise levels in DO setup. AP-UE mean distance is $d_{mean} = 5m$. URA array geometry with 4λ antenna separation is used with $N_r = 10$.

Therefore, QPSK-GSM can survive at low to medium PN in the sub-THz channel more than SMX systems of the same SE, but more research is required to enhance the system performance with a high PN channel.

3.4.3.2 Optimal Detection Complexity

In this subsection, SMX and GSM receivers are compared from the detection complexity point of view. The ML complexity is measured by the number of real multiplications performed because the hardware complexity of the addition is negligible compared to the multiplications. The number of Euclidean distances being calculated in the ML detector for SMX is $M^{N_t} = 2^{\mathcal{L}_{SMX}}$ while it is $N_{TAC} M^{N_a} = 2^{\mathcal{L}_{GSM}}$ for GSM. The number of non-zero real multiplications in the matrix multiplication $\mathbf{H}\mathbf{x}$ is $4N_r N_t$ for SMX and $4N_r N_a$ for GSM since each complex multiplication is 4 real multiplications and 2 real additions. In addition, the Frobenius norm contains $2N_r$ real multiplications, so the total ML detector complexity for SMX and GSM in terms of real multiplications can be expressed as:

$$\mathcal{C}_{SMX} = 2^{\mathcal{L}_{SMX}+1} (2N_t + 1) N_r \quad (3.20)$$

$$\mathcal{C}_{GSM} = 2^{\mathcal{L}_{GSM}+1} (2N_a + 1) N_r. \quad (3.21)$$

It is clear that GSM and SMX have the same detector computational complexity when they have the same system SE $\mathcal{L}_{SMX} = \mathcal{L}_{GSM}$, number of activated TAs and RAs, even with higher modulation order in SMX system. However, SMX suffers from higher computational complexity when the number of TAs in SMX $N_t > N_a$ is increased to maintain the same efficiency and modulation order as GSM for better robustness to PN using low modulation order. The complexity of SMX in both configurations compared to GSM with the same spectral efficiency (12bpcu) is illustrated in Fig. 3.18, where MIMO QPSK-SMX is 1.86 times more complex than QPSK-GSM.

3.4.3.3 PAPR Discussion

In this sub-section, we will complete our analysis by considering other important factors for sub-THz communication. MIMO systems in sub-THz bands require using low order modulation schemes as QPSK mainly for two reasons: 1) higher robustness to PN and 2) the limited resolution of ultra-high-speed low power ADCs to few bits (limited quantization levels). Thus, low order modulation schemes with GSM or other IM techniques are required to achieve ultra-high data rates in the sub-THz environment.

When using the same modulation schemes, GSM and SMX have the same PAPR only if an RF antenna switching is applied after the PA, as detailed in Section 3.2.7.2. However, the full-RF transmitter architecture without RF switching is preferred to avoid any SE loss and transmission rate dependency on the physical RF switching rate, as discussed in Section 3.2.7.1. This solution leads

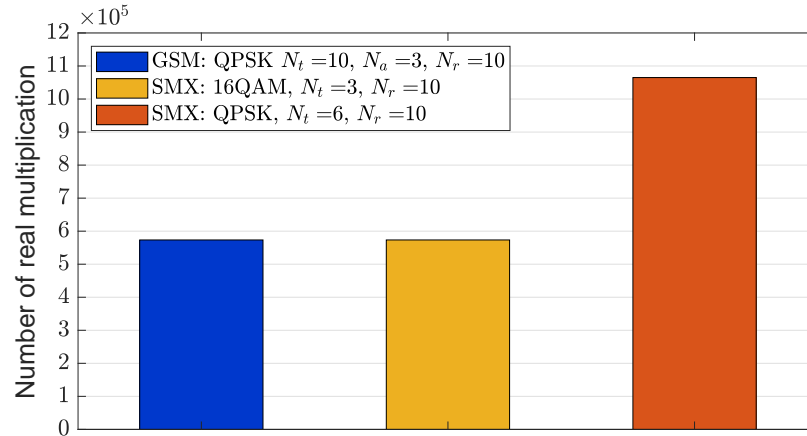


Figure 3.18 – ML detector computational complexity for GSM and SMX with same spectral efficiency 12bpcu.

to higher transmitter cost (for AP can be tolerated) and a higher PAPR compared to SMX since GSM PAPR highly depends on the modulation schemes and the number of inactive TAs (refer to Section Section 3.2.7.2). Note that the PAPR affects the PA efficiency and thus the system power consumption. Simple PAPR reduction techniques can mitigate this drawback of GSM. In conclusion, the RF switching, when performed after the PA to maintain the same PAPR, induces a SE decrease in the GSM transmitter. Whereas the GSM with full-RF Tx architecture, i.e., more RF chains, has a slightly higher PAPR compared to QPSK-SMX, and PAPR reduction techniques can compensate it. Note that the cost of GSM TX with full-RF architecture can be tolerated for the base stations/APs, and this solution is more appropriate for ultra-high data rates system since the RF-switching is no more needed and the SE gain by IM is conserved.

3.4.3.4 Link budget for systems in sub-THz environment

In this subsection, the link budget for SMX and full-RF GSM subjected to PN in indoor sub-THz channels for downlink ultra-high wireless data rates is presented. In this link budget estimation, the system configuration shown in Fig. 3.16b with medium PN is used to estimate the required transmit power for achieving the needed SNR at un-coded BER= 10^{-4} . The link budget, the estimated total power consumption, and the data rates using GSM and SMX are presented in Table 3.5 with different values of the total system bandwidth.

In Table 3.5, the required transmit power P_t with small distance communication is calculated from the required SNR according to the following parameters to the equations summarized in Table 3.2. Furthermore, the power consumption is deduced based on the PA efficiency, which is affected by the PAPR. It is clear from Table 3.5 that GSM has a lower power consumption compared to SMX even when using full-RF GSM that suffers from higher PAPR and thus lower PA efficiency. Note that the

Table 3.5 – Link budget of SMX and GSM systems over sub-THz channels and subjected to medium PN.

System Parameters	GSM	SMX
Carrier frequency (GHz)	150.00	
Distance (m)	2 to 8	
Channel Bandwidth W (GHz)	0.50	
Spectral Efficiency (bpcu)	12	
Data Rates per Channel (Gbps)	up to 6	
Pulse Shaping: Rolloff	Root Raise cosine: 0.2	
Spectral efficiency (b/s/Hz)	10	
Required Transmit Power P_t (dBm)	-1.96 to 10.08	2.04 to 14.08
Transmit antenna gain G_t (dBi)	15.00	
EIRP (dB)	13.04 to 25.08	17.04 to 29.08
f_{spl} (dB)	81.98 to 94.02	
Receive antenna gain G_r (dBi)	5.00	
Received power $R_{x_{level}}$ (dBm)	-63.94	-59.94
Thermal noise (Power Spectral Density (PSD)) (dBm/Hz)	-174.00	
Noise figure N_{Figure} (dBm)	7.00	
Thermal noise $N_{Thermal}$ (dBm)	-86.94	
Noise floor N_{floor}	-79.94	
SNR with medium PN (dB)	16.00	20.00
Average PAPR (dB)	7.66	6.18
PA efficiency	0.32	0.38
Power consumption (dBm/channel)	2.99 to 15.03	6.24 to 18.28
12.5 GHz channel bonding (25 channels)		
Data Rates (Gbps)	125	
Total Power consumption (dBm)	16.97 to 29.01	20.22 to 32.26
48 GHz channel bonding and aggregation (96 channels)		
Data Rates (Gbps)	480	
Total Power consumption (dBm)	22.81 to 34.85	26.06 to 38.10

required EIRP for both systems to reach AP-UE distance up to 8 m is less than the maximum allowed EIRP in regulations (40 dBm). The required transmit power for GSM is achievable using the existing electronic technology, while for SMX system, it is 14.08 dBm for 8 m AP-UE distance, which is more than the currently available output power at the sub-THz band.

In our example, the PAPR is estimated after the pulse shaping of QPSK-GSM, and it is 1 – 2 dB higher compared to QPSK-SMX. However, GSM keeps a lower power consumption due to its lower SNR requirement for the same BER. For clarification, GSM requires 3.25 dB less than SMX system, which means less than half of the required power with SMX system. Moreover, the total power consumption and data rates are estimated with different total system bandwidths that are available in the band between 90 GHz and 175 GHz. SMX and GSM systems can reach up to 125 Gbps and 480 Gbps (0.5 Tbps) when the considered total system bandwidth, after channel aggregation and bonding, is 12.5 GHz and 48 GHz respectively with 0.2 pulse shaping roll-off factor. Therefore, if the residual

PN before detection is at a medium level, the presented system QPSK-GSM can be considered an appropriate solution for ultra-high wireless data rates system in the sub-THz while having an acceptable AP power consumption between 0.2 and 3 Watts for 0.5 Tbps.

In conclusion, the different APM schemes with GSM subjected to realistic sub-THz impairments in an indoor environment are compared from different perspectives, where QPSK-GSM proves its superiority compared to other APM-GSM. In addition, GSM and SMX are compared from different perspectives with the same conditions. The simulation results reveal that MIMO GSM outperforms SMX for all PN levels in the sub-THz channels using ULA or URA array geometry with non-coherent detection. The performance gap increases with the increase in PN, where GSM outperforms SMX in terms of BER even when both systems use the same modulation order. Among SMX systems, QPSK-SMX achieves better performance than 16QAM-SMX at the cost of higher detection complexity. The performance of higher-order QAM-SMX is primarily limited due to higher sensitivity to PN. In addition, GSM system with non-coherent detection achieves good performance in the presence of low and medium PN, and a PN mitigation is required for high PN case.

Finally, compared to SMX system, the GSM system with low modulation order offers better performance, lower complexity, lower power consumption (less than half compared to SMX) and higher robustness to PN and few-bits ADC resolution requirement, which make it a potential candidate for ultra-high data rates in sub-THz bands. However, full-RF GSM may suffer from higher transmitter cost and PAPR, but it overcomes the ultra-fast RF switching issue and the SE possible degradation. Moreover, we would like to highlight that low order modulation schemes are required to allow related systems to survive with sub-THz technological limitations, which imposes the use of spectral-efficient IM techniques to achieve ultra-high data rates. In the next sections, the high detection complexity problem for SMX and GSM using the optimal ML is addressed by proposing low-complexity quasi-optimal detector for each system.

3.5 Near-Optimal Performance with Low Complexity ML-based detector for SMX

MIMO SMX technique allows reaching high SE. However, the decoding of the received signal at the receiver side becomes a very complex task with larger modulation order and large-scale MIMO.

In general, the performance of such systems highly depends on the receiver detection methods where the best estimate is obtained by the ML detector. However, the ML detector complexity increases exponentially with the number of TAs and it is not practical for high order modulation schemes due to the huge number of possible multiplexing combinations. Consequently, the complexity of soft detection of MIMO-QAM is reduced by avoid computing all the Euclidean Distances (EDs) [181].

Moreover, some known solutions in the state of art which make use of ML criteria such as Sphere Decoding (SD) [182–184] and QR decomposition with order M Maximum Likelihood Decoding (QRM-MLD) [185] preserve the optimal performance, but they still suffer from major drawbacks. For instance, the SD complexity is highly dependent on the initial value for the search radius: if the search radius is chosen too small, there may be no solution in the hypersphere, but if the search radius is chosen too large, the number of points to explore may become too large, and the algorithm will encounter the same issue as ML-based detection algorithms [186]. Also, its complexity is very dependent on the SNR and on the channel modeling parameters used for implementing the algorithm. Compared with SD, QRM-MLD technique, which only keeps the best M candidates for the next level search, has fixed throughput and is suitable for pipelined hardware implementation. However, it involves a very high complexity, especially for higher modulation schemes like 256 QAM. Finally, these techniques cannot be implemented on highly parallel hardware architecture and are thus not suitable for real-time high data rate transmission.

In addition, the linear detector based on ZF or MMSE [187] or OSIC criteria [96] have a low complexity but the overall performance is limited by an error-floor compared to the ML detector. Moreover, the performance of OSIC detector highly depends on the strongest detected signal and can suffer from an error propagation due to the added interference when a symbol is wrongly detected.

In this section, a new detection technique, called OSIC-ML [19, 188], is investigated which combines the linear technique OSIC with the non-linear technique ML. It aims to approach the complexity of linear detectors while maintaining the performance of non-linear detectors. The system performance with perfect/imperfect channel estimation and the computational complexity of the proposed detector are evaluated with different configurations to highlight its advantages.

3.5.1 Proposed OSIC-ML Detector

The MIMO-SMX system model and the joint ML detector that estimates the N_t APM symbols are summarized in Section 2.3.1.

3.5.1.1 Detection algorithm

A possible implementation for an OSIC-ML based receiver (RCV) is depicted in Fig. 3.19. The receiver aims to estimate the N_t emitted symbols, $\hat{x}_1, \hat{x}_2, \hat{x}_3, \dots, \hat{x}_{N_t}$. This detector can include any existing ordering technique used with the conventional OSIC detector for better interference cancellation. In the following, we consider a detection without any ordering and with the simplest ordering technique based on the channel matrix columns norm ($\|\mathbf{h}_i\|^2$). This power ordering technique computes once the N_t norms and sorts them in decreasing order to identify the order of symbol detection. The notation $x_{(i)}$ is used to represent the i^{th} symbol after ordering, while x_i represents the emitted symbol from the i^{th}

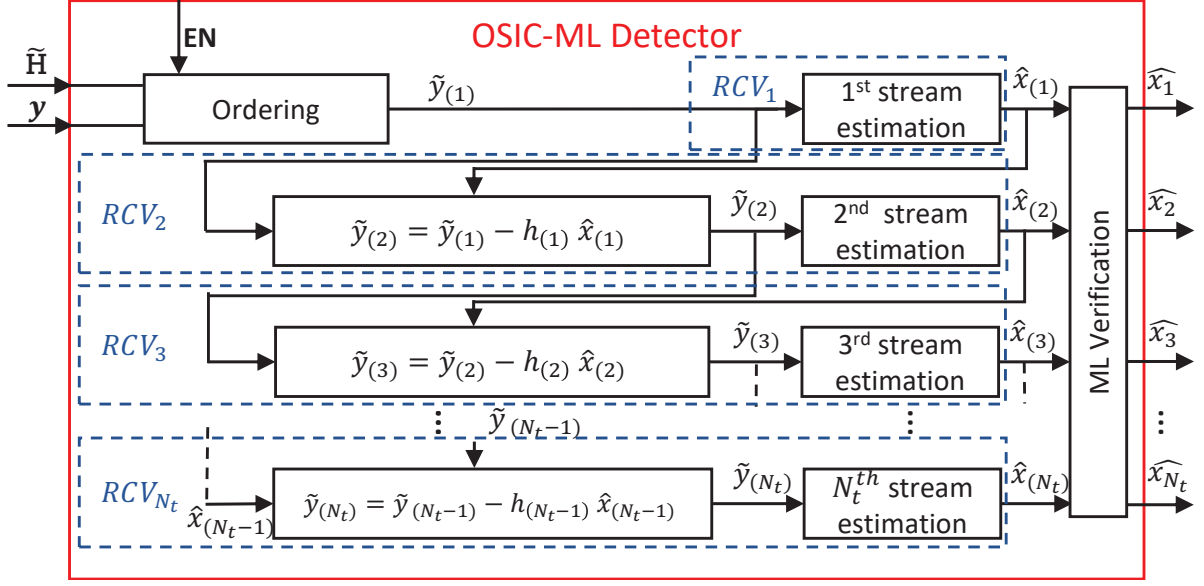


Figure 3.19 – OSIC-ML model with/without ordering. 'EN' is a boolean variable to activate the ordering technique prior to detection and interference cancellation. The stream estimator in the N_t receive circuits is based on a linear symbol detection.

TA. Note that $x_{(i)}$ and x_i are the same when the ordering is not considered (OSIC-ML without power priority).

The received signal \mathbf{y} can be expanded as:

$$\mathbf{y} = \mathbf{h}_{(1)}x_{(1)} + \mathbf{h}_{(2)}x_{(2)} + \mathbf{h}_{(3)}x_{(3)} + \dots + \mathbf{h}_{(N_t)}x_{(N_t)} + \mathbf{v}, \quad (3.22)$$

where $\mathbf{h}_{(i)}$ represents the $(i)^{th}$ column vector of the ordered (if any) channel matrix \mathbf{H} . Each of the N_t receiving circuits (RCV_1, \dots, RCV_{N_t}) computes and removes the interference successively while detecting the symbols. The successive interference cancellation is performed in cascade by subtracting the interference of the previous detected symbol $\hat{x}_{(i-1)}$ from the reduced-interference observation $\tilde{\mathbf{y}}_{(i-1)}$ as shown in Fig. 3.19. The interference cancellation process in each RCV_i can be expressed as:

$$\tilde{\mathbf{y}}_{(i)} = \tilde{\mathbf{y}}_{(i-1)} - \mathbf{h}_{(i-1)}\hat{x}_{(i-1)}. \quad (3.23)$$

Note that if the symbol is correctly detected, then the interference is successfully canceled in the course of estimating $x_{(i+1)}$. Otherwise, an error propagation is incurred.

To avoid this possibility that impairs the decoding processing, we consider not only the sliced (quantized) estimate $\hat{x}_{(i)}$, but also the N_{ei} nearest neighbors of the raw estimate (non-sliced) $\check{x}_{(i)}$ to create the neighbor subset $C_{(i)}$ for $i = 1, \dots, N_t$.

For clarification, each receiving circuit RCV_i computes first the raw estimation $\check{x}_{(i)}$ for the symbol in the i^{th} order of detection using a linear detector like ZF and MMSE, then they are sliced (quantized

to N_{ei} nearest symbols by taking the N_{ei} constellation points that have the minimum EDs between $\check{x}_{(i)}$ and the M possible constellation points) to provide the constellation set $C_{(i)}$ of N_{ei} nearest sliced estimates. Other detection techniques are also possible, as the proposed detector is not restricted to any specific technique. In the following, we will consider the ZF equalization/decoding where its weight matrix is defined as:

$$\mathbf{W}_{ZF}^{\mathbf{H}^{(i)}} = (\mathbf{H}_{(i)}^H \cdot \mathbf{H}_{(i)})^{-1} \mathbf{H}_{(i)}^H. \quad (3.24)$$

where the sub-matrix $\mathbf{H}_{(i)}$ obtained from \mathbf{H} by removing the columns of the previously detected symbols $\{(1) \text{ to } (i - 1)\}$. Thus, the raw estimation can be deduced by using the $(i)^{th}$ row of $\mathbf{W}_{ZF}^{\mathbf{H}^{(i)}}$ as follows:

$$\check{x}_{(i)} = \mathbf{W}_{ZF}^{\mathbf{H}^{(i)}} ((i), :) \mathbf{y}, \quad (3.25)$$

The next receiving circuit RCV_{i+1} is executed for each possible estimated symbol in the constellation subset $C_{(i)}$, and similarly for the subsequent receiving circuits in order to generate the different constellation subsets $C_{(1)}, C_{(i)}, \dots, C_{(N_t)}$.

Then, these constellation subsets are provided to the ML verification module as candidates to select a final estimate $\hat{\mathbf{x}}_{\text{OSICML}}$ for the vector \mathbf{x} :

$$\begin{aligned} \hat{\mathbf{x}}_{\text{OSICML}} &= \arg \min_{\hat{x}_{(1)} \in C_{(1)}, \dots, \hat{x}_{(N_t)} \in C_{(N_t)}} \|\mathbf{y} - \mathbf{H}\hat{\mathbf{x}}\|^2 \\ &= \arg \min_{\hat{x}_{(1)} \in C_{(1)}, \dots, \hat{x}_{(N_t)} \in C_{(N_t)}} \|\mathbf{W}_{ZF} \mathbf{y} - \hat{\mathbf{x}}\|^2. \end{aligned} \quad (3.26)$$

This problem can be represented as a search in a tree of height N_t and branching factor N_{ei} , as depicted in Fig. 3.20. The number of possible transmit MIMO vector provided by the tree is $N_{ei}^{N_t}$.

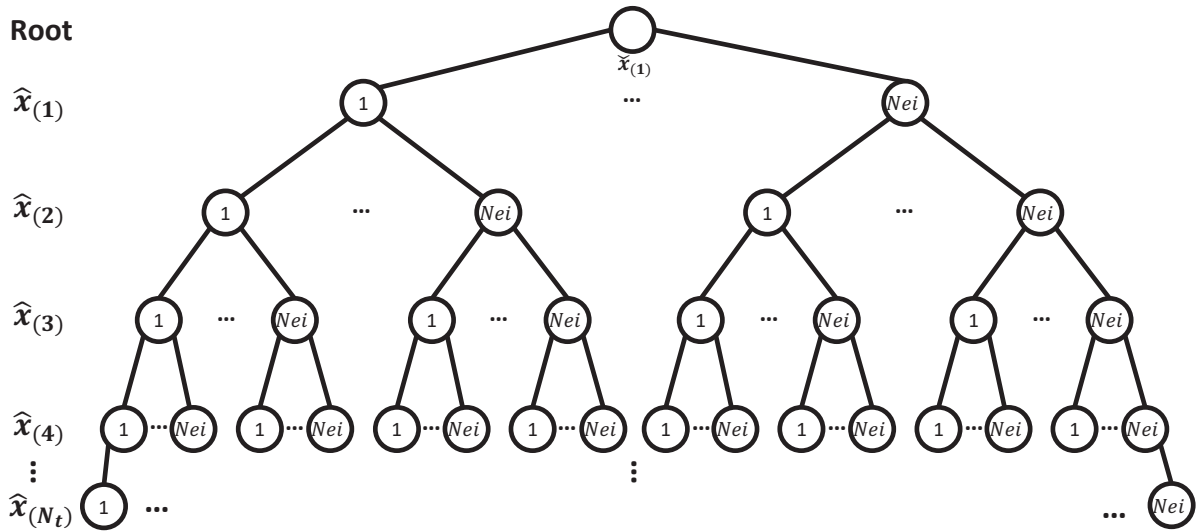


Figure 3.20 – The tree search for the OSIC-ML MIMO detectors of N_t height and N_{ei} branching factor. The corresponding branches of each node in the tree are numbered from 1 to N_{ei} .

For the ML optimal MIMO detection, N_{ei} will be equal to the modulation scheme order M ($N_{ei} = M$) that results in M^{N_t} possible transmit vectors. It is clear that the ML complexity increases exponentially with the number of TAs and leads to a huge complexity with high order modulation schemes. However, the proposed OSIC-ML allows controlling the system's performance-complexity by selecting a suitable $1 \leq N_{ei} \leq M$. The raw estimate $\check{x}_{(1)}$ is the root of the tree, and its N_{ei} nearest neighbors constitutes the set $C_{(1)}$ containing the candidate for the first symbol in the detection order. Then, for each branch of $C_{(1)}$ the corresponding interference cancellation is performed prior to the next raw estimate $\check{x}_{(2)}$ and its N_{ei} nearest neighbor selections. Similarly, the constellation subsets for all the N_t transmitted symbols are obtained successively. Finally, the ML verification step is performed on the reduced subset of $N_{ei}^{N_t}$ possible transmit vector instead of the M^{N_t} possibilities as in ML detector.

The OSIC-ML algorithm to estimate $\hat{\mathbf{x}}_{\text{OSICML}}$ is summarized in Algorithm 1, where $Q_{N_{ei}}(\cdot)$ denotes the quantization operation that gives the N_{ei} nearest sliced neighbors of the raw estimate $\check{x}_{(i)}$. Note the Matlab matrix notations were used, and the input to this algorithm can be the ordered $\tilde{\mathbf{y}}$, and ZF can be replaced by MMSE to deduce the raw estimations.

Algorithm 1 Proposed OSIC-ML detector for MIMO SMX systems.

```

1: procedure OSIC-ML( $\mathbf{y}, \mathbf{H}, N_{ei}, N_t$ )
2:    $\mathbf{C} = \mathbf{0}^{N_t \times N_{ei}^{N_t}}$                                      ▶ OSIC-ML MIMO vector candidates
3:    $\mathbf{W}_{ZF}^{\mathbf{H}} = (\mathbf{H}^H \cdot \mathbf{H})^{-1} \mathbf{H}^H$                                      ▶ ZF weight matrix over  $\mathbf{H}$ 
4:    $\check{x}_{(1)} = \mathbf{W}_{ZF}^{\mathbf{H}}(1, :) \mathbf{y}$                                      ▶ Zero-Forcing equalization
5:    $\hat{\mathbf{x}}_{(1)} = Q_{N_{ei}}(\check{x}_{(1)})$                                      ▶ Find  $N_{ei}$  nearest sliced neighbors
6:    $\mathbf{C} = \text{RECURSION}(\hat{\mathbf{x}}_{(1)}, \mathbf{y}, \mathbf{H}, N_t, \mathbf{C}, 1, 1)$ 
7:    $\hat{\mathbf{x}}_{\text{OSICML}} = \arg \min_{\hat{\mathbf{x}} \in \mathbf{C}} \|\mathbf{W}_{ZF} \mathbf{y} - \hat{\mathbf{x}}\|^2$ .                                     ▶ ML Verification
8: end procedure

```

```

9: function RECURSION( $\hat{\mathbf{x}}, \mathbf{y}_p, \mathbf{H}_p, N_t, \mathbf{C}, i, m$ )
10:  for  $j = 1 + (m - 1)N_{ei}$  to  $mN_{ei}$  do
11:     $\mathbf{v} = 1 + (j - 1)N_{ei}^{N_t - i} : jN_{ei}^{N_t - i}$ 
12:     $\mathbf{C}(i, \mathbf{v}) = \hat{x}(j - (m - 1)N_{ei})$ 
13:     $\mathbf{y} = \mathbf{y}_p - \mathbf{H}_p(:, 1)\hat{x}(j - (m - 1)N_{ei})$                                      ▶ Cancel interference
14:     $\mathbf{H}_{(i)} = \mathbf{H}_p(:, 2 : \text{end})$                                      ▶ Remove 1st column in  $\mathbf{H}_p$ 
15:    if  $\mathbf{H}_{(i)}$  not empty then                                     ▶ End of tree if  $\mathbf{H}_{(i)}$  is empty
16:       $\mathbf{W}_{ZF}^{\mathbf{H}(i)} = (\mathbf{H}_{(i)}^H \cdot \mathbf{H}_{(i)})^{-1} \mathbf{H}_{(i)}^H$ 
17:       $\check{x} = \mathbf{W}_{ZF}^{\mathbf{H}(i)}(1, :) \mathbf{y}$                                      ▶ Zero-Forcing equalization
18:       $\hat{\mathbf{x}} = Q_{N_{ei}}(\check{x})$                                      ▶ Find  $N_{ei}$  nearest sliced neighbors
19:       $\mathbf{C} = \text{RECURSION}(\hat{\mathbf{x}}, \mathbf{y}, \mathbf{H}_{(i)}, N_t, \mathbf{C}, i + 1, j)$ 
20:    end if
21:  end for
22: return  $\mathbf{C}$ 

```

3.5.1.2 Complexity Analysis

The offline complexity of the pre-computations C_{Offline} in OSIC-ML includes the ZF weight matrix estimation of size $N_t \times N_r$ (line 3 in Algorithm I), and those for the raw estimation of size $N_{rem} \times N_r$ (line 16) where the number of remained un-detected APM symbols N_{rem} decreases progressively from $(N_t - 1)$ to 1 in the recursion nested calls. Note that the pseudo inverse of a matrix of $N_{rem} \times N_r$ contains $N_{rem}^3 + 2N_{rem}^2 N_r$ Complex Multiplications (CMs) and $N_{rem}^3 + N_{rem}^2 (N_r - 1) + N_{rem} (N_{rem} - 1) N_r$ Complex Additions (CAs).

$$C_{\text{Offline}}^{CM} = \sum_{i=0}^{N_t-1} \left((N_t - i)^3 + 2(N_t - i)^2 N_r \right) \quad (3.27)$$

$$C_{\text{Offline}}^{CA} = \sum_{i=0}^{N_t-1} \left((N_t - i)^3 + (N_t - i)^2 (N_r - 1) + (N_t - i)(N_t - i - 1) N_r \right) \quad (3.28)$$

The number of Real Multiplications (RMs) and Real Additions (RAs) for offline computations can be easily deduced as follows $4C_{\text{Offline}}^{CM}$ RMs and $2C_{\text{Offline}}^{CM} + 2C_{\text{Offline}}^{CA}$ RAs respectively since each CM contains 4 RMs and 2 RAs. Note that when the channel is static over a long period, the complexity of any pre-processing steps becomes negligible.

The online computational complexity comes mainly from raw estimations, neighbors search, interference cancellation, and ML verification. The row multiplication in line (4) and (17) of Algorithm 1 includes N_r CMs and $N_r - 1$ CAs, and these operations are performed on each node that leads to $\frac{1 - N_{ei}^{N_t}}{1 - N_{ei}}$ times. Note that each CM in these steps can be computed with 3 RMs and 3 RAs since W_{ZF} is known in advance [189, Eq. (12)]. Note that the quantization (slicing) of raw estimations and the selection of the N_{ei} nearest neighbors requires M EDs ($\|\check{x} - x\|^2$) equivalent to $2M$ RMs and $3M$ RAs, and it is done after each raw estimation. The number of operations for interference cancellation is one less than that of raw estimations, where each one contains a CM between a column of \mathbf{H} with a complex number, which is equivalent to $4N_r$ RMs and $2N_r$ RAs. Finally, there are $N_{ei}^{N_t}$ EDs in OSIC-ML, and the complexity of each square of ED for the vector with N_t complex elements is $2N_t$ RMs and $4N_t - 1$ RAs. Thus, the online computational complexity C of the proposed detector in terms of RMs and RAs are given by:

$$C_{\text{online}}^{RM} = (7N_r + 2M) \left(\frac{1 - N_{ei}^{N_t}}{1 - N_{ei}} \right) - 4N_r + 2N_t N_{ei}^{N_t} \quad (3.29)$$

$$C_{\text{online}}^{RA} = (7N_r + 3M - 2) \left(\frac{1 - N_{ei}^{N_t}}{1 - N_{ei}} \right) - 2N_r + (4N_t - 1) N_{ei}^{N_t} \quad (3.30)$$

Therefore, the total complexity in terms of real operations is $C_{\text{OSIC-ML}} = 4C_{\text{Offline}}^{CM} + 2C_{\text{Offline}}^{CA} + C_{\text{online}}^{RA} + C_{\text{online}}^{RM}$.

Therefore, it is clear that the proposed method allows a tremendous complexity reduction compared to the ML-based solutions, by taking benefit of the reduced subset of the possible vectors \mathbf{x} estimated through linear detection methods. Moreover, this solution has dramatically better performance than the linear methods as it will be shown in the next section.

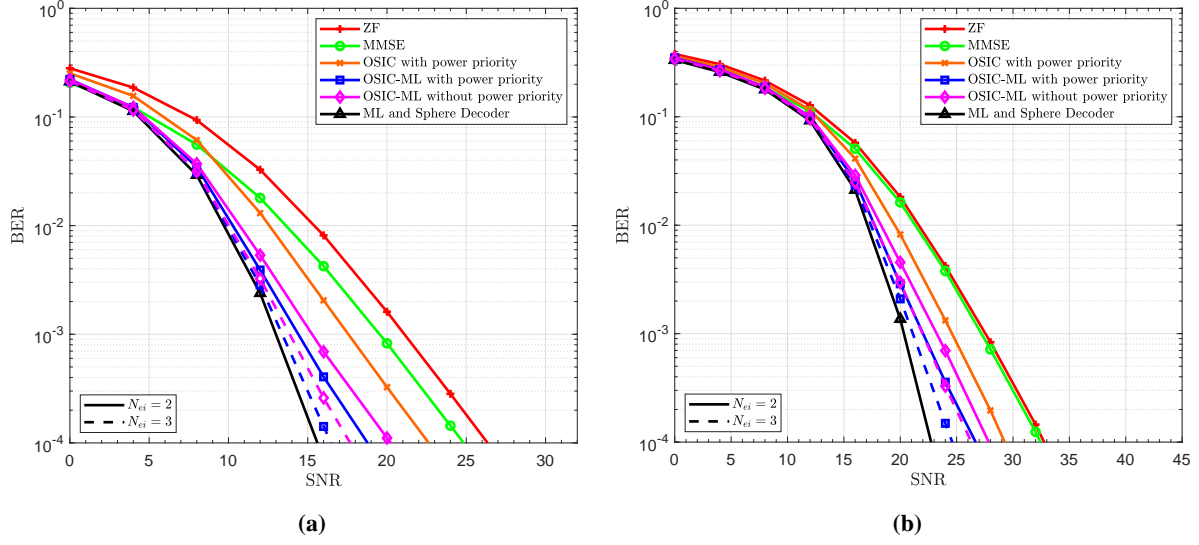


Figure 3.21 – Uncoded BER performance of SMX-MIMO system using different detectors. The system parameters are: $N_t = 4$, $N_r = 5$, $N_{ei} = 2$ and 3: (a) QPSK (SE=8 bpcu), (b) 16-QAM (SE=16 bpcu).

3.5.2 Proposed SMX detector OSIC-ML results and discussions

The performance of MIMO-SMX systems with the proposed OSIC-ML detector is evaluated through the measurement of uncoded BER versus SNR. It is assumed that the MIMO flat fading channel \mathbf{H} is following Rayleigh distribution with their complex values are i.i.d complex Gaussian $\mathcal{CN}(0, 1)$, and it is perfectly known at the receiver. Hence, the SNR per RA can be expressed as $\text{SNR} = \frac{1}{\sigma_v^2}$. The proposed detector with/without power priority (ordering) is compared to the linear detectors (ZF and MMSE), conventional OSIC with power priority, the non-linear SD and the optimal ML detector. The BER in these simulations is the average BER over different channel realizations.

In Fig. 3.21a, the performance of MIMO-SMX transmitting QPSK symbols using $N_t = 4$, $N_r = 5$, $N_{ei} = 2$ and 3 is provided. The performance of the linear detectors ZF and MMSE is far from the ML optimal performance by around 10 dB, whereas the conventional OSIC with power priority reduces this gap to 7 dB. However, the performance of the proposed OSIC-ML using $N_{ei} = 2$ without/with power priority has 2.5 dB and 3.8 dB SNR gain, respectively, compared to the conventional OSIC with power priority. Moreover, further performance enhancement with OSIC-ML can be achieved by increasing the number of considered nearest neighbors, i.e., OSIC-ML using $N_{ei} = 3$, where 5 dB and 6.2 dB SNR gain are respectively obtained without/with power priority. This makes the OSIC-ML detector at only 0.8 dB far from the ML optimal detector.

In Fig. 3.21b and 3.22, the performance is illustrated with the same system parameters used in Fig. 3.21a but with a larger modulation schemes: 16-QAM and 64-QAM. Similar results are achieved, where the quasi-linear OSIC-ML detector remains the best performance-complexity tradeoff even with higher modulation schemes using small $N_{ei} = 2, 3$ and 4. For instance with 64-QAM and $N_{ei} = 4$,

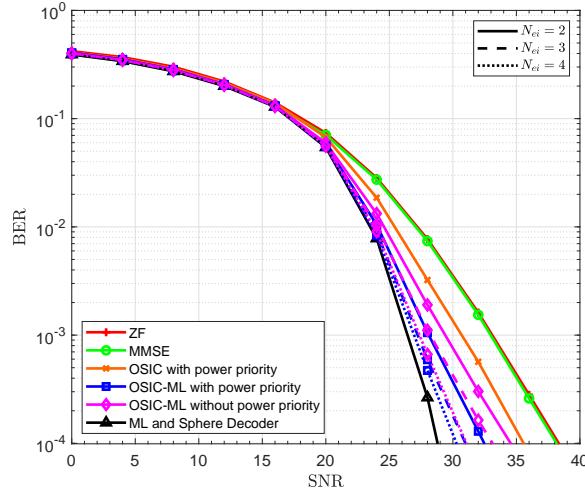


Figure 3.22 – Uncoded BER performance of SMX-MIMO system using different detectors. The system parameters are: 64-QAM, $N_t = 4$, $N_r = 5$, $N_{ei} = 2, 3$ and 4 that has a spectral efficiency of 24 bpcu.

there are $M^{N_t} = 2^{24}$ vector candidates in ML detection whereas only $N_{ei}^{N_t} = 2^8$ candidates in OSIC-ML detection for a SNR loss of only 1 dB. Hence, the N_{ei} value should be selected to achieve a balanced complexity-performance tradeoff where a near-optimal performance can be achieved with $N_{ei} \ll M$. Note that the proposed detector becomes similar to ML when $N_{ei} = M$.

Moreover, the proposed OSIC-ML detector is evaluated with different N_t and N_r in Fig. 3.23 to highlight its advantages for a larger MIMO scale. The results of Fig. 3.23 reveals that OSIC-ML reaches the optimal performance with low complexity due to using small $N_{ei} = 4$ when $M = 16$ even with high SE. Furthermore, the robustness of OSIC-ML to imperfect Channel Side Information (CSI) at the receiver is presented in Fig. 3.24. The performance of the system depicted in Fig. 3.24 with 12 bcpu and different channel estimation error variance σ_e^2 shows that the system performance using SD and OSIC-ML detectors degrades by less than 0.5 dB with $\sigma_e^2 = 10^{-3}$. Whereas a higher performance degradation with all detectors is observed with $\sigma_e^2 = 10^{-3}$, but a low error floor at 3.2×10^{-5} is obtained with SD and OSIC-ML in contrast to OSIC and ZF/MMSE equalizers.

Finally, the relative complexity reduction ($\frac{C_{ML} - C_{OSIC-ML}}{C_{ML}}$) and the required SNR to reach a BER = 10^{-4} for different system configurations are summarized in Table 3.6. It is clear from this Table that the proposed detector allows reaching the optimal performance while having very low complexity, and a slight increase of the N_{ei} parameter has a significant impact on performance with negligible complexity increase. In addition, Table 3.6 gives an idea about how to configure a dynamic system in terms of complexity or SE requirements.

It is worth mentioning that the computational complexity of the proposed OSIC-ML is also lower than that of SD detector. For instance, the dominant complexity for both detectors from the ML verification module is proportional to $N_{ei}^{N_t}$ for OSIC-ML, M^{N_t} for ML, and lower bounded by $M^{\gamma N_t}$

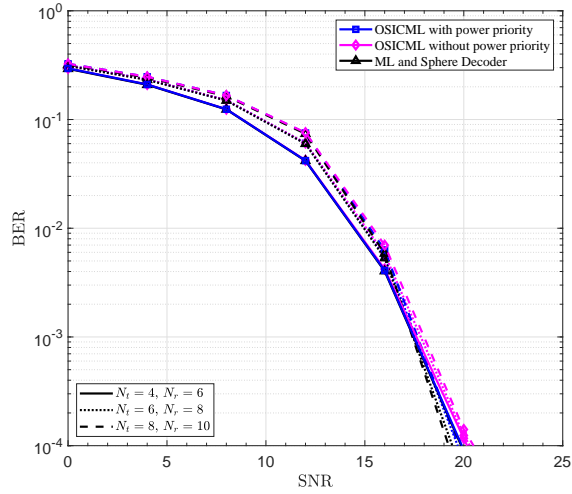


Figure 3.23 – Uncoded BER performance of SMX-MIMO system using different detectors with different number of TAs. The system parameters are: 16-QAM, $N_t = [4, 6, 8]$, $N_r = N_t + 2$, $N_{ei} = 4$. The SE is [16, 24, 32] bpcu.

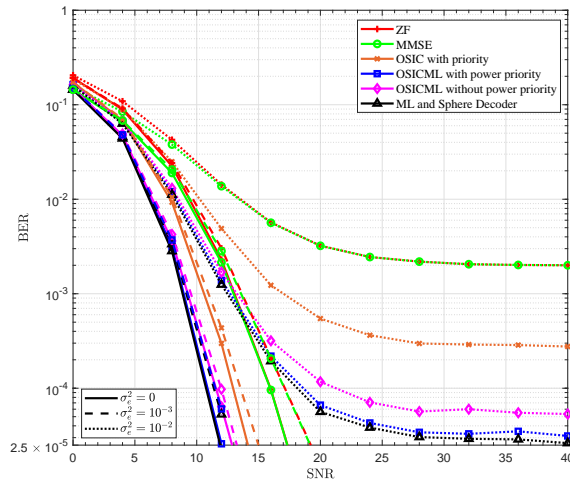


Figure 3.24 – Uncoded BER performance of SMX-MIMO system using different detectors with perfect and imperfect channel estimation. The system parameters are: QPSK, $N_t = 6$, $N_r = 10$, $N_{ei} = 2$ and $\sigma_e^2 = [0, 10^{-2}, 10^{-3}]$. The SE is 12 bpcu.

Table 3.6 – Relative Complexity reduction vs SNR for different system configurations at BER= 10^{-4} .

System Configuration	SE (bpcu)	SNR for ML (dB)	SNR for OSIC-ML (dB)	Relative Complexity Reduction with respect to ML (%)
$N_t = 4, N_r = 5, M = 16, N_{ei} = 2$	16	22.8	26.7	99.9518
$N_t = 4, N_r = 5, M = 16, N_{ei} = 3$	16	22.8	24.7	99.9075
$N_t = 4, N_r = 5, M = 16, N_{ei} = 4$	16	22.8	23.1	99.8164
$N_t = 4, N_r = 5, M = 64, N_{ei} = 3$	24	28.8	30.8	99.9994
$N_t = 4, N_r = 5, M = 64, N_{ei} = 4$	24	28.8	30.3	99.9988
$N_t = 6, N_r = 8, M = 16, N_{ei} = 4$	24	19.4	19.7	99.994
$N_t = 8, N_r = 10, M = 16, N_{ei} = 4$	32	19.2	19.7	99.9997

for SD where γ depends mainly on the SNR ρ and constellation order M [186]. The exponent factor γ is $\gamma \ll 1$ for low M and it is large with high M -ary scheme (γ up to 1) [186]. For illustrating the complexity of these detectors, the following example with $M = 16$ is provided: $C_{\text{ML}} \propto 2^{4N_t}$, $C_{\text{SD}} \propto 2^{4N_t\gamma} = [2^{2.8N_t}, 2^{2.2N_t}]$ respectively for $\rho = [10, 15]$ dB [186], and $C_{\text{OSIC-ML}} \propto N_{ei}^{N_t} = [2^{N_t}, 2^{2N_t}]$ for $N_{ei} = [2, 4]$ respectively.

Therefore, the presented results show clearly that the performance of the OSIC-ML method with a convenient N_{ei} is similar to the high-complexity optimal ML and SD detectors even with large-scale MIMO and imperfect CSI. Moreover, the OSIC-ML reduces prominently the complexity while attaining the near-optimal performance, thanks to the added ML verification step on a limited constellation subset.

In conclusion, the OSIC-ML quasi-linear detector is proposed for MIMO spatial multiplexing, which enables an important performance enhancement while keeping a lower complexity compared to non-linear detectors of similar performance. The proposed algorithm avoids redundant computations of ML detector on all possible transmit vectors by selecting N_{ei} nearest neighbors around the estimated symbols and avoids the tremendous complexity increase with the number of TAs especially for high order modulation schemes. In addition, the number of considered nearest neighbors for each raw symbol estimation N_{ei} controls the tradeoff performance-complexity of the proposed OSIC-ML detector where higher value achieves better performance and increases the constellation subset in the ML verification. Simulation results show that the proposed algorithm provides substantial complexity reduction compared to the non-linear detectors and hence exhibits a better performance-complexity tradeoff compared to the existing linear/non-linear detectors even with imperfect CSI and large-scale MIMO.

Moreover, other more complex ordering techniques like SNR, Signal-to-Interference-plus-Noise Ratio (SINR) and Received Signal based ordering used with conventional OSIC detector can be used with the proposed OSIC-ML to enhance the performance more but also at the price of higher complexity.

Finally, the complexity of OSIC-ML can be further reduced by pruning the search-tree as an example, but this will lead to a variable complexity upper bounded by $N_{ei}^{N_t}$ EDs estimation. Note that this complexity reduction can be a drawback for the hardware implementation compared to the fixed-rate initially proposed by the OSIC-ML detector that can be easily implemented in a parallel architecture. For instance, the detection techniques that have variable search space as SD have undesirable highly variable decoding delays, and thus they require additional buffers, which is a drawback for hardware implementation [190].

3.6 Near-Optimal Performance with Low Complexity ML-based detector for GSM

Upon the results presented in this chapter, GSM showed its significant SE/EE enhancement. However, the optimal joint ML (presented in Section 3.2.2) that detects the activated TAC and the transmitted symbols suffers from high complexity, especially when this scheme is used with large modulation order and number of activated TAs to reach high rates. Consequently, a low complexity linear detection is proposed in [105], but it leads to substantial performance degradation. Another low complexity detector named OB-MMSE and its improved version have been proposed in [165, 191]. The OB-MMSE based detector permits to enhance the performance without reaching the optimal performance unless high receive diversity is set: $N_r \geq 2N_a$ where N_r and N_a are the number of receive and activated transmit antennas respectively. More powerful detection based on Sphere Decoder (SD) was also explored, but its complexity is affected by the initial search radius [192]. Hence, two SD approaches for spatial modulation, Transmit-based Sphere Decoder (Tx-SD) and Receive-based Sphere Decoder (Rx-SD), are developed in [192] in order to reduce the conventional SD complexity. Recently, two improved SD techniques based on Tree search Sphere Decoder (T-SD) and Path-based Sphere Decoder (P-SD) were proposed to provide greater complexity reduction [193], which is still much higher than linear detectors. In this section, a novel detection technique is developed and denoted by Ordered TAC-Ordered Successive Interference Cancellation with ML verification (O^2 SIC-ML). This technique is inspired by [19, 188] that showed in previous section a balanced tradeoff performance-complexity for MIMO SMX. For each TAC detection, the technique uses the conventional OSIC method in order to mitigate the IAI induced by the activated TAs, but the OSIC method is applied on a set of potential candidates (neighbor symbols) instead of a single symbol. Afterward, an ML verification is applied on a reduced set of candidates to alleviate the error floor of the conventional OSIC method while maintaining a low complexity by incorporating a TAC ordering layer with early termination..

3.6.1 Proposed GSM Detector: O^2 SIC-ML

3.6.1.1 Detection algorithm

In this section, we propose the O^2 SIC-ML detector for GSM systems (presented in Section 3.2.1) that considers the interference cancellation similar to OSIC detector. However, it will be performed on several possible candidate symbols to reach the near-optimal performance with a good complexity-performance tradeoff. Firstly, this detector will sort the TACs to start the algorithm on the most probable activated TAC. For this reason, a metric z_p for each transmitted antenna is computed which isolates the potential transmitted symbol through it and mitigates the corresponding interference. The weights w_i

of each TAC i are extracted based on the different combinations of N_a z_p metrics as shown below:

$$z_p = \mathbf{h}_p^\dagger \mathbf{y} \text{ with } \mathbf{h}_p^\dagger = \frac{\mathbf{h}_p^H}{\mathbf{h}_p^H \mathbf{h}_p} \quad (3.31)$$

$$w_i = z_{i_1} + z_{i_2} + \dots + z_{i_{N_a}} = \sum_{n=1}^{N_a} z_{i_n}, \quad (3.32)$$

where $p \in \{1, 2, \dots, N_t\}$, $i \in \{1, 2, \dots, N_{TAC}\}$ and i_n is the index of the n^{th} activated TA in the i^{th} TAC. Then, these weights $\mathbf{w} = [w_1, \dots, w_{N_{TAC}}]$ are sorted in descending order:

$$[k_1, k_2, \dots, k_{N_{TAC}}] = \arg \text{sort}(\mathbf{w}, \text{descending}), \quad (3.33)$$

where k_1 is the index of the TAC with the maximum weight. Then, an OSIC-ML is performed for each TAC \mathbb{I}_{k_i} following the ordered list in (3.33) using the submatrix $\mathbf{H}_{\mathbb{I}_{k_i}}$ in order to detect the N_a APM symbols $\hat{\mathbf{s}} = [\hat{s}_1, \hat{s}_2, \dots, \hat{s}_{N_a}]$, as shown in Fig. 3.19. The final decision is deduced by taking the TAC and APM symbol vector that gives the overall minimum distance.

More precisely, the OSIC-ML receiver (RCV) shown in Fig. 3.19 proposed for SMX is used as sub-block for each TAC k_i , but N_t and \mathbf{H} in Fig. 3.19 are replaced by N_a and $\mathbf{H}_{\mathbb{I}_{k_i}}$ respectively. Note that these RCV circuits can contain any symbol ordering technique used with MIMO SMX for better interference cancellation. In the following, the detection without any symbol ordering and with the simplest symbol ordering based on the channel matrix columns norm ($\|\mathbf{h}_p\|^2$) is considered. Note that these N_t norms are calculated once, and sorted in decreasing order to identify the order of symbol detection for each considered TAC. The notation $s_{(n)}$ and s_n represent the n^{th} APM symbol after ordering and the transmitted symbol from the n^{th} activated TA, respectively, similar notation is used for the corresponding \mathbf{h} . Thus, the received signal \mathbf{y} in (3.2) can be rewritten as:

$$\mathbf{y} = \mathbf{h}_{(1)}s_{(1)} + \mathbf{h}_{(2)}s_{(2)} + \mathbf{h}_{(3)}s_{(3)} + \dots + \mathbf{h}_{(N_a)}s_{(N_a)} + \mathbf{z}. \quad (3.34)$$

Hence, each of the N_a RCV circuits (instead of N_t for SMX) shown in Fig. 3.19 will cancel the interference contribution of the previous $(n - 1)$ detected APM symbol from the reduced-interference observation $\tilde{\mathbf{y}}_{(n-1)}$, then estimate the n^{th} symbol using linear equalizer/detector (e.g. ZF or any other). The interference cancellation step can be expressed as:

$$\tilde{\mathbf{y}}_{(n)} = \tilde{\mathbf{y}}_{(n-1)} - \mathbf{h}_{(n-1)}\hat{s}_{(n-1)}. \quad (3.35)$$

It should be noted that $\tilde{\mathbf{y}}_{(1)} = \mathbf{y}$ so the first APM symbol is detected with complete IAI. In the following, the ZF equalizer will be used, where its weight matrix \mathbf{W}_{ZF} is the pseudo-inverse of the sub-matrix with the columns of $H_{\mathbb{I}_{k_j}}$ corresponding to non-detected symbols only. The linear equalizer gives the raw estimation $\check{\mathbf{s}}$ that will be quantized to the sliced estimation $\hat{\mathbf{s}}$ before the interference cancellation. Upon

this step, an OSIC detection is performed, but the misdetection of one of the first $N_a - 1$ APM symbols leads to error propagation to subsequent RCVs, and it will highly impact the system performance. To overcome this drawback, we propose to consider not only the sliced \hat{s} but the N_{ei} sliced neighbors near the raw estimated symbol \check{s} . Consequently, the next RCV will consider all these N_{ei} neighbors, and so on until the last RCV circuit is reached. This process can be described by a tree search of height N_a and branching factor N_{ei} , as depicted in Fig. 3.20 for SMX but N_t is replaced by N_a . Note that $\hat{s}_{(i)}$ contains the different sliced neighbors at each i -th activated TA and the interference cancellation of (3.23) should be ran over the different symbols of vector $\hat{s}_{(i)}$. Thus, the number of possible \mathbf{s} vectors provided by the tree for a given TAC is $N_{ei}^{N_a}$, that are stored in the set \mathbf{C} . Note that this detector becomes an ML when $N_{ei} = M$, but choosing a smaller N_{ei} permits to avoid the tremendous complexity increase with large modulation order and number of TAs as it will be shown in the next sub-section. Consequently, this reduced set \mathbf{C} is passed to the ML verification module to deduce the $\hat{\mathbf{s}}_{\text{OSIC-ML}}$ for the vector \mathbf{s} :

$$\begin{aligned}\hat{\mathbf{s}}_{\text{OSIC-ML}} &= \arg \min_{\hat{\mathbf{s}} \in \mathbf{C}} \|\mathbf{y} - \mathbf{H}_{i,k_j} \hat{\mathbf{s}}\|^2 \\ &= \arg \min_{\hat{\mathbf{s}} \in \mathbf{C}} \|\mathbf{W}_{ZF} \mathbf{y} - \hat{\mathbf{s}}\|^2.\end{aligned}\quad (3.36)$$

The proposed O²SIC-ML algorithm is performed successively for the ordered TACs until the computed distance in (3.36) satisfies the following condition:

$$\|\mathbf{W}_{ZF} \mathbf{y} - \hat{\mathbf{s}}\|^2 \leq V_{th}, \quad (3.37)$$

where V_{th} is a predefined threshold $V_{th} = N_r \sigma_v^2$. This threshold is set for which the transmitted vector is correctly estimated, and thus the distance contains only the noise power. Note that this termination will occur in the early search stage with one of the TACs of highest weights, and thus it allows a further complexity reduction compared to the joint ML that searches in $N_{TAC} \cdot M^{N_a}$ candidate vectors. Therefore, the proposed GSM O²SIC-ML detector provides a good controlled performance-complexity tradeoff by selecting a suitable $1 \leq N_{ei} \leq M$.

The proposed O²SIC-ML detector for GSM systems is summarized in Algorithm 2 using the Matlab matrix notations. The main procedure deduces the final decisions $(\hat{\mathbf{l}}, \hat{\mathbf{s}})$, while the function OSICML (line (18) to (25)) with the help of recursion function (line (26) to (39)) estimates $\hat{\mathbf{s}}_{\text{OSICML}}$ for a given TAC. Note that $\mathcal{Q}_{N_{ei}}(\cdot)$ denotes the quantization operation that gives the N_{ei} nearest sliced neighbors of the raw estimate $\check{s}_{(i)}$, and the used ‘min’ operator in line (24) of Algorithm 2 returns the minimum distance and its argument. The input to this algorithm can be the ordered $\tilde{\mathbf{y}}$, and ZF equalizer can be replaced by the MMSE equalizer to deduce the raw estimations.

Algorithm 2 Proposed O^2 SIC-ML detector for GSM that generalizes several transmit spatial IM schemes as shown in Fig. 3.2.

```

1: procedure GSM- $O^2$ SIC-ML( $\mathbf{y}, \mathbf{H}, N_{ei}, N_t, N_a, N_{TAC}, \sigma_v, \mathcal{I}$ )
2:    $\mathbf{z} = [z_1, z_2, \dots, z_{N_t}], z_p = (\mathbf{h}_p)^\dagger \mathbf{y}, \mathbf{h}_p^\dagger = \frac{\mathbf{h}_p^H}{\mathbf{h}_p^H \mathbf{h}_p}$ ;
3:    $\mathbf{w} = [w_1, w_2, \dots, w_{N_{TAC}}], w_i = \sum_{n=1}^{N_a} z_{i_n}^2, i \in \{1, 2, \dots, N_{TAC}\}$ ;
4:    $[k_1, k_2, \dots, k_{N_{TAC}}] = \arg \text{sort}(\mathbf{w}, \text{descending})$ ;
5:   Initialize:  $j = 1, V_{th} = N_t \sigma_v^2$ 
6:   while  $j \leq N_{TAC}$  do
7:      $(\hat{\mathbf{s}}_j, d_j) = \text{OSICML}(\mathbf{y}, \mathbf{H}_{\mathbb{I}_{k_j}}, N_{ei}, N_a)$ 
8:     if  $d_j < V_{th}$  then
9:        $\hat{\mathbb{I}} = \mathbb{I}_{k_j}, \hat{\mathbf{s}} = \hat{\mathbf{s}}_j; \text{break}$ ;
10:    else
11:       $j = j + 1$ 
12:    end if
13:  end while
14:  if  $j > N$  then
15:     $u = \arg \min_j d_j, j \in \{1, \dots, N\}$ 
16:     $\hat{\mathbb{I}} = \mathbb{I}_{k_u}, \hat{\mathbf{s}} = \hat{\mathbf{s}}_u$ ;
17:  end if
18:  Output the detected  $(\hat{\mathbb{I}}, \hat{\mathbf{s}})$ 
19: end procedure

```

```

18: function OSICML( $\mathbf{y}, \mathbf{H}, N_{ei}, N_t$ )
19:    $\mathbf{C} = \mathbf{0}^{N_t \times N_{ei}^{N_t}}$  ▷ OSIC-ML MIMO vector candidates
20:    $\mathbf{W}_{ZF} = (\mathbf{H}^H \mathbf{H})^{-1} \mathbf{H}^H$ 
21:    $\check{\mathbf{s}}_{(1)} = \mathbf{W}_{ZF} (1, :) \mathbf{y}$  ▷ Zero-Forcing equalization
22:    $\hat{\mathbf{s}}_{(1)} = \mathcal{Q}_{N_{ei}}(\check{\mathbf{s}}_{(1)})$  ▷ Find  $N_{ei}$  nearest sliced neighbors
23:    $\mathbf{C} = \text{RECURSION}(\hat{\mathbf{s}}_{(1)}, \mathbf{y}, \mathbf{H}, N_t, \mathbf{C}, 1, 1)$ 
24:    $[d, \widehat{\text{OSICML}}] = \min_{\hat{\mathbf{s}} \in \mathbf{C}} (\|\mathbf{W}_{ZF} \mathbf{y} - \hat{\mathbf{s}}\|^2)$  ▷ ML Verification
25: return  $(\widehat{\text{OSICML}}, d)$ 

```

```

26: function RECURSION( $\hat{\mathbf{s}}, \mathbf{y}_p, \mathbf{H}_p, N_t, \mathbf{C}, i, m$ )
27:   for  $j = 1 + (m - 1)N_{ei}$  to  $mN_{ei}$  do
28:      $\mathbf{v} = 1 + (j - 1)N_{ei}^{N_t - i} : jN_{ei}^{N_t - i}$ 
29:      $\mathbf{C}(i, \mathbf{v}) = \hat{\mathbf{s}}(j - (m - 1)N_{ei})$ 
30:      $\mathbf{y} = \mathbf{y}_p - \mathbf{H}_p(:, 1) \hat{\mathbf{s}}(j - (m - 1)N_{ei})$  ▷ Cancel interference
31:      $\mathbf{H} = \mathbf{H}_p(:, 2 : \text{end})$  ▷ Remove 1st column in  $\mathbf{H}_p$ 
32:     if  $\mathbf{H}$  not empty then ▷ End of tree if  $\mathbf{H}$  is empty
33:        $\mathbf{W}_{ZF} = (\mathbf{H}^H \mathbf{H})^{-1} \mathbf{H}^H$ 
34:        $\check{\mathbf{s}} = \mathbf{W}_{ZF} (1, :) \mathbf{y}$  ▷ Zero-Forcing equalization
35:        $\hat{\mathbf{s}} = \mathcal{Q}_{N_{ei}}(\check{\mathbf{s}})$  ▷ Find  $N_{ei}$  nearest sliced neighbors
36:        $\mathbf{C} = \text{RECURSION}(\hat{\mathbf{s}}, \mathbf{y}, \mathbf{H}, N_t, \mathbf{C}, i + 1, j)$ 
37:     end if
38:   end for
39: return  $\mathbf{C}$ 

```

3.6.1.2 Complexity Analysis

The offline complexity of the pre-computations C_{Offline} in $O^2\text{SIC-ML}$ includes the ZF weight matrix estimation of size $N_a \times N_r$ (line 20), and those for the raw estimation of size $N_{rem} \times N_r$ (line 33) where the number of remained un-detected APM symbols N_{rem} decreases progressively from $(N_a - 1)$ to 1 in the recursion nested calls. Thus, the online computational complexity in terms of Real Multiplication (RM) comes mainly from TAC ordering, raw estimations, neighbors search, interference cancellation, and ML verification. The TAC ordering (line (2-3)) requires $N_a N_r$ Complex Multiplications (CM). The row multiplication in line (21) and (34) of Algorithm 2 includes N_r CM, and this multiplication is performed on each node that leads to $\frac{1-N_{ei}^{N_a}}{1-N_{ei}}$ times. Note that each Complex Multiplication (CM) in these steps can be computed with 3 RMs and 3 real additions since W_{ZF} is known in advance [189, p. 4, (12)]. Note that the quantization of raw estimations and the selection of the N_{ei} nearest neighbors requires M Euclidean Distances (EDs) ($\|\check{s} - s\|^2$) equivalent to $2M$ RM, and it is done after each raw estimation. The number of operations for interference cancellation is one less than that of raw estimations, where each one contains a CM between a column of H with a complex number which is equivalent to $3N_r$ RMs. Finally, there are $N_{ei}^{N_a}$ EDs in OSIC-ML with each given TAC, and the complexity of each square of ED for the vector with N_a complex elements is $2N_a$ RMs. The early termination with TAC ordering reduces the number of tested TAC to \check{N} , where $\check{N} \leq N_{TAC}$. Thus, the online computational complexity C of the proposed detector is given by:

$$C_{\text{online}} = 3N_a N_r + \check{N} \left((6N_r + 2M) \left(\frac{1 - N_{ei}^{N_a}}{1 - N_{ei}} \right) - 3N_r + 2N_a N_{ei}^{N_a} \right). \quad (3.38)$$

Note that when the channel is static over a long period, the complexity of any pre-processing steps becomes negligible. To analyze the proposed detector advantage especially with massive MIMO and large modulation order, the theoretical relative complexity reduction (complexity Saving) of $O^2\text{SIC-ML}$ is defined by:

$$C_{\text{Saving}} = \frac{C_{\text{ML}} - C_{\text{detector}}}{C_{\text{ML}}} = 1 - \frac{C_{\text{detector}}}{C_{\text{ML}}} \quad (3.39)$$

where the complexity of ML detector in terms of real multiplications is expressed as:

$$C_{\text{ML}} = NM^{N_a} (4N_r N_a + 2N_r) \quad (3.40)$$

3.6.2 Proposed GSM detector $O^2\text{SIC-ML}$ results and discussions

The performance of GSM system with the proposed $O^2\text{SIC-ML}$ detector is compared to different existing linear and non-linear detectors (ML, Tx-SD, Rx-SD, Tree-SD, Path-SD, ZF/MMSE, and OB-MMSE). In addition, a Reduced complexity Sphere Decoders (Rc-SDs) is considered by using

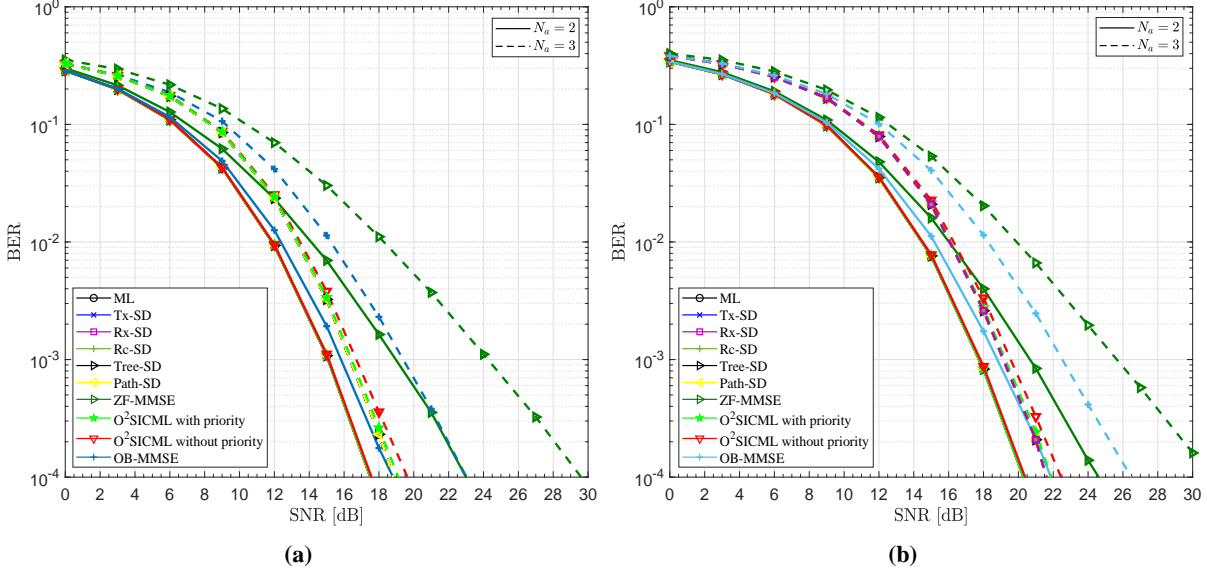


Figure 3.25 – Uncoded GSM performance with $N_t = N_r = 5$ and $N_a = [2, 3]$ and different linear and non-linear detectors: (a) 16QAM, (b) 32QAM

the candidate sorting technique proposed in [194]. The average uncoded BER versus SNR is evaluated over different Rayleigh channel realizations by Monte Carlo simulations with 3×10^5 frames where each one contains 100 symbols. The proposed detector is considered with/without APM detection ordering.

Figures 3.25a-3.25b shows the performance of different detectors with $N_t = N_r = 5$, $N_a = [2, 3]$, $N_{ei} = 2$, and $M = [16, 32]$ QAM. As expected the performance of all nonlinear detectors, ML and SD, are overlapped. It is clear that O^2SICML with $N_{ei} = 2$ achieves the performance of optimal nonlinear detectors when $N_a = 2$, and a gap of 0.3 and 0.8 dB appears when $N_a = 3$ using the proposed detector with/without priority respectively. Whereas, a gain of 1.7 (4) dB with 16QAM and 1.7 (4.7) dB with 32QAM are achieved compared to the low-complexity OB-MMSE when using $N_a = 2$ ($N_a = 3$). These results are maintained for large MIMO system, $N_t = 8$ and $N_r = 6$, and large $N_a = 4$ with $M = [8, 16]$ QAM as shown in Fig. 3.26.

In addition, the relative complexity reduction/saving in 3.39 of O^2SICML is compared to that of SD-based detectors [195] in Figs. 3.27a-3.27b. In addition, the complexity saving of the proposed detector is calculated using (3.38)-(3.40) for several configurations as shown in Table 3.7, where different N_t , N_r , N_a , M and N_{ei} values are considered to highlight the O^2SICML complexity advantage for large MIMO systems. These results reveal that the upper-bound relative complexity reduction ($\ddot{N} = N_{TAC}$) of the proposed detector is in order 99% while reaching the optimal performance with different M -ary QAM, N_t and N_a as shown in Figs. 3.25-3.26. Thanks to the interference cancellation and the added ML verification step on a limited constellation subset ($N_{ei}^{N_a}$ instead of M^{N_a}

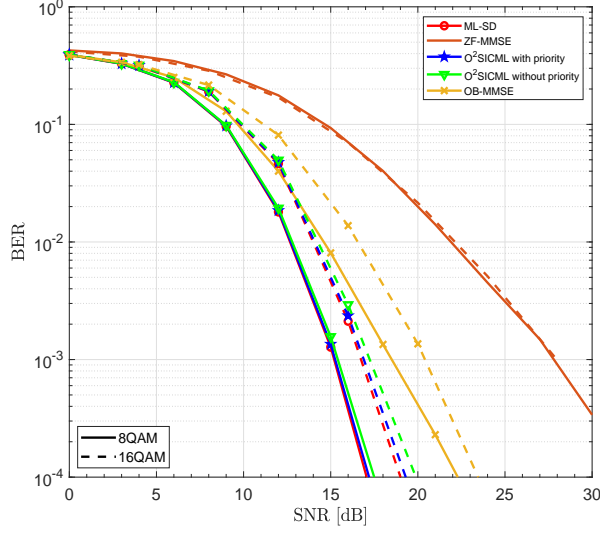


Figure 3.26 – Uncoded GSM performance with $N_t = 8$, $N_r = 6$, $N_a = 4$, $N_{ei} = 2$ and $M = [8, 16]$ QAM compared to linear and non-linear detectors.

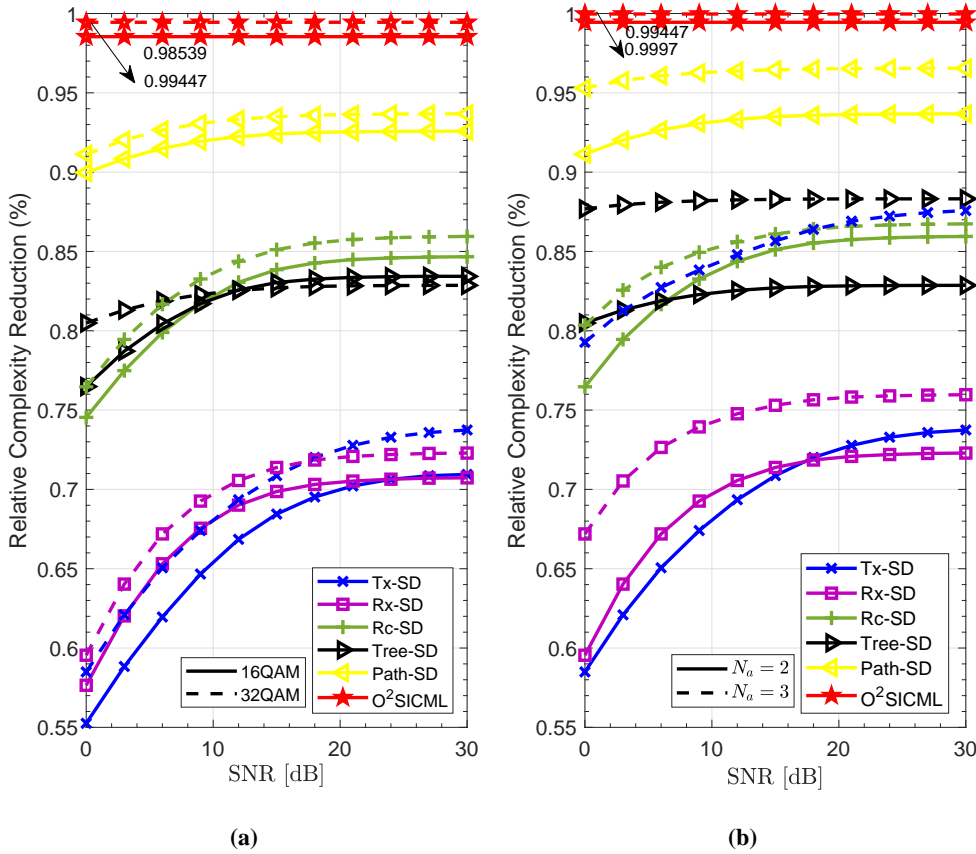
with ML) that allowed O^2 SIC-ML to reduce the complexity prominently while attaining the optimal performance.

Finally, we would like to highlight that the proposed detector reach the optimal performance even with $N_r \leq N_t$ as shown in Fig. 3.26 in contrast to the optimal SD based technique in [196] that can operate only when $N_r \geq N_t \geq N_a$. It is worth mentioning that different SD based optimal detection with reduced complexity are also proposed in [197, 198], where their complexity saving is varying in terms of SNR and is within a range 45%-75% (86%-93%) compared to original SD (ML detector) [197]. Hence, its maximum saving remains lower than 99% complexity saving achieved with the proposed detector. Recalling that the variable complexity of SD-based techniques can be a drawback for the hardware implementation due to the variable detection delay compared to the fixed-rate proposed detector [190].

In this section, we proposed O^2 SIC-ML detector for GSM that generalizes many other schemes in the spatial IM domain. The proposed detector takes the advantages of ML and OSIC without their disadvantages of high complexity and possible error propagation respectively. More precisely, the O^2 of the proposed algorithm comes from the: TAC ordering according to their reliability weight, and ordering of APM symbol detection. The former ensures the low complexity by early search termination, while the latter allows a better interference cancellation. For further enhancement of OSIC performance, a set of N_{ei} nearest neighbors for each raw symbol estimation is used to perform a tree-search and ML verification on a reduced subset. These adopted strategies give more control on the performance-complexity tradeoff, and allows to reach the optimal performance of non-linear detectors with much lower complexity (dominant by $\tilde{N} \cdot N_{ei}^{N_a}$ where $\tilde{N} \ll N_{TAC}$ and $N_{ei} \ll M$). Finally, we would like to highlight that other adaptive APM symbol detection ordering can be used to enhance

Table 3.7 – Complexity of the proposed GSM detector O²SIC-ML and its complexity saving for different system configurations with $N_r = N_t$.

System Configuration	SE (bpcu)	C_{ML}	$C_{O^2SIC-ML}$	O ² SIC-ML C_{Saving} (%)
$N_t = 4, N_a = 2, M = 16, N_{ei} = 2$	10	4.096×10^4	712	98.26
$N_t = 4, N_a = 2, M = 64, N_{ei} = 4$	14	6.554×10^5	3272	99.50
$N_t = 8, N_a = 4, M = 8, N_{ei} = 2$	18	3.775×10^7	6.819×10^4	99.82
$N_t = 8, N_a = 4, M = 16, N_{ei} = 2$	22	6.04×10^8	8.355×10^4	99.99
$N_t = 8, N_a = 4, M = 16, N_{ei} = 4$	22	6.04×10^8	5.648×10^5	99.91
$N_t = 8, N_a = 4, M = 64, N_{ei} = 4$	30	1.546×10^{11}	1.087×10^6	99.9993
$N_t = 16, N_a = 4, M = 64, N_{ei} = 4$	34	4.948×10^{12}	2.154×10^7	99.99956
$N_t = 16, N_a = 8, M = 64, N_{ei} = 4$	61	1.254×10^{21}	4.868×10^{10}	99.99999
$N_t = 16, N_a = 12, M = 64, N_{ei} = 4$	82	3.869×10^{27}	1.695×10^{12}	99.99999
$N_t = 24, N_a = 12, M = 4, N_{ei} = 2$	45	4.222×10^{16}	1.511×10^{12}	99.99642
$N_t = 24, N_a = 16, M = 4, N_{ei} = 2$	51	3.566×10^{18}	6.322×10^{12}	99.99982
$N_t = 24, N_a = 22, M = 4, N_{ei} = 2$	52	9.728×10^{18}	2.105×10^{11}	99.99999


Figure 3.27 – Relative complexity reduction compared to ML of different optimal GSM detectors with $N_t = N_r = 5$: (a) $N_a = 2$ and $M = [16, 32]$ QAM, (b) $N_a = [2, 3]$ and 32QAM.

more the performance at the price of some complexity increase. Also, the TAC ordering technique proposed in [191] with a predefined number of tested TAC lower than N_{TAC} can be used to allow a better early termination and thus lower complexity with small performance degradation. Also, the

QR decomposition or a tree pruning can be incorporated with our proposed algorithm for a further complexity reduction.

3.7 Dual Polarized GSM

Despite the multiple advantages of GSM system, the latter suffers from a performance degradation with Rician channel and in spatially correlated channels. Note that the degradation due to spatial correlation is reduced in Section 3.3 [15], but cannot be completely eliminated. In addition, the space occupancy of Uni-Polarized antenna (UP) antenna arrays in MIMO systems can limit the number of antennas due to physical space limitation especially at low frequency bands. To deal with the space limitation, an efficient solution has been proposed for the SM-MIMO system, by adding a polarization dimension to the transmitter and receiver using Dual Polarized antenna (DP) antennas that can transmit simultaneously through two orthogonal polarization directions. But in DP-SM [146] only one polarization is used to allow better separation between channels and thus better performance in highly correlated channel.

In this Section, we incorporate DP antennas with GSM (DP-GSM) to improve mainly the SE by exploiting the polarization dimension, and to reduce the space occupancy by half without any performance degradation. To avoid any ambiguity, the notation for uni-polarized GSM previously presented is changed to UP-GSM. Moreover, the joint ML detector and a Modified Ordered Block Minimum Mean-Squared Error (MOB-MMSE) detector algorithm are proposed to detect the complex symbols and the virtual bits conveyed by the activated polarization and the TAC index. The performance of DP-GSM system over correlated Rayleigh/Rician fading and sub-THz channels is studied. In addition, an Average Bit-Error Probability (ABEP) upper bonding is derived and analyzed for the DP-GSM system over correlated Rayleigh/Rician fading channels. The DP-GSM system is studied by considering the sub-THz impairments, since the sub-THz band suffers from many technological limitations and severe RF-impairments as previously discussed in Section 1.2. Moreover, the DP-SMX and the UP-GSM are compared with the DP-GSM system.

More precisely, our main contributions in this section are summarized as follows.

1. The DP-GSM scheme is proposed, where we incorporate DP antennas with GSM to enhance the system SE by exploring the polarization dimension. In addition, DP-GSM allows to reduce the space occupancy of antenna arrays by half without any performance degradation compared to UP-GSM.
2. Unlike the UP-GSM, proposed DP-GSM scheme has to be able to detect the bits conveyed through the antenna polarization (horizontal or vertical), to the estimation of the bits spatially indexed over every active antenna, and finally the modulated symbol bits. For this reason, the joint ML detector for DP-GSM that achieves optimal performance is presented, and a sub-optimal

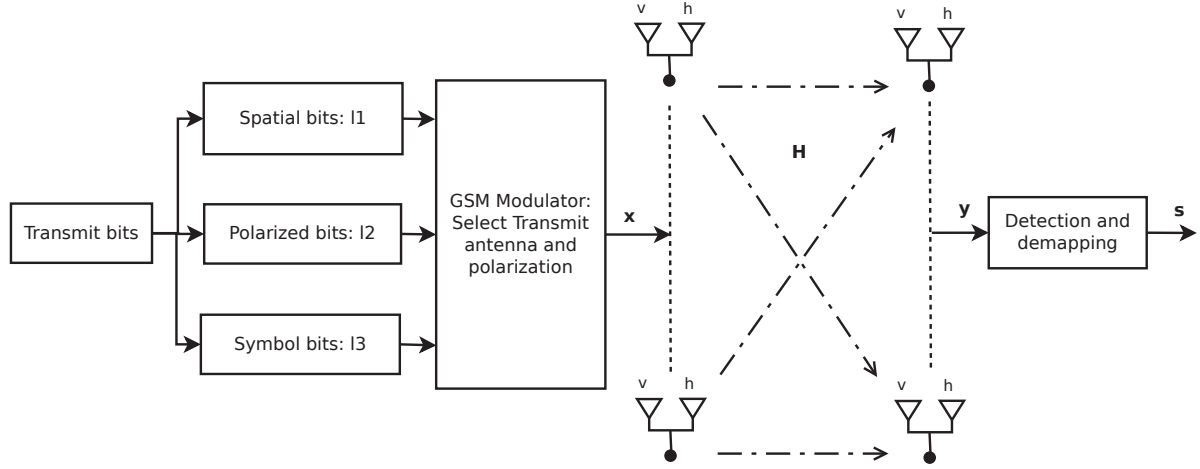


Figure 3.28 – $N_r \times N_t$ DP-GSM system model.

detector with lower complexity named Modified OB-MMSE (MOB-MMSE) is developed to estimate the polarization bits, spatial bits and symbol bits.

3. The theoretical ABEP upper bound of the DP-GSM system under the ML detector over correlated Rayleigh/Rician channels is developed and verified to be tight with Monte-Carlo simulation results.
4. The performance analysis of the proposed DP-GSM system is addressed over spatially correlated Rayleigh/Rician channels with different spatial correlations, and also over a ray-based deterministic channel model for sub-THz Band [36]. To illustrate the potential of proposed DP-GSM system for sub-THz channels we compared this scheme with the UP-GSM and the DP-SMX.
5. Finally, a complete analysis is provided for the proposed DP-GSM system experiencing different levels of PN impairments and compared with the DP-SMX system.

3.7.1 DP-GSM System model

The proposed system model is a MIMO system with N_t and N_r DP antennas at transmitter and receiver, respectively, and based on the GSM, in which N_a ($N_a < N_t$) antennas are activated in each time slot. Therefore, the number of TAC combinations is $C_{N_t}^{N_a}$. However, only $2^{\lfloor \log_2(C_{N_t}^{N_a}) \rfloor}$ antenna combinations are permitted to keep the bits length an integer number. The $N_r \times N_t$ DP-GSM system leads to $2N_r \times 2N_t$ dimensional channel between transmitter and receiver due to the implemented dual polarization. The DP-GSM system is shown in Fig. 3.28.

At each transmission instant, a block of $\mathcal{L}_{DP-GSM} = \mathcal{L}_1 + \mathcal{L}_2 + \mathcal{L}_3$ incoming data bits are selected and constituted of three parts named: $\mathcal{L}_1 = \lfloor \log_2(C_{N_t}^{N_a}) \rfloor$ bits are used to select the N_a activated

antennas at the transmitter, $\mathcal{L}_2 = N_a \log_2 N_p$ bits used to select the polarizations of the selected antennas. Here $N_p = 2$ stands the polarization dimension. Note that the polarization directions can be vertical, denoted by 'v' or horizontal denoted 'h'. The remaining $\mathcal{L}_3 = N_a \log_2 M$ represent the bits mapped into N_a M -ary symbol of the transmitted constellation symbol vector $\mathbf{s} = [s_1, s_2, \dots, s_{N_a}]^T$ where $[\cdot]^T$ is the transpose operator. Thus, the total achieved SE in bit per channel use (bpcu) can be expressed as:

$$\mathcal{L}_{DP-GSM} = \lfloor \log_2 \left(C_{N_t}^{N_a} \right) \rfloor + N_a \log_2 M + N_a \quad (3.41)$$

By doing so, the number of possible TACs is $N_1 = 2^{\lfloor \log_2 (C_{N_t}^{N_a}) \rfloor}$ and the number of possible Transmit Polarization Combinations (TPCs) is $N_2 = 2^{N_a}$. Thus the total number of possible combinations using TACs and TPC is $N_{TAPC} = N_1 N_2$.

The transmitted signal is denoted by \mathbf{x} and represented by a $2N_t \times 1$ vector whose entries have N_a non-zero elements. The position of the non-zero elements in \mathbf{x} allows the identification of the selected TAs as well as their polarizations and the transmitted symbols. We denote in this work i_1, i_2, \dots, i_{N_a} as the indices of N_a active antenna in the i -th TAC, where $i \in \{1, 2, \dots, N_1\}$ and we denote $\ell_1, \ell_2, \dots, \ell_{N_a}$ as the corresponding polarization of the activated antennas at the ℓ -th TPC where $\ell \in \{1, 2, \dots, N_2\}$. The TA with index $i_q \in \{1, 2, \dots, N_t\}$ and polarization $\ell_q \in \{v, h\}$ sends out symbols s_q where $q \in \{1, 2, \dots, N_a\}$. The transmit signal vector \mathbf{x} is given by:

$$\mathbf{x} = [\dots, [0, 0], [0, \underset{\substack{\downarrow \\ i_1 \\ \ell_1=h}}{s_1}], \dots, [\underset{\substack{\downarrow \\ i_2 \\ \ell_2=v}}{s_2}, 0], \dots, [0, \underset{\substack{\downarrow \\ i_{N_a} \\ \ell_{N_a}=h}}{s_{N_a}}], \dots]^T \quad (3.42)$$

At receiver, N_r DP antennas receive the modulated signal transmitted over a slow fading and frequency-flat MIMO channel. The channel matrix \mathbf{H} is equivalent to a $2N_r \times 2N_t$ matrix represented as:

$$\mathbf{H} = \begin{bmatrix} h_{1v,1v} & h_{1v,1h} & h_{1v,2v} & \cdots & h_{1v,N_th} \\ h_{1h,1v} & h_{1h,1h} & h_{1h,2v} & \cdots & h_{1h,N_th} \\ h_{2v,1v} & h_{2v,1h} & h_{2v,2v} & \cdots & h_{2v,N_th} \\ \vdots & \vdots & \vdots & \vdots & \vdots \\ h_{N_r,h,1v} & h_{N_r,h,1h} & h_{N_r,h,2v} & \cdots & h_{N_r,h,N_th} \end{bmatrix}, \quad (3.43)$$

where each $h_{i'u,j'u'}$ and $u, u' \in \{v, h\}$, represents the fading coefficient between polarization u of i' -th receive antenna and the polarization u' of j' -th TA. If $u' = u$, $h_{i'u,j'u'}$ represents the co-polar channel coefficient; otherwise, it represents the cross-polar channel coefficient. We can reformulate (3.43) as $\mathbf{H} = [\mathbf{H}_1, \mathbf{H}_2, \dots, \mathbf{H}_{N_t}]$ where $\mathbf{H}_{j'} = [\mathbf{h}_{j'v}, \mathbf{h}_{j'h}] \in \mathbb{C}^{2N_r \times 2}$ and $\mathbf{h}_{j'v} = [h_{1v,j'v}, h_{1h,j'v}, h_{2v,j'v}, \dots, h_{N_r,h,j'v}]^T$ is the a $2N_r \times 1$ channel matrix for polarization v of j' -th TA. Similarly, $\mathbf{h}_{j'h} = [h_{1v,j'h}, h_{1h,j'h}, h_{2v,j'h}, \dots, h_{N_r,h,j'h}]^T$ is the a $2N_r \times 1$ channel matrix for polarization h of the j' -th TA.

To be able to model correctly the channel \mathbf{H} , two kind of polarizations are investigated in this section. Correlations induced by polarization effects within each antenna, and the limited spacing between antennas [146]. These effects will be studied in the next section. The received signal $\mathbf{y} \in \mathbb{C}^{2N_r \times 1}$ can be formulated as:

$$\mathbf{y} = \mathbf{H}\mathbf{x} + \mathbf{v} = \sum_{q=1}^{N_a} \mathbf{h}_{i_q \ell_q} s_q + \mathbf{v} = \mathbf{H}_{\mathbb{I}, P} \mathbf{s} + \mathbf{v} \quad (3.44)$$

where $\mathbf{v} \in \mathbb{C}^{2N_r \times 1}$ is AWGN with zero mean and variance σ^2 , $\mathbf{H}_{\mathbb{I}, P} = [\mathbf{h}_{i_1 \ell_1}, \mathbf{h}_{i_2 \ell_2}, \dots, \mathbf{h}_{i_{N_a} \ell_{N_a}}]$ is the sub-matrix with N_a columns of \mathbf{H} , corresponding to the TAC set \mathbb{I} and TPC set P . We recall that \mathbf{x} is power normalised to have unity power. In the following, the optimal DP-GSM joint ML and the proposed low complexity detector are presented.

3.7.2 DP-GSM Joint-ML Detector

The receiver estimates the activated antennas, their polarizations and the transmitted symbols by using joint ML detection which performs exhaustive search over all the possible transmitted signal vectors and is given by:

$$\hat{\mathbf{x}} = \arg \min_{\mathbf{x} \in \mathcal{X}} \|\mathbf{y} - \mathbf{H}\mathbf{x}\|^2 \quad (3.45)$$

where \mathcal{X} denotes the set of all possible transmit vectors in spatial, polarization and signal constellation domains, and $\hat{\mathbf{x}}$ is the estimated transmit vector. Based on (3.44), $\hat{\mathbf{x}}$ can be written as:

$$(\hat{\mathbb{I}}, \hat{P}, \hat{\mathbf{s}}) = \arg \min_{\mathbb{I} \in \mathcal{I}, P \in \mathcal{P}, \mathbf{s} \in \mathcal{Q}} \|\mathbf{y} - \mathbf{H}_{\mathbb{I}, P} \mathbf{s}\|^2 \quad (3.46)$$

where $\mathcal{I} = \{\mathbb{I}_1, \mathbb{I}_2, \dots, \mathbb{I}_{N_1}\}$, \mathbb{I}_i is defined as the set of the N_a active TAs in the i -th TAC, $\mathcal{P} = \{P_1, P_2, \dots, P_{N_2}\}$, P_ℓ is defined as the set of the N_a active polarization in the ℓ -th TPC, and \mathcal{Q} is the set of N_a -dimensional modulation symbol vectors.

3.7.3 Modified OB-MMSE Detector for DP-GSM

In order to reduce complexity by avoiding the use of the joint ML detector, we propose a modified version of OB-MMSE detector which has been successfully used for UP-GSM where polarization dimension is not used [165] as shown in Section 3.2.3. Therefore, in addition to the estimation of the indices of the N_a possible activated TAs, we propose to estimate their polarizations. Concretely, the pseudo-inverse of channel column $z_{i_q \ell_q}$ is computed and then weighting factors $w^{i, \ell}$ are calculated to

measure the joint reliability of (TAC, TPC) as follows:

$$w^{i,\ell} = \sum_{q=1}^{N_a} z_{i_q \ell_q}^2 \quad \text{with } z_{i_q \ell_q} = \frac{\mathbf{h}_{i_q \ell_q}^H \mathbf{y}}{\mathbf{h}_{i_q \ell_q}^H \mathbf{h}_{i_q \ell_q}} \quad (3.47)$$

We recall the reader that the total number of TA and polarization combination (i, ℓ) corresponds to N . Sorting the weighing factor values of the vector $\mathbf{w} = [w^{i,\ell}; i \in \{1, 2, \dots, N_1\}, \ell \in \{1, 2, \dots, N_2\}]^T$ in descending order, we obtain the ordered Transmit antenna and polarization combinations (TAPCs) as follows:

$$[k_1, k_2, \dots, k_{N_{TAPC}}] = \text{arg sort}(\mathbf{w}, \text{descending}) \quad (3.48)$$

Note that the TAPCs index k_n contains implicitly the TAC and TPC indices (i, ℓ) and it is represented by $\mathbb{I}_{i \leftarrow k_n} P_{\ell \leftarrow k_n}$. Consequently, a block MMSE detector with dimension of $2N_r \times N_a$ is used for each possible TAPCs to detect the vector symbol $\tilde{\mathbf{s}}_n$ with $n \in \{1, 2, \dots, N_{TAPC}\}$:

$$\tilde{\mathbf{s}}_n = \mathcal{Q} \left(\left(\mathbf{H}_{\mathbb{I}_{i \leftarrow k_n} P_{\ell \leftarrow k_n}}^H \mathbf{H}_{\mathbb{I}_{i \leftarrow k_n} P_{\ell \leftarrow k_n}} + \sigma^2 \mathbf{I} \right)^{-1} \mathbf{H}_{\mathbb{I}_{i \leftarrow k_n} P_{\ell \leftarrow k_n}}^H \mathbf{y} \right) \right) \quad (3.49)$$

where \mathbf{I} is the $N_a \times N_a$ identity matrix. For the reduction of the detection complexity of all N_{TAPC} possible TAPCs, the MOB-MMSE will end once the output $(i, \ell, \tilde{\mathbf{s}}_n)$ satisfies the following relation:

$$\|\mathbf{y} - \mathbf{H}_{\mathbb{I}_{i \leftarrow k_n} P_{\ell \leftarrow k_n}} \tilde{\mathbf{s}}_n\|^2 \leq V_{th} \quad (3.50)$$

where $V_{th} = 2N_r \sigma^2$ is a threshold to be set to produce the detected signal vector. If the n -th output satisfies the condition (3.50), the detector will provide the optimal TAC $\hat{\mathbb{I}}$ and TPC \hat{P} , and the estimated symbol vector $\tilde{\mathbf{s}}_n$. Otherwise, the detector will continue the same procedure with $n = n + 1$ until $n > N_{TAPC}$. In this case, the detector becomes equivalent to the optimal ML algorithm as follows:

$$\begin{cases} u = \arg \min_n d_n, n \in \{1, 2, \dots, N_{TAPC}\} \\ \hat{\mathbb{I}} = \mathbb{I}_{i \leftarrow k_u}, \hat{P} = P_{\ell \leftarrow k_u}, \hat{\mathbf{s}} = \tilde{\mathbf{s}}_u. \end{cases} \quad (3.51)$$

The MOB-MMSE detection algorithm is summarized in Algorithm 3.

3.7.4 MIMO Channel models with Dual-Polarized antennas

3.7.4.1 Channel model with spatial and cross-polarization correlation

The DP-GSM system may experience spatial correlation at transmitter and receiver due to the insufficient spacing among antennas and can be modeled as a matrix form, Σ_t and Σ_r , respectively.

Algorithm 3 MOB-MMSE detection algorithm for DP-GSM

```

1: procedure MOB-MMSE( $\mathbf{y}, \mathbf{H}, N_t, N_a, \dots, V_{th} = 2N_r\sigma^2$ )
2:    $\mathbf{z} = [z_{1v}, z_{1h}, \dots, z_{N_tv}, z_{N_th}]^T$ , with  $z_{i_q\ell_q} = \frac{\mathbf{h}_{i_q\ell_q}^H \mathbf{y}}{\mathbf{h}_{i_q\ell_q}^H \mathbf{h}_{i_q\ell_q}}$ ;
3:    $\mathbf{w} = [w^{1,1}, w^{1,2}, \dots, w^{N_1, N_2}]^T$ ,  $w^{i,\ell} = \sum_{q=1}^{N_a} z_{i_q\ell_q}^2$ ,  $i \in \{1, 2, \dots, N_1\}$  and  $\ell \in \{1, 2, \dots, N_2\}$ ;
4:    $[k_1, k_2, \dots, k_{N_{TAPC}}] = \text{arg sort}(\mathbf{w}, \text{descending})$ ;
Main:
5:   for  $n = 1$  to  $N_{TAPC}$  do
6:      $\tilde{\mathbf{s}}_n = \mathcal{Q}\left(\left(\mathbf{H}_{i \leftarrow k_n}^H P_{\ell \leftarrow k_n} \mathbf{H}_{i \leftarrow k_n} P_{\ell \leftarrow k_n} + \sigma^2 \mathbf{I}\right)^{-1} \mathbf{H}_{i \leftarrow k_n}^H P_{\ell \leftarrow k_n} \mathbf{y}\right)$ 
7:      $d_n = \|\mathbf{y} - \mathbf{H}_{i \leftarrow k_n} P_{\ell \leftarrow k_n} \tilde{\mathbf{s}}_n\|^2$ 
8:     if  $d_n < V_{th}$  then
9:        $\hat{\mathbb{I}} = \mathbb{I}_{i \leftarrow k_n}$ ,  $\hat{P} = P_{\ell \leftarrow k_n}$ ,  $\hat{\mathbf{s}} = \tilde{\mathbf{s}}_n$ 
10:      break;
11:     else
12:        $n = n + 1$ 
13:     end if
14:   end for
15:   if  $n > N_{TAPC}$  then
16:      $u = \arg \min_n d_n$ ,  $n \in \{1, 2, \dots, N_{TAPC}\}$ 
17:      $\hat{\mathbb{I}} = \mathbb{I}_{i \leftarrow k_u}$ ,  $\hat{P} = P_{\ell \leftarrow k_u}$ ,  $\hat{\mathbf{s}} = \tilde{\mathbf{s}}_u$ 
18:   end if
19: return  $\hat{\mathbb{I}}, \hat{P}, \hat{\mathbf{s}}$ 

```

Various models are used to describe the spatial correlations, and the exponential correlation model is used in this study [168]. Therefore, the correlation among i' -th and j' -th antenna is affected by the correlation factor $|\beta| < 1$: $|\Sigma_t|_{i',j'} = \beta^{|i'-j'|}$.

The DP-GSM system may suffer also from the cross polarization correlation (XPC) between orthogonal polarization directions as shown in [199]. The polarization correlation at the transmitter and the receiver can be expressed as follows:

$$\mathbf{\Pi}_t = \begin{bmatrix} 1 & \gamma_t \\ \bar{\gamma}_t & 1 \end{bmatrix}, \quad \mathbf{\Pi}_r = \begin{bmatrix} 1 & \gamma_r \\ \bar{\gamma}_r & 1 \end{bmatrix}, \quad (3.52)$$

respectively, with:

$$\gamma_t = \frac{E\{h_{i'v,i'v}\bar{h}_{i'h,i'h}\}}{\sqrt{\mu(1-\mu)}} = \frac{E\{h_{i'h,i'v}\bar{h}_{i'h,i'h}\}}{\sqrt{\mu(1-\mu)}} \quad (3.53)$$

$$\gamma_r = \frac{E\{h_{j'v,j'v}\bar{h}_{j'h,j'h}\}}{\sqrt{\mu(1-\mu)}} = \frac{E\{h_{j'h,j'v}\bar{h}_{j'h,j'h}\}}{\sqrt{\mu(1-\mu)}} \quad (3.54)$$

where the parameter $0 < \mu \leq 1$ is the amount of power leakage from one polarization to the other [200]. Assuming the symmetry condition between different polarization, the leakage parameter is given as

follows $\mu = E\{|h_{i'v,i'h}|^2\} = E\{|h_{i'h,i'v}|^2\}$ and $1 - \mu = E\{|h_{i'v,i'v}|^2\} = E\{|h_{i'h,i'h}|^2\}$. In the literature, the Cross-Polarization Discrimination (XPD) is defined as the ratio between $1 - \mu$ and μ . For larger XPD values, the two polarization directions are easier to be discriminated. In [201], it has been demonstrated that the impact of the cross-polarization is relatively small and $0 \leq |\gamma_r|, |\gamma_t| \leq 0.2$.

In our study, we consider a slow fading MIMO channel matrix as Rayleigh or Rician multipath fading channel with/without spatial correlation and with polarization correlation. Therefore, the $2N_r \times 2N_t$ DP-polarized channel matrix is expressed in the Kronecker form given by:

$$\mathbf{H} = \sqrt{\frac{K}{1+K}} (\mathbf{1}^{N_r \times N_t} \otimes \mathbf{\Gamma}) \odot \mathbf{H}_{\text{LoS}} + \sqrt{\frac{1}{1+K}} (\mathbf{1}^{N_r \times N_t} \otimes \mathbf{\Gamma}) \odot (\mathbf{\Psi}_r^{\frac{1}{2}} \mathbf{H}_{\text{NLoS}} \mathbf{\Psi}_t^{\frac{1}{2}}) \quad (3.55)$$

where $\mathbf{\Gamma}$ is the leakage matrix:

$$\mathbf{\Gamma} = \begin{bmatrix} \sqrt{1-\mu} & \sqrt{\mu} \\ \sqrt{\mu} & \sqrt{1-\mu} \end{bmatrix} \quad (3.56)$$

K is the Rician factor, \mathbf{H}_{LoS} and \mathbf{H}_{NLoS} are the $2N_r \times 2N_t$ LoS and the NLoS channel matrices respectively. The elements of \mathbf{H}_{LoS} are deterministic and we will assume that the elements are all one, and \mathbf{H}_{NLoS} is considered as Rayleigh channel whose elements are i.i.d. circularly symmetric zero mean complex Gaussian variables with unit variance denoted $\mathcal{CN}(0, 1)$. Finally, the matrices $\mathbf{\Psi}_r = \mathbf{\Sigma}_r \otimes \mathbf{\Pi}_r$ and $\mathbf{\Psi}_t = \mathbf{\Sigma}_t \otimes \mathbf{\Pi}_t$ are the $2N_r \times 2N_r$ and $2N_t \times 2N_t$ composite transmit and receive correlation matrices, combining spatial and polarization correlations.

3.7.4.2 Sub-Terahertz MIMO channel

The sub-THz channel are generated using a ray-based deterministic model according to [36] but using DP antennas. Note that these channels are generated by our BRAVE partner SIRADEL in indoor office environment with the same settings described in Section 3.4.1.

3.7.5 sub-THz PN model for DP MIMO systems

The received baseband vector of an equivalent $N_r \times N_t$ MIMO DP-system with PN can be expressed as:

$$\tilde{\mathbf{y}} = \Phi_r \mathbf{H} \Phi_t \mathbf{x} + \mathbf{v}, \quad (3.57)$$

where Φ_t and Φ_r are the $2N_t \times 2N_t$ and $2N_r \times 2N_r$ diagonal matrices of PN from the transmitter and receiver oscillators respectively. These PN matrices can be represented as follows:

$$\Phi_t = \text{diag}\left([e^{j\theta_1^{Tx}}, \dots, e^{j\theta_{2N_t}^{Tx}}]^T\right) \quad (3.58)$$

$$\Phi_r = \text{diag}\left([e^{j\theta_1^{Rx}}, \dots, e^{j\theta_{2N_r}^{Rx}}]^T\right), \quad (3.59)$$

where θ_ι^{Tx} and θ_κ^{Rx} represent the PNs at the TAs and RA respectively, and $\iota = \{1, 2, \dots, 2N_t\}$ and $\kappa = \{1, 2, \dots, 2N_r\}$. The even/odd values of ι and κ are for the vertical/horizontal polarization, at the $\lfloor \frac{\iota-1}{2} \rfloor$ TA and $\lfloor \frac{\kappa-1}{2} \rfloor$ RAs respectively. These θ can be described in sub-THz band by a truncated Gaussian distribution $\mathcal{N}(0, \sigma_g^2)$ with zero-mean and variance σ_g^2 similar to SISO PN model described in [11]. In the DO setup, the PN at the different TA are independent, similarly at the receiver side. However, in the Centralized or Common Oscillator (CO) setup with independent oscillators for Tx and Rx sides (same oscillator is used for all antennas on each side but different oscillators for the Tx and Rx), $\theta_\iota^{Tx} = \theta^{Tx}$ for all $\iota = \{1, \dots, 2N_t\}$ and $\theta_\kappa^{Rx} = \theta^{Rx}$ for all $\kappa = \{1, \dots, 2N_r\}$. Thus, the received signal in the CO setup can be simplified to:

$$\tilde{\mathbf{y}} = e^{j\theta^{Tx}} e^{j\theta^{Rx}} \mathbf{H}\mathbf{x} + \mathbf{v} \quad (3.60)$$

3.7.6 Analytical Performance: Average error probability bound

In this sub-section, we provide the theoretical ABEP analysis and we derive the upper bound of the ABEP which depends on the Pairwise Error Probability (PEP). In addition, we provide validation through channel simulations. The upper bound of the ABEP, denoted by P_b , of the ML detection is obtained first by evaluating the Average Pairwise Error Probability (APEP), denoted by \bar{P}_e and then averaging the set of ABEP for all possible pairs of symbols [202]. In fact, the PEP is a function of fading channel coefficients and required to be averaged over the Probability Density Function (PDF) of channel coefficients to provide the APEP, and finally to find the ABEP.

According to the union bounding technique, the ABEP of DP-GSM can be upper bounded by using the upper bounding relation [203]:

$$P_b \leq \frac{1}{2^{\mathcal{L}_{DPGSM}}} \sum_{i=1}^{2^{\mathcal{L}_1}} \sum_{\hat{i}=1}^{2^{\mathcal{L}_1}} \sum_{\ell=1}^{2^{\mathcal{L}_2}} \sum_{\hat{\ell}=1}^{2^{\mathcal{L}_2}} \sum_{v=1}^{2^{\mathcal{L}_3}} \sum_{\hat{v}=1}^{2^{\mathcal{L}_3}} \frac{N_e(i, \hat{i}, \ell, \hat{\ell}, v, \hat{v})}{\mathcal{L}_{DPGSM}} \bar{P}_e(i, \hat{i}, \ell, \hat{\ell}, v, \hat{v}) \quad (3.61)$$

where $N_e(i, \hat{i}, \ell, \hat{\ell}, v, \hat{v})$ is the number of bits in error between the respective channel/polarization and vector symbols pair $(\mathbf{H}_{i, P_\ell}, \mathbf{s}_v)$ and $(\mathbf{H}_{\hat{i}, P_{\hat{\ell}}}, \mathbf{s}_{\hat{v}})$, $\bar{P}_e(i, \hat{i}, \ell, \hat{\ell}, v, \hat{v})$ is the APEP, \mathcal{L}_{DPGSM} is the total number of bits in DP-GSM symbol, $2^{\mathcal{L}_{DPGSM}} = N_1 N_2 M^{N_a}$ is the total number of configurations, and $N_e(i, \hat{i}, \ell, \hat{\ell}, v, \hat{v}) / \mathcal{L}_{DPGSM}$ is summation weight for the pairwise probability.

To evaluate the conditional PEP analytically, we assume that an DP-GSM symbol consisting of the i -th TAC, ℓ -th TPC, and the digitally modulated symbol vector \mathbf{s}_v are transmitted. Due to noise and fading, it is detected in error as the TAC, TPC and digitally modulated symbol. Accordingly, the PEP representing the probability of incorrectly detecting \mathbf{s}_v as $\mathbf{s}_{\hat{v}}$ conditioned on \mathbf{H} is given by:

$$P_e(i, \hat{i}, \ell, \hat{\ell}, v, \hat{v}) = Pr(\mathbf{x} \rightarrow \hat{\mathbf{x}} | \mathbf{H}) \quad (3.62)$$

$$= Pr\left(\|\mathbf{y} - \mathbf{H}_{i, P_\ell} \mathbf{s}_v\|^2 > \|\mathbf{y} - \mathbf{H}_{\hat{i}, P_{\hat{\ell}}} \mathbf{s}_{\hat{v}}\|^2 \middle| \mathbf{H}\right) \quad (3.63)$$

$$= Pr\left(\text{tr}\left[-2\Re\{(\mathbf{H}_{\mathbb{I},P\mathbf{S}_v} - \mathbf{H}_{\hat{\mathbb{I}},\hat{P}\mathbf{S}_{\hat{v}}})\mathbf{v}^H\}\right] > \|\mathbf{H}_{\mathbb{I},P\mathbf{S}_v} - \mathbf{H}_{\hat{\mathbb{I}},\hat{P}\mathbf{S}_{\hat{v}}}\|^2 \middle| \mathbf{H}\right) \quad (3.64)$$

$$= Pr\left(-2\Re\{\mathbf{v}^H(\mathbf{H}_{\mathbb{I},P\mathbf{S}_v} - \mathbf{H}_{\hat{\mathbb{I}},\hat{P}\mathbf{S}_{\hat{v}}})\} > \|\mathbf{H}_{\mathbb{I},P\mathbf{S}_v} - \mathbf{H}_{\hat{\mathbb{I}},\hat{P}\mathbf{S}_{\hat{v}}}\|^2 \middle| \mathbf{H}\right) \quad (3.65)$$

$2\Re\{\mathbf{v}^H(\mathbf{H}_{\mathbb{I},P\mathbf{S}_v} - \mathbf{H}_{\hat{\mathbb{I}},\hat{P}\mathbf{S}_{\hat{v}}})\}$ is a real Gaussian random variable with zero mean and variance $2\sigma^2\|\mathbf{H}_{\mathbb{I},P\mathbf{S}_v} - \mathbf{H}_{\hat{\mathbb{I}},\hat{P}\mathbf{S}_{\hat{v}}}\|^2$ (see Appendix B for more details). Therefore, the probability that \mathbf{x} is transmitted but $\mathbf{x} \neq \hat{\mathbf{x}}$ is given by:

$$Pr(\mathbf{x} \rightarrow \hat{\mathbf{x}} | \mathbf{H}) = Q\left(\sqrt{\frac{\|\mathbf{H}_{\mathbb{I},P\mathbf{S}_v} - \mathbf{H}_{\hat{\mathbb{I}},\hat{P}\mathbf{S}_{\hat{v}}}\|^2}{2\sigma^2}}\right) \quad (3.66)$$

The average PEP is given by:

$$Pr(\mathbf{x} \rightarrow \hat{\mathbf{x}}) = \mathbb{E}_{\mathbf{H}}\left\{Q\left(\sqrt{\frac{\|\mathbf{H}_{\mathbb{I},P\mathbf{S}_v} - \mathbf{H}_{\hat{\mathbb{I}},\hat{P}\mathbf{S}_{\hat{v}}}\|^2}{2\sigma^2}}\right)\right\} \quad (3.67)$$

Defining a new vector $\mathbf{z} = \frac{1}{\sqrt{2\sigma^2}}(\mathbf{H}_{\mathbb{I},P\mathbf{S}_v} - \mathbf{H}_{\hat{\mathbb{I}},\hat{P}\mathbf{S}_{\hat{v}}}) \in \mathbb{C}^{2N_r \times 1}$, the previous equation is equivalent to:

$$Pr(\mathbf{x} \rightarrow \hat{\mathbf{x}}) = \mathbb{E}_{\mathbf{z}}\left\{Q\left(\sqrt{\|\mathbf{z}\|^2}\right)\right\} \quad (3.68)$$

$$= \frac{1}{\pi} \int_0^{\pi/2} \int_{\mathbf{z}} \exp\left(-\frac{\mathbf{z}^H \mathbf{z}}{2 \sin^2 \theta}\right) f_{\mathbf{z}}(\mathbf{z}) d\mathbf{z} d\theta \quad (3.69)$$

where $f_{\mathbf{z}}(\mathbf{z})$ is the PDF of \mathbf{z} which is a proper complex Gaussian vector as defined in [204] with PDF given as:

$$f_{\mathbf{z}}(\mathbf{z}) = \frac{1}{\pi^{2N_r} |\Sigma_{\mathbf{z}}|} \exp\left(-(\mathbf{z} - \mathbf{m}_{\mathbf{z}})^H \Sigma_{\mathbf{z}}^{-1} (\mathbf{z} - \mathbf{m}_{\mathbf{z}})\right) \quad (3.70)$$

According to the channel model \mathbf{H} given by (3.55), the expression of \mathbf{z} is given by:

$$\begin{aligned} \mathbf{z} &= \sqrt{\frac{K}{2\sigma^2(1+K)}} \left((\mathbf{1}^{N_r \times N_t} \otimes \Gamma) \odot \mathbf{H}_{\text{LOS}} \right) (\mathbf{x} - \hat{\mathbf{x}}) \\ &+ \sqrt{\frac{1}{2\sigma^2(1+K)}} \left((\mathbf{1}^{N_r \times N_t} \otimes \Gamma) \odot (\Psi_r^{\frac{1}{2}} \mathbf{H}_{\text{NLOS}} \Psi_t^{\frac{1}{2}}) \right) (\mathbf{x} - \hat{\mathbf{x}}). \end{aligned} \quad (3.71)$$

As a consequence, the expectation $\mathbf{m}_{\mathbf{z}} = \mathbb{E}\{\mathbf{z}\}$ and the covariance matrix $\Sigma_{\mathbf{z}} = \mathbb{E}\{(\mathbf{z} - \mathbf{m}_{\mathbf{z}})(\mathbf{z} - \mathbf{m}_{\mathbf{z}})^H\}$ are given by:

$$\mathbf{m}_{\mathbf{z}} = \sqrt{\frac{K}{2\sigma^2(1+K)}} \left((\mathbf{1}^{N_r \times N_t} \otimes \Gamma) \odot \mathbf{H}_{\text{LOS}} \right) (\mathbf{x} - \hat{\mathbf{x}}) \quad (3.72)$$

$$= \sqrt{\frac{K}{2\sigma^2(1+K)}} \left((\mathbf{x} - \hat{\mathbf{x}})^T \otimes \mathbf{I}^{2N_r \times 2N_r} \right) \text{vec}(\mathbf{1}^{N_r \times N_t} \otimes \mathbf{\Gamma}) \odot \text{vec}(\mathbf{H}_{\text{LOS}}) \quad (3.73)$$

$$\begin{aligned} \boldsymbol{\Sigma}_{\mathbf{z}} &= \frac{1}{2\sigma^2(1+K)} \left((\mathbf{x} - \hat{\mathbf{x}})^T \otimes \mathbf{I}^{2N_r \times 2N_r} \right) \text{vec}(\mathbf{1}^{N_r \times N_t} \otimes \mathbf{\Gamma}) \odot \\ &(\boldsymbol{\Psi}_t^T \otimes \boldsymbol{\Psi}_r) \odot \text{vec} \left(\mathbf{1}^{N_r \times N_t} \otimes \mathbf{\Gamma} \right)^H \left((\mathbf{x} - \hat{\mathbf{x}})^T \otimes \mathbf{I}^{2N_r \times 2N_r} \right)^H \end{aligned} \quad (3.74)$$

Finally, using the distribution of \mathbf{z} and following the technique of [205] to compute the double integral in equation (3.69), the APEP $Pr(\mathbf{x} \rightarrow \hat{\mathbf{x}})$ is then given by (see Appendix C for details):

$$Pr(\mathbf{x} \rightarrow \hat{\mathbf{x}}) = \frac{1}{\pi} \int_0^{\pi/2} \frac{\exp(-\mathbf{m}_{\mathbf{z}}^H (\boldsymbol{\Sigma}_{\mathbf{z}} + 2 \sin^2 \theta \mathbf{I})^{-1} \mathbf{m}_{\mathbf{z}})}{|\frac{\boldsymbol{\Sigma}_{\mathbf{z}}}{2 \sin^2 \theta} + \mathbf{I}|} d\theta \quad (3.75)$$

The closed-form expression of the integral form of the APEP is not available. In this case, the APEP is upper bounded by assuming:

$$Pr(\mathbf{x} \rightarrow \hat{\mathbf{x}}) \leq \frac{\exp(-\mathbf{m}_{\mathbf{z}}^H (\boldsymbol{\Sigma}_{\mathbf{z}} + 2\mathbf{I})^{-1} \mathbf{m}_{\mathbf{z}})}{|\frac{\boldsymbol{\Sigma}_{\mathbf{z}}}{2} + \mathbf{I}|} \quad (3.76)$$

3.7.7 DP-GSM results and discussions

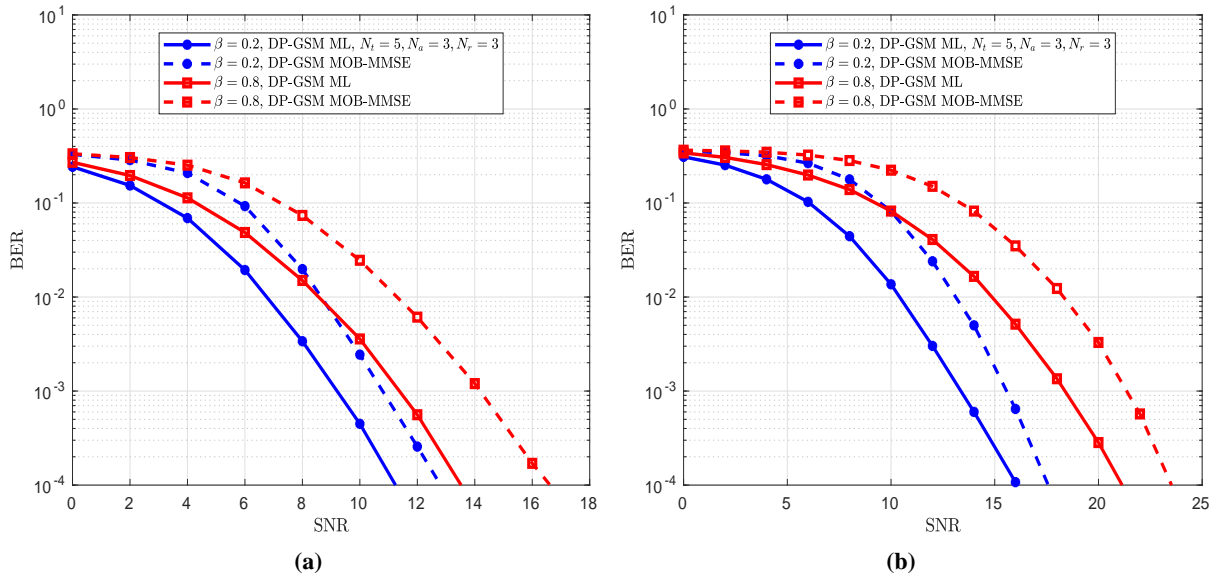
In this subsection, we provide the performance of the DP-GSM evaluated through Monte Carlo simulations of the BER and different values of SNR and compared to the theoretical ABEP upper bounds. The simulations are used over correlated Rayleigh and Rician channel with different values of β according to the mathematical model given by (3.55) and also over sub-THz channels shown in subsection 3.7.4.2. Different comparisons between our proposed DP-GSM system and the DP-SMX system for several parameters and different channel conditions are also provided and discussed.

The proposed DP-GSM system is evaluated using QPSK. The latter has shown a good performance with UP-GSM system comparing to the other modulations such as the DPSK and the 4-PAM [16] and compared to UP-SMX system in sub-THz environment [17]. For our case of study, we choose the configuration ($N_t = 5$, $N_a = 3$, $N_r = \{3, 5\}$). The corresponding SE is in the order of 12 bpcu. Moreover, the corresponding data rate is estimated with a total system bandwidths of 50 GHz which is available in the band between 90 GHz and 200 GHz. The current configuration for DP-GSM systems can reach up to 500 Gbps (0.5 Tbps) when the considered total system bandwidth, after channel aggregation and bonding is 50 GHz with 0.2 rolloff factor for the pulse shaping. The simulation parameters, the data rates estimation using DP-GSM is summarized in Table 3.8. In all our simulations, the Rician factor K is set to 3 and the polarization correlation for the transmit and the receive components are chosen identical $|\gamma_t| = |\gamma_r| = 0.1$.

First, to further illustrate the potential of DP-GSM with the MOB-MMSE detector, the ML detector is compared with our approach. Fig. 3.29, shows the simulation results of the DP-GSM system over

Table 3.8 – Simulation parameters for DP-GSM sub-THz system example.

Parameters	Value
APM	QPSK
DP-GSM configuration	$N_t = 5, N_a = 3, N_r = \{3, 5\}$
Carrier frequency (GHz)	150
Channel bandwidth (GHz)	0.50
Spectral Efficiency (bpcu)	12
Pulse Shaping: Rolloff	Root Raise cosine:0.2
Spectral efficiency (b/s/Hz)	10
Data Rates per Channel (Gbps)	5
Data Rates with 50 GHz (Gbps)	500
RF-impairments: PN	σ_g^2 Value
Low	0.001
Medium	0.01
Strong	0.1

**Figure 3.29** – BER performance of $N_r \times N_t$ DP-GSM system with spatial correlation $\beta \in \{0.2, 0.8\}$ and power leakage parameter $\mu = 0.2$ for QPSK over: (a) correlated Rayleigh channel and (b) correlated Rician channel ($K = 3$) using both MOB-MMSE and ML detectors. The spectral efficiency is 12 bpcu.

correlated Rayleigh channel (a) and correlated Rician channel (b) for QPSK with MOB-MMSE and ML detectors. The spatial correlation is chosen $\beta = \{0.2, 0.8\}$ and the leakage parameter $\mu = 0.2$. As it is shown in Fig. 3.29 there is quite acceptable difference of (1–2.5) dB between ML and MOB-MMSE at the BER of 10^{-4} . Thus, the MOB-MMSE for DP-GSM system can achieve sub-optimal performance with low complexity.

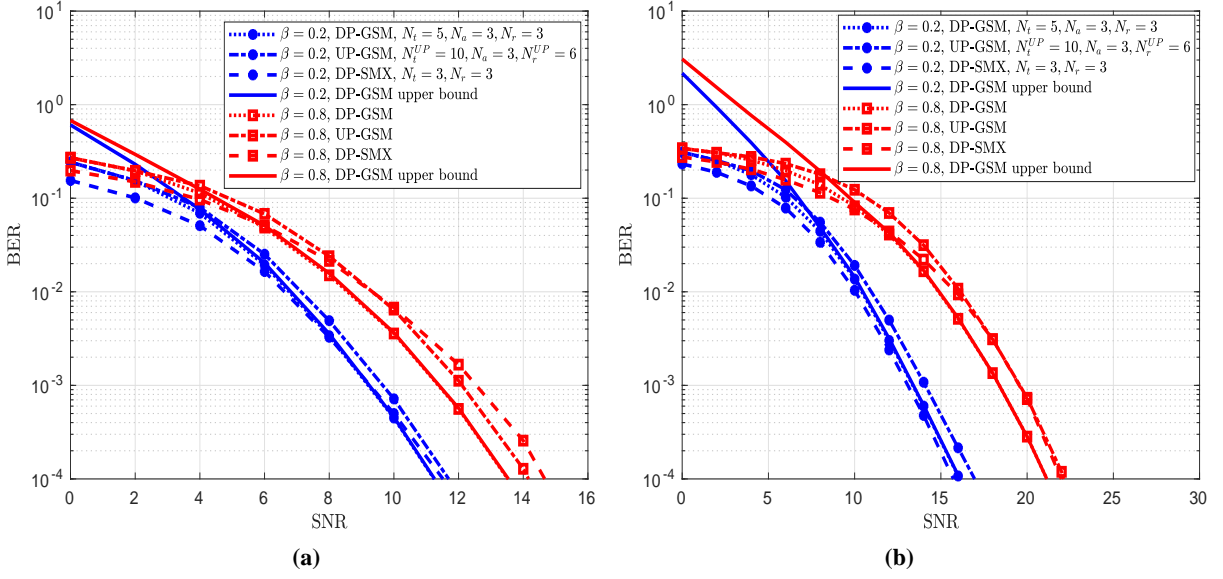


Figure 3.30 – BER performance comparison of DP-GSM , DP-SMX, and UP-GSM systems with spatial correlation $\beta \in \{0.2, 0.8\}$ and power leakage $\mu = 0.2$ over: (a) correlated Rayleigh channel and (b) correlated Rician channel ($K = 3$) for QPSK using ML detector. The spectral efficiency is 12 bpcu.

In the second experiment, the DP-SMX and the UP-GSM are compared with the DP-GSM system. We recall the reader that the SMX is a particular case of the GSM technique where symbols are transmitted simultaneously from N_t TAs to N_r receive antennas and all the TAs are activated. In the DP-SMX system, all transmit and receive antennas use the dual polarization to convey simultaneously different symbols on each polarization. The comparison is made using different spatial correlation configurations, $\beta \in \{0.2, 0.8\}$, and under different fading channels, Rayleigh and Rician channel. The comparison is made using the optimal ML detector where the number of antennas for the compared systems: DP-GSM , DP-SMX, and UP-GSM are respectively: ($N_t = 5, N_a = 3, N_r = 3$), ($N_t = 3, N_r = 3$), and ($N_t^{UP} = 10, N_a = 3, N_r^{UP} = 6$) to have the same SE given by 12bpcu for a fair comparison. It can be seen in Fig. 3.30 that the DP-GSM outperforms the UP-GSM system in both channels and both spatial correlations. In all cases, the DP-GSM allows to have a more compact antenna array physical size compared to UP-GSM, which is crucial for UE. Fig. 3.30 shows clearly that the DP-GSM and the DP-SMX have the same performance with the ML detector in low spatial correlation and for both fading channels. In the context of high spatial correlation, the DP-GSM outperforms the DP-SMX in both channels and the SNR difference between them is about 1 – 1.5 dB at a BER= 10^{-4} . Fig. 3.30 shows also that the derived ABEP upper bounds accurately match with the simulation results of the DP-GSM especially in the high SNR range.

The third experiment consists to study the performance of the DP-GSM system using the sub-THz PN model described in the previous section. The study is also extended to the case of DP-SMX for fair comparison with our system and performed with different PN levels (low $\sigma_g^2 = 0.001$, medium $\sigma_g^2 = 0.01$, strong $\sigma_g^2 = 0.1$) without applying any PN mitigation technique. Fig. 3.31 and 3.32

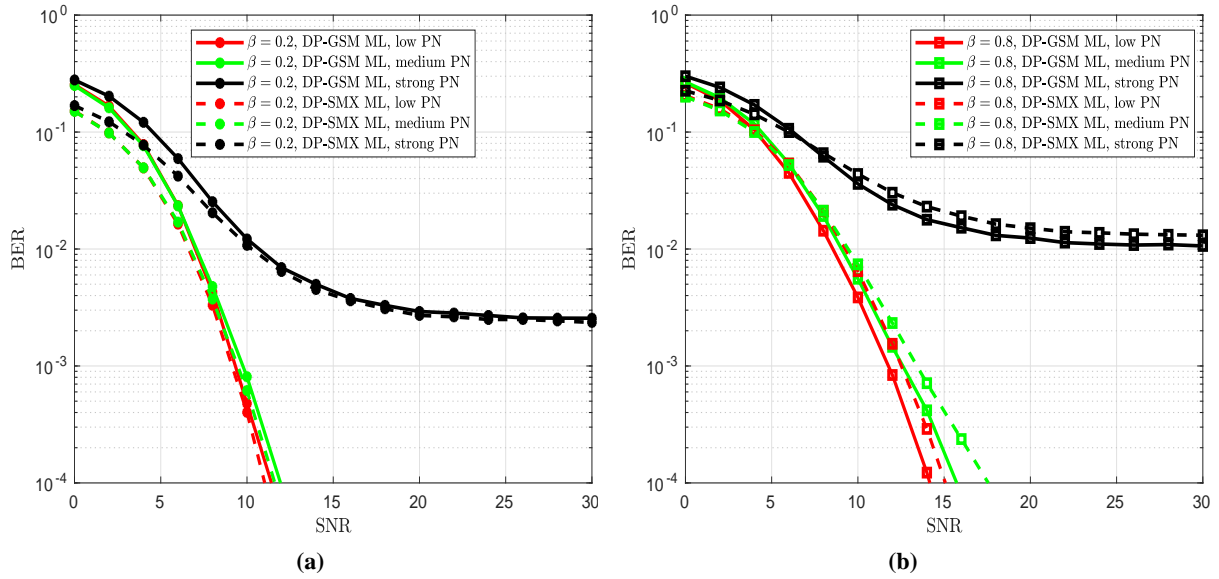


Figure 3.31 – BER performance of DP-GSM and DP-SMX systems for QPSK over correlated Rayleigh channel with spatial correlation: (a) $\beta = 0.2$ and (b) $\beta = 0.8$ using ML detector. Both systems are affected by PN with different levels (low, medium and strong noise). The power leakage parameter is $\mu = 0.2$ and the spectral efficiency is 12 bpcu.

show these comparisons between DP-GSM and DP-SMX systems for QPSK over correlated Rayleigh channel and correlated Rician channel ($K = 3$) respectively with spatial correlation (a) $\beta = 0.2$ and (b) $\beta = 0.8$. It is clear that the performance for both system are very close especially when the fading channel is Rayleigh and the spatial correlation is small ($\beta = 0.2$). When this value increases, the DP-GSM outperforms the DP-SMX by 1.5 to 2.5 dB with low and medium PN respectively. It is also worth to mention that the performance for both systems degrade considerably for strong PN. In the case of Rician fading channel (Fig. 3.32), the performance of both systems is acceptable for low value of spatial correlation but when it increases, the performance for both systems is degraded especially for medium and strong PN.

Finally, we extended our analysis using a more realistic sub-THz channel different from that presented in (3.55). In hereafter we compare the performance of the DP-SMX and the UP-GSM systems using a ray-based deterministic channel modeling for sub-THz band (90-200 GHz) developed by our BRAVE partner SIRADEL in [36]. We adopt here the downlink hotspot (or kiosk) indoor scenario generated using the ray-based channel model described in Section 3.7.4.2. Here, the ULA for antennas geometry is considered with antenna element separation of 4λ for a lower spatial correlation [169], where λ is the wavelength. Also, different channel realizations are considered by using the 10 APs marked in red and distributed throughout the room, and the 50 UEs highlighted with yellow circles in Fig. 3.13. The considered range for UE is going from 2m to 8m, i.e., we use in average a 5m separation distance between UE and AP.

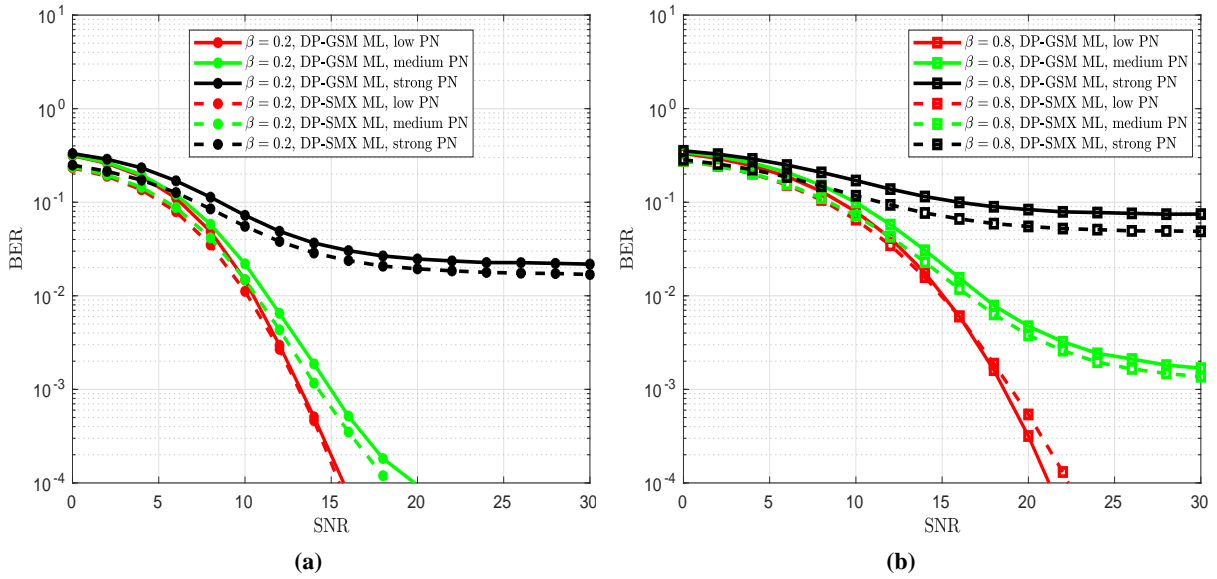


Figure 3.32 – BER performance of DP-GSM and DP-SMX systems for QPSK over correlated Rician channel ($K = 3$) with spatial correlation: (a) $\beta = 0.2$ and (b) $\beta = 0.8$ using ML detector. Both systems are affected by PN with different levels (low, medium and strong noise). The power leakage parameter is $\mu = 0.2$ and the spectral efficiency is 12 bpcu.

For a fair comparison, the DP-SMX and the UP-GSM are compared with the DP-GSM system under the same SE which is 12bpcu using same detector, same number of RA, same APM for all systems, and same number of activated TA for UP-GSM and DP-GSM. The following configurations are adopted: for DP-GSM ($N_t = 5$, $N_a = 3$, $N_r = 3$), for DP-SMX ($N_t = 3$, $N_r = 3$) and UP-GSM ($N_t^{UP} = 10$, $N_a = 3$, $N_r^{UP} = 6$). Fig. 3.33, shows such a comparison using the ML detector for the three systems. It can be seen that the DP-GSM and DP-SMX have nearly the same performance and they outperform the UP-GSM with a difference of 1 dB at the BER of 10^{-4} (see solid lines). Moreover, when the number of DP receive antennas increases: $N_r = 5$ for both DP-GSM and DP-SMX, and $N_r^{UP} = 10$ for UP-GSM, the performances of the three systems improve and the DP-GSM and DP-SMX systems always keep their superiority compared to UP-GSM.

Other effects related to sub-THz impairment can be observed in Fig. 3.34, where different PN levels are used and different number of received DP antennas $N_r = 3$ in Fig. 3.34a, and $N_r = 5$ in Fig. 3.34b are used for comparing the performances between the DP-GSM and the DP-SMX systems. Fig. 3.34, shows clearly that both systems achieve same performance for any value of N_r with low PN. The gain achieved by the DP-SMX is slightly higher (about 1.5 dB at a BER of 10^{-4}) with medium PN and $N_r = 3$ when is compared with the DP-GSM. However, it is important to highlight that both systems fail to detect correctly the conveyed bits in their respective systems and suffer from a high error floor when they experiment a strong PN impairment even when the value of N_r is high, because the system considers uncoherent detection without any PN cancellation. When the number of received DP antennas increases to $N_r = 5$, the performance of the DP-GSM and the DP-SMX systems improves compared to

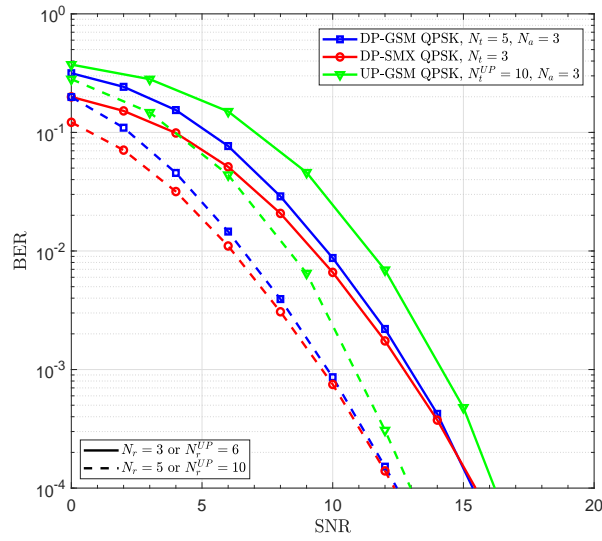


Figure 3.33 – BER performance of DP-GSM , DP-SMX and UP-GSM systems with sub-THz channels and QPSK using ML detector.

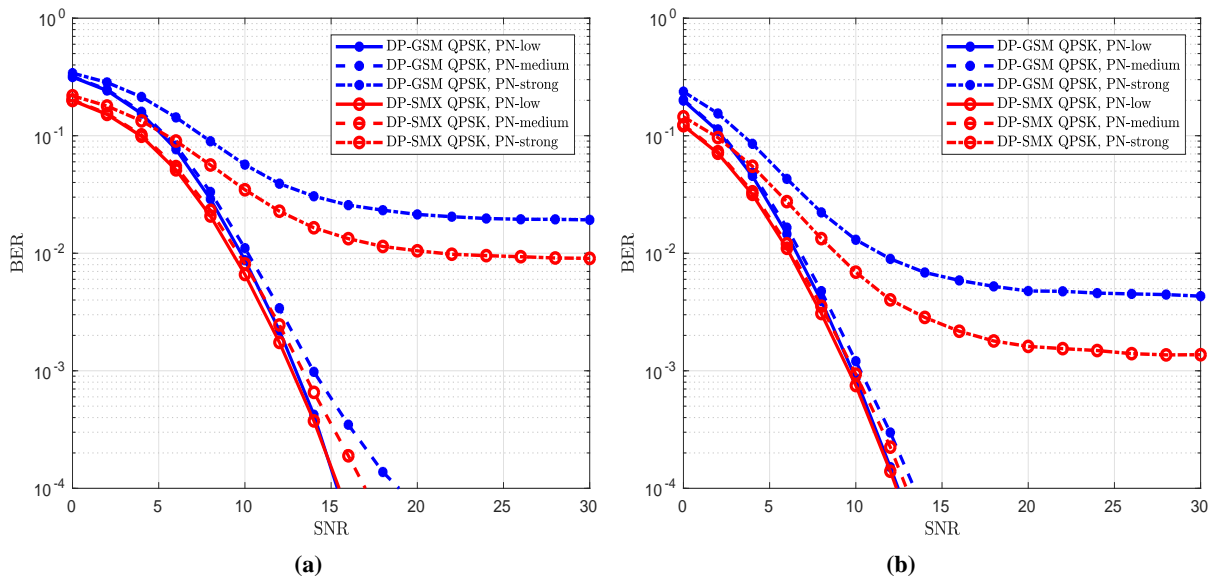


Figure 3.34 – BER performance of DP-GSM and DP-SMX systems with sub-THz channels and different PN levels. The spectral efficiency is 12 bpcu.(a) $N_r = 3$ and (b) $N_r = 5$.

the case where $N_r = 3$ and the performances of both systems become similar. By comparing Fig. 3.34a and Fig. 3.34b, we can notice that the DP-GSM system register a gain of 2 dB at BER= 10^{-4} at low PN and a gain of 3.5 dB at medium PN.

In conclusion, the implementation of GSM system with DP antennas is evaluated over correlated Rayleigh/Rician channels and sub-THz channels with/without RF-impairments such as the PN. Adding the polarization indexation layer into the GSM system leads to an increase of the SE by $N_a \log_2(N_p)$. To be able to detect at the DP-GSM systems the activated antennas indices, their polarization, and

the transmitted APM symbols a MOB-MMSE detector is proposed and compared to joint ML optimal detector. Theoretical analysis and Monte-Carlo simulations reveal that the DP-GSM system provides a 1 dB gain in comparison to the UP-GSM system which needs to have twice as much number of UP antennas, and same number of RF chains for full-RF transmitter architecture. It is also shown that the proposed DP-GSM scheme is more robust against the Rician fading effects with inter-antenna correlation, and therefore is advantageous for improving the overall SE and EE. In addition, the DP-GSM outperforms the DP-SMX in Rayleigh channel by 1.5 to 2.5 dB with low and medium PN respectively. Besides, the proposed scheme has demonstrated to have a good performance in a case of sub-THz RF-impairments especially for the case of low and medium PN levels. Moreover, the depicted results using the ray-based deterministic channel modeling for sub-THz band (90 – 200 GHz) with RF-impairments reveal that the performance of DP-GSM with low and medium PN levels are very close with help of receive diversity.

3.8 Conclusions and Discussions

In this Chapter 3, we investigated MIMO SMX and GSM for ultra-high data rate indoor scenarios. The results reveal that such a wireless system with low power consumption can be achieved by spectral-efficient IM schemes such as GSM with a power-efficient single carrier as QPSK motivated by the low PAPR [14]. In addition, it worth mentioning that exploiting IM to transmit most of the information bits with low order M -ary schemes (e.g., GSM-QPSK) to reach a high system SE is more power-efficient than SMX system and other GSM configuration that uses higher-order modulation and/or less virtual bits by means of spatial IM as summarized in Fig. 3.5. However, GSM system is more sensitive to channel correlation because highly correlated channels can lead to a detection error of activated TAC and thus the transmitted symbols. For this reason, we proposed some techniques to enhance the performance by properly selecting the legitimate TACs without instantaneous CSIT (S-EGSM), and using efficient spatial bit mapping [15].

Moreover, we proved that the power-efficient APM with GSM has many important advantages in sub-THz channels with RF impairments compared to MIMO-SMX especially when considering the complexity/energy constraints of UE receiver [16, 17]. For instance, GSM-QPSK with non-coherent detection compared to other systems has: (1) better performance; (2) lower power consumption; (3) less complexity; (4) higher robustness to PN; (5) a few-bits ADC resolution requirement, as summarized in Fig. 3.35. However, the GSM systems mainly have three drawbacks: (1) the requirement of larger TA array where only a subset is activated at a time to convey more virtual bits by IM; (2) the higher transmitter cost if full-RF architecture is adopted; (3) the PAPR increase with full-RF GSM as highlighted in Fig. 3.6 and [17] [173]. However, the antenna array size is not a critical factor in mmWave and sub-THz bands, where the small antenna size allows having a large antenna array in a compact area. Also, the transmitter cost is still feasible, especially in the downlink scenarios, where the AP serves as the transmitter. In addition, the increased power consumption due to the slight PAPR

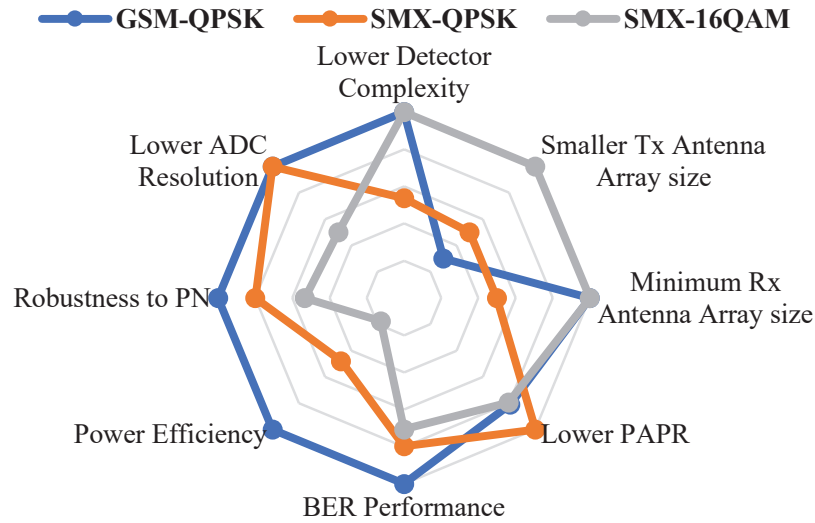


Figure 3.35 – Comparison of MIMO Systems in sub-THz channels. Axes are normalized by the best achieved value among the 3 systems of same spectral efficiency.

degradation is counterbalanced by significant SNR gain and EE/SE improvement achieved by IM. It is worth mentioning that the proposed system with channel bonding and aggregation in sub-THz bands allows reaching scaled Tbps downlink rates [17], where different users can be served simultaneously on different channels.

Although the GSM system has lower detection complexity than SMX, both system complexities increase dramatically with the number of activated TA and the APM modulation order. To avoid such a problem, we proposed a near-optimal detector with low complexity for SMX and GSM system that can achieve ML performance with 99% complexity reduction even with channel estimation error and large-scale MIMO.

Moreover, we proposed DP-GSM scheme, where the DP antennas are incorporated with GSM scheme for further SE and EE enhancement by exploiting the polarization IM dimension. Also, this improvement is validated by deriving the analytical system performance in Rayleigh/Rician channels. Then, DP-SMX and GSM are compared in the sub-THz environment to DP-GSM, where the latter maintains GSM advantages while achieving better performance and robustness to spatial correlation. Thus, the tackled challenges in this chapter for GSM and SMX MIMO systems are presented along with the proposed solutions in Table 3.9.

Finally, the presented analysis for GSM, SMX, and DP-GSM in the sub-THz environment confirms that the combination of power-efficient low-order modulation with MIMO and spectral-efficient IM is a promising solution for low-power ultra-high wireless data rate systems. In the next Part, we will follow the same approach (power efficient SC + MIMO + spectral-efficient IM) but with our novel proposed IM domain that can achieve even better SE/EE accompanied with several other critical advantages for sub-THz bands.

Table 3.9 – Our proposed solutions for the main challenges of GSM and SMX MIMO systems.

Challenge	Proposed Solution
GSM high performance degradation due to spatial correlation	S-EGSM system: that reduces detection error by avoiding the most correlated TACs based on the transmit spatial correlation information.
	Best-effort gray spatial bit-mapping: that minimizes the BER due to the ambiguity between neighbor TACs.
	DP-GSM: that exploits polarization IM dimension to provide better robustness against spatial correlation while enhancing the SE.
SMX and GSM high detection complexity with large-scale MIMO and high APM order	OSIC-ML and O^2 SIC-ML detectors for SMX and GSM respectively: that provide a controllable complexity-performance tradeoff while achieving the optimal performance with 99% complexity reduction compared to ML detector.

Part II

Novel Domain/Dimension for Index Modulation

Chapter 4

Novel IM domain

Contents

4.1	Introduction	123
4.2	Filter IM domain	125
4.3	Filter Shape Index Modulation (FSIM)	127
4.3.1	FSIM Transmitter System model	127
4.3.2	FSIM Receiver System model	129
4.3.2.1	Joint ML Detector	130
4.3.2.2	Matched Filter-based Detector	130
4.3.2.3	ISI Estimation and Cancellation	132
4.3.3	Filter Bank Design requirements	133
4.3.4	Theoretical performance analysis	134
4.3.5	Numerical results analysis and discussions	137
4.3.5.1	FSIM vs Media-Based Modulation (MBM)	144
4.3.6	Conclusions	146
4.4	Quadrature Filter Shape Index Modulation (IQ-FSIM)	146
4.4.1	Introduction	146
4.4.2	IQ-FSIM Transmitter System model	147
4.4.3	IQ-FSIM Receiver System model	149
4.4.3.1	Joint ML Detector	149
4.4.3.2	Matched Filter-based Detector	150
4.4.3.3	ISI Estimation and Cancellation	151
4.4.4	Theoretical Performance Analysis	153
4.4.5	Numerical Results Analysis and Discussions	156
4.4.5.1	Performance Analysis based on Theoretical Lower Bound	157
4.4.5.2	Comparison to Equivalent M -ary QAM	158

4.4.5.3	Comparison to Equivalent FSIM System	161
4.4.6	Conclusions	162
4.5	MIMO Spatial Multiplexing with FSIM	163
4.5.1	System Model: MIMO Spatial Multiplexing with FSIM	164
4.5.1.1	SMX FSIM Transmitter	164
4.5.1.2	SMX-FSIM Receiver	166
4.5.1.2.1	Equalization	166
4.5.1.2.2	Detection	167
4.5.2	Theoretical Performance	168
4.5.3	Results and Discussions	171
4.5.3.1	Theoretical and simulated performance comparison of SMX-FSIM to equivalent SMX-QAM system	171
4.5.3.2	Spectral Efficiency Analysis: SMX-FSIM vs existing MIMO techniques	172
4.5.3.3	Comparison of SMX-FSIM, conventional SMX and GSM in sub- THz environment	175
4.5.3.3.1	Performance in sub-THz channel with RF impairments	175
4.5.3.3.2	Detection Complexity	176
4.5.3.3.3	Hardware cost and design issues	178
4.5.3.3.4	PAPR, Link Budget and Power consumption	178
4.5.4	Conclusion	180
4.6	Summary	181

4.1 Introduction

The previous Chapter investigated the spatial IM domain and mainly GSM-based schemes to achieve low-power ultra-high wireless rates in sub-THz. The spectral-efficient spatial IM scheme with power-efficient APM (e.g., GSM-QPSK [16]) is shown to be more advantageous in sub-THz bands than the systems used in recent standards (e.g., IEEE 802.11ax) where SMX with high order QAM is adopted, as discussed in [17] using their optimal detectors. However, GSM requires a full-RF transmitter architecture (i.e., high-cost) to maintain its SE while using only few TAs for multiplexing APM symbols, and it suffers from performance degradation when a TAC index is mis-detected due to its propagation to all APM symbols. Consequently, these results and drawbacks motivate us to propose a novel IM domain that provides even higher SE/EE in SISO prior to its MIMO exploitation. It is worth mentioning that each single bit SE enhancement in the SISO context will be multiplied by the multiplexing order in the MIMO context and turns into important SE gain, especially with larger-scale MIMO. Hence, an intelligent strategy that should significantly impact the overall MIMO system design is to enhance the SE of SISO systems while keeping using power-efficient low-order APMs suitable for sub-THz bands with the technological limitation and RF impairments.

In this Chapter, a novel domain for IM is proposed where a more significant SE/EE enhancement is targeted in SISO with a better performance compared to the equivalent system with/without IM. The proposed filter IM domain generalizes the existing time and frequency IM domains and provides another degree of freedom to better exploit IM advantages. Moreover, two novel schemes are proposed to achieve higher SE and EE enhancement. Furthermore, the filter IM domain is incorporated with MIMO SMX to highlight the different advantages of our proposed domain especially in sub-THz environment. Finally, a complete analysis and comparison with the results of Chapter 3 is presented to conclude both chapters.

The major contributions of this chapter are summarized as follows:

1. A novel domain for index modulation, named Filter IM Domain, is proposed where another degree of freedom for IM is introduced. In addition, the special cases of the proposed domain and its different potential indexation techniques are discussed.
2. Within the filter domain/dimension, a novel modulation scheme named Filter Shape Index Modulation (FSIM) is proposed. To the best of our knowledge, this is the first time such an indexing dimension is used as a method for SE enhancement purpose. The pulse-shaping filter is indexed to convey additional information bits to those transmitted in the APM data symbols. The information bits in FSIM are mapped into both signal domain (any M -ary APM) and filter domain. As a new approach, we consider a filter bank with different shapes that can be changed at each symbol period rather than a single pulse shaping filter to further explore the indexation gain.

3. Within the filter IM domain/dimension, another novel modulation scheme named IQ-FSIM is proposed. In contrast to FSIM, the pulse shaping filters for the In-phase (I) and Quadrature (Q) components are indexed separately to double the virtual information bits in addition to those transmitted in the APM symbols. The bits in IQ-FSIM are mapped into both traditional signal domain (any M -ary APM) and filter IM domain. This scheme generalizes the previously proposed FSIM, which in turn generalizes most of SISO-IM schemes in frequency and time IM domains. By considering different filter shapes at each symbol period at the transmitter and the separate indexation on I and Q, a higher EE and SE is enabled by this scheme.
4. The FSIM and IQ-FSIM system models are presented where a low complexity detector based on MF is proposed. Compared to the joint ML detection that considers the joint detection of both APM symbols and filter shapes' indices on I and Q, the proposed MF based detector performs the filter shape detection firstly, and then the APM symbols being received. A prominent computational complexity reduction is obtained while achieving the optimal ML performance.
5. An ISI estimation and cancellation block is proposed for both schemes to eliminate the ISI introduced by the designed filter shapes.
6. Theoretical analysis and Monte Carlo simulations substantiating the efficiency of the proposed FSIM and IQ-FSIM schemes are presented. A lower bound for the error probability for filter index detection is derived. Also, the APM error is incorporated to truly characterize the FSIM and IQ-FSIM system performance in terms of total Symbol-Error Rate (SER) and BER. This lower bound can be evaluated numerically with any number of filters and M -ary APM scheme. Simulation results demonstrate the superior performance of FSIM compared to the other systems of the same SE with/without IM in AWGN and frequency selective fading channels.
7. The performance of both proposed schemes FSIM and IQ-FSIM are compared at the same SE using theoretical and numerical results with the currently designed filters. The results highlight that IQ-FSIM with a realistic filter bank allows reaching a higher EE due to the lower modulation scheme order or the number of filters, especially when the larger filter bank is not optimally designed.
8. A generalized MIMO SMX system is proposed by incorporating FSIM scheme to achieve high SE and EE gain. The proposed SMX-FSIM system conveys information bits in the signal and filter IM domains. The VBs are encapsulated by the different filter shapes indices that are used for pulse shaping of the N_t simultaneously transmitted APM symbols. Note that the transmit spatial IM (e.g., GSM system) conveys all the VBs by a single index (index of activated TAC), and its misdetection leads to bit errors in most of the VBs and also in the real bits of all transmitted APM symbols (i.e., N_a APM symbols in GSM will be most probably mis-detected when an error occurs in the TAC index detection). However, the decentralization of VBs encapsulation in SMX-FSIM avoids the highlighted single point of failure in GSM system.

9. A simple receiver for SMX-FSIM is presented, which is based on Zero-Forcing (ZF) sample level equalizer followed by a parallel MF-based detector. The proposed parallel detection for SMX-FSIM provides good performance with prominent complexity reduction compared to the joint Maximum Likelihood (ML)-based detector.
10. The analytical performance of SMX-FSIM using ZF equalizer is derived and validated by Monte Carlos simulations. Then, they are compared to those of the conventional SMX QAM system of the same SE. The results show an important SE and EE gain can be achieved even with a low number of filter shapes.
11. The performance of the proposed SMX FSIM scheme is evaluated under sub-THz channels generated using ray-based deterministic channel model [36] and with RF impairments, then compared to the existing ultra-high data rate candidates presented in Chapter 3 (GSM and conventional SMX QAM [17]).
12. These sub-THz candidate schemes are compared and analyzed from different perspectives (performance, robustness to PN, SE/EE, cost, PAPR, and power consumption). The results reveal that the spectrally efficient SMX-FSIM with power-efficient APM is the most promising candidate for such systems in sub-THz bands because it has better performance and robustness to PN, higher SE and EE gain, lower power consumption, and cost, as well as it avoids the RF switching problem that appears with transmitter spatial IM (e.g., GSM).

The remainder of this chapter is organized as follows. Section 4.2 introduces the novel Filter IM domain that generalizes most of SISO-IM schemes. The novel FSIM transceiver along with different detectors, its theoretical performance derivation, and simulation results are presented in section 4.3. Similarly, in Section 4.4, the proposed IQ-FSIM is presented with a similar study, and it also provides a comparison between both proposed schemes: FSIM and IQ-FSIM. Furthermore, the proposed filter IM domain is extended to MIMO SMX in section 4.5, along with its theoretical performance analysis, evaluation in the sub-THz environment, and comparison to other sub-THz candidates from different perspectives. Finally, Section 4.6 summarizes this chapter.

4.2 Filter IM domain

In this section, the filter IM domain is proposed aiming at further enhancing the SE gain. It will be first applied to SISO systems prior to its exploitation in MIMO context. It is worth to mention that the filter IM domain can include all kind of communication systems because all of these systems have at least one filter used for band-limitation of the emitted signal. In addition, the filter IM domain allows the indexation of several filter property to convey information bits with or without an APM symbol. Adopting filter indexation strategy, one can cover as many schemes as it can be imagined to convey VBs by indexing: the bandwidth, the roll-off factor, the filter shapes, the filter time shift,....etc.

Hence, the frequency domain IM (presented in Section 2.2) can be seen as a special case of the filter IM domain because the activation/deactivation of a frequency band or a subcarrier is just an application of a band-pass/zero filters in single mode IM. Similarly, the time domain IM counterpart (presented in Section 2.2) can also be considered as a special case of the filter IM domain, where the transmit filter is shifted by multiple of symbol period without allowing overlapping of different symbols. Note that in the single mode time domain IM, the transmitter sends APM symbols only during activated time slots where a non-zero filter is used.

In modulation type IM domain, the transmission of data symbols in all time slots or subcarriers is enabled by using distinguishable APM schemes between primary and secondary activated resources. The DM-IM systems in [80] [79] [81] consider two distinguishable constellation alphabets drawn from the inner and the outer constellation points of different average power levels using same or different normalized constellation points. Note that DM-IM can be achieved by using same normalized APM alphabets followed by different filters to change power and phase, by using different APM constellations with same filter or using both different APM constellations and filters between primary and secondary active resources. The filter domain IM generalizes the single-mode IM by selecting only different filters between active and non-active sub-carriers or time slots. However, the filter IM domain needs also to select different APM mapper (constellation alphabets) between primary and secondary active resources to generalize all cases of DM-IM.

For clarification, the modulation type IM can be realized by considering one of the following strategies that use:

1. same normalized APM alphabets followed by different filters to change power and phase between the different active resources, e.g., the inner and outer QPSK constellations used in [81].
2. different APM constellations with different filters if the constellations' sets in APM mappers/de-mappers are the normalized version and the filters modify them (i.e., by scaling the power levels for each APM, rotating the constellation points) to get distinguishable constellations (e.g., the two constellations used in [79, 80]).
3. different APM constellations with same filter like most modulation type IM schemes (e.g., the two constellations used in [79, 80]).

Note that the first strategy fits well in the proposed filter IM domain with unique APM mapper/de-mapper.

Moreover, the non-orthogonal time/frequency IM schemes in single and dual mode where the filters overlap in the time/frequency domain in Faster Than Nyquist (FTN)/SeFDM based schemes, are also special cases of filter IM where the filters are adapted according to compression factor ν , and the overlap and add block that we will present in the next section is modified for FTN based schemes. Therefore, the filter IM domain can generalize most of SISO IM schemes.

Furthermore, the filter IM dimension also includes the conventional modulation schemes as the PPM and its generalization, Pulse-Width Modulation (PWM), OOK because they convey bits by means of indexing a filter property. Hence, our proposed domain generalizes most of SISO-IM schemes and its exploration allows more innovation in communication systems. To the best of our knowledge, such a domain has never been investigated in the literature but the investigation of some special cases in this domain as OOK or PPM started before many decades.

In this chapter, many possible indexations in filter IM domain (e.g., the filter roll-off) are not explored currently, because they involve a bandwidth variation, and/or they cannot be modified and detected at symbol rate, and thus negatively impacting the SE which is contradictory with our ultimate goal: the SE enhancement. In the following, we will introduce our proposed novel schemes in this IM domain/dimension to convey additional information by indexing the filter shapes. These schemes use all frequency and time resources where the filter shape can be changed at each symbol period to maximize the possible SE enhancement as it be explained in the next sections.

4.3 Filter Shape Index Modulation (FSIM)

4.3.1 FSIM Transmitter System model

The proposed system considers a SISO transmission mode, where the binary source information sequence b is divided into two streams b_1 and b_2 as shown in Fig. 4.1. The bit-stream b_1 is mapped by the M -ary APM, such as QAM or PSK, etc. The bit-stream b_2 is encapsulated in the index i of the selected filter. Then, the selected filter $f_i[m]$ of length L samples is used as a pulse shaping filter where m is the sample index taking values between 0 and $L - 1$. The filter is truncated in the time domain to η APM symbols and sampled with a rate of λ samples per symbol, which yields $L = \eta \cdot \lambda + 1$ samples. L is restricted to be odd in order to have a linear phase filter without a half sample period shift.

We suppose that there is a filter bank with N distinguishable filters as shown in Fig. 4.1 (N is a power of 2), and its design is addressed in the next Chapter 5. Accordingly, the number of bits per FSIM symbol $\mathcal{L}_{\text{FSIM}}$ can be expressed as:

$$\mathcal{L}_{\text{FSIM}} = \log_2 N + \log_2 M. \quad (4.1)$$

Thus, the SE is enhanced by $\log_2 N$ compared to conventional M -ary APM systems thanks to the filter indexation at each symbol period.

The output of the filter bank for the n -th APM complex symbol c_n is denoted by signals $s_n[m]$ and given as follows:

$$s_n[m] = (f_{i_n} * c'_n)[m] = c_n f_{i_n}[m] \quad (4.2)$$

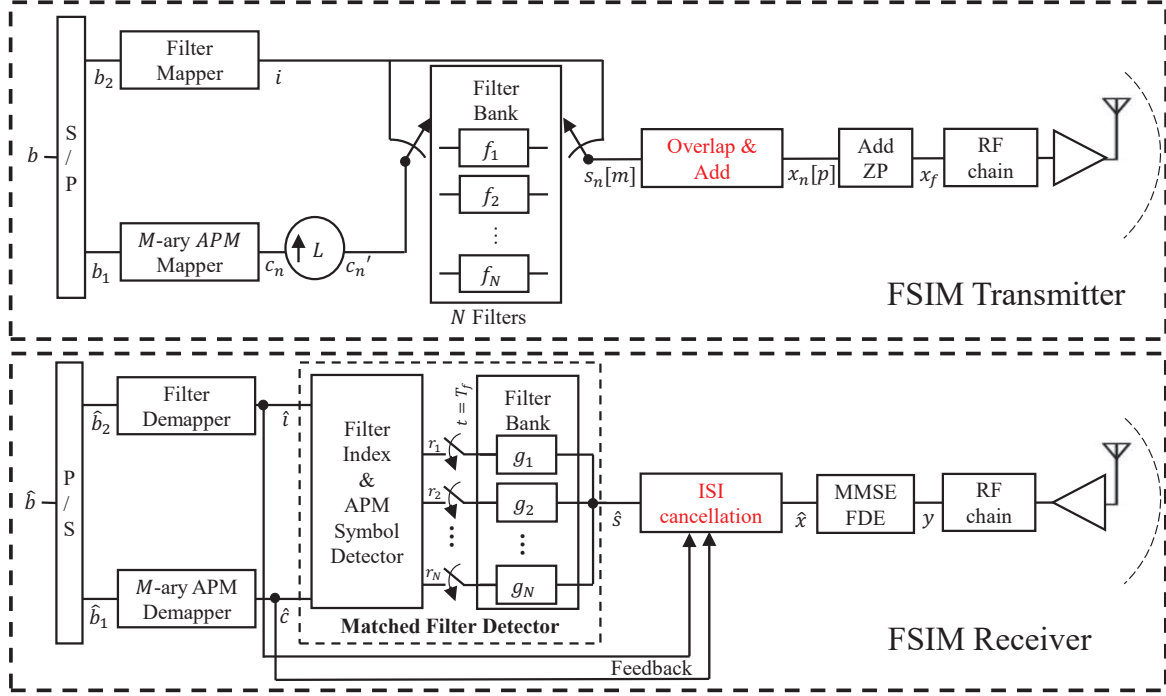


Figure 4.1 – System model of the FSIM-based transmitter and receiver with MF-based detector using N filters of length L and M -ary APM. Note that the detector can be replaced by the joint ML detector.

where c'_n is an up-sampled version of c_n by a factor L , and $i_n \in \{0, 1, \dots, N - 1\}$ is the index of the filter being selected for the n^{th} symbol according to the bit-stream b_2 .

Then, the signals $s_n[m]$ are passed through the Overlap and Add (OLA) block as shown in Fig. 4.1 in order to generate the λ samples for each APM symbol. The λ desired samples for the n^{th} APM symbol c_n is given by $x_n[p]$ as follows:

$$x_n[p] = \sum_{n' = n - \lceil \eta/2 \rceil}^{n + \lfloor \eta/2 \rfloor} s_{n'}[p - (n' - n)\lambda], \quad (4.3)$$

where the index $p = p_{\text{center}} - \lceil \lambda/2 \rceil + 1, \dots, p_{\text{center}} + \lfloor \lambda/2 \rfloor$ and the index of the middle desired sample is $p_{\text{center}} = \frac{L-1}{2}$.

An example for the OLA with $\eta = 6$ is illustrated in Fig. 4.2. Note that each row in this figure represents the L output samples of the filter bank for the n^{th} symbol c_n which contains: the desired λ samples \mathbf{s}_n at the center and the undesired samples \mathbf{I}_j^n for $j = \pm 1, \pm 2, \pm 3$. The λ samples \mathbf{s}_n will be affected and interfered by the undesired samples of the $\lceil \eta/2 \rceil = 3$ APM symbols prior the instant n (for $j > 0$) and of $\lfloor \eta/2 \rfloor = 3$ APM symbols posterior to the instant n (for $j < 0$) as depicted in the red vertical box (for $n = 3$) of Fig. 4.2. Hence, the equation (4.3) can be rewritten in terms of interference as:

$$\mathbf{x}_n[p] = \mathbf{I}_{\lceil \eta/2 \rceil}^{n - \lceil \eta/2 \rceil} + \dots + \mathbf{I}_1^{n-1} + \mathbf{s}_n + \mathbf{I}_{-1}^{n+1} + \dots + \mathbf{I}_{-\lfloor \eta/2 \rfloor}^{n + \lfloor \eta/2 \rfloor} \quad (4.4)$$

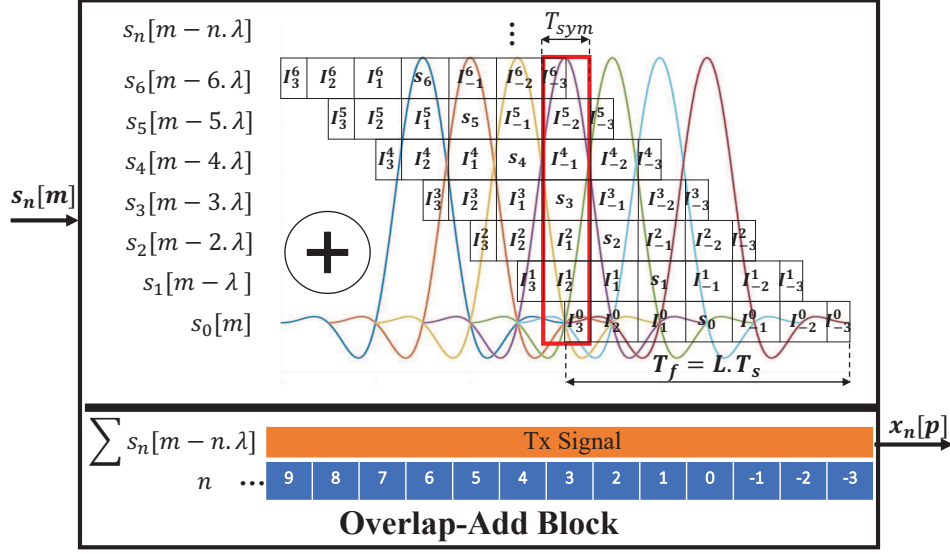


Figure 4.2 – An example for the Overlap-Add block in the proposed scheme assuming $\eta = 6$ symbols.

Note that the conventional transceiver with any M -ary APM schemes can be considered as a special case from our proposed system where all the filters in the bank are all substituted by the same Nyquist pulse shaping filter e.g., RRC. In other words, the proposed system is equivalent to conventional transceiver when using the same Nyquist filter for all symbols, and this proof is presented in Appendix D. Finally, a frame \mathbf{x}_f is created by padding the signal of N_s FSIM symbols by a zero-prefix of length λN_{ZP} samples in order to eliminate the inter-frame interference: $\mathbf{x}_f = [0_1, \dots, 0_{N_{ZP}}, \mathbf{x}_{-\lfloor \eta/2 \rfloor}, \dots, \mathbf{x}_{\lceil N_s - 1 + \eta/2 \rceil}]$. Hence, the SE of FSIM is attenuated by a factor of $N_s / (N_s + N_{ZP})$ only when ZP is used, but adding a ZP is without any power penalty in contrast to using CP.

4.3.2 FSIM Receiver System model

The receiver scheme proposed by our approach is represented in Fig. 4.1, where the received signal y is expressed in time domain as:

$$y(t) = (h * x_f)(t) + v(t), \quad (4.5)$$

where $h(t)$ is the impulse response of a multipath frequency-selective fading channel with J paths and maximum delay spread of $(J - 1)T_{sym}$, where $T_{sym} = \lambda T_s$ is the APM symbol period and T_s is the sampling period. Note that $N_{ZP} \geq (J - 1)$ in order to avoid the inter-frame interference. $v(t)$ is the AWGN with zero mean and variance σ_v^2 , i.e., $\mathcal{CN}(0, \sigma_v^2)$. The power of transmitted symbols c_n and the used filters f_{i_n} are normalized: $\mathbb{E}[\|c_n\|] = 1$ and $\|\mathbf{f}_i\|^2 = \sum_{m=0}^{L-1} f_i^2[m] = 1$, respectively.

Firstly, the receiver compensates for the fading channel distortion on all received samples that contain the implicit information of the selected filter index. For each received frame, the zero-prefix

is removed, then a linear equalizer like MMSE-FDE [206] is used to mitigate the channel effect and recover the signal \hat{x} as depicted in Fig. 4.1.

Afterward, the equalized signal \hat{x} shown in Fig. 4.1 is passed to the ISI estimation and cancellation that remove the controlled ISI from the used filter shapes. The ISI cancellation is required if the used filters don't satisfy the Nyquist ISI criterion. The condition for zero ISI in AWGN channel is:

$$(f_i * g_i)(n.T_{sym}) = \begin{cases} 1 & n = 0 \\ 0 & n \neq 0 \end{cases} \quad (4.6)$$

for any integer n and $i = 1, \dots, N$, where g_i is the impulse response of the MF. Note that when this condition is satisfied, only one pulse has an effect at the integer multiple of the symbol period as shown in Fig. 4.2. However, this condition is relaxed in the proposed system when the target is to enhance the SE of M -ary APM, and then ISI will occur naturally. Therefore, an ISI cancellation process is mandatory before detecting the APM symbol and the selected filter index. The APM symbol and index detection can be performed jointly using the joint ML detector or separately using the MF detector. The proposed detectors are described in the following.

4.3.2.1 Joint ML Detector

The equalized signal \hat{x} is fed to the ISI cancellation block that aims at regenerating free-ISI signals \hat{s} composed each of L samples. These signals \hat{s} are then fed to the detector to jointly recover the filter index and the transmitted symbols. The detection can be performed using an ML detector that makes an exhaustive search over all possible APM symbols and filters \mathbf{f}_i combinations as described below:

$$\{\hat{i}, \hat{c}\} = arg \min_{\mathbf{f}_i \in \psi, c \in \chi} \|\hat{\mathbf{s}} - \mathbf{f}_i * c\|^2 \quad (4.7)$$

where ψ and χ denote the set of N filter's shapes and the M -ary APM constellation, respectively. \hat{i} and \hat{c} are the estimated filter index of \mathbf{f}_i and the estimated APM symbol, respectively. Such a receiver's system model is similar to that illustrated in Fig. 4.1 but by replacing the MF-based detector by an ML detector.

4.3.2.2 Matched Filter-based Detector

The detection of the selected filter index can be performed using a bank of MFs or a bank of correlators. In this section, we will consider the MF-based detector, knowing that both detectors provide the same results [203]. Figure 4.1 depicts the system model where the detection is performed after the ISI cancellation. The detector is composed of N matched filter g_k where $g_k(t) = f_k(T_f - t)$ with $0 \leq t \leq$

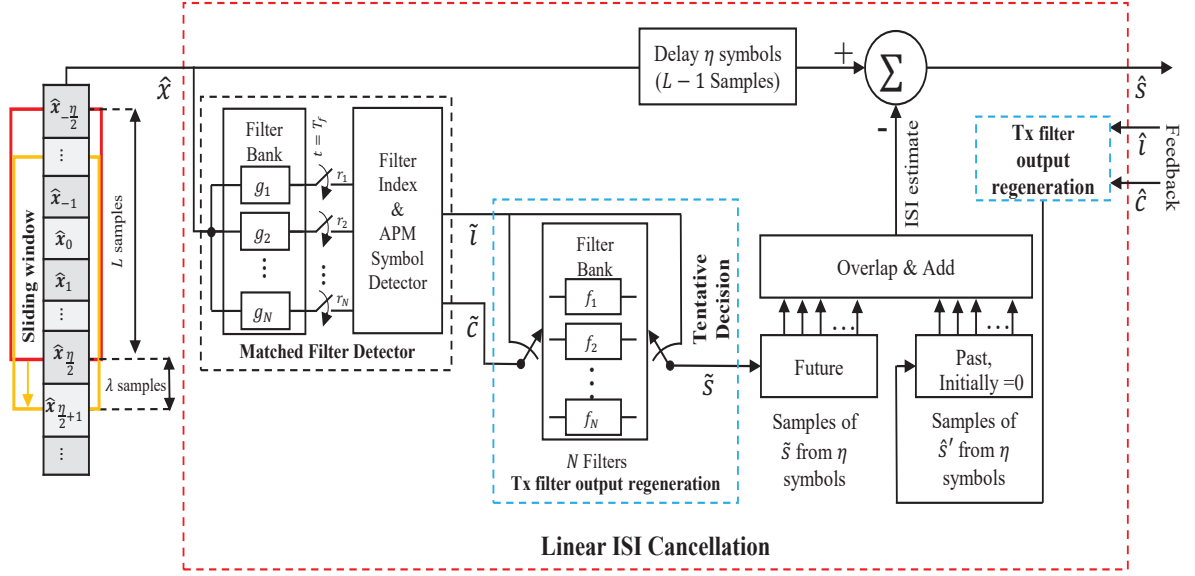


Figure 4.3 – ISI estimation and cancellation using feedback decisions $\{\hat{i}, \hat{c}\}$ for past symbols and tentative decisions $\{\tilde{i}, \tilde{c}\}$ for future symbols.

$T_f, T_f = L.T_s$. The outputs of these filters $r_k(t)$ are given by:

$$\begin{aligned} r_k(t) &= \int_0^t \hat{s}(\tau) g_k(t - \tau) d\tau, \quad k = 1, 2, \dots, N \\ &= \int_0^t \hat{s}(\tau) f_k(T_f - t + \tau) d\tau. \end{aligned} \quad (4.8)$$

These filter outputs are evaluated at the instant T_f

$$r_k = \int_0^{T_f} \hat{s}(\tau) f_k(\tau) d\tau, \quad k = 1, 2, \dots, N. \quad (4.9)$$

Thus, the decision on the selected filter index, being used at the transmitter, is based on selecting the largest energy of the sampled MF outputs as follows:

$$\hat{i} = \arg \max_k \|r_k\|^2. \quad (4.10)$$

Once the filter index is detected, $r_{\hat{i}}$ is decoded by using the APM detector that determines the ML transmitted symbol \hat{c} in the constellation set χ . Note that any other APM detector can be used. Finally, the detected APM symbol \hat{c} and the filter index \hat{i} are sent to the corresponding demappers to deduce the bit-stream \hat{b}_1 and \hat{b}_2 , respectively.

4.3.2.3 ISI Estimation and Cancellation

The principle of FSIM is to convey additional information bits through the index of the transmission filter being selected at the transmitter. Thus, this modulation's success is based on the capability of detecting correctly at the first stage, the index of the selected filter f_i . For this reason, the filter bank cannot contain only Nyquist filters due to the inherent high cross-correlation between the possible Nyquist filters. One of the solutions that could allow the detection of correlated Nyquist filter is to use the same filter shape for many successive symbols. However, this solution contradicts the FSIM approach, aiming to increase the SE in contrast to other SISO-IM schemes presented in Section 2.2. Therefore, the filter bank used in this modulation is expected to generate ISI but predictable depending on the filter shapes, and the filter bank design will be considered in Chapter 5.

Considering an AWGN channel, equation (4.5) can be rewritten as follows:

$$y(t) = x(t) + v(t) = \sum_n s_n(t - n.T_{sym}) + v(t) = \sum_n c_n f_{i_n}(t - n.T_{sym}) + v(t). \quad (4.11)$$

The received signal is sampled at the rate of T_s and the L received samples corresponding to APM symbol c_n is given as follows:

$$\begin{aligned} y_n[m] &= (c_n \cdot f_{i_n}[m] + \underbrace{\sum_{n'>n} c_{n'} \cdot f_{i_{n'}}[m - (n' - n)\lambda]}_{\text{anticausal ISI}} + \underbrace{\sum_{n'<n} c_{n'} \cdot f_{i_{n'}}[m - (n' - n)\lambda]}_{\text{causal ISI}}) + v_n[m] \\ &= c_n \cdot f_{i_n}[m] + ISI_n[m] + v_n[m], \end{aligned} \quad (4.12)$$

where f_{i_n} represents the i^{th} filter used to transmit the n^{th} symbol and $v_n[m]$ is the noise sampled at $t = n.T_{sym} + m.T_s$. Note that if the used pulse shaping filters satisfy Nyquist condition for zero-ISI, then the received signal in AWGN channel is ISI free ($ISI = 0$ in (4.12)) which is not the case in the proposed system.

Thus, the perfect ISI cancellation for the L samples around any symbol requires the knowledge of the filter index and APM symbols for the η past and η future symbols (as shown in Fig. 4.2 where the ISI in the samples \mathbf{I}_3^0 of the first APM symbol c_0 can be eliminated by knowing all the future $\eta = 6$ symbols). The proposed ISI cancellation algorithm takes the past η detected APM symbols $\hat{c}_{n'<n}$ along with their filter indices $\hat{i}_{n'<n}$ as a feedback from the previous final decisions as shown in Fig. 4.1. However, a tentative decision as in [207] [208] is required for the η future symbols. Thus, the ISI cancellation and detection for the current symbol will be delayed by η symbols after receiving the L samples of c_n as depicted in Fig. 4.3 in order to be able to mitigate the anticausal ISI. Note that the conventional transceiver delay is $d_{conv.} = \frac{\eta \cdot \lambda}{2} + \lfloor \frac{\lambda}{2} \rfloor$ samples, which corresponds to filter ramp-up delay and time needed to receive all λ samples for first symbol. Thus, the additional FSIM system delay compared to conventional transceiver is $d_{FSIM} = L + \eta\lambda - d_{conv.} = 3\frac{\eta \cdot \lambda}{2} + 1 - \lfloor \frac{\lambda}{2} \rfloor$ samples, which corresponds to the delay needed to receive the rest of the first L samples and to eliminate the anticausal

ISI from the η future symbols.

The FSIM receiver with linear ISI cancellation is depicted in Fig. 4.3. The tentative decision of the APM symbol $\tilde{c}_{n'>n}$ and the filter index $\tilde{i}_{n'>n}$ for future η symbols are detected by the matched filter as described in the subsection 4.3.2.2 using their corresponding L samples of the received signal $y_{n'}[m]$. These tentative decisions $\{\tilde{i}_{n'}, \tilde{c}_{n'}\}$ are used to regenerate the filter bank output originally generated at the transmitter side as $\tilde{s}_{n'}[m] = \tilde{c}_{n'} f_{\tilde{i}_{n'}}[m]$. Similarly, this regeneration is performed for the past symbols using the feedback decisions $\{\hat{i}_{n'}, \hat{c}_{n'}\}$ to get $\hat{s}_{n'}[m] = \hat{c}_{n'} f_{\hat{i}_{n'}}[m]$. As shown in Fig. 4.3, the regenerated signals are saved in their corresponding registers and then used to generate the ISI estimation. Finally, the ISI cancellation is performed by subtracting the estimated ISI from the corresponding L samples of the received signal $y_{n'}[m]$. This aims to generate the estimated transmitter filter output $\hat{s}_n[m]$ for the APM symbol c_n that can be expressed as follows:

$$\hat{s}_n[m] = c_n f_{i_n}[m] + ISI_{resid}[m] + v_n[m], \quad (4.13)$$

where $m = 0, \dots, L - 1$. The $ISI_{resid}[m]$ represents the residual ISI that might still persist due to the non-perfect ISI cancellation. Note that if the filters are well designed, the $ISI_{resid}[m]$ approaches zero. Finally, $\hat{s}_n[m]$ is passed through the filter index and the APM symbol detectors to recover the bitstreams b_1 and b_2 as described in Fig. 4.1.

4.3.3 Filter Bank Design requirements

Note that the proper design of the filter shape is crucial to allow the correct detection of the indexed filter. In this sub-section, the filter bank design problem is summarized, and it will be addressed and solved in the next chapter 5. In brief, this problem shares some requirements with the conventional pulse shaping problem, but more constraints are added to maximize the correct detection of the selected filter index. The proposed system insists that ISI is not necessarily undesirable while it is controllable. The aim is to achieve better system capacity rather than enforcing zero interference.

The filter bank design problem is not a trivial task because all filters f_i in the bank should be jointly designed to satisfy the following conditions and constraints:

1. f_i is strictly band-limited with a bandwidth B within the channel bandwidth B_c , where $B \leq B_c$ should be as large as possible. In addition, the filters f_i should be around the center frequency of the channel (around the carrier frequency in the pass-band or around zero in the base-band).
2. Minimum cross-correlation between all normalized filters f_i in the bank is required to maximize the correct filter index detection at the receiver side. The cross-correlation between two filters f_i and f_j from the bank is given by:

$$(\bar{f}_i \star f_j)[d] = \sum_{l=-\infty}^{l=+\infty} \bar{f}_i[l] \cdot f_j[l-d], \quad \forall i, j = 1, 2, \dots, N \text{ and } d = 0, 2, \dots, 2L - 1. \quad (4.14)$$

More precisely, the dot-product square between filters $\langle \mathbf{f}_i, \mathbf{f}_j \rangle^2$ should be minimized since the MF detector output taken at $t = T_f$ depends on this dot-product value.

3. All the filters should have an acceptable level of Out-of-Band (OOB) radiations with a feasible filter length. Thus, the Magnitude response $|F_i(\omega)|$ of all filters \mathbf{f}_i should satisfy the following condition: $|F_i(\omega)| \leq OOB_{max}$ for $\omega \geq \omega_s$, where ω_s is the stop-band angular frequency.
4. The filter length L should be kept the minimum possible to allow practical implementation. Hence, the tails of their impulse responses should decay to zero after a feasible number of symbols in order to have, after the time domain truncation to η symbols, the best tradeoff filter length-OOB.
5. The performance of FSIM depends on the ability of correct ISI estimation and cancellation, and mainly on the correct tentative decisions in presence of ISI. Thus, the introduced ISI distortion should be minimized while respecting the previous conditions and constraints, to avoid any error floor in terms of SER and BER.

A straightforward solution for this filter design problem is to have orthogonal filters that occupy each different bandwidth by dividing B_c into N sub-bands. In this case, the first condition to have the same center frequency is not satisfied, which will lead to a lower SE when high M -ary schemes are used according to Table 2.1. This case was discussed in [67] when applying IM in the frequency domain on the OFDM sub-carriers. Hence, the frequency IM domain is a special case of the proposed filter index modulation without a noticeable SE enhancement.

Finally, for a proper filter shape design, we have to jointly minimize the injected ISI distortion on the transmitted symbols and the cross-correlation between all filters of the bank while keeping the highest possible bandwidth ($B \approx B_c$).

4.3.4 Theoretical performance analysis

In this sub-section, the probability of error for the filter index is evaluated, then the SER and the total BER is deduced to truly characterize the FSIM system performance. Note that both proposed detectors (MF and joint ML) achieve similar performance (negligible difference), as it will be shown in the next section. For this reason, the low complexity MF-based detector is only considered in the following theoretical derivations.

The probability of error for filter index pilots the system performance because the error in filter detection leads to an additional ISI and thus more errors can appear in the detection of APM symbols.

For each symbol period, the input to matched filter detector is the L samples as expressed in (4.13). In the following, we will assume that the filter bank is well designed where the ISI is perfectly canceled (*i.e.*, $ISI_{resid} = 0$). Hence, the probability of error that will be derived can be considered the lower bound of the proposed system.

The output of the matched filter bank sampled at $t = T_f$ given by r_k in (4.9) can be rewritten as:

$$r_k = \langle \mathbf{f}_k, \mathbf{f}_{i_n} \rangle \cdot c_n + \langle \mathbf{f}_k, \mathbf{v}_n \rangle = \begin{cases} c_n + \langle \mathbf{f}_k, \mathbf{v}_n \rangle & \text{for } k = i_n \\ \langle \mathbf{f}_k, \mathbf{f}_{i_n} \rangle \cdot c_n + \langle \mathbf{f}_k, \mathbf{v}_n \rangle & \text{for } k \neq i_n \end{cases} \quad (4.15)$$

Note that when the N filters are orthogonal $\langle \mathbf{f}_k, \mathbf{f}_i \rangle = 0$, the system will be transformed into frequency band indexation, which results in a limited SE enhancement. However, in our proposed system, the filters are not orthogonal because they occupy the same bandwidth, and they have the same center frequency to target a more significant SE enhancement.

To evaluate the probability of error, let us suppose that the filter f_1 is selected at the transmitter side for the APM symbol c_n . Then, the vector \mathbf{r}_k composed of the elements r_k for $k = 1, \dots, N$ is given as follows:

$$\mathbf{r}_k = [c_n + v_1, \langle \mathbf{f}_2, \mathbf{f}_1 \rangle \cdot c_n + v_2, \dots, \langle \mathbf{f}_N, \mathbf{f}_1 \rangle \cdot c_n + v_N], \quad (4.16)$$

where $v_k = \langle \mathbf{f}_k, \mathbf{v}_n \rangle$ are complex valued zero-mean mutually statistically independent Gaussian random variables with equal variance $\sigma^2 = \sigma_k^2 = \frac{1}{2}N_0$, where N_0 is the noise spectral density [203]. According to (4.10), the detection of the filter index selects the maximum $U_k = \|r_k\|^2$ which represents the energy of r_k . U_k is described as a statistically independent non-central chi-square distribution [203] for all k , each having 2 degrees of freedom where the non-centrality parameter α^2 with the energy of APM symbol \mathcal{E}_q is given by:

$$\alpha_{k,q}^2 = \begin{cases} \|c_n\|^2 = \mathcal{E}_q & \text{for } k = 1 \\ \langle \mathbf{f}_k, \mathbf{f}_1 \rangle^2 \cdot \|c_n\|^2 = \langle \mathbf{f}_k, \mathbf{f}_1 \rangle^2 \cdot \mathcal{E}_q & \text{for } k \neq 1, \end{cases} \quad (4.17)$$

where \mathcal{E}_q is the energy of the transmitted APM symbol c_n . Thus, we obtain the PDF of U_k as

$$p(u_k) = \frac{1}{2\sigma^2} e^{-\frac{u_k + \alpha_k^2}{2\sigma^2}} \mathcal{I}_0 \left(\frac{\alpha_k \sqrt{u_k}}{\sigma^2} \right), \quad (4.18)$$

where $u_k \geq 0$ and $\mathcal{I}_0(\rho)$ is the zero order modified Bessel function of 1st kind given by [203]:

$$\mathcal{I}_0(\rho) = \sum_{\beta=0}^{\infty} \frac{(\rho/2)^{2\beta}}{(\beta!)^2} \rho \geq 0. \quad (4.19)$$

The error probability of the filter index can be deduced by deriving the probability that the detector makes a correct index decision. This is the probability that u_1 is larger than all other $N - 1$ u_k values for $k \neq 1$. This probability of correct decision for a given APM symbol energy \mathcal{E}_q may be expressed as:

$$P_{c,\mathcal{E}_q} = P(U_2 < U_1, U_3 < U_1, \dots, U_N < U_1) = \int_0^{\infty} P(U_2 < U_1, \dots, U_N < U_1 | u_1) \cdot p(u_1) du_1 \quad (4.20)$$

where $P(U_2 < U_1, U_3 < U_1, \dots, U_N < U_1 | U_1)$ denotes the joint probability that u_2, u_3, \dots, u_N are all less than u_1 conditioned on a given u_1 . Then this joint probability is averaged over all u_1 . The filters are considered orthogonal when deriving the lower bound, thus these $N - 1$ variables u_k becomes statistically independent under this assumption with chi-square distribution ($\alpha_{k,q}^2 = 0$ for $k \neq 1$). Since the u_k are statistically independent, the joint probability can be factorized as a product of $N - 1$ marginal probabilities of the form:

$$P(u_k < u_1 | u_1) = \int_0^{u_1} p_{u_k}(x_k) dx_k, \quad k = 2, 3, \dots, N. \quad (4.21)$$

Thus, the probability of a correct decision is given by:

$$P_{c,\mathcal{E}_q} = \int_0^\infty \left(\prod_2^N P(u_k < u_1 | u_1) \right) \cdot p(u_1) du_1 \quad (4.22)$$

and the probability of a filter index error with a given APM symbol energy \mathcal{E}_q is as follows:

$$P_{e,\mathcal{E}_q} = 1 - P_{c,\mathcal{E}_q}. \quad (4.23)$$

Hence, the average probability of filter index error is the weighted average of filter error over the Q possible energy levels of APM symbols, given as follows:

$$P_{e,filter} = \sum_{q=1}^Q P_{e,\mathcal{E}_q} \cdot P(\mathcal{E}_q), \quad (4.24)$$

where $P(\mathcal{E}_q)$ is the probability of occurrence of the energy level \mathcal{E}_q . For example, when the used APM is 16-QAM, there are $Q = 3$ possible energy levels $\mathcal{E}_q = [0.2, 1, 1.8]$ and their probability of occurrence is $P(\mathcal{E}_q) = [0.25, 0.5, 0.25]$ if all APM symbols are equiprobable.

An erroneous detection of a filter index leads to the attempt of APM demodulation using the signal output of an mismatched filter with more ISI most probably. Thus, the total probability of APM symbol error $P_{e,APM}$ in FSIM system can be written according to the law of total probability as follows:

$$\begin{aligned} P_{e,APM} &= P_{(APM \text{ error} \cap \text{correct filter})} + P_{(APM \text{ error} \cap \text{false filter})} \\ &= (1 - P_{e,filter}) P_{(APM \text{ error} / \text{correct filter})} + P_{e,filter} P_{(APM \text{ error} / \text{false filter})}, \end{aligned} \quad (4.25)$$

where $P_{APM \text{ error} / \text{correct filter}}$ ($P_{APM \text{ error} / \text{false filter}}$) is the probability of APM symbol error knowing that the filter index is correctly estimated (mis-detected). Hence, we are deriving the lower bound under the perfect ISI cancellation assumption, then the probabilities of APM symbol error in both cases are equal to the probability of APM symbol error in conventional transceiver with Nyquist filters.

Consequently, the correct FSIM symbol detection occurs when both the filter and the APM symbol are correctly estimated, then the probability of a correct FSIM decision is $(1 - P_{e,filter})(1 - P_{e,APM})$ and the SER is given by:

$$SER = 1 - (1 - P_{e,filter})(1 - P_{e,APM}). \quad (4.26)$$

The average probability of virtual (real) bit error can be deduced from filter (APM symbol) error similar to [203, p. 262 (5-2-24)], thus they can be expressed respectively as follows:

$$P_{b,filter} = \frac{N}{2(N-1)} P_{e,filter} \quad (4.27)$$

$$P_{b,APM} = \frac{M}{2(M-1)} P_{e,APM}, \quad (4.28)$$

Similarly to SER, the total BER is deduced but while taking into consideration the weight of real and virtual bits:

$$BER = \frac{\log_2 N}{\mathcal{L}_{FSIM}} P_{b,filter} + \frac{\log_2 M}{\mathcal{L}_{FSIM}} P_{b,APM}. \quad (4.29)$$

Finally, we should mention that the cross-correlation between all filters affects the proposed system's performance and should be minimized to enhance the system performance. Besides, the introduced ISI by all filters should also be minimized to approach the lower bound of the error probability for the filter index that affects the APM symbols' detection. This probability confirms that the proposed system's success is based on the filter bank design where the cross-correlation of these filters and their introduced ISI should be jointly minimized. Finally, these theoretical lower bound for error probabilities of filter index detection and BER are validated in the next section.

4.3.5 Numerical results analysis and discussions

In this section, firstly, the theoretical error probability of filter index detection (4.24) using the MF-based detector is evaluated and compared to the numerical results obtained with Monte Carlo simulations under different configurations. Secondly, the performance of the proposed system is evaluated when a joint ML and an MF-based detector are employed and compared at different transmission rates to the theoretical lower bound (4.29) and to the performance of the equivalent APM scheme of the same SE in AWGN channel and a multipath frequency-selective fading channel.

It is worth mentioning that the filter bank design of N filter shapes is not a trivial problem with these new constraints and conditions. For this reason, we designed 2 and 4 non-optimal filter shapes to prove the feasibility of the proposed scheme and to illustrate the minimum performance gain and SE enhancement that can be achieved. The impulse responses of the two filters are presented in Fig. 4.4, and their magnitude and phase responses are shown in Fig. 4.5 and 4.6. Note that the dot product of these filters is $\langle \mathbf{f}_1, \mathbf{f}_2 \rangle = 0.2057$. Moreover, the complete filter responses at the receiver, after correct

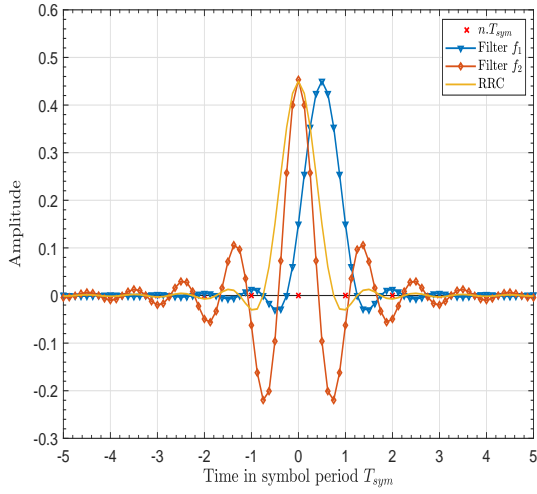


Figure 4.4 – Impulse Response for the two filters used in our simulations compared to RRC pulse shaping filter, where $\eta = 10$ and $\lambda = 8$.

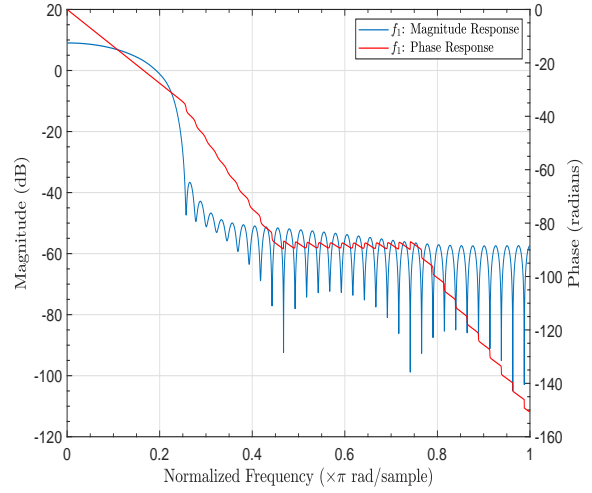


Figure 4.5 – Magnitude and phase response of the filter f_1 depicted in Fig. 4.4.

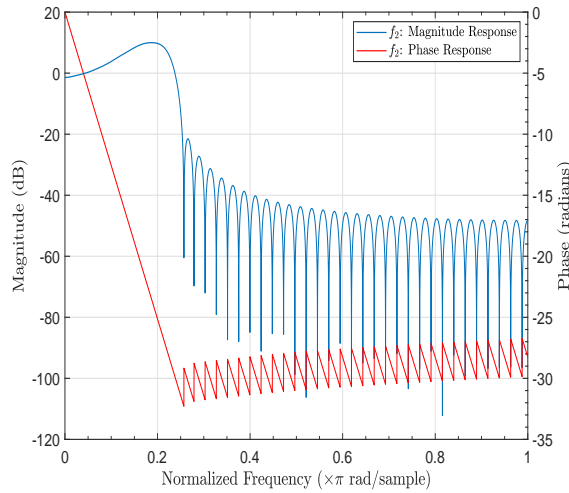


Figure 4.6 – Magnitude and phase response of the filter f_2 depicted in Fig. 4.4.

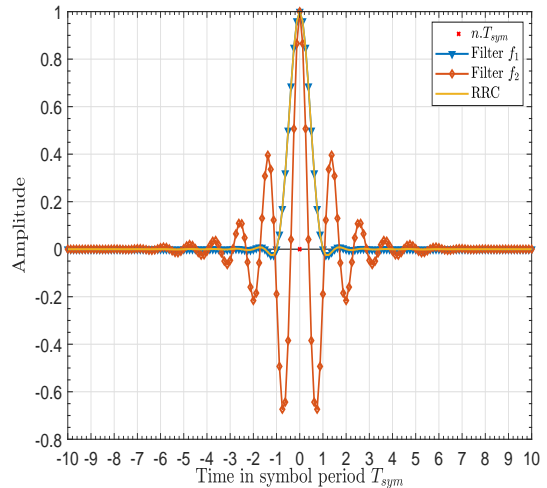


Figure 4.7 – Complete responses of the 2 filters obtained after correct matched filtering at the receiver side, where $\eta = 10$ and $\lambda = 8$.

matched filtering ($\mathbf{f}_i * \mathbf{g}_i$) are depicted in Fig. 4.7. The introduced ISI clearly appears in f_2 because the result of $\mathbf{f}_2 * \mathbf{g}_2$ doesn't have a zero-crossing at $t = n.T_{sym}$ for all n .

The proposed system is studied at different transmission rates (3 to 7 bits/symbol) by using different numbers of filter shapes and different QAM orders. The used simulation parameters are summarized in Table 4.1.

Figure 4.8a and 4.8b compare the theoretical lower bound (4.24) and simulated probabilities of error of filter index detection with perfect ISI cancellation, and with ISI estimation and cancellation as

Table 4.1 – Simulation parameters

Parameters	Value
M -ary QAM	[4, 8, 16, 32, 64]
Number of filters N	[2, 4]
η	10
Oversampling factor: λ	8
Number of symbols	5×10^5
Pulse shaping filter for Conventional Transceiver	RRC

described in subsection 4.3.2.3. Note that perfect ISI cancellation means that the tentative decisions for filter index and APM symbol are correctly detected, but those decisions for past symbols are fed back after the final detection. This comparison is performed with $N = 2$ filters and different M -ary QAM where the notation N -FSIM-MAPM is adopted for our proposed system's performance analysis.

It can be observed from Figs 4.8a-4.8b that the theoretical lower bound (4.24) derived under the assumption of perfect ISI cancellation and orthogonal filters matches the simulation results of perfect ISI cancellation with a small difference due to non-orthogonal filters (dot-product is 0.2057), and thus the theoretical lower bound is validated. In addition, the performance of 2-FSIM-QPSK with ISI estimation is near the optimal ISI cancellation as shown in Fig. 4.8a, because QPSK can support a high ISI level without leading to a false detection (high minimum distance d_{min} between constellations), so a better ISI estimation and cancellation are achieved. Similarly, this probability with ISI estimation and cancellation using 2-FSIM-8QAM and 2-FSIM-16QAM is very tight to the lower bound at low Signal-to-noise Ratio (SNR) values, while the gap between them increases at high SNR values due to the residual ISI. In addition, it is clear that this degradation due to residual ISI is more important with higher M -ary QAM as shown with 2-FSIM-32QAM in Fig. 4.8b. This can be justified by the fact that higher M -ary QAM schemes are more sensitive to ISI (smaller d_{min}) compared to QPSK.

Note that the two used filter shapes satisfy all the filter bank design requirements mentioned in subsection 4.3.3, but they are not the optimal filters. Thus, the performance of FSIM can become tighter to the lower bound when the filter's bank shapes are optimally designed. Hence this analytical bound is a helpful indicator for evaluating the performance of the proposed system.

In the following, the proposed FSIM system is compared to the conventional transceivers under different configurations but with same SE. The BER of these systems as function of the average SNR is evaluated using Monte Carlo Simulations and theoretical lower bound according to (4.29). The comparison in Figs. 4.9a-4.10b is performed with ISI estimation and cancellation under an AWGN channel with MF and joint ML detectors. It should be highlighted that the theoretical BER lower bound (4.29) and the simulated BER with perfect ISI cancellation are very tight, and they are represented by a single curve named FSIM lower bound in Fig. 4.9a-4.10b. In addition, these figures show that the performance with the MF detector is very tight to that with the joint ML detector but with an

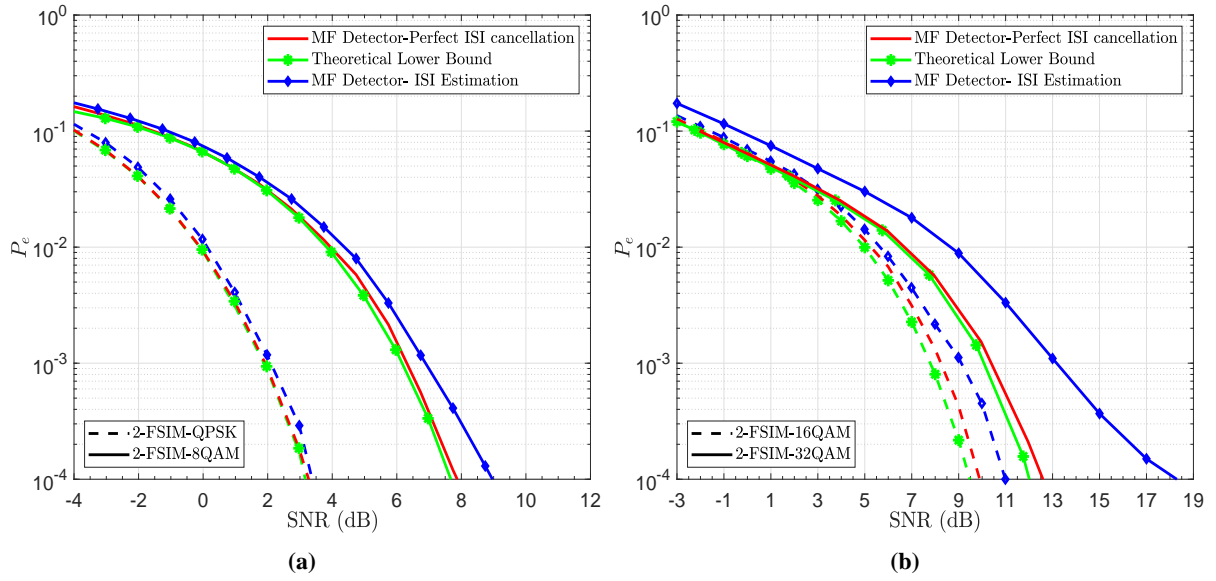


Figure 4.8 – The error probabilities of filter index detection with ISI estimation and cancellation, perfect ISI cancellation, and the derived theoretical lower bound, $N = 2$ (2-FSIM- M QAM). The SE is: (a) [3, 4] bits/symbol using $M = [4, 8]$, (b) [5, 6] bits/symbol using $M = [16, 32]$.

extremely lower complexity. The propagation of error issue is clearly appearing in Fig. 4.10b using both detectors (or any other) which is due to residual ISI from the error in tentative and feedback decisions in the preceding block for ISI estimation and cancellation. Thus, the error propagation is an issue with any detector, and it can be minimized by optimal filter design that allows mainly the correct tentative decisions.

In order to conduct a fair comparison, the performance of the proposed system is compared to an equivalent conventional transceiver (M -ary QAM scheme with RRC filter) of the same SE. The system 2-FSIM-QPSK is depicted in Fig. 4.9a, where an important SNR gain of 3.8 dB is obtained at $\text{BER} = 10^{-4}$ compared to the equivalent 8QAM scheme. Accordingly, for the same BER performance, the SE enhancement by 1 bit/symbol requires an additional 0.9 dB only to the required SNR of QPSK. However, for the same SE enhancement with respect to 8QAM and 16QAM, an additional 2 dB is required with 2-FSIM-8QAM and 2-FSIM-16QAM as shown in Figs. 4.9b and 4.10a respectively. While the higher-order equivalent schemes as 16QAM and 32QAM need an additional 2.2 dB and 3.1 dB respectively instead of 2 dB with 2-FSIM-8QAM and 2-FSIM-16QAM. It is worth mentioning that a higher SNR gain is achieved when the proposed system, using two filters, is applied to a square QAM, so this system allows us to avoid the inherited performance degradation of non-square QAM by using FSIM with the lower square M -ary QAM order. In other words, as depicted in Fig. 4.9b the system 2-FSIM-8QAM has a smaller SNR gain due to the fact that the SNR gap between the performance of the non-square constellations of 8QAM and that of 16QAM is small for the same BER performance.

It is worth mentioning that these FSIM schemes are able to achieve SE and EE gain even with non-optimal filters compared to conventional APM schemes. In addition, this superiority is maintained

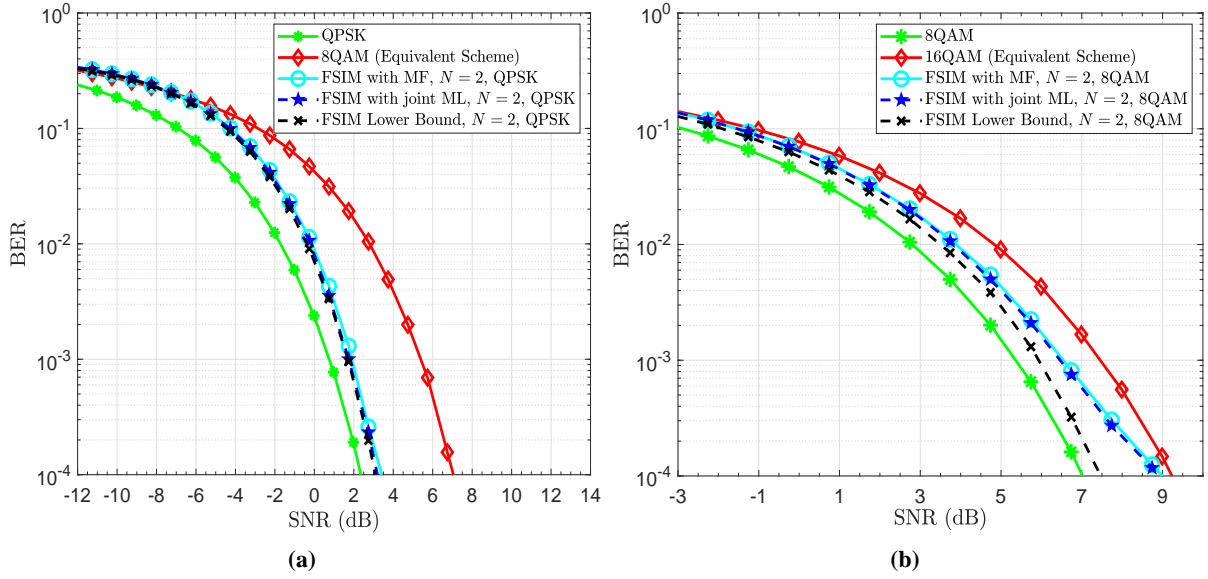


Figure 4.9 – Uncoded BER performance of 2-FSIM-MQAM, its analytical lower bound and its equivalent scheme $2MQAM$ of the same SE: (a) 3 bits/symbol using $M = 4$, (b) 4 bits/symbol using $M = 8$.

when the FSIM is compared to existing single and dual-mode SISO-IM schemes of worse EE due to the need of higher power to maintain the same SE by using larger M -ary and/or to detect the transmitted VBs (see [164] and references therein).

For further analysis of the proposed scheme, the results with higher-order APM as 2-FSIM-32QAM and 2-FSIM-64QAM are presented in Fig. 4.10b, where their performance with ISI estimation and cancellation starts to degrade compared to equivalent schemes 64QAM and 128QAM respectively at high SNR values. It can be noticed that at low SNR, the performance of the proposed systems with high M -ary APM is better than their equivalent schemes. An error floor appears with the higher-order M -ary APM caused by the residual ISI not completely mitigated by the receiver, and which has been induced by the non-optimal filters being used.

However, the BER of the latter two schemes with perfect ISI cancellation is very tight to the performance of 32QAM and 64QAM, respectively, while enhancing the SE by 1 bit. Hence, this maximum achievable performance shows that there is always room for future improvements by designing an optimal filter bank and proposing better ISI mitigation techniques.

The spectrum of the conventional transceiver and the 2-FSIM-MQAM are compared in Fig. 4.11. It can be observed that most of the emitted power of both systems are concentrated on the same bandwidth. However, the OOB radiations of the proposed system is 10 dB higher than that of a conventional transceiver due to the fact the used filter f_2 has higher OOB radiation compared to f_1 and RRC filters. Hence, the OOB radiation will be considered in the future filter bank design to be kept as low as possible.

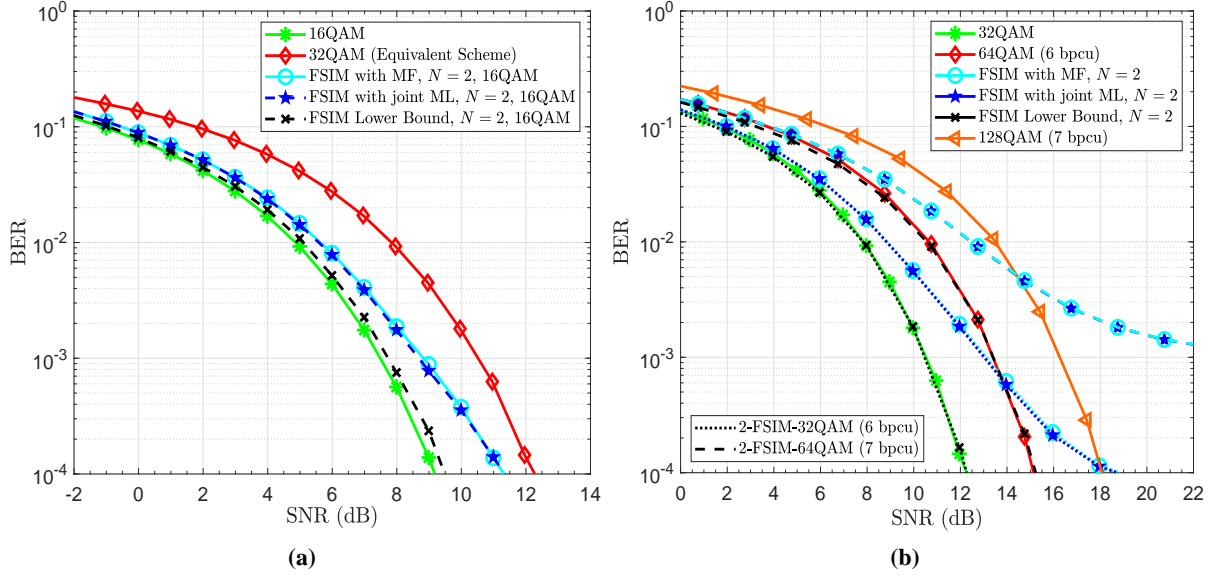


Figure 4.10 – Uncoded BER performance of 2-FSIM-MQAM, its analytical lower bound and its equivalent scheme 2MQAM of the same SE: (a) 5 bits/symbol using $M = 16$, (b) 6 and 7 bits/symbol using $M = 32$ and $M = 64$ respectively.

By considering the filter bank design requirements mentioned in sub-section 4.3.3, a set of $N = 4$ filters is designed by using η and λ as mentioned in Table 4.1, and the complete filter response is depicted in Fig. 4.12. The mean of the signal to the introduced ISI power ratio for all possible filter sequence permutations is 26.29 dB, and the dot-product symmetric matrix between these non-optimal filters is:

$$\Xi = \begin{bmatrix} 1 & 0.7615 & 0.7284 & 0.334 \\ 0.7615 & 1 & 0.6376 & 0.0887 \\ 0.7284 & 0.6376 & 1 & 0.67 \\ 0.334 & 0.0887 & 0.67 & 1 \end{bmatrix} \quad (4.30)$$

The results using these 4 filters with QPSK and 16QAM is depicted in Fig. 4.13a and Fig. 4.13b, where 4-FSIM-QPSK (4-FSIM-16QAM) has 1.7 (2.2) dB gain compared to its equivalent scheme 16QAM (64QAM). Note that 4-FSIM-QPSK (4-FSIM-16QAM) requires 3.9 (3.6) dB more than its lower bound due to high dot-product between some filters.

After presenting these encouraging FSIM scheme results, its BER vs E_s/N_0 (E_s is the energy per symbol) is evaluated and compared in a frequency selective fading channel to the competitors SC schemes in single and dual-mode. A Rayleigh fading channel is considered with J -paths of an integer multiple of symbol period delays, and the MMSE-FDE is used for all schemes of the same SE (DM-SC-IM, SC-TIM and their Reduced Correlation (RC) versions with interleaver [66]). Note that the optimal joint ML detector is used for these schemes, while a MF-based detector of lower complexity is used for FSIM. The frame setup in symbol length is: $N_s = 1015$, $N_{ZP} = N_{CP} = 9$, and the schemes' configuration, to have average SE ≈ 3 bits/symbol, are: (RC-)SC-TIM: $M = 16$, $N_a = 3$, $N_g = 5$, $G =$

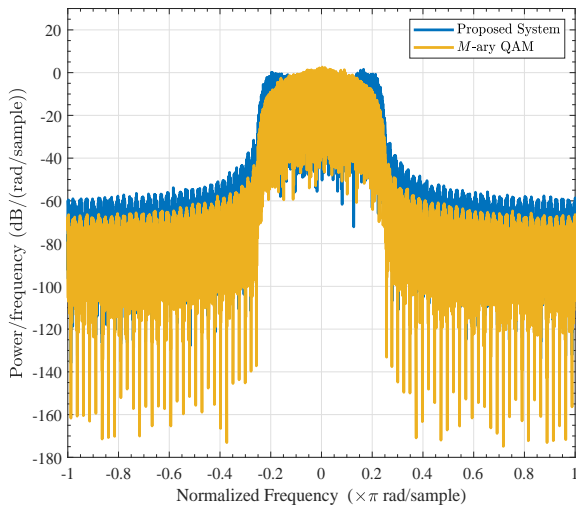


Figure 4.11 – Spectrum comparison between the proposed FSIM system with 2 non-optimal filters and the conventional transceivers with QAM and RRC filters.

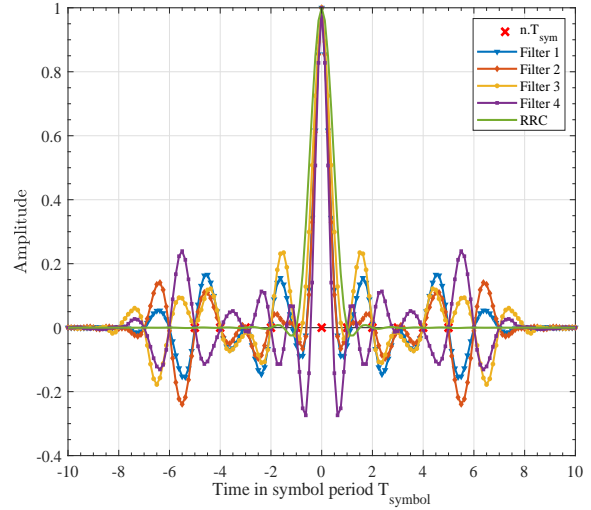
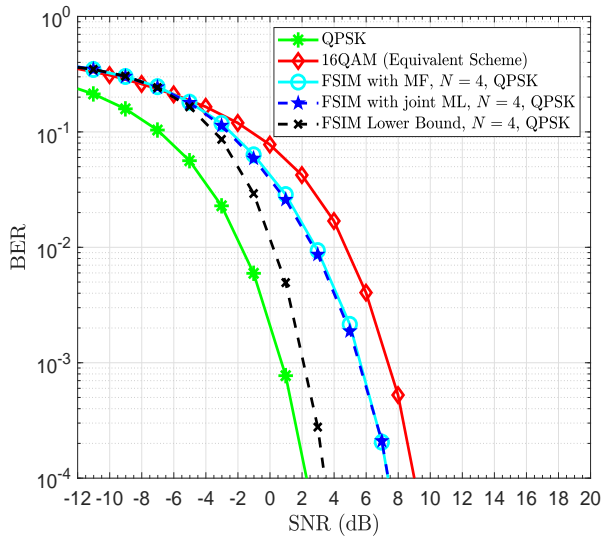
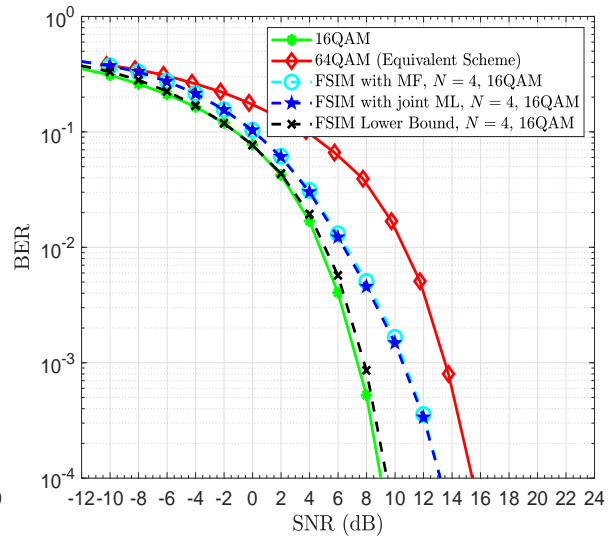


Figure 4.12 – Complete responses of the 4 filters obtained after correct matched filtering at the receiver side, where $\eta = 10$ and $\lambda = 8$.



(a)



(b)

Figure 4.13 – Uncoded BER performance of 4-FSIM-MQAM, its analytical lower bound and its equivalent scheme 4MQAM of the same SE: (a) 4 bits/symbol using $M = 4$, (b) 6 bits/symbol using $M = 16$.

203, (RC-)DM-SC-IM : $M_A = 8$, $M_B = 4$, $N_a = 2$, $N_g = 5$, $G = 203$, and FSIM: $M = 4$, $N = 2$. Figs. 4.14a-4.14b show clearly that FSIM with ISI estimation and cancellation outperforms all other schemes with a minimum gain of 6 dB (4.2 dB) compared to the second-best scheme Reduced Correlation Single Carrier with Time Index Modulation (RC-SC-TIM) in Rayleigh selective channel with $J = 2$ ($J = 4$).

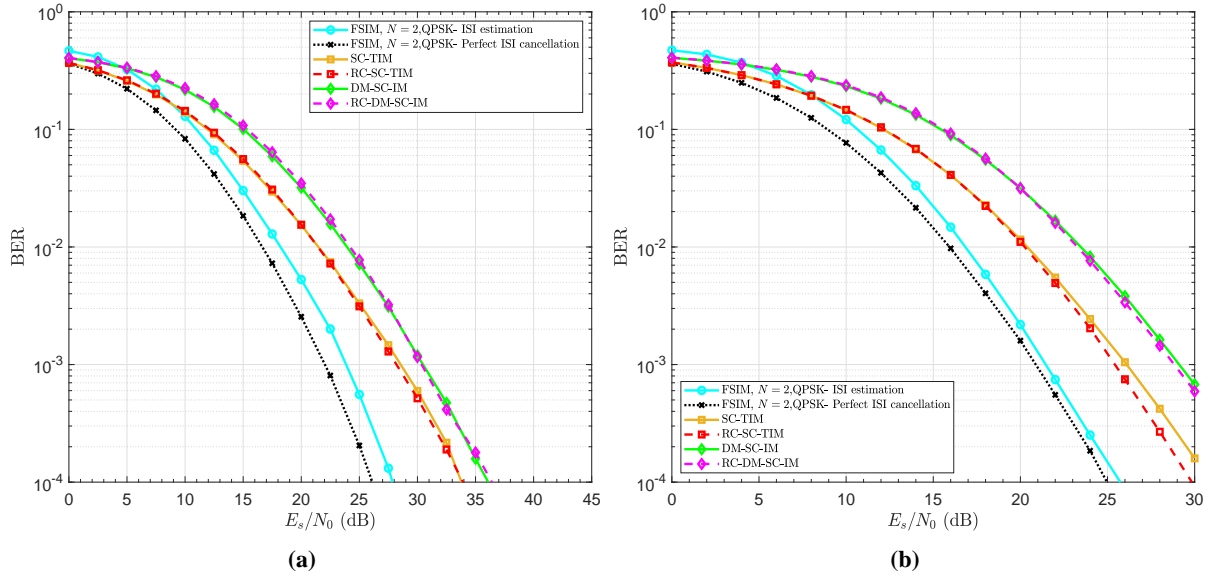


Figure 4.14 – Average BER comparison of different SC schemes with IM in a frequency selective Rayleigh fading: (a) $J = 2$, (b) $J = 4$.

Furthermore, we would like to mention that the proposed system can achieve a better performance and a higher EE gain by using optimal filter bank satisfying the requirement mentioned in sub-section 4.3.3.

4.3.5.1 FSIM vs Media-Based Modulation (MBM)

In this chapter, we proposed a novel domain for IM based on filter dimension that generalizes many existing modulations and IM domains, and we focused on SISO mode SE enhancement by proposing FSIM. In the following, SISO-MBM reviewed in Section 2.4.3 is considered for a fair comparison with our proposed scheme in current stage and according to [140] the main similarities/differences are extracted and summarized as follows:

- FSIM uses N filter shapes to convey $\log_2(N)$ additional information bits, while MBM uses $N_{RF\ mirrors}$ RF mirrors to generate different channel states and convey $N_{RF\ mirrors}$ additional information bits as long as the independence of the generated radiation patterns is guaranteed.
- For high data rates system, the design of SISO-MBM schemes with such high number of RF mirrors (different states) is a challenging research problem because it needs to jointly optimize the radiation-related parameters, such as reflection coefficient, antenna gain, radiation efficiency, and so on. Similarly, FSIM is facing a challenging research problem to design a large filter bank that satisfies the requirements highlighted in sub-section 4.3.3.

- FSIM is not based on any channel condition, whereas MBM requires rich scattering environment (Non Line-of-Sight (LoS) Rayleigh Channel) and it is very challenging task in LoS scenario to obtain sufficiently independent fade realizations for MBM systems [140].
- In contrary to FSIM, SISO-MBM has an inherent diversity gain due the superposition of the same transmitted symbol from the different reflections caused by $N_{RF\ mirrors}$ RF mirrors. Note that SISO-MBM allows using a single RF chain while achieving some diversity gain, and it is very similar in SE enhancement to ExSSK [113] with the number of transmit antennas $N_t = N_{RF\ mirrors}$.
- For the same spectral efficiency, MBM provides a significantly better error performance compared to traditional M -ary modulated systems since the Euclidean distance between MBM constellation points, which are random fade realizations, remains the same even with increasing spectral efficiency values. The advantage of MBM further increases for higher order constellations and a higher number of receive antennas [140]. However, this gain is achieved only where more than one receive antenna (SIMO mode) is used as shown in Fig. 4 of [140] and it is one of the main listed disadvantages that states the MBM performance is not satisfactory for a small number of receive antennas. Whereas the results of FSIM shows that a significant gain is achieved even using non-optimal filters in SISO mode especially with low order modulations.
- FSIM requires the channel estimation using limited number of pilots or training sequence only with any number of filters, whereas the main shortcomings of the MBM system is the excessive channel sounding burden. In order to obtain the CSI, the receiver has to be trained with pilot signals from all possible antenna states, that is, $2^{N_{RF\ mirrors}}$ test signals are required for a single reconfigurable antenna.
- MBM comes with challenging design and practical implementation difficulties. A high number of sufficiently different radiation patterns is not a straightforward task. Similarly, FSIM in the current stage of research comes with a challenging design difficulty for high number of filters.
- MBM is a linear time varying system that can expand the spectrum [142]. In addition, the antenna pattern switching between different signaling intervals may cause spectral growth due to the discontinuity in the band-limited MBM signal. However, this problem is not faced in filter domain IM in general and in FSIM.
- The possible high correlation among different radiation patterns (fade realizations) that make them indistinguishable at the receiver may become the Achilles' heel of MBM-based systems by limiting the achievable performance. Note that an accurate and a realistic mathematical correlation models to quantify the different fade realizations is still not available. However, this problem is not faced with FSIM where a very small correlation can be achieved, but it may limits the possible number of filters (the possible SE gain) that satisfy the requirements highlighted in the filter requirements sub-section 4.3.3.

4.3.6 Conclusions

Index Modulation is explored mainly in the spatial, temporal and frequency domain. In this section, we propose a novel domain for IM, named the “Filter domain” and a novel scheme “Filter Shape Index Modulation” where the index of the filter is used at the transmitter to convey additional information bits and enhance the SE by $\log_2 N$. Note that this domain allows a SE enhancement by at least 1 bit/s/Hz in contrast to the existing SISO-IM schemes (mainly not multi-domain IM scheme) where their maximum enhancement is limited to 0.6 bit/s/Hz or less according to Table 2.1 with feasible system configuration.

This novel domain is investigated by proposing the FSIM system, where a bank with different filter’s shapes is used. In addition, the joint ML detector that detects the filter index and the transmitted APM symbol is presented. Then, a low complexity optimal detection scheme based on Matched filter is proposed. Moreover, an ISI cancellation process is proposed due to the fact that FSIM introduces a controlled ISI. Note that the proposed system can be reconfigured to be as a conventional transceivers by using same Nyquist filter for all symbols.

The theoretical lower bounds for filter error probability and BER are derived and the analysis validates the achieved performance using the proposed FSIM approach. Monte Carlo simulations showed that the FSIM-QPSK system with 2 and 4 non-optimal filters offers, at BER= 10^{-4} and same SE, a gain of 3.8 dB and 1.7 dB as compared to their equivalent systems 8QAM and 16QAM, similarly 4-FSIM-16QAM achieves a gain of 2.2 dB. It is worth mentioning that FSIM maintains its superiority in a frequency selective multipath channel compared to existing SC SISO-IM schemes where the former achieves a minimum gain of 4 to 6 dB. Thus, the proposed scheme demonstrates that ISI is not necessarily undesirable while it is controllable and predictable, since it permits to achieve a higher system capacity compared to systems that enforce zero interference. Finally, it can be concluded that FSIM scheme can achieve even higher SE after designing a larger filter bank (higher N), and it is useful for ultra-high rate wireless communication. In the next section, our second filter IM scheme is proposed.

4.4 Quadrature Filter Shape Index Modulation (IQ-FSIM)

4.4.1 Introduction

In the previous Section 4.2 and [22], the filter IM domain is proposed where any filter property at the transmitter side can be indexed, whenever the receiver can detect this property. The filter IM domain generalizes most of existing SISO-IM and several existing modulations schemes as shown in Section 4.2 (Section II in [22]). In addition, a novel scheme named FSIM is proposed in Section 4.3 where different filter shapes can be selected on each symbol period at the transmitter side to convey VB by means of IM, and it allows to reach a higher SE and EE gain in SISO in contrast to most SISO-IM schemes.

In this section, a novel IQ-FSIM is proposed for further SE and EE enhancement compared to the equivalent conventional APM, and FSIM that achieves the best gain compared to existing SISO-IM schemes.

The main contributions of this section can be summarized as follows.

1. Within the filter IM domain/dimension, a novel modulation scheme named IQ-FSIM is proposed. In contrast to FSIM, the pulse shaping filters for the In-phase (I) and Quadrature (Q) components are indexed separately to convey the double of virtual information bits, and in addition to those transmitted in the APM symbols. The bits in IQ-FSIM are mapped into both traditional signal domain (any M -ary APM) and filter IM domain. This scheme generalizes the previously proposed FSIM [22] which in turn generalizes the most of SISO-IM schemes in frequency and time IM domains. By considering different filter shapes at each symbol period at the transmitter and the separate indexation on I and Q, a higher EE and SE is enabled by this scheme.
2. The IQ-FSIM transceiver system model is presented along with two different detectors. The joint Maximum Likelihood (ML) detector is presented where a joint detection of APM symbols and both filter shapes' index on I and Q is performed. Subsequently, the IQ-FSIM detector based on MF is proposed to achieve the optimal performance while providing lower complexity. The latter estimates firstly the filter shapes on I and Q in parallel, and then detects the APM symbols in contrast to the MF-based detector for FSIM in section 4.3.2.2.
3. The previously proposed ISI estimation and cancellation for FSIM that eliminates the effect of the introduced ISI by the designed filter shapes, is modified to consider the different filter shapes on I and Q.
4. The theoretical lower bounds for the total Symbol-Error Rate (SER), BER and filter error probability are derived to evaluate the proposed IQ-FSIM scheme that can use different shapes on I and Q in contrast to FSIM scheme. Then, these analytical expressions are compared and validated by Monte Carlo simulations. Furthermore, different simulations are provided to show the tremendous EE and SE gain achieved by the proposed IQ-FSIM compared to the equivalent conventional APM scheme.
5. The performance of IQ-FSIM and the previously proposed FSIM are compared at the same SE using theoretical and numerical results with the currently designed filters. The results highlight that IQ-FSIM allows reaching a higher EE due to the lower modulation scheme order or the number of filters, especially when the larger filter bank is not optimally designed.

4.4.2 IQ-FSIM Transmitter System model

The proposed IQ-FSIM transceiver in SISO system is depicted in Fig. 4.15, where the initial bit-stream b is divided into three streams b_1 , b_2^I , and b_2^Q . The bitstream b_1 is mapped by the M -ary APM, such

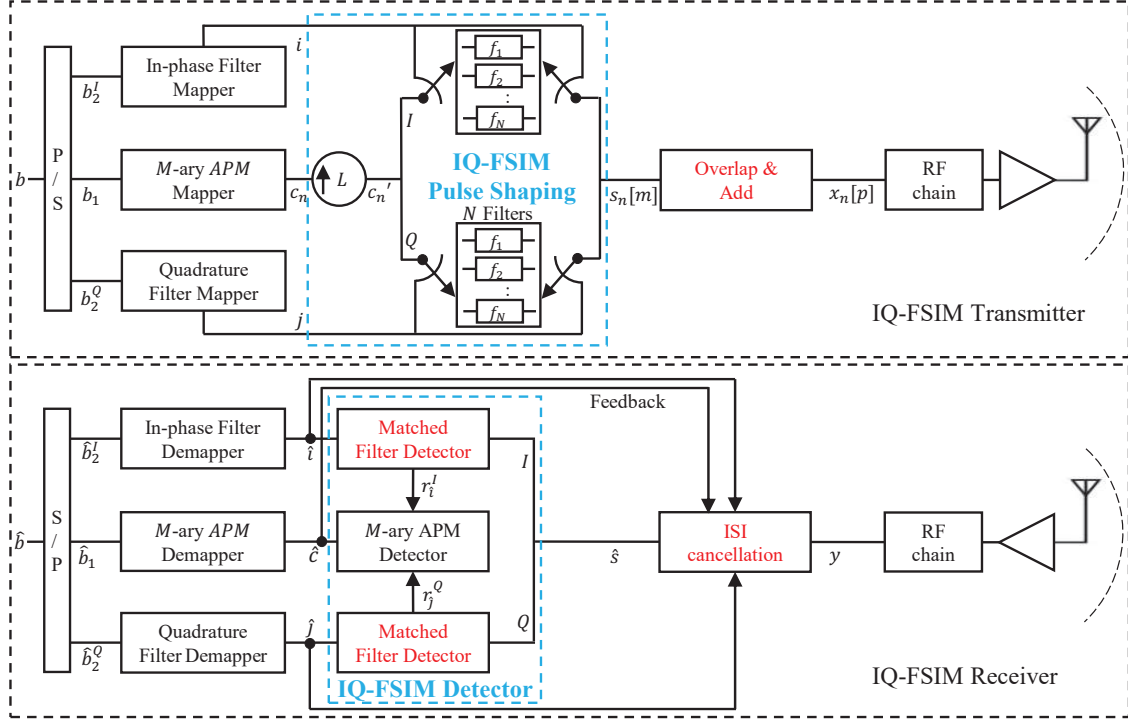


Figure 4.15 – System model of the IQ-FSIM based transceiver with MF-based detector using N filters of length L and M -ary APM. Note that the joint ML detector can replace the IQ-FSIM detector.

as QAM or PSK, etc. Whereas, the bitstreams b_2^I and b_2^Q are encapsulated in the indices i and j of the selected filters at the I and Q components, respectively. Note that i and j are not necessarily the same in contrast to FSIM [22] that uses the same filter on I and Q. These filters $\mathbf{f}_i[m]$ and $\mathbf{f}_j[m]$ are used also as pulse shaping for I and Q components respectively, where the sample index is $m = 0, 1, \dots, L - 1$, and L is the filter length. The filter is truncated in the time domain to η APM symbols and sampled with a rate λ samples per symbol, which yield $L = \eta \cdot \lambda + 1$ samples.

Similar to FSIM scheme, the filter bank in Fig. 4.15, contains N different filter shapes where N is a power of 2. Hence, the number of bits per IQ-FSIM symbol $\mathcal{L}_{\text{IQ-FSIM}}$ can be expressed as:

$$\mathcal{L}_{\text{IQ-FSIM}} = 2 \log_2 N + \log_2 M. \quad (4.31)$$

Thus, the SE enhancement is $2 \log_2(N)$ compared to conventional M -ary APM systems, and it is the double of previous enhancement by FSIM because IQ-FSIM performs the filter indexation separately on I and Q at each symbol period.

The filter bank's output on I and Q branch for the n -th APM complex symbol c_n are denoted respectively by signals $s_n^I[m]$ and $s_n^Q[m]$ given as follows:

$$s_n^I[m] = (f_{i_n} * \Re\{c_n'\})[m] = c_n^I f_{i_n}[m] \quad (4.32)$$

$$s_n^Q[m] = (f_{j_n} * \mathfrak{I}\{c'_n\})[m] = c_n^Q f_{j_n}[m] \quad (4.33)$$

where c'_n is an up-sampled version of $c_n = c_n^I + j c_n^Q$ by a factor L with $j = \sqrt{-1}$, i_n and $j_n \in \{0, 1, \dots, N-1\}$ are the index of the filter being selected at I and Q for the n^{th} symbol according to the bit-stream b_2^I and b_2^Q respectively. Then, the complex signal $s_n[m]$ is deduced by combining both components $s_n[m] = s_n^I[m] + j s_n^Q[m]$.

Afterward, the OLA block generates the λ samples for each APM symbol by using their signals $s_n[m]$, as depicted in Fig. 4.15. The λ corresponding samples for the n^{th} APM symbol c_n is given by $x_n[p]$ as in (4.3).

Similar to FSIM scheme, the traditional transceiver with Nyquist pulse shaping (e.g., RRC) and any M -ary APM schemes remains a special case of the proposed IQ-FSIM system (see Appendix D). This reconfiguration of IQ-FSIM system is done by using the same Nyquist filter for all symbols on I and Q.

4.4.3 IQ-FSIM Receiver System model

The proposed IQ-FSIM receiver is represented in Fig. 4.15, where the received signal y is expressed in time domain as:

$$y(t) = x(t) + v(t), \quad (4.34)$$

where $v(t)$ is the AWGN with zero mean and variance σ_v^2 , i.e., $\mathcal{CN}(0, \sigma_v^2)$. The power of transmitted symbols c_n as well as all the filters f in the bank for I and Q components are normalized according to $\mathbb{E}\{\|c_n\|^2\} = 1$ and $\sum_{m=0}^{L-1} f^2[m] = 1$ respectively.

The Nyquist ISI condition (4.6) is relaxed in the proposed system to enhance the SE of conventional APM schemes by using distinguishable filter shapes. Thus the ISI will occur naturally, and an ISI cancellation block is required in IQ-FSIM receiver before the detection as shown in Fig. 4.15.

In the next sub-sections, the two proposed detectors for IQ-FSIM are described, where it is shown that the filter indices on I/Q and the APM symbol can be jointly detected by using the joint ML detector or successively by using the MF based detector.

4.4.3.1 Joint ML Detector

The ISI cancellation block targets to eliminate the introduced ISI from the received signal y and generate the signal \hat{s} of L samples for each symbol. Then, these signals \hat{s} are fed to the detector to estimate the filter indices and the APM symbol. The joint ML detector performs an exhaustive search over all possible combinations between the APM symbols, filters \mathbf{f}_i on I and filters \mathbf{f}_j on Q as described below:

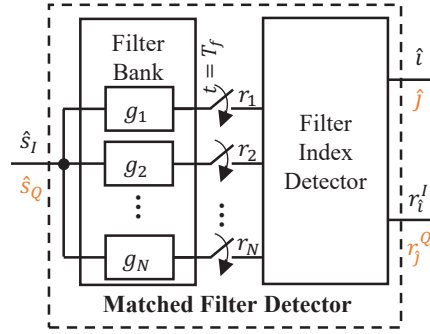


Figure 4.16 – Matched filter detector with input either \hat{s}^I or \hat{s}^Q to detect the index of the used filter shape \hat{i} or \hat{j} respectively.

$$\{\hat{i}, \hat{j}, \hat{c}\} = \arg \min_{\mathbf{f}_i \in \psi^I, \mathbf{f}_j \in \psi^Q, c \in \chi} \|\hat{\mathbf{s}} - (c^I \mathbf{f}_i + j c^Q \mathbf{f}_j)\|^2 \quad (4.35)$$

where ψ^I/ψ^Q and χ denote the set of N filter's shapes used for the I/Q components and the M -ary APM constellation, respectively. The detected \hat{i}/\hat{j} and \hat{c} are the recovered indices of $\mathbf{f}_i/\mathbf{f}_j$ on I/Q, and the APM symbol respectively. Thus, the corresponding IQ-FSIM system model can be obtained by replacing the IQ-FSIM detector in Fig. 4.15 by the joint ML detector.

4.4.3.2 Matched Filter-based Detector

After ISI cancellation, the IQ-FSIM detector based on MFs performs the detection of filter indices used on I and Q components in parallel, before proceeding to M -ary APM detection as depicted in Fig. 4.15. Note that the bank of correlators can replace the MFs, and provides the same results [203]. Each MF detector is composed of N matched filter g_k where $g_k(t) = f_k(T_f - t)$ with $0 \leq t \leq T_f$, $T_f = L.T_s$ as shown in Fig. 4.16. The filters' outputs $r_k(t)$ on the I branch are given by:

$$\begin{aligned} r_k^I(t) &= \int_0^t \hat{s}^I(\tau) g_k(t - \tau) d\tau, \quad k = 1, 2, \dots, N \\ &= \int_0^t \hat{s}^I(\tau) f_k(T_f - t + \tau) d\tau. \end{aligned} \quad (4.36)$$

These filter outputs are sampled at the instant T_f

$$r_k^I = \int_0^{T_f} \hat{s}^I(\tau) f_k(\tau) d\tau, \quad k = 1, 2, \dots, N. \quad (4.37)$$

Hence, the selected filter index is estimated by taking the maximum of the sampled MF squared outputs as follows:

$$\hat{i} = \arg \max_k (r_k^I)^2. \quad (4.38)$$

Similarly, the filter index on the Q branch is detected to deduce \hat{j} using the input signal \hat{s}^Q . Once the filter indices (\hat{i}, \hat{j}) are detected, $r = r_{\hat{i}}^I + j r_{\hat{j}}^Q$ is decoded by using the APM detector that determines the ML transmitted symbol \hat{c} in the constellation set χ . Note that any other APM detector can be used. Finally, the detected APM symbol \hat{c} and the filter indices (\hat{i}, \hat{j}) are passed to the corresponding demappers to deduce the bit-stream \hat{b}_1 and \hat{b}_2 , respectively.

4.4.3.3 ISI Estimation and Cancellation

The filter bank implemented in the IQ-FSIM system is not intended to satisfy the Nyquist criterion for zero-ISI, since a low cross-correlation filter is only required to allow correct filter index detection, which cannot be guaranteed with only Nyquist filters. This relaxation with FSIM and IQ-FSIM is added only to achieve higher SE enhancement in contrast to most SISO-IM schemes. Thus, these different filter shapes on I and Q will induce a predictable ISI that could be estimated and then removed or at least minimized before proceeding with the APM symbol detection.

In contrast to (4.5) for FSIM in AWGN channel that uses same filter on I and Q, the equation (4.34) can be rewritten as follows with IQ-FSIM:

$$\begin{aligned} y(t) &= x(t) + v(t) = \sum_n s_n(t - n.T_{sym}) + v(t) \\ &= \sum_n \left(c_n^I f_{i_n}(t - n.T_{sym}) + j c_n^Q f_{j_n}(t - n.T_{sym}) \right) + v(t). \end{aligned} \quad (4.39)$$

The received signal is sampled at the rate of T_s and the L received samples corresponding to APM symbol c_n is given as follows:

$$\begin{aligned} y_n[m] &= \left(c_n^I f_{i_n}[m] + j c_n^Q f_{j_n}[m] \right) + \underbrace{\sum_{n' > n} (c_{n'}^I f_{i_{n'}} + j c_{n'}^Q f_{j_{n'}})[m - (n' - n)\lambda]}_{\text{anticausal ISI}} \\ &+ \underbrace{\sum_{n' < n} (c_{n'}^I f_{i_{n'}} + j c_{n'}^Q f_{j_{n'}})[m - (n' - n)\lambda]}_{\text{causal ISI}} + v_n[m] \\ &= \left(c_n^I f_{i_n}[m] + j c_n^Q f_{j_n}[m] \right) + ISI_n[m] + v_n[m], \end{aligned} \quad (4.40)$$

where f_{i_n} and f_{j_n} represents the i^{th} and j^{th} shapes used to filter the real and imaginary parts of the n^{th} APM symbol respectively, and $v_n[m]$ is the noise sampled at $t = n.T_{sym} + m.T_s$. In contrast to a conventional transceiver that uses Nyquist filters, the received signal in the proposed scheme contains some ISI ($ISI \neq 0$ in (4.40)).

Since the detection of filter needs all the L samples around each symbol, the ISI cancellation requires eliminating the causal and anti-causal ISI introduced on all related samples. Thus, the filter indices on I and Q, along with the η past and η future APM symbols, are required. For clarification, as

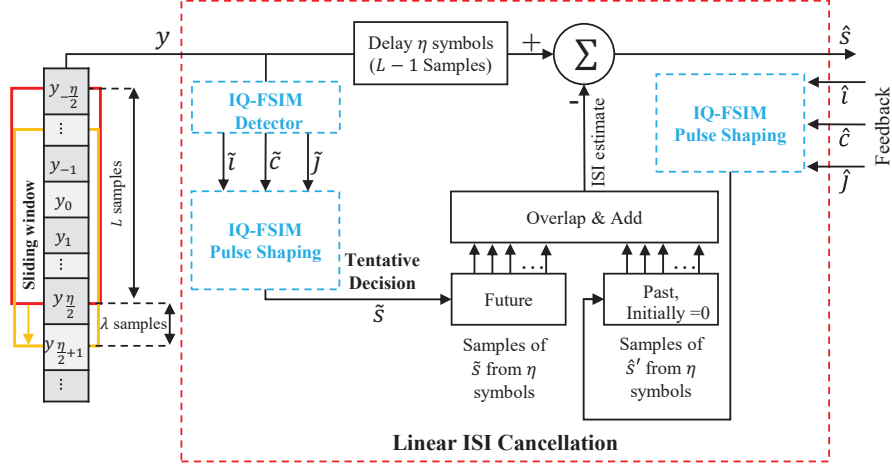


Figure 4.17 – ISI estimation and cancellation using feedback decisions $\{\hat{i}, \hat{j}, \hat{c}\}$ for past symbols and tentative decisions $\{\tilde{i}, \tilde{j}, \tilde{c}\}$ for future symbols.

shown in Fig. 4.2, the ISI in the samples \mathbf{l}_3^0 of the first APM symbol c_0 can be eliminated by knowing all the future $\eta = 6$ symbols. Hence, similar to ISI cancellation for FSIM scheme, the additional IQ-FSIM system delay compared to the conventional transceiver is $d_{\text{IQ-FSIM}} = d_{\text{FSIM}} = 3\frac{\eta-\lambda}{2} + 1 - \lfloor \frac{\lambda}{2} \rfloor$ samples [22], which corresponds to the required delay to receive the rest of the first L samples and to mitigate the anti-causal ISI from the η future symbols.

The ISI estimation and cancellation technique for IQ-FSIM scheme is depicted in Fig. 4.17. This circuit receives first the y_n signal composed of L samples related to the symbol s_n and passes them through the delay block. Second, the samples related to future symbols $s_{n'}, n < n' < n + \eta$, i.e., $y_{n'}[m]$, where $n' \times \eta \leq m \leq n' \times \eta + L$, are progressively received and a tentative detection is performed immediately on each of them using the IQ-FSIM detector that generates the $\hat{c}_{n'>n}$ along with their filter indices pairs $(\hat{i}_{n'}, \hat{j}_{n'})$, $n < n' < n + \eta$. Note that a low complexity MF based detector is considered. These tentative decisions $\hat{c}_{n'>n}$ along with their filter indices are passed through the IQ-FSIM pulse shaping to regenerate the signal $\tilde{s}_{n'}[m]$ originally generated at the Tx side, and then overlapped and added as shown in Fig.4.2. Similarly, the past η detected APM symbols $\hat{c}_{n'}$ along with their filter indices pairs $(\hat{i}_{n'}, \hat{j}_{n'})$, $n' < n$, are received as feedback to reconstruct their associated symbols $\hat{s}_{n'}$. Then the reconstructed future and past symbols are overlapped and added and finally their sum that represents the ISI to the symbols s_n is subtracted and the decided symbol \hat{s}_n is obtained.

However, a residual ISI can remain in $\hat{s}_n[m]$ when an error occurs in past and/or future decisions, and thus $\hat{s}_n[m]$ is given by:

$$\hat{s}_n[m] = \left(c_n^I f_{i_n}[m] + j c_n^Q f_{j_n}[m] \right) + \text{ISI}_{\text{resid}}[m] + v_n[m], \quad (4.41)$$

where $m = 0, \dots, L - 1$, and $ISI_{resid}[m]$ represents the residual ISI. Note that if the filters are well designed, the $ISI_{resid}[m]$ approaches zero. Finally, the IQ-FSIM detector takes $\hat{s}_n[m]$ to estimate the final decisions $\{\hat{i}_n, \hat{j}_n, \hat{c}_n\}$ as shown in Fig. 4.15.

Finally, the filter bank design requirements and constraints for IQ-FSIM system are similar to those for FSIM detailed in Section 4.3.3. These requirements can be summarized as the follows: 1) the filters dot-product and 2) the introduced ISI should be kept as low as possible while having the same bandwidth and center frequency; 3) the level OOB radiations should remain within the norm; 4) the filter length should be as low as possible. The first two factors should be minimized to allow correct detection of filter indices and APM symbols, while the OOB and filter length constraints are needed to be minimized to limit the adjacent channel interference, and maintain a low hardware complexity, respectively.

4.4.4 Theoretical Performance Analysis

In this section, the lower bound analytical expression for the probability of error for filter indices detection is derived, then the APM symbol error detection is considered to truly evaluate the IQ-FSIM system performance in terms of total SER and BER. Note that the low complexity MF based detector approaches the joint ML performance as it will be shown in the next section. Hence, the analytical expressions will consider only the former.

The errors in filter indices detection affect the subsequent APM symbol due to mismatched filtering on I and/or Q that leads to higher ISI most probably, which thus, degrades the IQ-FSIM overall performance.

For deriving the lower bound expressions, we will assume that the filter bank is well designed to allow perfect ISI cancellation (*i.e.* $ISI_{resid} = 0$). As shown in Fig. 4.16, the bank of MFs on I/Q took on each symbol period the signal \hat{s}^I/\hat{s}^Q of L samples that represents the real/imaginary part of \hat{s} expressed in (4.41). Then, these outputs are sampled at $t = T_f$ given by r_k^I in (4.37) and r_k^Q . Firstly, the probability of error for filter detection on the in-phase component is derived, then that on the quadrature component can be deduced similarly. Thus, the outputs on I branch r_k^I can be rewritten as:

$$r_k^I = \langle \mathbf{f}_k, \mathbf{f}_{i_n} \rangle \cdot c_n^I + \langle \mathbf{f}_k, \mathbf{v}_n^I \rangle = \begin{cases} c_n^I + \langle \mathbf{f}_k, \mathbf{v}_n^I \rangle & \text{for } k = i_n \\ \langle \mathbf{f}_k, \mathbf{f}_{i_n} \rangle \cdot c_n^I + \langle \mathbf{f}_k, \mathbf{v}_n^I \rangle & \text{for } k \neq i_n. \end{cases} \quad (4.42)$$

The filters are correlated in our proposed system because they share the same bandwidth around the same center frequency to allow a more significant SE improvement.

Let us suppose that the filter f_1 is selected at the transmitter side on I component for the APM symbol c_n . Then, the vector \mathbf{r}_k^I composed of the elements r_k^I for $k = 1, \dots, N$ is given as follows:

$$\mathbf{r}_k^I = [c_n^I + v_1^I, \langle \mathbf{f}_2, \mathbf{f}_1 \rangle \cdot c_n^I + v_2^I, \dots, \langle \mathbf{f}_N, \mathbf{f}_1 \rangle \cdot c_n^I + v_N^I], \quad (4.43)$$

where $v_k^I = \langle \mathbf{f}_k, \mathbf{v}_n^I \rangle$ are real-valued zero-mean mutually statistically independent Gaussian random variables with equal variance $\sigma^2 = \sigma_k^2 = \frac{1}{2}N_0$, where N_0 is the noise spectral density [203]. The filter index on I is estimated by taking the maximum squared component of the vector \mathbf{r}_k^I : $U_k^I = (r_k^I)^2$. Similarly, the detection is performed on Q component using U_k^Q that represents the square of the matched filter output in the Q branch. Thus, U_k in general is described as a statistically independent non-central chi-square distribution for all k , each having 1 degree of freedom where the non-centrality parameter $(\alpha)^2$ is given by:

$$\alpha_{k,q}^2 = \begin{cases} \mathcal{E}_q & \text{for } k = 1 \\ \langle \mathbf{f}_k, \mathbf{f}_1 \rangle^2 \cdot \mathcal{E}_q & \text{for } k \neq 1, \end{cases} \quad (4.44)$$

where \mathcal{E}_q is the square of the real part (imaginary part) of the transmitted APM symbol c_n when estimating the PDF of U_k^I (U_k^Q). In the following, the superscripts I and Q for U_k are omitted for the sake of simplicity. The probabilities of error for filter index on I and Q are considered similar with the following differences: the selected filter at the transmitter, and \mathcal{E}_q . Thus, we obtain the PDF of U_k in general as:

$$p(u_k) = \frac{1}{\sigma \sqrt{2\pi} u_k} e^{-\left(\frac{u_k + \alpha_k^2}{2\sigma^2}\right)} \cosh\left(\frac{\alpha_k \sqrt{u_k}}{\sigma^2}\right) \quad (4.45)$$

where $u_k \geq 0$.

The error probability on the indexed filter can be deduced by deriving the probability that the detector makes a correct filter index decision. This is the probability that u_1 is larger than all other $N - 1$ u_k values for $k \neq 1$. This probability of correct decision for a given \mathcal{E}_q may be expressed as:

$$P_{c,\mathcal{E}_q} = P(U_2 < U_1, U_3 < U_1, \dots, U_N < U_1) = \int_0^\infty P(U_2 < U_1, \dots, U_N < U_1 | u_1) \cdot p(u_1) du_1, \quad (4.46)$$

where $P(U_2 < U_1, U_3 < U_1, \dots, U_N < U_1 | U_1)$ denotes the joint probability that u_2, u_3, \dots, u_N are all less than u_1 conditioned on a given u_1 . Then this joint probability is averaged over all u_1 . The filters are considered orthogonal when deriving the lower bound, thus these $N - 1$ variables u_k becomes statistically independent under this assumption with central chi-square distribution ($\alpha_{k,q}^2 = 0$ for $k \neq 1$). Since the u_k are statistically independent, the joint probability can be factorized as a product of $N - 1$ marginal probabilities of the form:

$$P(u_k < u_1 | u_1) = \int_0^{u_1} p_{u_k}(x_k) dx_k, \quad k = 2, 3, \dots, N. \quad (4.47)$$

Hence, the probability of a correct decision is given by:

$$P_{c,\mathcal{E}_q} = \int_0^\infty \left(\prod_2^N P(u_k < u_1 | u_1) \right) \cdot p(u_1) du_1 \quad (4.48)$$

and the probability of a filter index error with a given \mathcal{E}_q is as follows:

$$P_{e,\mathcal{E}_q} = 1 - P_{c,\mathcal{E}_q}. \quad (4.49)$$

Thus, the average probability of filter index error on I/Q is the weighted average of filter error over the set of possible energy levels $\mathfrak{Q}^I/\mathfrak{Q}^Q$ for real/imaginary part of the APM symbols, given as follows:

$$P_{e,filter} = \sum_{\mathcal{E}_q \in \mathfrak{Q}} P_{e,\mathcal{E}_q} \cdot P(\mathcal{E}_q), \quad (4.50)$$

where $P(\mathcal{E}_q)$ is the probability of occurrence of the energy level \mathcal{E}_q . For example, when the used APM is a rectangular 8-QAM, $\mathfrak{Q}^I = \{1/6, 1/2\}$ (2 possible energy levels for the real part), and their probability of occurrence is $P(\mathcal{E}_q^I) = [0.5, 0.5]$ if all APM symbols are equiprobable. Also, there is one level for the imaginary part $\mathfrak{Q}^Q = \{1/6\}$. Hence, the probability of error for filter index on I and Q can be expressed as follows:

$$P_{e,filter \text{ on } I \text{ and } Q} = \frac{1}{2} \sum_{\mathcal{E}_q^I \in \mathfrak{Q}^I} P_{e,\mathcal{E}_q^I} + \frac{1}{2} \sum_{\mathcal{E}_q^Q \in \mathfrak{Q}^Q} P_{e,\mathcal{E}_q^Q}, \quad (4.51)$$

For this example, it can be simplified to:

$$P_{e,filter \text{ on } I \text{ and } Q} = \frac{1}{2} \sum_{\mathcal{E}_q^I \in \mathfrak{Q}^I} P_{e,\mathcal{E}_q^I} + \frac{1}{2} P_{e,\mathcal{E}_q^Q=1/6}. \quad (4.52)$$

Since the perfect ISI cancellation is assumed to derive the lower bound, then the probabilities of APM symbol error $P_{e,APM}$ is equal to the probability of APM symbol error in conventional transceiver with Nyquist filters.

Consequently, the correct IQ-FSIM symbol detection occurs when both the filter on I and Q as well the APM symbol are correctly estimated, then the probability of a correct IQ-FSIM decision is $(1 - P_{e,filter I})(1 - P_{e,filter Q})(1 - P_{e,APM})$ and the SER is given by:

$$SER = 1 - (1 - P_{e,filter I})(1 - P_{e,filter Q})(1 - P_{e,APM}). \quad (4.53)$$

The average probability of virtual (real) bit error can be deduced from filters (APM symbol) error similar to [203, p. 262 (5-2-24)], thus they can be expressed respectively as follows:

$$P_{b,filter I} = \frac{N}{2(N-1)} P_{e,filter I} \quad (4.54)$$

$$P_{b,filter Q} = \frac{N}{2(N-1)} P_{e,filter Q} \quad (4.55)$$

$$P_{b,APM} = \frac{M}{2(M-1)} P_{e,APM}. \quad (4.56)$$

Similarly to SER, the total BER is deduced, but while taking into consideration the weight of real and virtual bits:

$$BER = \frac{\log_2 N}{\mathcal{L}_{IQ-FSIM}} P_{b,filter I} + \frac{\log_2 N}{\mathcal{L}_{IQ-FSIM}} P_{b,filter Q} + \frac{\log_2 M}{\mathcal{L}_{IQ-FSIM}} P_{b,APM}. \quad (4.57)$$

Finally, it is clear from (4.44) that the dot-product between all filters affects the filter error probability, and thus the system performance because the filter error affects the subsequent APM symbols detection. In addition, the introduced ISI can also degrade the performance if it was not correctly estimated and canceled. Therefore, the filter bank design should consider the joint minimization of these two factors to approach both lower bounds for SER and BER of IQ-FSIM system. In the next section, these theoretical lower bounds for error probabilities of filter indices and BER are validated with different IQ-FSIM configurations.

4.4.5 Numerical Results Analysis and Discussions

Firstly, the theoretical error probability of filter index detection (4.51) using the MF-based detector is evaluated and compared to the Monte Carlo simulated results obtained under different configurations. Secondly, the performance of the proposed system with joint ML and MF-based detectors is evaluated and compared at different SEs (4 to 8 bits/symbol) to the theoretical lower bound (4.57) and to the performance of the equivalent APM scheme of the same SE. The simulation parameters for IQ-FSIM are maintained similar to those of FSIM in Table 4.1.

In the following, the 2 and 4 filter shapes designed in Chapter 5 are used on both I and Q components to demonstrate the feasibility of the proposed scheme, and to show the minimum performance gain and SE improvement that can be achieved. Fig. 4.18 presents the impulse response of the two filters, whereas Figs. 4.19 and 4.20 show their magnitude and phase responses. In addition, after correct matched filtering ($\mathbf{f}_i * \mathbf{g}_i$) the complete filter responses at the receiver are shown in Fig. 4.21. The added ISI clearly appears in f_2 because, the result of $\mathbf{f}_2 * \mathbf{g}_2$ has non-zero values for some $t = n.T_{sym}$. Note that the 2 filters shown in these figures are an enhanced version of the filter pair in Fig. 4.4 to achieve lower cross-correlation.

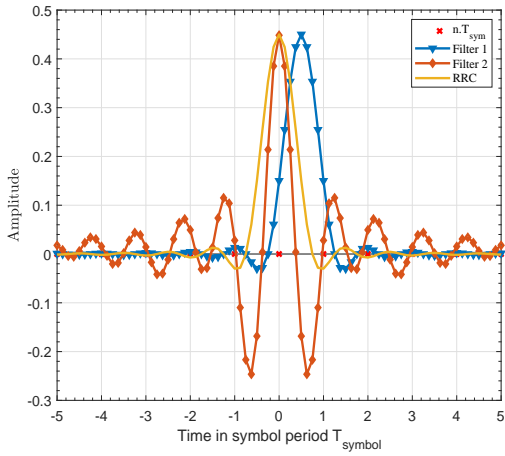


Figure 4.18 – Impulse Response for the two filters used in our simulations compared to RRC pulse shaping filter, where $\eta = 10$ and $\lambda = 8$.

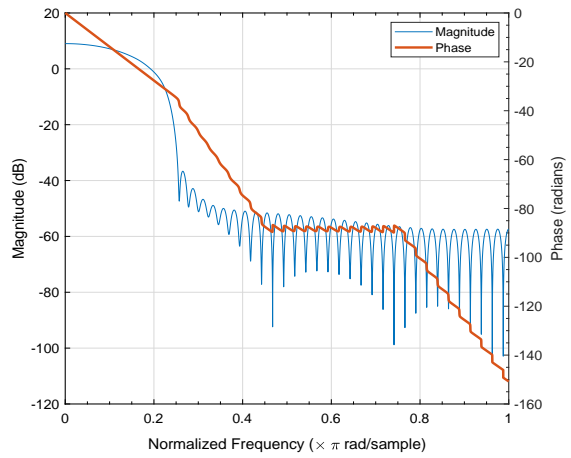


Figure 4.19 – Magnitude and phase response of the filter f_1 depicted in Fig. 4.18.

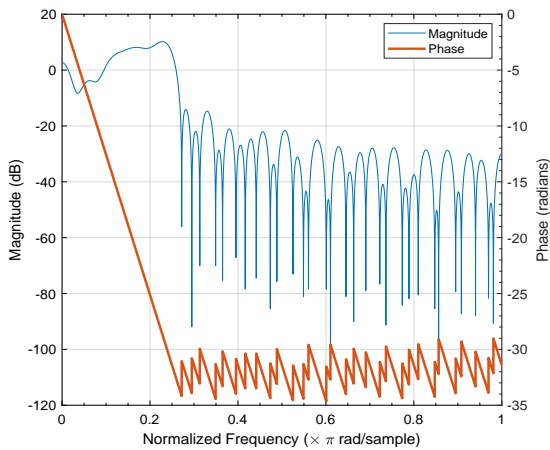


Figure 4.20 – Magnitude and phase response of the filter f_2 depicted in Fig. 4.18.

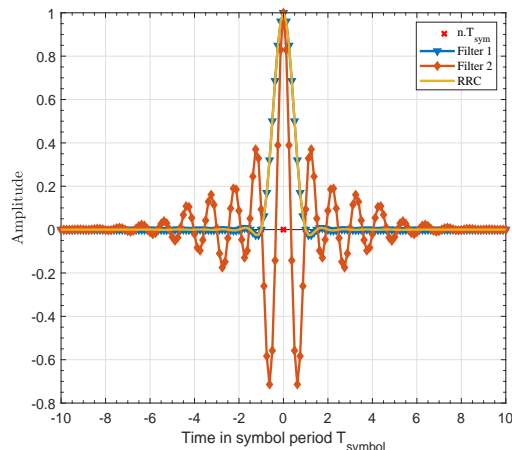


Figure 4.21 – Complete responses of the 2 filters obtained after correct matched filtering at the receiver side, where $\eta = 10$ and $\lambda = 8$.

4.4.5.1 Performance Analysis based on Theoretical Lower Bound

The theoretical lower bound and simulated filter index error probabilities with perfect ISI cancellation, and with ISI estimation and cancellation are compared in Figs. 4.22a and 4.22b. Note that perfect ISI cancellation means that the tentative decisions for filter indices and APM symbols are detected correctly, but the decisions for past symbols are fed back after final detection. In the following, the notation N -IQ-FSIM-MAPM is adopted for performance analysis of our proposed system.

It is clear from Figs. 4.22a-4.22b that the simulation results with perfect ISI cancellation validate the analytical lower bound (4.51) derived under the assumption of perfect ISI cancellation and orthogonal filters. However, a Signal-to-noise Ratio (SNR) gap between these curves may appear

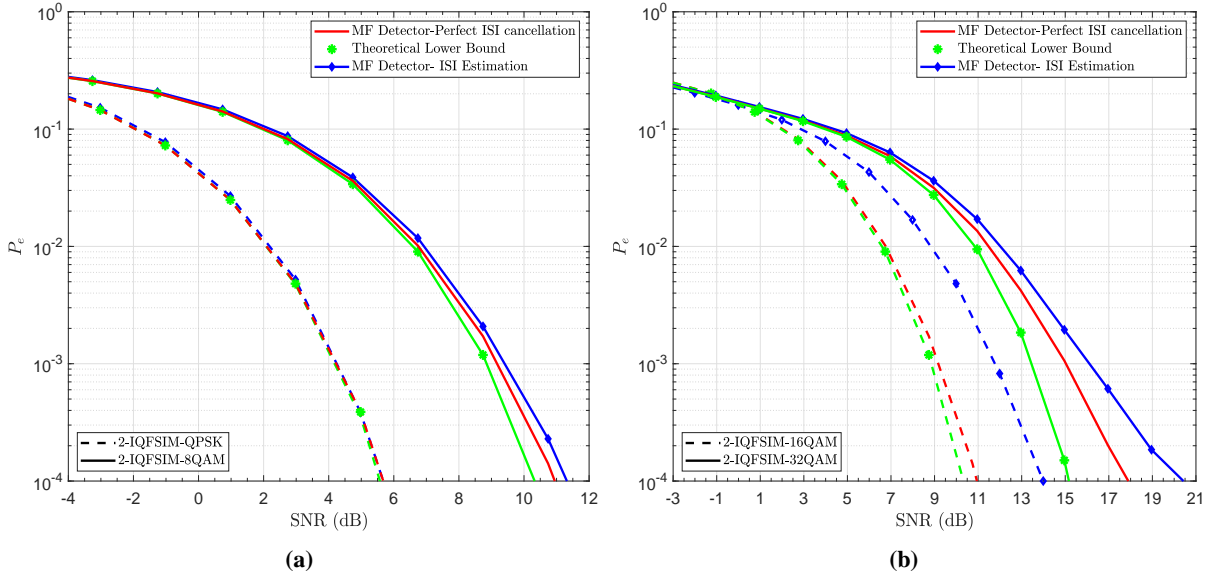


Figure 4.22 – The error probabilities of filter index detection on I and Q with ISI estimation and cancellation, perfect ISI cancellation, and the derived theoretical lower bound, $N = 2$ (2-IQ-FSIM- M QAM). The SE is: (a) [4, 5] bits/symbol using $M = [4, 8]$, (b) [6, 7] bits/symbol using $M = [16, 32]$.

due to non-orthogonal filters and to a possible error in feedback decisions that increases with higher M -ary APM. Moreover, the difference between simulated results with perfect ISI cancellation and ISI estimation and cancellation is due to residual ISI when the ISI estimation proposed in subsection 4.4.3.3 is adopted. It is worth mentioning that 2-IQ-FSIM-QPSK with ISI estimation is very tight to its lower bound because QPSK can support a high ISI level. However, the degradation due to residual ISI is more important with higher M -ary QAM that are more sensitive to ISI as shown in Fig. 4.22b, but it is minimal at low SNR values. Note that the two used filter shapes are non-optimal, and they satisfy all the filter bank design requirements summarized at the end of Section 4.3.3. Thus, better results can be achieved when optimal filter shapes are used. Therefore, this theoretical lower bound can be considered as a helpful indicator for evaluating the proposed system's performance.

4.4.5.2 Comparison to Equivalent M -ary QAM

In the following, our proposed system IQ-FSIM is compared to its equivalent conventional transceivers with the same SE that use M -ary QAM scheme with RRC filter. The system performance is evaluated in AWGN channel using theoretical lower bound (4.57) and Monte Carlo simulations with ISI estimation and cancellation. Figs. 4.23a-4.24b shows the comparison between the BER performance of N -IQ-FSIM- M and its equivalent QAM with the same SE. It is clear that the low-complexity MF based detector achieves the joint ML performance in all configurations, and the proposed IQ-FSIM system with up to 16QAM has an important performance gain at all SNR range compared to the equivalent system. It is worth mentioning that the BER of 2-IQ-FSIM-QPSK with ISI estimation is very tight to

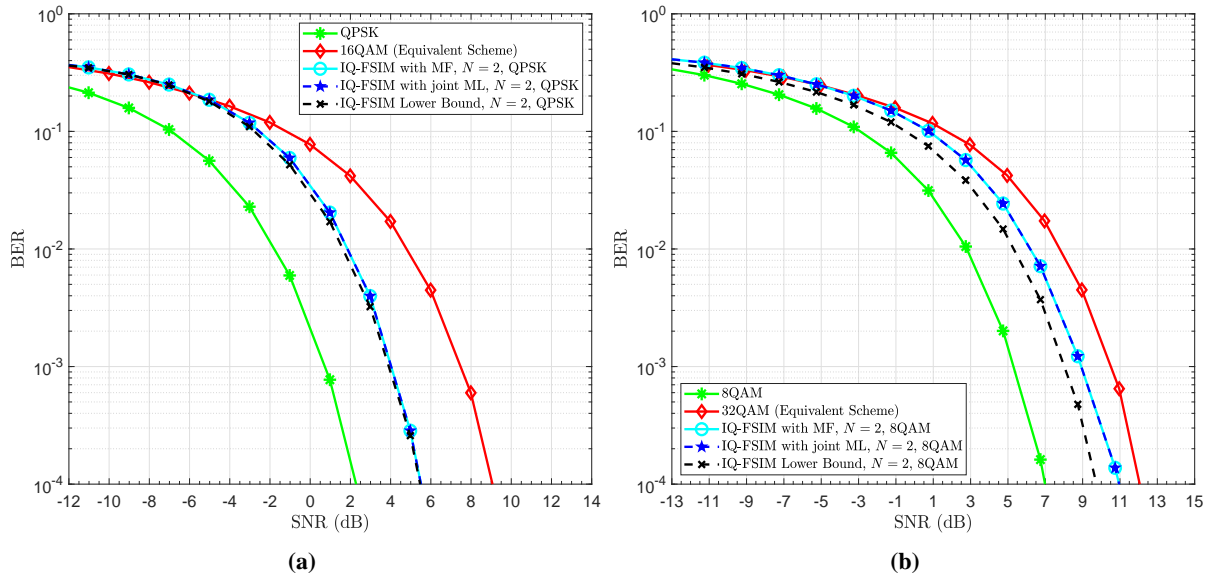


Figure 4.23 – Uncoded BER performance of 2-IQ-FSIM- M QAM, its theoretical lower bound and its equivalent scheme 4 M QAM of the same SE: (a) 4 bits/symbol using $M = 4$, (b) 5 bits/symbol using $M = 8$.

its lower bound while achieving 3.55 dB gain at $\text{BER} = 10^{-4}$ compared to its equivalent system 16 QAM as shown in Fig. 4.23a. However, the BER of 2-IQ-FSIM-16QAM system is 3.55 dB far from its lower bound due to residual ISI, but it requires 2 dB less than its equivalent system 64QAM to achieve the same performance. Note that 2-IQ-FSIM-8QAM has a lower gain of 1 dB compared to 32QAM due to the inherited performance degradation when using non-square QAM. Moreover, as M -ary QAM scheme is increased with IQ-FSIM system, the residual ISI effect becomes more important, as shown in Fig. 4.24b, but the 2-IQ-FSIM-32QAM and 2-IQ-FSIM-64QAM systems can achieve some gain at low SNR region. This degradation appears due to sensitivity of high M -ary QAM to ISI and due to error propagation that results from the residual ISI caused by the error in tentative and feedback decisions in the preceding block for ISI estimation and cancellation. However, the IQ-FSIM BER lower bound depicted in Fig. 4.24b shows that there is always room for future improvements by designing an optimal filter bank and a better ISI mitigation techniques.

The spectrum of the proposed IQ-FSIM scheme is compared to that of the conventional transceiver in Fig. 4.25. The proposed scheme conserves most of the radiated power on the targeted bandwidth, similar to the conventional M -ary QAM system, but a higher OOB radiation is observed. Hence, the OOB radiation will be considered in the future filter bank design to be kept as low as possible.

For further analysis of the proposed system, the 4 non-optimal filters in Fig. 4.12 are used also to evaluate IQ-FSIM. the performance of 4-IQ-FSIM-QPSK (6 bits/symbol) is depicted in Fig. 4.26a, where a 4.3 dB gain is achieved compared to 64 QAM at $\text{BER} = 10^{-4}$. However, the gain with 4-IQ-FSIM-16QAM is more important at the low SNR region (5.2 dB at $\text{BER} = 10^{-1}$), as shown in Fig. 4.26b, and it decreases to reach 0.5 dB at $\text{BER} = 10^{-4}$ due to residual ISI effect on higher M -ary QAM.

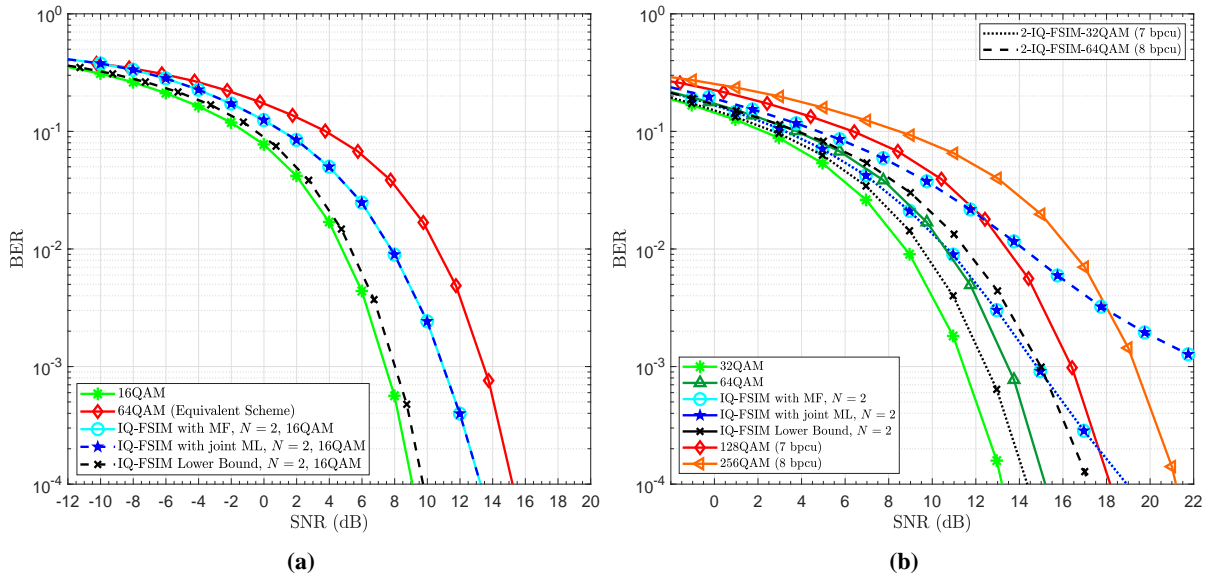


Figure 4.24 – Uncoded BER performance of 2-IQ-FSIM- M QAM, its theoretical lower bound and its equivalent scheme $4M$ QAM of the same SE: (a) 6 bits/symbol using $M = 16$, (b) 7 and 8 bits/symbol using $M = 32$ and $M = 64$ respectively.

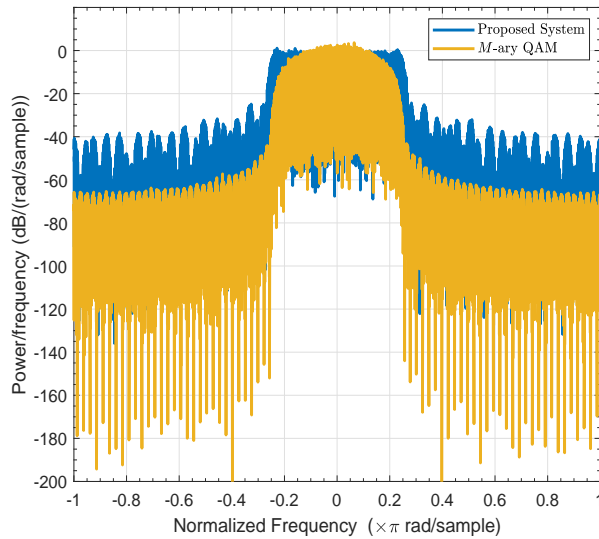


Figure 4.25 – Spectrum of the proposed IQ-FSIM system with 2 non-optimal filters compared to the traditional transceivers with QAM and RRC filters.

Note that the residual ISI and the high dot-product between some filters lead to a degradation between the 4-IQ-FSIM performance systems with ISI estimation and cancellation and their lower bounds.

Nevertheless, this IQ-FSIM scheme can achieve SE and EE gain even with non-optimal filters compared to conventional APM schemes. In addition, this superiority is maintained when the IQ-FSIM is compared to existing single and dual-mode SISO-IM schemes of worse EE due to the need of higher

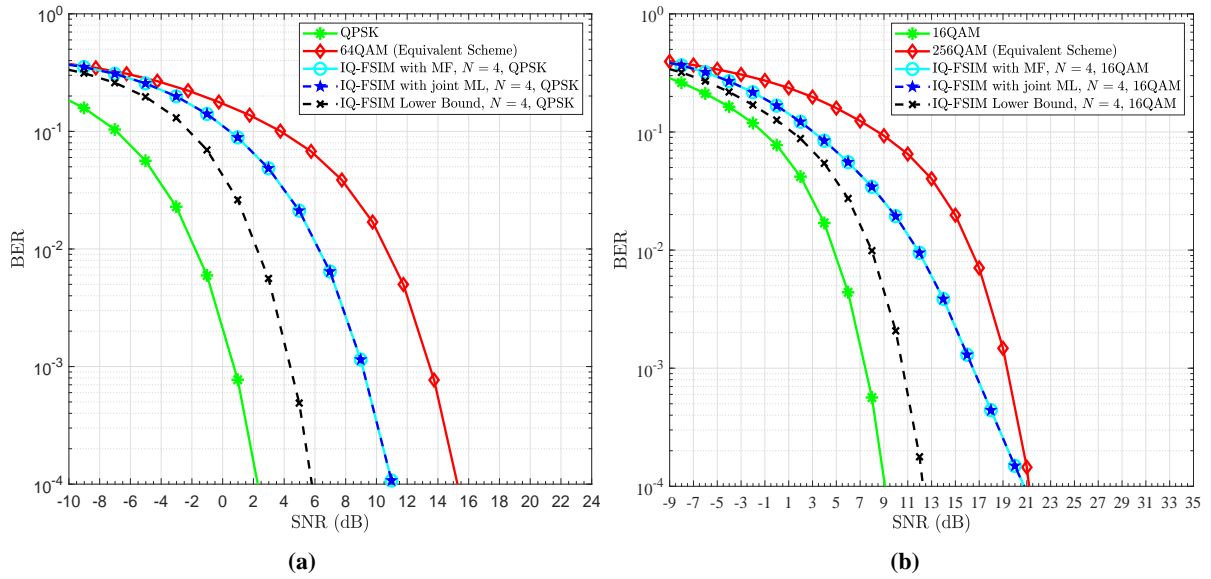


Figure 4.26 – Uncoded BER performance of 4-IQ-FSIM-MQAM, its theoretical lower bound and its equivalent scheme 16MQAM of the same SE: (a) 6 bits/symbol using $M = 4$, (b) 8 bits/symbol using $M = 16$.

power to maintain the same SE by using larger M -ary and/or to detect the transmitted VBs (see [164] and references therein).

Furthermore, better performance and higher EE gain can be achieved by using an optimal filter bank satisfying the IQ-FSIM requirements and constraints.

4.4.5.3 Comparison to Equivalent FSIM System

Finally, the comparison between the two proposed schemes in filter IM domain FSIM and IQ-FSIM with their equivalent scheme of the same SE 4 bits/symbol is provided in Fig. 4.27. It is clear that, in terms of the lower bound, the scheme with a higher N has the best performance. However, when using non-optimal filters, FSIM with 4 filters has an important degradation due to the high filters dot-product as compared to IQ-FSIM with 2 filters. It is worth mentioning that IQ-FSIM-QPSK with the 2 filters achieves the best realistic performance with 1.85 and 3.5 dB gain compared to 4-FSIM-QPSK (same modulation order) and 2-FSIM-8QAM (same number of filters) respectively. However, both schemes are much better than the equivalent 16QAM scheme at all SNR range. In conclusion, IQ-FSIM shows an important advantage over FSIM with the current designed filters because it allows using lower order modulation scheme, which is more robust to ISI, or half the number of filters where we can achieve a lower dot-product.

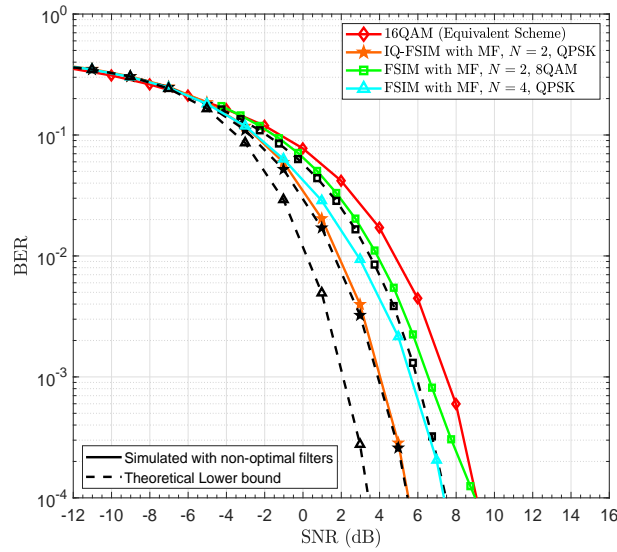


Figure 4.27 – BER performance comparison between FSIM, IQ-FSIM and their equivalent scheme 16QAM of the same SE 4 bits/symbol.

4.4.6 Conclusions

In this section, a novel scheme IQ-FSIM is proposed in the filter IM domain. The proposed scheme conveys information bits by an APM symbol and the indices of filter shapes being used on the in-phase and quadrature components. Thus, IQ-FSIM system allows a SE improvement by $2 \log_2 N$, which is double the gain obtained with FSIM scheme, and achieves the highest SE enhancement among all SISO-IM schemes. It is worth mentioning that the proposed system generalizes the previously proposed FSIM scheme, and thus most of the existing SISO-IM schemes in time and frequency domains [22].

This novel scheme is proposed along with a joint ML detector that estimates jointly both filter indices and APM symbol using an exhaustive search. In addition, a low complexity optimal detector based on Matched Filter is proposed to estimate the filter indices on I and Q in parallel then the transmitted APM symbol is deduced. Moreover, a linear ISI cancellation technique is presented to mitigate the ISI effects introduced by the filter shapes being used on I and Q.

The system performance of IQ-FSIM is characterized by deriving the theoretical lower bound of filter error probability, symbol error rate, and total BER. The numerical results using Monte Carlo simulations validated these lower bounds and showed that the IQ-FSIM-QPSK system with 2 and 4 non-optimal filters offers, at $\text{BER} = 10^{-4}$ and same SE, an important gain of 3.55 dB and 4.3 dB as compared to their equivalent systems 16QAM and 64QAM respectively. In addition, 2-IQ-FSIM-QPSK achieves a gain of 1.85 and 3.5 dB compared to 4-FSIM-QPSK and 2-FSIM-8QAM, respectively, with the filters currently designed. Thus, the results of the filter IM domain, mainly FSIM and IQ-FSIM schemes, insist that accepting a certain level of controllable and predictable ISI allows reaching a

higher system capacity using a low order M -ary APM. Finally, IQ-FSIM can achieve even higher SE by designing a larger filter bank (higher N), which is useful for ultra-high rate wireless communication.

The filter bank design for the filter IM domain will be considered in the next chapter and in our future work to achieve higher SE and EE gain.

4.5 MIMO Spatial Multiplexing with FSIM

In section 4.2, a novel domain for IM named “Filter domain” is proposed [22]. Recalling that this new dimension generalizes many existing modulations and SISO-IM domains (e.g., time and frequency IM domains described previously). In addition, the sections 4.3 and 4.4 show that the proposed domain permits to achieve the highest SE gain in SISO since it can be configured to fully use all the available time and frequency resources.

In this section, a generalized SMX system is proposed motivated by the different advantages of FSIM scheme and its generalizations for various existing IM schemes. Thus, this system includes different existing schemes as special cases (e.g., SMX with conventional APM, MIMO-OFDM-SIM [88], and SMX with any time/frequency IM), since filter IM domain can be configured to change the emitted symbol as highlighted in Section 4.2 and [22]. The transmission of different FSIM symbols from the TAs allows to achieve a higher SE and EE gain. In other words, any small SE enhancement by FSIM in SISO has a tremendous impact when it is extended to MIMO system, where the overall SE gain by SMX FSIM compared to SMX QAM is $N_t \log_2 N$ for $N_t \leq N_r$. In addition, a simple receiver for SMX-FSIM is presented in this section, where a sample level equalization is performed followed by a parallel MF based detector. Moreover, the theoretical system performance is derived and validated by Monte Carlo simulation, then compared with other equivalent systems. The main contributions are summarized as follows:

1. A generalized MIMO SMX system is proposed by incorporating FSIM scheme to achieve high SE and EE gain. The proposed SMX-FSIM system conveys information bits in the signal and filter IM domains. The VBs are encapsulated by the different filter shapes indices that are used for pulse shaping of the N_t simultaneously transmitted APM symbols. Note that the transmit spatial IM (e.g., GSM system) conveys all the VBs by a single index (index of activated TAC), and its misdetection leads to bit errors in most of the VBs and also in the real bits of all transmitted APM symbols (i.e., N_a APM symbols in GSM will be most probably mis-detected when an error occurs in the TAC index detection). However, the decentralization of VBs encapsulation in SMX-FSIM avoids the highlighted single point of failure in GSM system.
2. A simple receiver for SMX-FSIM is presented, which is based on Zero-Forcing (ZF) sample level equalizer followed by a parallel MF-based detector. The proposed parallel detection for

SMX-FSIM provides good performance with prominent complexity reduction compared to the joint Maximum Likelihood (ML)-based detector.

3. The analytical performance of SMX-FSIM using ZF equalizer is derived and validated by Monte Carlo simulations. Then, they are compared to those of the conventional SMX QAM system of the same SE. The results show an important SE and EE gain can be achieved even with a low number of filter shapes.
4. The performance of the proposed SMX FSIM scheme is evaluated under sub-THz channels with RF impairments, then compared to the existing ultra-high data rate candidates (GSM and conventional SMX QAM [17]).
5. These sub-THz candidates are compared and analyzed from different perspectives (performance, robustness to PN, SE/EE, cost, PAPR, and power consumption). The results reveal that the spectrally efficient SMX-FSIM with power-efficient APM is the best promising candidate for such systems in sub-THz bands because it has better performance and robustness to PN, higher SE and EE gain, lower power consumption and cost, as well as it avoids the RF switching problem that appears with transmitter spatial IM (e.g., GSM).

4.5.1 System Model: MIMO Spatial Multiplexing with FSIM

4.5.1.1 SMX FSIM Transmitter

Consider a $N_t \times N_r$ MIMO-SMX system ($N_t \leq N_r$), where N_t and N_r are the number of transmit and receive antennas respectively. In this section, FSIM scheme that conveys information bits by the index of the different filter shapes and the APM symbols is considered to achieve high SE and EE gain. Note that this system SMX-FSIM in the filter IM domain allows to use all available resources in contrast to other IM domains (time, frequency, antennas, etc.).

The input bitstream b is divided into N_t sub-streams b_1, b_2, \dots, b_{N_t} , as shown in Figure 4.28, and passed through its corresponding FSIM modulator.

Each sub-stream b_j contains the real and virtual information bits denoted by b_j^R and b_j^V respectively. The former is mapped using the M -ary APM (e.g., QAM, PSK), while the latter is translated to an index i^j , which represents the index of the selected filter f_{i^j} at the j^{th} TA. Then, the APM symbol c^j is pulse shaped, as depicted in Fig. 4.29, using the filter $f_{i^j}[m]$ of length L samples with m is the sample index from 0 to $L - 1$. Note that the filter is truncated in the time domain to η APM symbols, and it is sampled at a rate of λ samples per symbol, which yields $L = \eta \cdot \lambda + 1$. Then, the FSIM modulators' outputs are transmitted simultaneously from the N_t TAs.

The filter bank for each FSIM modulator shown in Fig. 4.29 includes N different filter shapes where N is a power of 2. Without loss of generality, we consider that SMX-FSIM uses the same filter

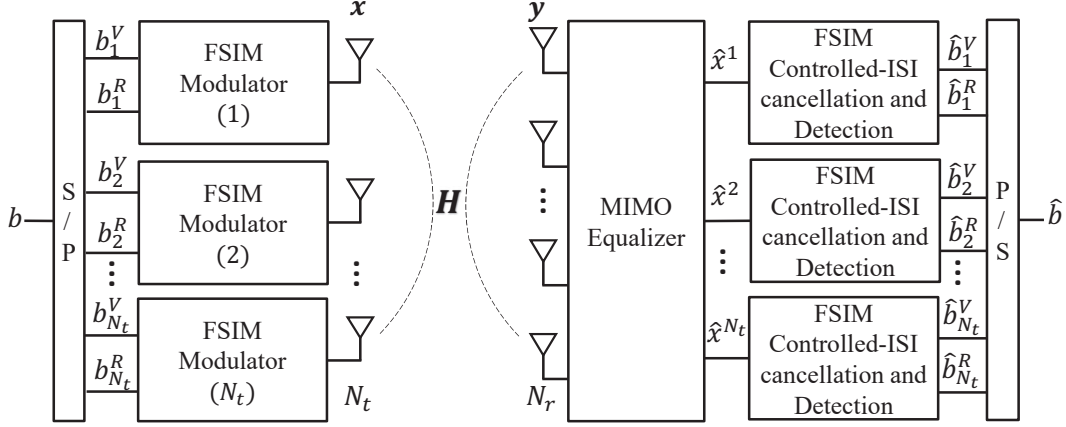


Figure 4.28 – System model of $N_t \times N_r$ SMX-FSIM transceiver.

bank and APM for all TAs. Subsequently, the total number of bits per SMX-FSIM symbol $\mathcal{L}_{\text{SMX-FSIM}}$ can be expressed as:

$$\begin{aligned} \mathcal{L}_{\text{SMX-FSIM}} &= N_t (\log_2 N + \log_2 M) \\ &= N_t \log_2 N + \mathcal{L}_{\text{SMX}}. \end{aligned} \quad (4.58)$$

where $\mathcal{L}_{\text{SMX}} = N_t \log_2 M$ is the number of transmitted bits of a conventional MIMO-SMX system with N_t TAs and M -ary APM. It is clear that the SE gain increases linearly with the number of TAs, and it is $N_t \log_2 N$ higher than that of the conventional MIMO-SMX system with the same M -ary APM.

The output of the filter bank $s_n^j[m]$ for the n^{th} APM symbol c_n^j at the j^{th} TA is:

$$s_n^j[m] = (f_{i_n^j} * c_n^{j'})[m] = c_n^j f_{i_n^j}[m]. \quad (4.59)$$

where $c_n^{j'}$ is the up sampled copy of c_n^j by a factor L .

Then, the signals $s_n^j[m]$ are passed through the OLA block as shown in Fig. 4.29 to generate the emitted signal $x_n^j[p]$ as follows:

$$x_n^j[p] = \sum_{n'=n-\lceil \eta/2 \rceil}^{n+\lfloor \eta/2 \rfloor} s_{n'}^j[p - (n' - n)\lambda], \quad (4.60)$$

where the index $p = p_{\text{center}} - \lceil \lambda/2 \rceil + 1, \dots, p_{\text{center}} + \lfloor \lambda/2 \rfloor$ and the index of the middle desired sample is $p_{\text{center}} = \frac{L-1}{2}$ [22]. Note the used filters introduce ISI since Nyquist condition for zero ISI is relaxed in FSIM scheme to achieve higher SE by indexing distinguishable filter shapes.

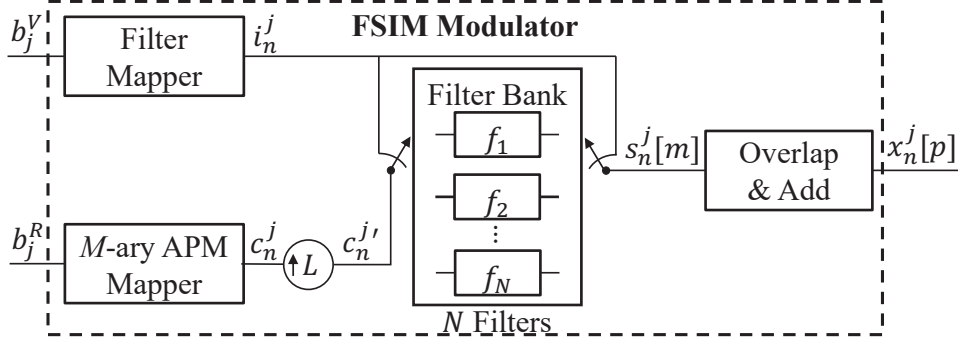


Figure 4.29 – System model of FSIM Modulator with M -ary APM mapping and a filter bank of N filters.

4.5.1.2 SMX-FSIM Receiver

At the receiver, the received signal in time domain \mathbf{y} can be expressed as:

$$\mathbf{y} = \mathbf{H}\mathbf{x} + \mathbf{v}. \quad (4.61)$$

where $\mathbf{H} = [\mathbf{h}_1, \dots, \mathbf{h}_{N_t}]$ is the $N_r \times N_t$ MIMO channel matrix with \mathbf{h}_i is the column vector of N_r elements, $\mathbf{x} = [x_1, \dots, x_{N_t}]^T$ is the transmitted vector that contains N_t different FSIM symbols, \mathbf{v} is $N_r \times 1$ channel noise vector and its v_r elements are complex Gaussian variables, i.i.d., with zero-mean and variance σ^2 , i.e, $CN(0, \sigma^2)$ for $r = 1, \dots, N_r$.

4.5.1.2.1 Equalization

The received signal suffers from IAI and inter-symbol interference due to the MIMO transmission and the used non-Nyquist filters in FSIM scheme respectively. In other words, the former represents the interference from simultaneously transmitted symbols from other antennas, while the latter is the interference contribution from the previous and the future symbols emitted from the same antenna (within a filter period). When the receiver intends to detect the j^{th} FSIM symbol transmitted from the j^{th} TA, the received signal can be rewritten as follows to highlight the IAI components :

$$\mathbf{y} = \mathbf{h}_j x^j + \sum_{l=1, l \neq j}^{N_t} \mathbf{h}_l x^l + \mathbf{v}. \quad (4.62)$$

In addition to IAI, the symbols suffer from ISI due to filters used at the transmitter that do not satisfy Nyquist ISI criterion. At the first stage in receiver side, the received signal is passed through an equalizer to eliminate the effect of the channel \mathbf{H} . Note that ZF or MMSE equalizers can be used, or any other equalizer that conserves the FSIM filter contribution. Here the equalization is performed at sample level before matched filter and down-sampling and not at symbol level as usual, since the pulse shaping filter used at the transmitter is still unknown at this stage. In the following, the linear ZF equalizer is adopted to eliminate channel effect on all received samples and allow the detection of the

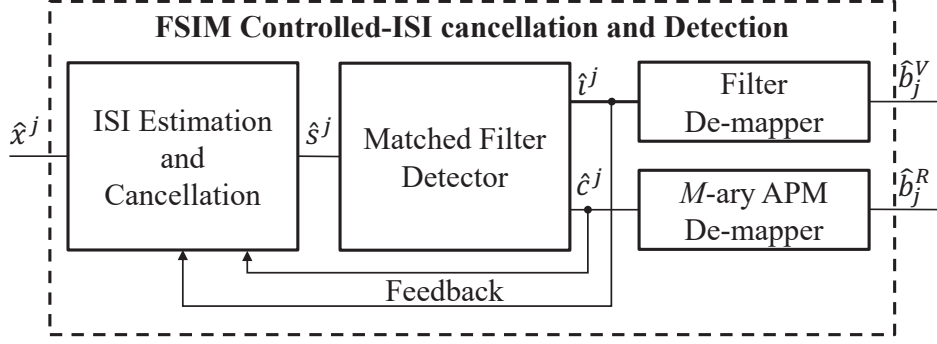


Figure 4.30 – System model of FSIM demodulator with the controlled-ISI cancellation and detection.

transmitted FSIM symbol (APM symbol and index of the used filter). Then the output of the equalizer can be written as follows:

$$\hat{\mathbf{x}} = \mathbf{W}\mathbf{y} = \mathbf{x} + \mathbf{W}\mathbf{v}, \quad (4.63)$$

where $\hat{\mathbf{x}}$ is the vector of equalized samples and $\mathbf{W} = [\mathbf{w}_1^T, \mathbf{w}_2^T, \dots, \mathbf{w}_{N_t}^T]^T$ is the ZF weight matrix expressed as:

$$\mathbf{W} = (\mathbf{H}^H \mathbf{H})^{-1} \mathbf{H}^H. \quad (4.64)$$

and \mathbf{w}_j is the j^{th} row of \mathbf{W} .

Afterward, in order to have an effective detection of the transmitted FSIM symbol (filter index and APM symbol), the estimation and cancellation of the controlled-ISI from the used non-Nyquist filters is performed in parallel as shown in Fig. 4.28 on the equalized stream of samples \hat{x}^j similar to the simplified SISO FSIM receiver depicted in Fig. 4.30.

Hence, the samples stream \hat{x}^j corresponding to the j^{th} TA is passed to the ISI Estimation and Cancellation block [22], that intend to remove the ISI generated from the used filters that do not satisfy Nyquist zero-ISI criterion. The output of the ISI Cancellation block can be expressed as follows:

$$\hat{s}_n^j[m] = c_n^j f_{i_n}^j[m] + ISI_{resid}^j[m] + \mathbf{w}_j \mathbf{v}[m] \quad (4.65)$$

where the $ISI_{resid}^j[m]$ represents the residual ISI that might still persist due to the non-perfect ISI cancellation.

Then, for each $j = 1, \dots, N_t$, the ISI cancellation output signal $\hat{s}_n^j[m]$ is passed through a MF-based detector to estimate the APM symbol and the index of the selected filter at the j^{th} TA.

4.5.1.2.2 Detection

In the following, the detection of the APM symbol and filter index is considered for one TA, since all TAs perform in parallel a similar detection. Each MF-based detector contains a bank of N matched

filters g_k where $g_k(t) = f_k(T_f - t)$ with $0 \leq t \leq T_f$, $T_f = L.T_s$ and T_s is the sampling period [22]. The output of these filters r_k^j sampled at the instant T_f can be expressed as follows:

$$r_k^j = \int_0^{T_f} \hat{s}^j(\tau) f_k(\tau) d\tau, \quad k = 1, 2, \dots, N. \quad (4.66)$$

Then, the selected filter at the transmitter side on the j^{th} TA can be recovered by taking the maximum energy of the sampled MF outputs r_k^j as follows:

$$\hat{i}^j = \arg \max_k \|r_k^j\|^2. \quad (4.67)$$

After estimating the index of the filter being used at the j^{th} TA, the APM symbol detection is performed on $r_{\hat{i}^j}$. Afterward, the detected symbols \hat{c}^j and filter index \hat{i}^j are passed to their corresponding demappers to recover the sub-streams \hat{b}_j^R and \hat{b}_j^V respectively. The above mentioned steps are processed in parallel for the N_t transmitted FSIM symbols, and finally the parallel to serial recovers the bitstream \hat{b} as depicted in Fig. 4.28.

4.5.2 Theoretical Performance

In this section, the analytical lower bound in terms of Symbol Error Rate (SER) for the proposed system SMX-FSIM is derived, where we consider that the ZF equalizer and the parallel MF-based detector are used. The system performance of SMX-FSIM depends on the APM symbols and filter index detection. In addition, the lower bound theoretical SER and BER are deduced under the assumption of perfect ISI cancellation (*i.e.* $ISI_{resid} = 0$), and near-orthogonal filter shapes that can be achieved when the filter bank is well designed.

The output of the matched filter bank at j^{th} TA sampled at $t = T_f$ given by r_k^j in (4.66) can be rewritten as:

$$\begin{aligned} r_k^j &= \langle \mathbf{f}_k, \mathbf{f}_{i_n^j} \rangle . c_n^j + \langle \mathbf{f}_k, \mathbf{w}_j \mathbf{v}_n \rangle \\ &= \begin{cases} c_n^j + \langle \mathbf{f}_k, \mathbf{w}_j \mathbf{v}_n \rangle & \text{for } k = i_n^j \\ \langle \mathbf{f}_k, \mathbf{f}_{i_n^j} \rangle . c_n^j + \langle \mathbf{f}_k, \mathbf{w}_j \mathbf{v}_n \rangle & \text{for } k \neq i_n^j \end{cases} \end{aligned} \quad (4.68)$$

where \mathbf{v}_n are the L samples around the n^{th} symbol.

The detection of the filter index \hat{i}^j at the j^{th} TA is estimated according to (4.67) by choosing the maximum $U_k = \|r_k^j\|^2$ which represents the energy of r_k^j . Note that U_k follows the independent non-central Chi-Square distribution [203] for all k with degree of freedom equal 2 and the non-central

parameter α^2 that can be expressed as follows:

$$\alpha_{k,q}^2 = \begin{cases} \|c_n^j\|^2 = \mathcal{E}_q & \text{for } k = i_n^j \\ \langle \mathbf{f}_k, \mathbf{f}_{i_n^j} \rangle^2 \cdot \|c_n^j\|^2 = \langle \mathbf{f}_k, \mathbf{f}_{i_n^j} \rangle^2 \cdot \mathcal{E}_q & \text{for } k \neq i_n^j, \end{cases} \quad (4.69)$$

where $f_{i_n^j}$ is the selected filter at the j^{th} TA and \mathcal{E}_q is the transmitted energy of the APM symbol c_n^j .

Therefore, the PDF of U_k can be written as follows:

$$p(u_k) = \frac{1}{2\sigma_p^2} e^{-\frac{u_k + \alpha_k^2}{2\sigma_p^2}} \mathcal{I}_0\left(\frac{\alpha_k \sqrt{u_k}}{\sigma_p^2}\right), \quad (4.70)$$

where $u_k \geq 0$, σ_p^2 is the post-equalization noise variance, and $\mathcal{I}_0(\rho)$ is the zero order modified Bessel function of 1st kind given by (4.19).

Since the MF-based detector for all $j = 1, \dots, N_t$ performs APM and filter index estimation in parallel for all TAs similar to SISO-FSIM detection [22], we will consider the detection on one of the TA, and the index j is omitted. Let us suppose that the filter f_1 is selected at the transmitter side for the APM symbol c_n . The detector makes a correct index decision; if the probability of u_1 is greater than all other $N - 1$ u_k values for $k \neq 1$. The filters are considered orthogonal to derive the lower bound, and thus the u_k become statistically independent, then the joint probability can be factorized as a product of $N - 1$ marginal probabilities of the form:

$$P(u_k < u_1 | u_1) = \int_0^{u_1} p_{u_k}(x_k) dx_k, \quad k = 2, 3, \dots, N. \quad (4.71)$$

Hence, the probability of a correct decision is given as follows [22]:

$$\begin{aligned} P_{c,\mathcal{E}_q} &= P(U_2 < U_1, U_3 < U_1, \dots, U_N < U_1) \\ &= \int_0^\infty \left(\prod_2^N P(u_k < u_1 | u_1) \right) \cdot p(u_1) du_1 \end{aligned} \quad (4.72)$$

and the probability of a filter index error can be deduced from probability of a correct decision as:

$$P_{e,\mathcal{E}_q} = 1 - P_{c,\mathcal{E}_q}. \quad (4.73)$$

The average probability of filter index error ought to be the weighted average filter error across the Q possible energy levels of APM symbols, given as follows:

$$P_{e,filter} = \sum_{q=1}^Q P_{e,\mathcal{E}_q} \cdot P(\mathcal{E}_q), \quad (4.74)$$

where $P(\mathcal{E}_q)$ is the probability of occurrence of the energy level \mathcal{E}_q .

The SER of M -ary QAM modulation in AWGN channel is given by [203]:

$$P_{e,QAM} = \begin{cases} 4 \left(1 - \frac{1}{\sqrt{M}}\right) Q \left(\sqrt{\frac{3}{M-1}} SINR \right) & \text{k is even} \\ -4 \left[\left(1 - \frac{1}{\sqrt{M}}\right) Q \left(\sqrt{\frac{3}{M-1}} SINR \right) \right]^2 & \\ \left(\frac{4IJ - 2I - 2J}{M} \right) Q \left(\sqrt{\frac{6 \log_2(IJ)}{(I^2 + J^2 - 2)}} SINR \right) & \text{k is odd} \\ -\frac{4}{M} (1 + IJ - I - J) Q^2 \left(\sqrt{\frac{6 \log_2(IJ)}{(I^2 + J^2 - 2)}} SINR \right) & \end{cases} \quad (4.75)$$

where $SINR$ is SINR, $k = \log_2 M$, $I = 2^{\frac{k-1}{2}}$, and $J = 2^{\frac{k+1}{2}}$.

Subsequently, the correct detection of FSIM symbols arises when both the filter and the APM symbol are correctly estimated, therefore the probability of a correct FSIM decision at a given TA is $(1 - P_{e,filter})(1 - P_{e,QAM})$ and the SER_{FSIM} is given by:

$$SER_{FSIM} = 1 - (1 - P_{e,filter})(1 - P_{e,QAM}). \quad (4.76)$$

Then, the SINR estimation at the j^{th} branch can be written as:

$$SINR_j = \frac{\mathbb{E}\{\hat{s}_j^2\}}{\mathbb{E}\{\mathbf{w}_j \mathbf{v}_n\}} = \frac{P}{\|\mathbf{w}_j\|^2 \sigma^2} = \frac{SNR}{\|\mathbf{w}_j\|^2} \quad (4.77)$$

where P is the average power on each TA, and SNR is the average transmitted signal to noise ratio.

We defined $\omega_j = 1/\sqrt{\|\mathbf{w}_j\|^2}$, then ω_j meets general Rayleigh distribution with variance $1/2$ and degree of freedom $2(N_r - N_t + 1)$ when the channel matrix \mathbf{H} follows Rayleigh distribution. The PDF of ω_j is the following:

$$p_{\omega}(\omega_j) = \frac{2}{(N_r - N_t)!} (\omega_j)^{2(N_r - N_t) + 1} e^{-(\omega_j)^2} \quad (4.78)$$

In the ZF algorithm, the FSIM symbol detection is implemented independently on each branch of the equalizer output corresponding to the symbol emitted from the j^{th} TA with same configuration (filter bank, APM scheme and order), and the SINR of each sub data stream follows the same distribution with the same degree of freedom. Hence, the average SER of SMX FSIM symbol with ZF and MF based detector receiver can be obtained under the flat Rayleigh fading channel as follows:

$$SER_{SMX FSIM} = \frac{1}{N_t} \sum_{j=1}^{N_t} (SER_{SMX FSIM}^j) = SER_{SMX FSIM}^j$$

$$= \int_0^{\infty} SER_{FSIM}(\omega_j) p_{\omega}(\omega_j) d\omega_j \quad (4.79)$$

4.5.3 Results and Discussions

4.5.3.1 Theoretical and simulated performance comparison of SMX-FSIM to equivalent SMX-QAM system

In this section, Monte Carlo simulation in Rayleigh channel is performed to evaluate the proposed system SMX-FSIM and validate the derived theoretical lower bound SER performance (4.79). Note that the theoretical SER performance of SMX-QAM with ZF equalizer is according to [209, p. 2, (9)]. In addition, the SMX-FSIM system is compared at different transmission rates to its equivalent SMX-APM systems. For a fair comparison, both systems with ZF equalizer are compared with same number of receive antennas and under the same SE, which requires either the same modulation schemes with SMX-FSIM and SMX-QAM or the same number of transmit antennas. We cannot conserve the same values for both variables because SMX-QAM needs to accommodate the virtual bits conveyed in the filter IM domain by increasing one of these parameters. The simulation parameters for all configurations in this section are summarized in Table 4.2.

Table 4.2 – Simulation parameters

Parameters	Value
N_t for SMX-8QAM, SMX 2-FSIM-QPSK	[4, 8, 10]
N_t for SMX-QPSK	[6, 12, 15]
N_r	[8, 12, 16]
η	10
Oversampling factor: λ	8
Filter's length: L	81
Pulse shaping filter for Conventional Transceiver	Root Raised Cosine (RRC)
Number of channel realizations	500
Total Number of symbols	5×10^6

Figures 4.31a-4.32 show the SER performance for SMX-QAM and SMX-FSIM with/without perfect ISI cancellation in Rayleigh channel by transmitting 12 to 30 bits per MIMO symbol (or bit per channel use (bpcu)). In addition, the theoretical SER for both systems are compared to the Monte Carlo simulation results. The notation N -FSIM-APM is used to describe FSIM scheme with N filters and APM modulation schemes.

The different systems with 12 bpcu and $N_r = 8$ are: SMX-QPSK with $N_t = 6$, SMX 2-FSIM-QPSK and SMX 8QAM with $N_t = 4$. As we can notice that when we are using the same QAM order M for SMX-FSIM and SMX-QAM, N_t for the SMX-QAM system is larger to have the same SE. Similarly,

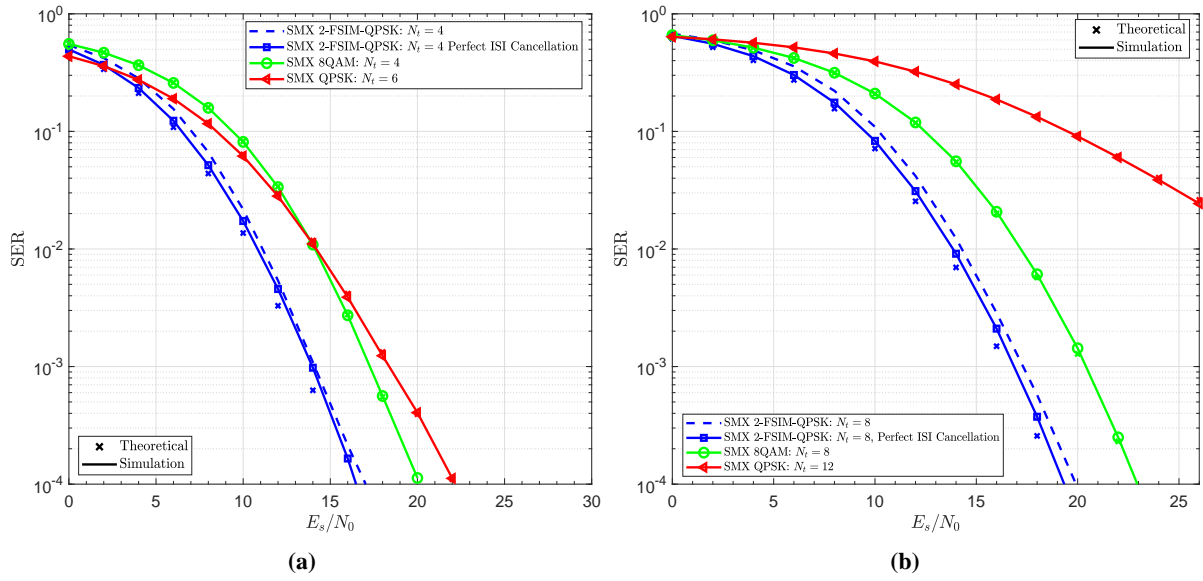


Figure 4.31 – SER performance of the proposed SMX 2-FSIM-QPSK system and its equivalent SMX-QAM systems of the same SE: (a) SE= 12 bpcu with $N_t = 8$, (b) SE= 24 bpcu with $N_t = 12$.

when the same N_t is used, the modulation order is increased for SMX-QAM for same reason. The SER performance of these systems are depicted in Fig. 4.31a, and it is clear that SMX 2-FSIM-QPSK system has 3 dB and 5.2 dB performance gain at $\text{SER} = 10^{-4}$ compared to the equivalent SMX-8QAM and SMX-QPSK systems respectively.

Similar comparisons with larger number of transmit antennas are provided to achieve higher SE. The results in Figs. 4.31b-4.32 show that SMX 2-FSIM-QPSK with $N_t = 8$ (SE=24 bpcu) and $N_t = 10$ (SE=30 bpcu) achieve around 3-3.5 dB performance gain compared to SMX-8QAM with same number of transmit antennas and more than 12 dB gain compared to SMX-QPSK.

Finally, it is worth mentioning that the simulated SER for SMX-QAM matches their theoretical curves, and the simulated SER for SMX-FISM system with perfect ISI cancellation is very tight to its theoretical lower bound in all configurations. Whereas, a slight performance degradation (less than 0.8 dB) can occur when using the proposed ISI estimation and cancellation technique due to residual ISI from the non-Nyquist filters.

4.5.3.2 Spectral Efficiency Analysis: SMX-FSIM vs existing MIMO techniques

In this section, the SE of different MIMO techniques with/without IM shown in Table 4.3 is analyzed using different number of TAs N_t and modulation order M . This comparison considers the conventional SMX with linear APM (QAM, PSK), and several transmit spatial modulations with/without APM that uses the TA(s) indices to convey additional information bits. The SE of these systems are summarized in Table 4.3 while assuming $N_r \geq N_t$, and Figs 4.33a-4.33b compare their SEs as function of number

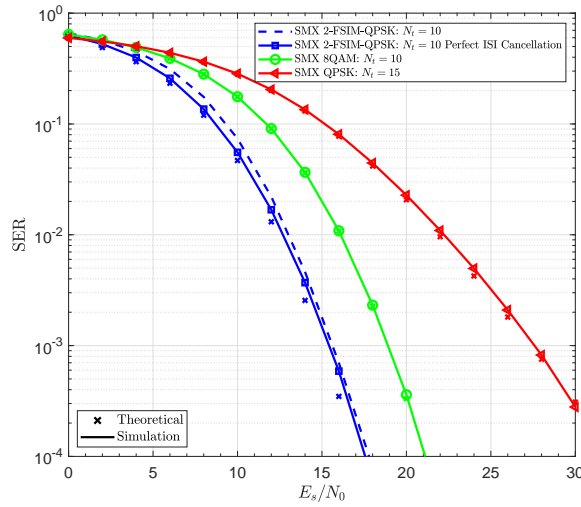


Figure 4.32 – SER performance of the proposed SMX 2-FSIM-QPSK system and its equivalent SMX-QAM systems of same SE= 30 bpcu and $N_r = 16$.

of TAs with $M = 4$ and $M = 16$ respectively. For clarification, the ExSSK and VGSM (shown in Table 4.3) allow a variable number of active TAs to increase the SE. For the same reason, a separate indexation for the in-phase and quadrature components is considered in Bi-SSK [107] and Quadrature SM [108].

Note that the SE of GSSK and GSM depends on the number of activated TAs N_a as shown in Table 4.3, and in these figures N_a is selected to achieve the maximum SE with a specific N_t that occurs when $N_a = \frac{N_t}{2}$ with GSSK (depends on M -ary order with GSM using $N_a < N_t$ to enable IM since GSM using $N_a = N_t$ is same as conventional SMX). Figs. 4.33a-4.33b show that the transmit spatial IM schemes without APM (i.e. SSK [102], GSSK [103], Bi-SSK [107], ExSSK [113]) suffer from a limited SE gain, and thus they are more suitable for low data rates applications. Whereas a higher SE is reached when incorporating APM symbol transmission with IM (i.e., SM, GSM, QSM, etc.). It is clear that the highest SE is achieved by the conventional SMX-APM, GSM, and the proposed SMX-FSIM system due to the important multiplexing gain with/without IM. However, SMX-FSIM achieves 1.5 (resp. 1.25) times higher SE with 2 filters only compared to SMX-QPSK (resp. SMX-16QAM) as depicted in Fig. 4.33a-4.33b where SMX-FSIM shows its superiority over all other MIMO techniques. In addition, it is worth mentioning that the number of activated TAs N_a with transmit spatial IM is less than N_t but they require full-RF transmit architecture (i.e. Number of RF chains= N_t) to avoid SE degradation. Note that the transmit spatial IM schemes with RF-switching having the number of RF chains equals to the maximum N_a suffer from spectral regrowth due to pulse shaping time truncation to symbol period, and thus a SE degradation will occur [174]. Moreover, the RF-switching time at each symbol period introduces additional SE degradation [175]. Thus, the obvious solution for all transmit spatial IM is to use a full-RF transmit architecture to avoid this SE problem.

Table 4.3 – Spectral efficiency of different $N_t \times N_r$ MIMO techniques (Selected from Table 2.2).

	System Name	Spectral Efficiency \mathcal{L} (bpcu)	N_a number of activated TA(s)
SMX	SMX-APM	$N_t \log_2 M$	N_t
	SMX-FSIM	$N_t \log_2 M + N_t \log_2 N$	N_t
Transmit Spatial IM	SSK [102]	$\lfloor \log_2 N_t \rfloor$	1
	GSSK [103]	$\lfloor \log_2 C_{N_t}^{N_a} \rfloor$	N_a
	Bi-SSK [107]	$2 \lfloor \log_2 N_t \rfloor$	$N_a = 1$ for I/Q: {1, 2}
	ExSSK [113]	N_t	$\{0, \dots, N_t\}$
	SM [98]	$\log_2 M + \lfloor \log_2 N_t \rfloor$	1
	GSM [105]	$N_a \log_2 M + \lfloor \log_2 C_{N_t}^{N_a} \rfloor$	N_a
	QSM [108]	$\log_2 M + 2 \lfloor \log_2 N_t \rfloor$	$N_a = 1$ for I/Q: {1, 2}
	VGSM [115]	$\approx \log_2 M + \log_2(2^{N_t} - 1)$	$\{1, \dots, N_t\}$

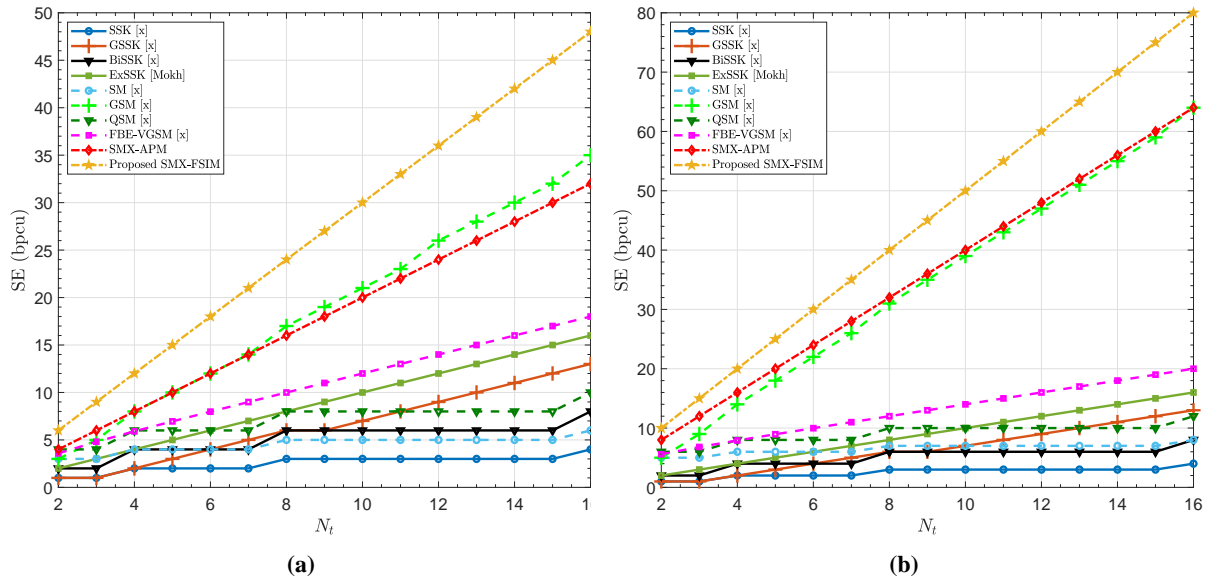


Figure 4.33 – Maximum SE for different MIMO techniques: $N_a = [1, \dots, N_t - 1]$ for fixed N_a schemes, $N = 2$ for FSIM, and different M for systems with APM: (a) $M = 4$, (b) $M = 16$.

4.5.3.3 Comparison of SMX-FSIM, conventional SMX and GSM in sub-THz environment

In this section, the best candidates in terms of SE highlighted in previous section are evaluated from different perspectives while considering sub-THz challenges and limitations. Note that SMX-QAM and GSM system are investigated in sub-THz environment in [16, 17], and the results show that using lower modulation order M is more efficient especially in sub-THz with RF impairments and limitations such as higher robustness to PN, lower transmit power and less ADC resolution requirements. For this reason, the proposed SMX-FSIM system using QPSK is compared to their equivalent GSM and SMX schemes with the same SE.

4.5.3.3.1 Performance in sub-THz channel with RF impairments

In this sub-section, the performance of these candidates is evaluated under indoor sub-THz channels and subjected to PN impairment. The sub-THz MIMO channels are generated using ray-based deterministic channel model [36] at 150 GHz carrier frequency with an in-office environment and a transceiver distance separation up to 8 meter. When considering a wide band system like our case in sub-THz, the PN impairment can be modeled by Gaussian distribution with zero mean and σ_g^2 variance [11], and in the following different PN levels are considered: low $\sigma_g = 10^{-3}$, medium $\sigma_g = 10^{-2}$, and high $\sigma_g = 10^{-1}$. For fair comparison, the SMX FSIM, SMX QAM and GSM systems are configured to achieve the same SE of 12 bpcu with same number of RAs, and same modulation scheme QPSK or same number of TAs. The configuration of these systems are summarized in Table 4.4 where we can observe the different systems of same SE either have the same M modulation order or same N_t , and they use the full-RF transmitter architecture. Note that a pulse shaping filter is considered with all MIMO systems before transmission with the same parameters shown in Table 4.2, and a low complexity receiver based on ZF equalizer is adopted with all systems to allow a practical implementation of downlink scenario where the user equipment have complexity and energy constraints.

Table 4.4 – System configuration for sub-THz candidates with 12 bpcu.

System	N_t	N_r	M	N_a	N
SMX-FSIM	4	10	4	4	2
SMX-QAM	4	10	8	4	1
SMX-QAM	6	10	4	6	1
GSM	6	10	4	5	1
GSM	9	10	4	3	1

The non-coherent SMX 2-FSIM-QPSK system with low and medium PN levels achieves the best performance compared to its competitor systems as depicted in Figs. 4.34a-4.34b. For instance, SMX 2-FSIM-QPSK has a 3.9 dB and 18 dB gain compared to SMX-8QAM with same number of TAs and SMX QPSK (same modulation) respectively. Similarly, SMX 2-FSIM-QPSK has 9.8 dB gain compared to GSM-QPSK with $N_t = 9$ and $N_a = 3$, while GSM-QPSK with $N_t = 6$ and $N_a = 5$ suffers from important error propagation that leads to error floor. The GSM system in general are

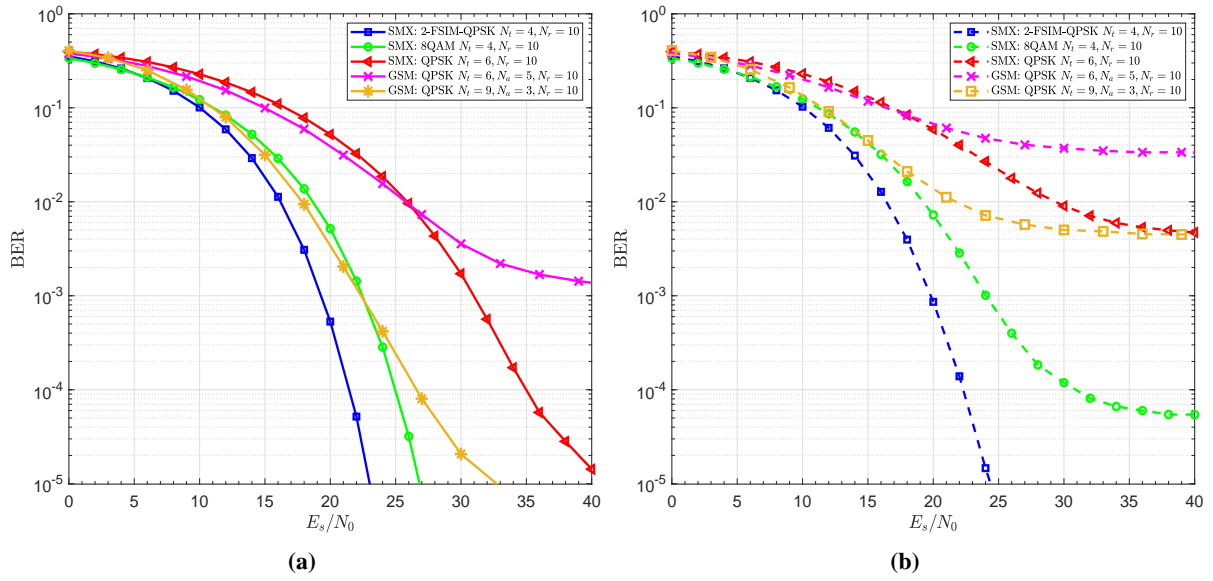


Figure 4.34 – Uncoded BER performance of the proposed non-coherent SMX FSIM compared to SMX-QAM and GSM in sub-THz channels. The SE for all systems is 12 bits/symbol (bcpu) and they are subjected to different PN levels: (a) low PN ($\sigma_g^2 = 10^{-1}$), (b) medium PN ($\sigma_g^2 = 10^{-2}$).

more prone to error since the mis-detection of the activated TAC does not cause only virtual bit errors but it propagates to the detection of all transmitted APM symbols in the same MIMO vector due to the attempt of APM symbols detection on non-activated TAs. This drawback of GSM clearly appears when $N_t = 6$ and $N_a = 5$ in both figures, while the other GSM configuration performs better since it is well known that GSM performance is enhanced when transmitting most of the information bits by means of IM. However, the SMX FSIM system overcomes GSM drawback of error propagation to all APM symbols by the decentralization of virtual bits transmission to N_t group of virtual bits, and thus a mis-detection of filter index can affect only the subsequent single APM symbol detection and not all the transmitted APM symbols like in GSM. Furthermore, the filter index mis-detection does not cause necessarily an APM symbol error since the transmitted APM symbol is not completely lost in contrast to GSM that drops the APM symbols on non-activated TAs.

A similar conclusion can be drawn at medium PN level ($\sigma_g^2 = 10^{-2}$) from Fig.4.34b. Besides, it worth mentioning that SMX FISM with linear receiver is the only system able to operate at this PN level without an error floor. However, all these system configurations suffer from an error floor when subjected to very high PN level ($\sigma_g^2 = 10^{-1}$). In conclusion, the non-coherent SMX FSIM provides the best PN robustness among these candidates, but a PN mitigation technique and/or an APM less sensitive to PN (e.g., PAM, spiral constellations [180], Polar QAM [210], ...) are necessary at very high PN level.

4.5.3.3.2 Detection Complexity

In this section, we characterize these systems in terms of the computational complexity of the optimal ML and the low complexity ZF based equalizer/detector. Their average complexity per symbol are expressed in terms of RMs and summarized in Table 4.5, where each Complex Multiplication (CM) consists of 4 RMs, and it can be computed using 3 RMs if one term is known in advance [189, p. 4, (12)]. The computational complexity of the ZF matrix for the $N_r \times N_t$ channel \mathbf{H} is expressed in terms of RMs as follows:

$$C_{W_{ZF}} = 4\left(\frac{2N_t^3 + 3N_t^2 - 5N_t}{6} + 2N_r N_t^2\right), \quad (4.80)$$

where the first term is for the square matrix $\mathbf{H}^H \mathbf{H}$ inversion and the second term represents the needed multiplications to deduce the pseudo inverse of \mathbf{H} . However, the ZF matrix calculation can be computed once when the channel is static for the duration of N_s symbols. Note that the ZF equalization for SMX-APM and GSM can be performed after matched filtering and down-sampling, while that for SMX-FSIM should be done for the whole received signal (all samples: $N_s \lambda + L - 1$) prior to the filter index detection, and then performs the matched filtering using the detected filter. Hence, the sample level equalization for FSIM is approximately λ times larger than that of symbol level equalization.

The complexity of SMX-FSIM receiver lies in the equalization, ISI estimation and cancellation block, and the matched filter detector. The matched filter on each TA performs N convolutions with a filter of length L known in advance, then the middle sample is used for detection after the sampling. Thus, this middle sample is computed by L CMs when the signals of the convolution are completely overlapped. For the filter index and APM symbol detection, $N + M$ Euclidean Distances (EDs) are computed respectively where ED consists of 2 RMs. Thus, the matched filter complexity is expressed as:

$$C_{MF} = 3NL + 2N + 2M \quad (4.81)$$

The ISI estimation and cancellation block (depicted in [22, Fig. 3] contains a MF detector for tentative decisions, and the Tx filter output regeneration that multiplies the estimated tentative APM symbol with the filter (L CMs= $3L$ RMs). Similarly, the feedback of the previously detected symbol contains L CMs= $3L$ RMs. Afterward, an overlap and add is performed to deduce the estimated ISI, then it is subtracted from the input signal where these steps contain only additions/subtractions. Therefore, the total complexity of the ISI estimation and cancellation block is:

$$C_{\text{ISI cancellation}} = C_{MF} + 6L, \quad (4.82)$$

The ZF based equalizer/detector provides a prominent complexity reduction for all systems compared to the ML counterpart, and SMX-FSIM suffers from higher receiver complexity which is proportional to the filter length L as shown in Table 4.5. However, it is clear from the results in subsections 4.5.3.1 and 4.5.3.3.1 that the performance of SMX-QAM and GSM with their linear detection are not satisfactory as SMX-FSIM and the formers have a high error floor with medium PN level ($\sigma_g = 10^{-2}$). Therefore, this additional complexity of SMX-FSIM linear receiver, compared to SMX-

Table 4.5 – Average computational complexity in terms of real multiplications for SMX-FSIM, SMX-APM, and GSM equalizers/detectors.

System	ZF equalizer/detector complexity	ML complexity
SMX-FSIM	$(\frac{N_s \lambda + L - 1}{N_s})4N_t N_r + N_t(C_{MF} + C_{\text{ISI cancellation}}) + C_{W_{ZF}}/N_s$	$2^{\mathcal{L}_{\text{SMX-FSIM}+1}}(2N_t + 1)LN_r$
SMX-APM	$4N_t N_r + 2MN_t + C_{W_{ZF}}/N_s$	$2^{\mathcal{L}_{\text{SMX}+1}}(2N_t + 1)N_r$
GSM	$4N_a N_r + 2MN_a + C_{W_{ZF}}/N_s$	$2^{\mathcal{L}_{\text{GSM}+1}}(2N_a + 1)N_r$

APM and GSM, comes with a tremendous system performance and robustness to PN that are critical factor for sub-THz system with RF impairments and limited SNR.

4.5.3.3.3 Hardware cost and design issues

The hardware cost depends on the number of used RF-chains that contains the most expensive hardware components. In Section 4.5.3.2, it is highlighted that the full-RF transmit architecture is required with transmit spatial IM schemes to avoid SE degradation. Therefore, the number of RF-chains at Tx side is same as number of TAs N_t with all schemes, and thus it is clear from Table 4.4 and Figs. 4.33a-4.33b using any M -ary modulation scheme that SMX-FSIM system with only 2 filter shapes requires the minimum number of TAs N_t (and thus RF-chains) to achieve any SE. Therefore, SMX-FSIM allows to have the minimum possible cost for the transceiver hardware. Note that GSM receiver with some configurations can have lower cost by using smaller number of RF-chains equal to N_a , but this condition ($N_r = N_a < N_t$) can highly degrades the system performance with low complexity detectors.

It is worth mentioning that the full-RF transmitter architecture with GSM eliminates the high-speed RF switching challenge at the price of higher cost. The practical implementation of these MIMO schemes requires careful antenna array design to have low spatial correlation, and especially for GSM system since the mis-detection of the activated Transmit Antenna Combination (TAC) leads also to APM symbols error and thus highly degrades GSM overall performance [14].

4.5.3.3.4 PAPR, Link Budget and Power consumption

Based on a MIMO SC transceiver with pulse shaping, the corresponding Complementary Cumulative Distribution Functions (CCDFs) of the PAPR of SMX-FSIM, SMX-QAM and GSM systems are shown in Fig. 4.35. The PAPR for all these schemes is evaluated over one TA, since all TAs for each system have similar PAPR when using same M -ary scheme for different TAs and TAs activation is equiprobable in GSM. SMX-FSIM use the non-Nyquist filter shapes designed for filter IM domain [22], while the pulse shaping for SMX-QAM and GSM system is performed with root raised cosine filter. The CCDF that represents the probability of having a PAPR higher than a $PAPR_0$ threshold depicted in Fig. 4.35 shows clearly that SMX QPSK have the lowest PAPR 3.65 dB at CCDF of 10^{-4} , and the PAPR increases to 5.8 dB SMX 8QAM due to the higher M -ary scheme (8QAM), and to 4.4 dB (resp. 8.3 dB) with GSM using $N_t = 6$, $N_a = 5$ (resp. $N_t = 9$, $N_a = 3$). It is clear that

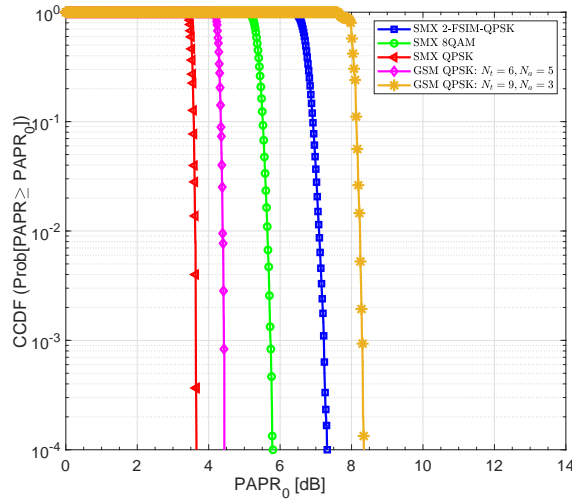


Figure 4.35 – Comparison of CCDF of PAPR for the SMX FSIM, the SMX QAM and the GSM systems with pulse shaping having SE= 12 bpcu. SMX FSIM uses the filter shapes presented in [22], while SMX QAM and GSM use RRC filter.

the PAPR of GSM increases when the ratio $\frac{N_a}{N_t}$ decreases due to the lower average power caused by zero symbol transmission when the TA is inactive. Concerning SMX-FSIM, its PAPR is 7.3 dB due to the used filter shapes that are designed to have low filter's correlation and limited ISI without any PAPR constraint. The higher PAPR reduces the Power Amplifier (PA) efficiency, and thus it affects the system power consumption. In the following, the link budget for these systems is calculated from the required SNR to achieve BER= 10^{-5} according to (3.2).

Furthermore, the power consumption of these systems are deduced based on the PA efficiency that depends on their PAPR.

The link budget for the different systems in indoor scenarios (Kiosk, enhanced throughput WLAN, etc.) with a distance up to 8 m is depicted in Table 4.6, where the GSM system with $N_t = 6$, $N_a = 5$ is omitted due to the high error floor. It is clear that SMX FSIM requires the lowest transmit power to guarantee BER= 10^{-5} due to better system performance. This low transmit power requirement is an important advantage for sub-THz bands, since the output transmit power is very limited at high frequencies with current technology. The required transmit power and the EIRP make SMX QPSK and GSM with linear ZF based detector impractical in current technology while respecting EIRP regulations in contrast to their results with ML detection discussed in [17].

In addition, it is worth mentioning that SMX-FSIM maintains its superiority in the power consumption despite the PAPR increase by the used filters due to the important performance SNR gain. For instance, SMX-FSIM with linear receiver provides a 3.21 dBm power gain compared to SMX 8QAM and more than 10 dBm compared to GSM and SMX QPSK as shown in Table 4.6. Finally, when considering a higher PN level, all systems with linear ZF based detector suffer from an error

Table 4.6 – Link budget and power consumption of SMX FSIM, SMX QAM and GSM systems with ZF based detection over sub-THz channels subjected to low PN.

System Parameters	SMX FSIM	SMX 8QAM	SMX QPSK	GSM ($N_t = 9, N_a = 3$)
Carrier frequency (GHz)			150.00	
Distance (m)			2 to 8	
Channel Bandwidth W (GHz)			0.50	
Required Transmit Power P_t (dBm)	0.04 to 12.09	3.94 to 15.99	18.04 to 30.09*	9.84 to 21.89*
Transmit antenna gain G_t (dBi)			20.00	
EIRP (dB)	20.04 to 32.09	23.94 to 35.99	38.04 to 50.09**	29.84 to 41.89**
f_{spl} (dB)			81.98 to 94.03	
Receive antenna gain G_r (dBi)			5.00	
Received power R_{xlevel} (dBm)	-56.94	-53.04	-38.94	-47.14
Thermal noise (PSD) (dBm/Hz)			-174.00	
Noise figure N_{Figure} (dBm)			7.00	
Thermal noise $N_{Thermal}$ (dBm)			-86.94	
Noise floor N_{floor}			-79.94	
Required SNR with low PN (dB)	23.00	26.90	41.00	32.80
PAPR (dB) at CCDF= 10^{-4}	7.3	5.8	3.65	8.3
PA efficiency	0.34	0.4	0.52	0.31
Power consumption (dBm)	4.71 to 16.75	7.92 to 19.96	20.87 to 32.92	14.93 to 26.97

* Required power exceeds the maximum available transmit power with current electronics technology.

** Large EIRP for indoor scenarios.

floor except SMX-FSIM as shown Fig. 4.34b, and the latter consumes only 1.5 dB more than its power consumption at the low PN level.

4.5.4 Conclusion

In this Section, a generalized MIMO Spatial Multiplexing system is proposed, thanks to filter IM domain that generalizes many existing modulation and time/frequency IM domains. In particular, FSIM scheme is considered in the proposed system to achieve the highest SE gain ($N_t \log_2 N$) among the existing MIMO systems by conveying the additional bits in the index of the used filter shape at each TA. The received signal of SMX FSIM suffers from IAI and ISI that are compensated using ZF equalizer and ISI estimation and cancellation block respectively. A linear receiver based on ZF equalizer and MF-based detector is proposed to avoid the high complexity of joint ML detector by performing parallel detection for all transmitted symbols. Note that the equalization is performed at sample level before matched filter and down-sampling, since the selected filter in FSIM symbol is still unknown for the receiver at this stage. In addition, the theoretical tight lower bound of the proposed SMX FSIM system is derived and verified by Monte Carlo simulations. The proposed SMX 2-FSIM-QPSK achieves at least 3 – 4 dB gain compared to SMX 8QAM of the same SE and number of TAs, and the performance gain increases to more than 12 dB compared to SMX QPSK of the same SE and APM order. Furthermore, the different candidates for ultra-high data rates in sub-THz bands (SMX FSIM, SMX QAM, and GSM with linear receiver) are evaluated in sub-THz channels with RF impairments and a complete analysis/comparison is provided. The results reveals that SMX FSIM has

better performance, higher robustness to PN, lower transceiver cost, higher SE/EE gain and less power consumption. However, these advantages comes with a slight receiver complexity increase which is in order of L times higher than other candidates, and this complexity can be reduced by proper design of filter bank with shorter filter length L while respecting FSIM scheme filter requirements. Finally, it is worth mentioning that SMX FSIM in sub-THz channel requires much lower SNR (4 – 18 dB less than other candidates) which is crucial for sub-THz systems with limited output power, and it is the only scheme among these candidates that can operates in a medium PN level with linear low complexity receiver.

4.6 Summary

In this Chapter 4, we first proposed a novel IM domain denoted “Filter IM domain” to further exploit IM advantages. The filter IM domain generalizes most of the existing SISO IM domains, such as time and frequency IM domains, but this domain allows a higher SE and EE enhancement due to using all available resources. We also showed that the filter IM domain could be easily reconfigured to a conventional transceiver (i.e., any APM with Nyquist pulse shaping filter, the system with OOK or PPM modulations, etc.), and most existing schemes in SISO IM (schemes in time/frequency IM domains) as shown in Fig. 4.36.

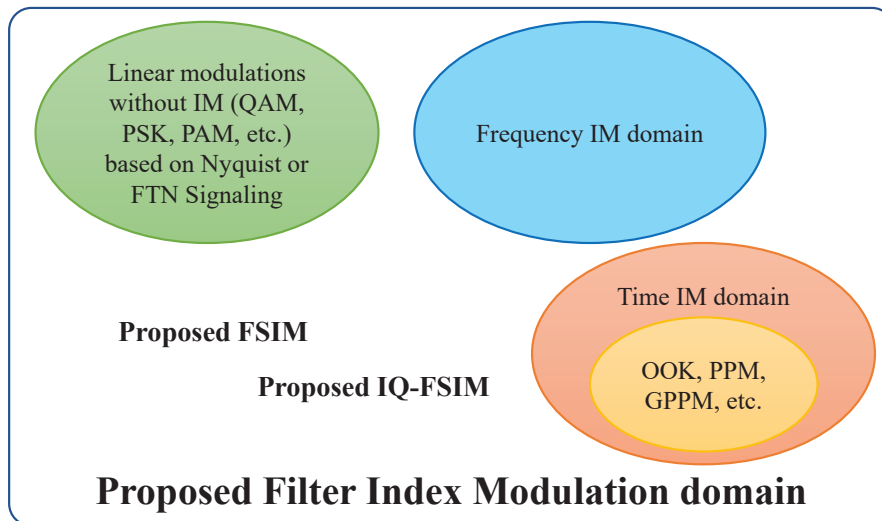


Figure 4.36 – Filter IM domain and its special cases.

In the filter IM domain, we also proposed two novel schemes that perform the indexation by using a bank of filter shapes. Both schemes maximize the IM SE gain by allowing the filter shape variation at each symbol period while transmitting an APM symbol. The first scheme, called FSIM, uses the same filter shape for the in-phase and quadrature components of the APM symbol, whereas the second one IQ-FSIM, performs separate indexation on I and Q to double the SE gain of the former. For

both schemes, the optimal joint ML detection is presented, and an MF-based detector is proposed to reach the optimal performance with a noticeable complexity reduction. The Nyquist ISI criterion is relaxed in our proposed schemes to have more distinguishable filter shapes with low-correlation. Hence, an ISI estimation and cancellation technique is developed to eliminate the predictable ISI from the used filter shapes, and the results show that this block allows reaching the optimal performance with perfect ISI cancellation when the filter bank is well designed. We then derived the theoretical lower bound for the filter error probability, BER, and SER to truly characterize our proposed systems. These theoretical results are validated by Monte Carlo simulations with different configurations. The analytical and simulated performances prove that the proposed MF-based detector reaches the optimal ML performance, and the performance of these two systems is very tight to lower bound when the designed filter bank is near-optimal. Furthermore, the proposed schemes are compared to the equivalent conventional transceiver at the same SE and under the same conditions. The results in the SISO context reveal that both FSIM and IQ-FSIM schemes have a significant performance and EE gain compared to equivalent conventional transceivers, especially when using low-order APM (e.g., QPSK) where the gain reaches more than 4 dB. The achieved gain with a non-optimal filter bank is more significant with low-order APM due to their robustness to ISI that cannot be completely compensated. However, the FSIM and IQ-FSIM with higher-order APM have a smaller gain (1 to 2 dB with 16QAM), but this gain is maintained only at a low SNR region with a very high constellation order (64QAM or higher) due to their sensitivity to ISI. Hence, it is clear that both proposed schemes enhance the performance, SE, and EE by using a non-Nyquist filter bank that adds a controllable and predictable ISI. These schemes' success is directly related to the ability to estimate the selected filter shape and the emitted APM symbol correctly prior to ISI cancellation. Therefore, the filter bank should be carefully designed to provide low cross-correlation (inter-filter correlation) and maintain a low ISI. In the next Chapter 5, the filter bank design will be addressed where the filter correlation and the introduced ISI are minimized while satisfying and considering the other constraints and requirements highlighted in sub-section 4.3.3 (bandwidth, OOB, filter length, etc.).

At the end of this chapter, the proposed FSIM system is extended to MIMO SMX system to achieve the highest SE gain among the existing MIMO systems with/without IM. For instance, the achieved gain with SMX FSIM system is $N_t \log_2 N$ higher than that of SMX QAM using the same modulation order and the number of antennas. It is also important to mention that SMX FSIM fully utilizes all time, frequency, and spatial resources in contrast to spatial IM (e.g., GSM,...) that activates a certain number of antennas and requires a full-RF architecture as highlighted in Section 3.2.7.1. In the current study, we are focusing on an ultra-high data rates system for indoor scenarios with power and complexity constraints for the UE receiver, like downlink kiosk application and enhanced throughput WLAN described in Section 1.1. For this reason, we developed and theoretically assessed the proposed SMX FSIM system with a linear receiver based on ZF equalizer and parallel MF detectors that allow us to maintain a low and feasible receiver complexity. The performance of SMX-FSIM is very tight to the derived theoretical lower bound. Compared to the equivalent SMX QAM system of the same

SE using either the same modulation order or the same number of TAs, the results reveal that SMX FSIM with a linear receiver and only two non-optimal filter shapes outperforms by 3.5 dB up to more than 12 dB these equivalent systems in Rayleigh channel. In order to complete our study and propose a new ultra-high data rate system in the sub-THz environment, a complete analysis in the sub-THz indoor environment with RF impairments is provided for the proposed system SMX FSIM, and the other candidates (SMX QAM and GSM). Finally, we showed that SMX FSIM with a linear receiver has better performance and robustness to phase noise, lower transceiver cost, higher SE/EE gain, and lower power consumption compared to its competitor candidates presented in Chapter 3. Therefore, this analysis and discussion summarized in Table 4.7 permits to conclude both Chapters 3 and 4, and it promotes SMX FSIM with a linear receiver as a very competitive candidate for low-power wireless ultra-high data rates system in sub-THz bands.

Table 4.7 – Summary of different MIMO techniques for low-power wireless ultra-high data rates systems in sub-THz bands.

MIMO systems with power-efficient low order APMs and ZF based linear receivers			
Parameter	SMX-FSIM	SMX-APM	GSM using full-RF Tx architecture
Spectral Efficiency (see Fig. 4.33)	$N_t(\log_2 M + \log_2 N)$ High	$N_t \log_2 M$ Medium	$N_a \log_2 M + \log_2 C_{N_t}^{N_a}$ where $N_a \leq N_t$ Medium
Robustness to PN (see Fig. 4.34)	High	Low to Medium	Low (High with ML, see previous Chapter)
PAPR (see Fig 4.35)	Medium	Low	Low to High (depend on M, N_a and N_t)
Energy Efficiency (see Table 4.6)	High	Medium	Medium
Linear Detector Complexity (see Table 4.5)	Medium to High (depend on filter length)	Medium	Low
Cost based on number of RF chains (see sub-Section 4.5.3.3.3)	Low	Low to Medium	High
Flexibility (Reconfigurable System)	High	Low	High

In the next chapter, the filter bank design is considered where this challenging problem is formulated as an optimization problem that allows us to successfully design the four filters used in this chapter.

Chapter 5

Filter Bank design

Contents

5.1	Introduction	186
5.2	Filter Design problem formulation	188
5.2.1	Filter Design $N = 2$	194
5.2.2	N -filter shapes design	197
5.3	Results	199
5.3.1	Filter bank of 2 filter shapes	199
5.3.2	Filter bank of N filter shapes	203
5.4	Conclusion	204

5.1 Introduction

In Chapter 4, a novel IM domain is proposed to enable a higher SE gain and generalize most existing SISO schemes with/without IM. The two proposed systems (FSIM and IQ-FSIM) in this filter IM domain convey additional information bits by indexing different filter shapes, and the Nyquist condition for zero-ISI is relaxed to find more distinguishable filter shapes and enhance the filter detection. These proposed schemes demonstrate that the ISI is not necessarily undesirable, while it is controllable and predictable. However, the introduced ISI should be kept as low as possible so that the receiver can correctly estimate the tentative decisions for estimating and canceling the introduced ISI. Hence, the filter shapes' cross-correlation and the introduced ISI should be minimized, but also other parameters (OOB radiation, filter bandwidth, filter length, etc...) should also be considered in the filter design process.

The Nyquist filter design is widely studied in the last decades [211, 212], where many methods tackle the filter design as an optimization problem. The filter optimization can consider jointly different filter properties such as:

- Filter length L , which is necessary to be kept the minimum possible while satisfying the other system requirements. This parameter minimization allows having a low and feasible system complexity. This minimization is non-convex, but it can be solved by bisection-based search on $[L_{infeasible}, L_{feasible}]$ for the minimum feasible length when all the constraints are convex (quasi-convex problem) [211].
- Self-orthogonality that means the filter impulse response f is orthogonal to translated versions of itself at integer multiples, like in wavelets and multi-rate filter banks. This constraint leads to non-convex quadratic constraints on f . This constraint can also be used to satisfy the Nyquist criterion for zero-ISI in the absence of channel distortion.
- Nyquist filters robustness to time synchronization error (timing jitter) that can be satisfied by keeping low tails' amplitude of the complete filter response (after matched filtering).
- Filter magnitude response (bandwidth, stop-band level, pass-band ripples, etc.) usually must fit within a predefined spectral mask.
- Filter phase response (linearity and bounds), where the phase linearity can also reduce the complexity by taking advantage of the filter symmetry.
- PAPR reduction of the modulated signal, which is affected by the pulse shaping filter, can be reduced by decreasing the filter tails.
- Filter normalization: the energy of the impulse response, or its DC gain.

The filter design problem with such constraints can be formulated as an optimization problem where the objective function is a weighted sum of several characteristics. Unfortunately, several constraints are non-convex in terms of the filter response. Indeed, some of these constraints (e.g., filter energy, self-orthogonality constraints, etc.) can be written as convex constraints in terms of the filter autocorrelation function instead of the filter response. When the autocorrelation-based formulation is used, another condition is required to ensure that a valid autocorrelation is found. Then, the spectral factorization techniques are used to extract the optimal filter response from its autocorrelation.

However, certain filter characteristics cannot be expressed in convex form, and thus such a non-convex problem has the potential for multiple locally optimal solutions. In this case, considerable judgment on behalf of the designer is typically required, and this intervention is also necessary when there is a tradeoff between competing filter properties.

In contrast to the state of the art Nyquist filter design, the filter shapes for the proposed FSIM/IQ-FSIM schemes have more sophisticated constraints, mainly due to the dependency between all the filters to be designed. For instance, the ISI minimization involves all the filter shapes in the bank since the filter shape in these schemes can change at the symbol rate. Similarly, the filter cross-correlation adds another layer of filters' dependency. These two constraints with the other filter bank requirements summarized in subsection 4.3.3 leads to a challenging filter design problem. Moreover, this non-trivial problem appears for the first time with the proposed schemes, to the best of our knowledge.

In the next sections, the filter constraints and requirements are developed, then two different optimization approaches are considered to tackle this filter bank design. Finally, some results and discussions are presented. The main contributions are summarized as follows:

1. **Filter design Problem formulation:** The fundamental non-convex optimization problem is formulated, then its transformation and simplification are presented. This problem deduces the filter shape by optimizing the ISI subjecting to FSIM requirements and constraints. Our aim is to minimize the ISI metric that can results from the different successive permutations of all filter shapes in the bank under the low cross-correlation (dot-product) and magnitude response (bandwidth, OOB,...) constraints with a predefined filter length. This formulation is a non-convex problem, and some relaxations are required to solve this problem. For instance, the procedure to design a bank of 2 filter shapes will take advantage of the previously designed filters by intuition, where the first filter is initialized by f_1 in Fig. 4.4, then the optimization search for its corresponding optimal filter f_2 .
2. **Recursive N filter design Algorithm:** Using the first problem formulation, a recursive optimization approach is discussed to design a larger filter bank ($N > 2$), where one filter is designed at each recursive iteration. This procedure needs to repeat until the required number of filters is designed, and it is based on the initial condition of the first filter.

3. **Joint filter design Algorithm:** Another problem formulation is considered for larger filter bank, where the different filter shapes are jointly designed while considering all filter IM schemes requirements. This strategy permits the design of a larger filter bank with lower filters' dot-product and ISI compared to the recursive approach. This procedure also requires some relaxations and initialization to overcome the non-convex limitation and enable the filter bank design.
4. **Design Insights:** Although the global optimal filter bank is not guaranteed, and the designer intervention is required to choose a good compromise for the optimization parameters, but the results reveal that the optimal performance is achieved with 2 optimized filters. The design of 4 filter shapes leads to significant performance and SE/EE gain, as shown in the previous chapter with FSIM and IQ-FSIM schemes.

5.2 Filter Design problem formulation

An FIR filter of length L is represented by its impulse response $f[m]$ (vector \mathbf{f}), $0 \leq m \leq L - 1$, or by its frequency response denoted by:

$$F(e^{j\omega}) = \sum_{m=0}^{L-1} f[m]e^{-j\omega m}. \quad (5.1)$$

When an odd-length linear phase FIR filter is considered, the design of one half of the filter impulse response $\tilde{\mathbf{f}} = [\mathbf{f}(0) \mathbf{f}(1) \dots \mathbf{f}((L-1)/2)]$ of length \tilde{L} is enough to deduce the filter impulse response f by using the (anti-) symmetric property. The vector \mathbf{f} can be written in terms of $\tilde{\mathbf{f}}$ as:

$$\mathbf{f} = \mathbf{E}\tilde{\mathbf{f}} \quad (5.2)$$

where $\mathbf{E} = \begin{bmatrix} \mathbf{I} \\ \mathbf{J} \end{bmatrix}$, \mathbf{I} is the identity matrix of size $\tilde{L} \times \tilde{L}$ and \mathbf{J} is the antidiagonal matrix of size $(\tilde{L}-1) \times \tilde{L}$ (without first row for L odd) illustrated as follows:

$$\mathbf{J} = \begin{bmatrix} 0 & \dots & 0 & 1 & 0 \\ 0 & \dots & 1 & 0 & 0 \\ \vdots & \vdots & \vdots & \vdots & \vdots \\ 1 & \dots & 0 & 0 & 0 \end{bmatrix} \quad (5.3)$$

Consequently, the frequency response of f can be expressed in terms of that of \tilde{f} as follows:

$$F(e^{j\omega}) = e^{j\theta(\omega)} \tilde{F}(e^{j\omega}) \quad (5.4)$$

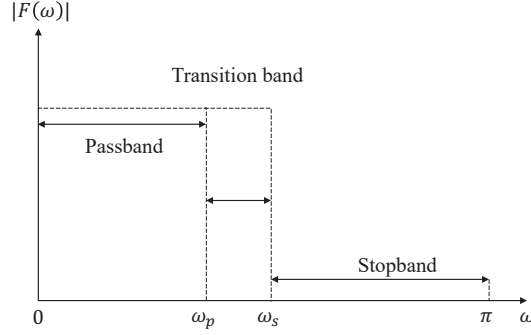


Figure 5.1 – Low pass filter magnitude response.

where $\theta(\omega) = \theta_0 + \varrho\omega$ depends only on the filter length and symmetry [211] ($\theta_0 = 0$ and $\varrho = -\frac{L-1}{2}$ for odd-length even symmetric filters), and the amplitude frequency response given by:

$$\tilde{F}(e^{j\omega}) = \mathbf{A}(\omega) \text{flip}\{\tilde{\mathbf{f}}\} \quad (5.5)$$

where $\mathbf{A}(\omega) = [1, 2 \cos(\omega), 2 \cos(2\omega), \dots, 2 \cos((\tilde{L} - 1)\omega)]$ and the flip operator is to reverse the elements order in the vector. Hence the three main bands of the frequency response can be deduced from the matrix \mathbf{A} as follows:

$$\mathbf{A}_{psb}(\omega) = \mathbf{A}(0 \leq \omega \leq \omega_p, :) \quad (5.6)$$

$$\mathbf{A}_{trb}(\omega) = \mathbf{A}(\omega_p \leq \omega \leq \omega_s, :) \quad (5.7)$$

$$\mathbf{A}_{stb}(\omega) = \mathbf{A}(\omega_s \leq \omega \leq \pi, :) \quad (5.8)$$

$$(5.9)$$

where \mathbf{A}_{psb} , \mathbf{A}_{trb} and \mathbf{A}_{stb} are the sub-matrices corresponding to the passband, transition band, and stopband respectively, ω_p and ω_s are the the passband and stopband angular frequencies, respectively as depicted in Fig. (5.1).

All filter shapes in the bank should satisfy the requirements mentioned in section 4.3.3, and they can be expressed as follows:

1. **Magnitude response constraints:** These conditions in our design are responsible for maintaining a maximum bandwidth within the channel bandwidth and a low OOB (stop-band) radiations. In real systems, these conditions are required so that the filter magnitude response lies within a predefined spectral mask (a typical spectral mask is depicted in Fig. 5.2). For instance, these constraints are semi-infinite, in the sense that there is one constraint for each $\omega \in [0, \pi]$ (each value of ω generates different constraints). These constraints should be represented in a finite manner to incorporate them in the optimization framework. Thus, a popular rule of thumb to overcome the semi-infinite issue is the uniform sampling in the frequency domain where the number of frequency samples should be in the order of $N_{f\text{-samples}} \approx 15L$ [211]. Therefore, the

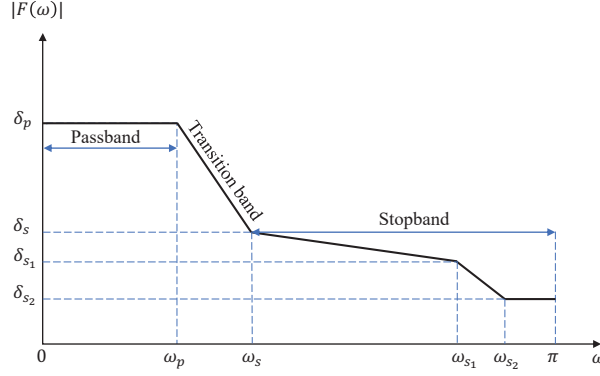


Figure 5.2 – A transmit spectral mask template.

vector ω is represented in a finite manner by $[0, \frac{\pi}{N_{f\text{-samples}}-1}, \frac{2\pi}{N_{f\text{-samples}}-1}, \dots, \pi]$, and the constraints for the transition and stopband according to Fig. 5.2 can be expressed using Matlab notations as follows:

$$|\mathbf{A}(\omega_p \leq \omega \leq \omega_s, :) \text{ flip}\{\tilde{\mathbf{f}}\}| \leq (\delta_p : \frac{(\delta_s - \delta_p)}{\text{length}(\omega_p \leq \omega \leq \omega_s) - 1} : \delta_s) \quad (5.10)$$

$$|\mathbf{A}(\omega_s < \omega \leq \omega_{s1}, :) \text{ flip}\{\tilde{\mathbf{f}}\}| \leq (\delta_s : \frac{(\delta_{s1} - \delta_s)}{\text{length}(\omega_s < \omega \leq \omega_{s1}) - 1} : \delta_{s1}) \quad (5.11)$$

$$|\mathbf{A}(\omega_{s1} < \omega \leq \omega_{s2}, :) \text{ flip}\{\tilde{\mathbf{f}}\}| \leq (\delta_{s1} : \frac{(\delta_{s2} - \delta_{s1})}{\text{length}(\omega_{s1} < \omega \leq \omega_{s2}) - 1} : \delta_{s2}) \quad (5.12)$$

$$|\mathbf{A}(\omega_{s2} < \omega \leq \pi, :) \text{ flip}\{\tilde{\mathbf{f}}\}|_{\infty} \leq \delta_{s2} \quad (5.13)$$

where these vectors' inequalities are an element by element comparison between the left-hand and right-hand sides. Note that the δ 's magnitude levels are in linear scale, and the 'length' operator returns the number of elements in the vector satisfying the condition (ω range). These upper-bounded constraints are finite and linear when considering the magnitude response (quadratic when considering the power spectrum) in $\tilde{\mathbf{f}}$ that leads to a feasible convex set in both cases.

2. **Low Filter shapes cross-correlation:** We are interested mainly in the sampled cross-correlation between the filter shapes, which is the dot-product between any filter pair given by:

$$\langle \mathbf{f}_i, \mathbf{f}_j \rangle^2 = (\mathbf{f}_i^T \mathbf{f}_j)^2 \leq \epsilon \quad i \neq j, \forall i \text{ and } \forall j \in \{1, \dots, N\} \quad (5.14)$$

where ϵ is a predefined dot-product threshold, and it should be carefully selected to guarantee that the filters are distinguishable for better detection. Hence, a near-zero ϵ value is preferred, but it should be slightly higher to allow solving the optimization problem with the other constraints (i.e., avoid restricting too much the feasible set to reach a low ISI level).

3. **Low ISI distortion (keep an acceptable level of Signal-to-Interference Ratio (SIR)):** This permits to have a low probability of error in tentative decisions under the presence of ISI. The correct tentative detections are crucial to estimate and cancel the introduced ISI in order to achieve a good system performance. Any detection error propagates to ISI estimation and can deteriorate the system performance since each estimated FSIM symbol (tentative or final decision feedback) is used to cancel the ISI from the η next symbols. Thus, the minimization of the introduced ISI from correct and false estimation should be considered to limit its propagation effect on the subsequent symbols.

Considering an AWGN channel, the ISI in conventional systems, that uses a single pulse shaping filter, is due to pulse tails with non-perfect zero-crossing at symbol periods after the matched filtering. However, in FSIM based schemes, there are several filters and the possibility of incorrect match filtering due to error in filter detection. Thus, the ISI in our case includes:

- (a) ISI resulting from correct matched filtering.
- (b) ISI resulting from incorrect matched filtering.

In the following, the ISI expressions for both cases are developed. Firstly, let's express the filter f in the z -domain similar to [212]:

$$F(z) = \sum_{m=0}^{L-1} f(m)z^{-m} = \mathbf{f}^T \mathbf{e}(z) \quad (5.15)$$

where $\mathbf{e}(z) = [1 \ z^{-1} \ \dots \ z^{-(L-1)}]$. Recalling that the equivalent transmit-receive filter (complete impulse response $q = f(m) * g(m) = f(m) * f(-m)$) is $Q(z) = F(z)F(z^{-1})$, we get:

$$Q(z) = (\mathbf{f}^T \mathbf{e}(z))(\mathbf{f}^T \mathbf{e}(z^{-1}))^T = \mathbf{f}^T \mathbf{e}(z) \mathbf{e}^T(z^{-1}) \mathbf{f} = \mathbf{f}^T \mathbf{R}(z) \mathbf{f} \quad (5.16)$$

where the $L \times L$ matrix $\mathbf{R}(z)$ is given by:

$$\mathbf{R}(z) = \mathbf{e}(z) \mathbf{e}^T(z^{-1}) \quad (5.17)$$

$$= \begin{pmatrix} 1 \\ z^{-1} \\ \vdots \\ z^{-(L-1)} \end{pmatrix} \begin{pmatrix} 1 & z & \dots & z^{(L-1)} \end{pmatrix} = \sum_{m=-L+1}^{L-1} z^{-m} \mathbf{S}_m \quad (5.18)$$

and \mathbf{S}_m are $L \times L$ constant matrices whose elements given by

$$[\mathbf{S}_m]_{u,v} = \begin{cases} 1, & u - v = m \\ 0, & \text{otherwise.} \end{cases} \quad (5.19)$$

where u and v are the row and column indices of the matrices \mathbf{S}_m , respectively. Substituting (5.18) in (5.16), we obtain

$$Q(z) = \sum_{m=-L+1}^{L-1} (\mathbf{f}^T \mathbf{S}_m \mathbf{f}) z^{-m} \quad (5.20)$$

The Nyquist condition for zero-ISI in AWGN (4.6) can be re-written using (5.20) as follows:

$$\mathbf{f}^T \mathbf{S}_m \mathbf{f} = \begin{cases} 1, & m = 0 \\ 0, & m = n\lambda, n \in \mathbb{Z}^* \\ \text{arbitrary}, & m \neq n\lambda. \end{cases} \quad (5.21)$$

These quadratic equalities defined by (5.21) form a set of non-convex hard constraints where mainly the samples of f at symbol rate (an integer multiple of λ) are restricted to the desired values denoted by a vector \mathbf{d} . Recalling that the Nyquist condition is relaxed for filter shapes indexation techniques to find distinguishable filters. Hence, these equalities are changed to soft equalities so that a filter bank with low dot-product can be designed while maintaining a low ISI, so these equalities become:

$$\mathbf{f}^T \mathbf{S}_m \mathbf{f} \approx \mathbf{d} = [\mathbf{0}^{\eta \times 1}, 1, \mathbf{0}^{\eta \times 1}]^T, m \in \Omega \quad (5.22)$$

where $\Omega = \{m = n\lambda : n \in \mathbb{Z} \text{ and } -\eta \leq n \leq \eta\}$ represents the set of constrained samples at integer multiple of symbol period. These conditions in (5.22) can be rewritten as follows:

$$\mathbf{B}\mathbf{f} \approx \mathbf{d} \quad (5.23)$$

where

$$\mathbf{B} = (\mathbf{I}^{2\eta+1 \times 2\eta+1} \otimes \mathbf{f}^T) \mathbf{S}_{\text{conditioned}} \quad (5.24)$$

$$\mathbf{S}_{\text{conditioned}} = [\mathbf{S}_{-\eta\lambda}^T, \mathbf{S}_m^T, \dots, \mathbf{S}_{\eta\lambda}^T]^T \text{ for } m \in \Omega. \quad (5.25)$$

We will use the notation \mathbf{B}_{f_i} to represent the \mathbf{B} matrix corresponding to filter f_i . Therefore, the matched filter output for both cases of correct and false match filtering can be deduced as follows:

$$\text{Correct Matched filter: } \mathbf{B}_{f_i} \mathbf{f}_i, \quad \forall i = 1, \dots, N, \quad (5.26)$$

$$\text{False Matched filter: } \mathbf{B}_{f_i} \mathbf{f}_j, \quad \forall i \text{ and } j \text{ with } i \neq j. \quad (5.27)$$

When the filter shapes are not symmetric at the center like f_1 in Fig. 4.4 (shifted version of RRC), there is $N^2 - N$ different possible false matched-filter outputs for a bank of N filter shapes ($f_i(m) * g_j(m) = f_i(m) * f_j(-m) \neq f_j(m) * g_i(m) = f_j(m) * f_i(-m)$ for $i \neq j$). For all correct

match filtering, the soft conditions in (5.23) are considered. Whereas, for the false one, the vector of desired values for samples at symbol rate defined in $\mathbf{B}_{f_i} \mathbf{f}_j$ is an all-zero vector to have low ISI and low filter shapes' dot-product (the center value square of $\mathbf{B}_{f_i} \mathbf{f}_j$ corresponds to the condition in (5.14)). Since the dot-product constraint is separately considered and a small non-zero values are tolerable, we will consider later on the minimization of the ISI square distortion ISI_{SD} given by:

$$[ISI_{SD}]_{i,j} = \|\mathbf{B}_{f_i}^* \mathbf{f}_j\|^2, \quad (5.28)$$

where \mathbf{B}^* does not consider the center symbol ($n \neq 0$) (computed using $\mathbf{S}_{\text{conditioned}}^*$ for $m \in \Omega^* = \{m = n\lambda : n \in \mathbb{Z}^* \text{ and } -\eta \leq n \leq \eta\}$).

When the transmit and receive filters are both linear phase FIR filter symmetric around the center sample, the half-responses $\tilde{\mathbf{f}}$ instead of \mathbf{f} can be used even with a false matched-filter. This approach guarantees the phase linearity and reduces the problem complexity by designing a half-filter response, and then deducing the complete impulse response according to (5.2). In this case, the matrices $\tilde{\mathbf{B}}$ and $\tilde{\mathbf{S}}$ are computed as follows: $\tilde{\mathbf{B}} = (\mathbf{I}^{\eta+1 \times \eta+1} \otimes \tilde{\mathbf{f}}^T) \tilde{\mathbf{S}}_{\text{conditioned}}$, $\tilde{\mathbf{S}}_{\text{conditioned}} = [\tilde{\mathbf{S}}_0^T, \tilde{\mathbf{S}}_m^T, \dots, \tilde{\mathbf{S}}_{\eta\lambda}^T]^T$, $\tilde{\mathbf{S}}_m = \mathbf{E}^T \mathbf{S}_m \mathbf{E}$ for $m \in \tilde{\Omega} = \{m = n\lambda : n \in \mathbb{N} \text{ and } 0 \leq n \leq \eta\}$ and $\tilde{\mathbf{d}} = [1, \mathbf{0}^{\eta \times 1}]^T$, while $n = 0$ is excluded for $\tilde{\mathbf{B}}^*$ and the identity matrix size is reduced to $\eta \times \eta$.

4. **Filter energy:** The energy of all filter shapes should be normalized to unity. This constraint avoids satisfying the above constraints by changing the filters' energy, while their normalized versions do not. Hence, the following condition should be considered:

$$\|\mathbf{f}_i\|^2 = \mathbf{f}_i^T \mathbf{f}_i = \sum_{m=0}^{L-1} f_i^2[m] = 1 \quad (5.29)$$

This quadratic equality constraint is also non-convex. Note that this constraint is included implicitly in the Nyquist condition (5.22) when $m = 0$, but we will insist on this restriction since the Nyquist condition is relaxed to soft equalities.

In our filter design, we target mainly to minimize the overall ISI resulting from false and correct match filtering defined by the following *objective*:

$$objective = \sum_{j=1, j \neq i}^N \sum_{i=1}^N [ISI_{SD}]_{i,j} + \gamma \sum_{i=1}^N \|\mathbf{B}_{f_i} \mathbf{f}_i - \mathbf{d}\|^2 \quad (5.30)$$

The ISI resulting from false and correct match filtering will be jointly minimized using *objective*, where the first and the second term in (5.30) represent the former and the latter, respectively, and the latter also includes the filters' energy to keep it near 1 while minimizing the ISI. Note that the ISI resulting from correct matched filtering is more crucial in the system performance. For this reason, a weighting factor γ is introduced in the objective function *objective* to emphasize the ISI minimization resulting from the latter.

Therefore, the fundamental optimization problem to jointly design the N filter shapes can be formulated for a given filter length L as follows:

$$\mathbf{P1} : \underset{\mathbf{f}_1, \dots, \mathbf{f}_N}{\text{minimize}} \quad \text{objective defined in (5.30)} \quad (5.31a)$$

subject to

$$|F_i(\omega)| \text{ within a predefined spectral mask according to (5.10-5.13)} \quad \forall i \in \{1, \dots, N\}, \quad (5.31b)$$

$$\langle \mathbf{f}_i, \mathbf{f}_j \rangle^2 = (\mathbf{f}_i^T \mathbf{f}_j)^2 \leq \epsilon \quad i \neq j, \forall i \text{ and } \forall j \in \{1, \dots, N\}, \quad (5.31c)$$

$$\|\mathbf{f}_i\|^2 = 1 \quad \forall i \in \{1, \dots, N\}. \quad (5.31d)$$

The multivariate optimization in **P1** (5.31) is a non-convex problem, and thus finding the global optimal solution is challenging mainly due to the following reasons::

1. The objective function (5.31a) is non-convex. In general, the optimal solution of multimodal quartic function (fourth-degree) can only be found iteratively [212], if a proper initial choice of the filter shapes could be made within the vicinity of the global minimum. Note that this optimization problem can re-formulated as a geometric program which is also non-convex, and since the filter samples can take non-strictly positive values ($f_i[m] \in \mathbb{R}$), the simple transformation to geometric program in convex form [213, p.162] cannot be applied.
2. The jointly constrained filters' dot-product (5.31c) is a quartic polynomial, and thus it is not a convex constraint. Note that its square is required to avoid the negative highly correlated filters ($\mathbf{f}_i^T \mathbf{f}_j \approx -1$) that cannot be correctly detected, especially in the presence of opposite constellations in the APM symbols set.
3. The filter energy restriction to unity (5.31d) is non-convex in terms of \mathbf{f} (quadratic equality). In the sequel, this equality is relaxed by upper bounding by one to get a convex constraint (quadratic upper-bound) as follows: $\|\mathbf{f}_i\|^2 = \mathbf{f}_i^T \mathbf{f}_i \leq 1$.

Thus **P1** requires some manipulations in order to be solved by a convex method. For the sake of optimization framework clarification, a bank of two filter shapes is designed firstly, and then it will be generalized to N filter shapes.

5.2.1 Filter Design $N = 2$

The problem **P1** contains several non-convex issues in the constraints and objective function. In the proposed problem formulation for $N = 2$, the first filter f_1 is initialized and the problem targets to find its corresponding optimal filter f_2 . The initialization of f_1 plays a major role in the problem feasibility,

so a good starting point is the previously designed filter f_1 (shown in Fig. 4.4). In this case, the condition in (5.31c) becomes an upper-bounded quadratic constraint that means a convex constraint, and the filter energy is also relaxed by upper bounding, as mentioned earlier. This new formulation leads to a quartic function optimization (due to the second term in (5.30)) with convex constraints, and thus the iterative approach is used to find the best filter shape f_2 . To deal with the non-convexity in the objective, the quartic term in the objective (later term in (5.30)) resulting from correct matched filtering is relaxed to a quadratic function. This relaxation is performed by initializing f_2 for use in \mathbf{B} computation of the later term of (5.30) only, where the initialized \mathbf{B} is denoted by $\mathbf{B}_{f_2^0}$ in first iteration $t = 1$. This filter is re-initialized at each iteration by the previous problem solution f_2^{t-1} . These relaxations lead to a quadratic optimization problem with convex constraints that can be efficiently solved. It is worth mentioning that the filter design for $N = 2$ can be seen as a bi-convex optimization problem after relaxing the energy constraint (5.31d) and initializing the filter in \mathbf{B} computation used in ISI estimation for correct matched filtering.

Hence, the problem **P1** can be reformulated for $N = 2$ to design a linear-phase \mathbf{f}_2 according to a given \mathbf{f}_1 as follows:

$$\mathbf{P2} : \underset{\tilde{\mathbf{f}}_2, \mathbf{f}_2 = \mathbf{E}\tilde{\mathbf{f}}_2}{\text{minimize}} \quad (\|\mathbf{B}_{f_1}^* \mathbf{f}_2\|^2 + \|\mathbf{B}_{f_2}^* \mathbf{f}_1\|^2) + \gamma \|\tilde{\mathbf{B}}_{f_2^{t-1}} \tilde{\mathbf{f}}_2 - \tilde{\mathbf{d}}\|^2 \quad (5.32a)$$

subject to

$$|\tilde{F}_2(\omega)| \text{ within a predefined spectral mask according to (5.10 – 5.13),} \quad (5.32b)$$

$$\langle \mathbf{f}_1, \mathbf{f}_2 \rangle^2 \leq \epsilon, \quad (5.32c)$$

$$\|\mathbf{f}_2\|^2 = \mathbf{f}_2^T \mathbf{f}_2 \leq 1 \quad (5.32d)$$

where the problem **P2** searches for the optimal \tilde{f}_2 , and the equation (5.2) is used to estimate f_2 when need it. The iterative approach will be used to solve the multimodal quartic objective function, and the stopping criteria can occur either when a predefined number of iteration N_{iter} is reached, or when the *objective* enhancement between successive stages is below a predefined tolerance threshold.

Recalling that the proposed schemes in the filter IM domain can use different filter shapes, and the MF based detector for tentative decisions performs the estimation on the received signal with ISI. Thus, to maximize the correct tentative detection and enhance the ISI estimation and cancellation, the Signal-to-Interference (SIR) ratio at the center sample of the matched filter output should be maximized. This center sample is affected by the past η and future η symbols that may have different filter shapes, and all these symbols are filtered in the MF bank by one of the filters. Thus, the false match filtering for the tails of several past and/or future pulses is occurring naturally in the tentative detection. We will neglect the possible APM symbols in the filter design process, and we will focus on searching for the

maximum-minimum SIR for all possible filter shapes permutations at these 2η symbols (past and future symbols). Hence, the number of possible filter permutations is $N^{2\eta}$ (permutations of 2η filter shapes taken from N possible filters), and let the $N^{2\eta} \times 2\eta$ matrix \mathfrak{P} be the permutation matrix that stores all the possible permutations of the transmit filter indices at the 2η positions as follows:

$$\mathfrak{P} = \begin{bmatrix} 1 & 1 & 1 & \dots & 1 & 1 & 1 \\ 1 & 1 & 1 & \dots & 1 & 1 & \vdots \\ 1 & 1 & 1 & \dots & 1 & 1 & N \\ 1 & 1 & 1 & \dots & 1 & 2 & 1 \\ 1 & 1 & 1 & \dots & 1 & 2 & \vdots \\ 1 & 1 & 1 & \dots & 1 & 2 & N \\ 1 & 1 & 1 & \dots & 1 & \vdots & \vdots \\ 1 & 1 & 1 & \dots & 1 & N & N \\ \vdots & \vdots & \vdots & \dots & \vdots & \vdots & \vdots \\ N & N & N & \dots & N & N & N \end{bmatrix} \quad (5.33)$$

Thus, knowing that f_i is used for the current symbol at the transmitter, the SIR for a filter permutation (row index p in \mathfrak{P}) at the output of correctly matched filtering for the current symbol can be expressed as follows:

$$SIR_{f_i}(p) = \frac{\text{Signal Power}}{\text{ISI Power}} = \frac{((\mathbf{B}_{f_i} f_i)_{(0)})^2}{\sum_{n=-\eta, n \neq 0}^{\eta} [(B_{f_{[\mathfrak{P}]_{p,n}}} f_i)_{(m-n\lambda)}]^2}$$

$$SIR = [SIR_{f_1}^T, \dots, SIR_{f_N}^T]^T \quad (5.34)$$

and the vector SIR of all possible SIR for the N possible transmit pulse shaping is of size $N^{2\eta+1}$. This SIR estimation considers that all tails at the current symbol are constructively overlapping, which means the worst SIR occurring when the 2η APM symbols multiplied by their corresponding filter shapes f_{i_n} have the same sign at the instant of the middle sample of the current symbol.

Therefore, to reach our ultimate goal of maximizing the minimum SIR for all filter permutations, we will track the highest minimum SIR in the iterative search to take the best filter shape f_2 as the final optimization result. Finally, Algorithm 4 summarizes the linear-phase filter shape f_2 design procedure by convex optimization given f_1 .

In this section, some introduced relaxations are based on the filter shapes' (f_1 and/or f_2) initialization. We acknowledge that the initialization of the former pilots the feasibility of the problem and the attainable minimum for ISI and filters' dot-products, but as we previously mentioned, the previous f_1 is a good starting point. In order to reduce the impact of the filter f_2 initialization (used in $\tilde{\mathbf{B}}_{\tilde{f}_2}$), the iterative approach searching for the best filter f_2 uses the previous filter shape obtained by solving **P2** as an initial value for the next stage. This iterative search for the best f_2 allows approaching

Algorithm 4 Proposed filter design procedure for linear-phase filter shape f_2 .

```

1: procedure FILTER DESIGN( $\mathbf{f}_1, \epsilon, N, \lambda, \eta, L, \text{Spectral Mask}, N_{iter}, \text{tolerance}$ )
2:   Initialization:
3:    $SIR_{min}^{best} = -\infty, objective^0 = \infty, f_1 = RRC(m - \lambda/2), f_2^0 = RRC.$ 
4:   Compute  $\mathbf{S}$  according to (5.19),  $\mathbf{B}_{f_1}, \mathbf{E}$ .

5:   Iterative search for best  $\mathbf{f}_2$ :
6:   for  $t = 1$  to  $N_{iter}$  do
7:     Update  $\tilde{\mathbf{B}}_{f_2}^{t-1}$  using the previous  $\tilde{\mathbf{f}}_2^{t-1}$  designed in iteration  $t - 1$ :
8:      $\tilde{\mathbf{B}}_{f_2}^{t-1} = (\mathbf{I}^{\eta+1 \times \eta+1} \otimes (\tilde{\mathbf{f}}_2^{t-1})^T) \tilde{\mathbf{S}}_{\text{conditioned}}$ 
9:     Solve the optimization problem P2 (5.32).
10:    Deduce  $\mathbf{f}_2$  according to (5.2).
11:    Normalize  $\mathbf{f}_2$  energy to unity  $\mathbf{f}_2 = \frac{\mathbf{f}_2}{\sqrt{\mathbf{f}_2^T \mathbf{f}_2}}$ .
12:    Estimate the  $SIR$  vector for all possible filter permutations according to (5.34).
13:    if  $\min(SIR) > SIR_{min}^{best}$  then
14:      Update  $\mathbf{f}_2^{best} = \mathbf{f}_2$  and  $SIR_{min}^{best} = \min(SIR)$  to save the filter shape that leads to highest minimum
       $SIR$  for any filter permutations.
15:    end if
16:    Compute the objective function  $objective^t$  (5.32a) using normalized  $\mathbf{f}_2$ .
17:    if  $|objective^t - objective^{t-1}| < \text{tolerance}$  then
18:      break
19:    end if
20:    Save  $\mathbf{f}_2$  in  $\mathbf{f}_2^{t-1}$  for next iteration.
21:  end for
22: return  $\mathbf{f}_2^{best}$ 

```

the optimal filter bank design if a proper initial choice of the filter shapes could be made within the vicinity of the global minimum.

5.2.2 N -filter shapes design

The bank of N filter shapes can be designed recursively and jointly. The recursive approach is based on designing one filter shape at each recursive stage, where the second filter shape is designed based on the first filter initialization, then the third filter is deduced by initializing the first two, and so on to design N filters. The maximum achievable number of filters in the bank, which can be designed recursively, is limited by the first f_1 filter shape's initialization. This means that the recursive optimization method may reach a limited number of filters N when the subsequent problem becomes infeasible with the used f_1 initialization, which is not trivial especially for $N > 2$. An alternative approach is to design the N filter shapes jointly where the initialization effect is reduced but not completely avoided, because in this case, the initialization of the N filter shapes is required to solve our non-convex optimization problem by a convex method. However, for a better convergence of N filter shape design, these filters are updated iteratively in the filter design procedure by the partially optimized filters from the previous iteration. This strategy is similar to the technique of solving jointly constrained multi-convex programming, but

unfortunately, our problem is a jointly constrained multi-non-convex problem where the convergence to a global optimum cannot be guaranteed.

In the following, the proposed recursive approach for N filter shapes design is omitted, while the joint design of N filter shapes is presented, since the latter method leads to better results with filter IM schemes. The proposed fundamental problem for N filter design is similar to **P1** (5.31), but we add another constraint concerning the relaxed Nyquist condition for zero-ISI in AWGN channel. Hence, the following condition is added to make sure that the resulting ISI from correct matched filtering remains within a predefined threshold ϵ_{ISI} :

$$\|\mathbf{B}_{f_i} \mathbf{f}_i - \mathbf{d}\|^2 \leq \epsilon_{ISI}, \quad (5.35)$$

where this quartic non-convex constraint is relaxed by initializing f_i in the matrix \mathbf{B} computations. Therefore, the relaxed problem to solve by convex approximation can be expressed as follows:

$$\mathbf{P3} : \underset{\mathbf{f}_1, \dots, \mathbf{f}_N}{\text{minimize}} \quad \sum_{i=1}^N \sum_{j=1}^N \|\mathbf{B}_{f_i^{t-1}}^* \mathbf{f}_j\|^2 \quad (5.36a)$$

subject to

$$\|\mathbf{B}_{f_i^{t-1}} \mathbf{f}_i - \mathbf{d}\|^2 \leq \epsilon_{ISI} \quad \forall i \in \{1, \dots, N\}, \quad (5.36b)$$

$$|F_i(\omega)| \text{ within a predefined spectral mask according to (5.10-5.13)} \quad \forall i \in \{1, \dots, N\}, \quad (5.36c)$$

$$\langle \mathbf{f}_i^{t-1}, \mathbf{f}_j \rangle^2 = ((\mathbf{f}_i^{t-1})^T \mathbf{f}_j)^2 \leq \epsilon \quad i \neq j, \forall i \text{ and } \forall j \in \{1, \dots, N\}, \quad (5.36d)$$

$$\|\mathbf{f}_i\|^2 = \mathbf{f}_i^T \mathbf{f}_i \leq 1 \quad \forall i \in \{1, \dots, N\}. \quad (5.36e)$$

where \mathbf{f}_i^{t-1} represents the initial value of the filter shape that will be updated by the previous results obtained in the iterative algorithm as shown in Algorithm 5. The problem **P3** targets to minimize all possible interference resulting from correct and false match filtering that can overlap with the current symbol in MF-based tentative detection defined in (5.36a). The multivariate optimization problem for the joint design of N filter shapes was multimodal non-convex objective (quartic) with three non-convex constraints (near-Nyquist filter, dot-product, and filter energy constraints) before the relaxations. The adopted relaxations by initialization transform the quartic equations to convex quadratic in the objective (5.36a) and the upper-bounded constraints (5.36b) and (5.36d), and the last constraint for filter energy is relaxed by replacing the quadratic equality by quadratic upper bound. Therefore, the relaxed problem can be solved by convex optimization for the Quadratically Constrained Quadratic Program (QCQP).

Recalling that the iterative search is required to minimize the multimodal quartic function, and thus N filter shape joint design is summarized in Algorithm 5 that solves the QCQP problem (5.36) and search iteratively for the best filter bank. Note that the optimization problem feasibility and convergence

cannot be guaranteed unless the initialization for the N filter shapes lies within the vicinity of the global minimum.

Algorithm 5 Proposed joint design procedure for N filter shapes.

```

1: procedure FILTER DESIGN( $\mathbf{f}_1^0, \mathbf{f}_2^0, \dots, \mathbf{f}_N^0, \epsilon, \epsilon_{ISI}, N, \lambda, \eta, L, \text{Spectral Mask}, N_{iter}, \text{tolerance}$ )
2:   Initialization:
3:    $SIR_{min}^{best} = -\infty, objective^0 = \infty$ , initialize  $\mathbf{f}_1, \mathbf{f}_2, \dots, \mathbf{f}_N$  by  $\mathbf{f}_1^0, \mathbf{f}_2^0, \dots, \mathbf{f}_N^0$ .
4:   Compute  $\mathbf{S}$  according to (5.19).

5:   Iterative search for best filter bank:
6:   for  $t = 1$  to  $N_{iter}$  do
7:     Update  $\mathbf{B}_{f_i}^{t-1}$  using the previous  $\mathbf{f}_i^{t-1}$  designed in iteration  $t - 1$  according to (5.24).
8:     Solve the optimization problem  $\mathbf{P3}$  (5.36).
9:     Re-initialize the filter shape  $f_i$  that contains any undefined sample value (NaN) due to
       inaccurate/infeasible optimization.
10:    Normalize  $\mathbf{f}_i$  energy to unity  $\mathbf{f}_i = \frac{\mathbf{f}_i}{\sqrt{\mathbf{f}_i^T \mathbf{f}_i}}$ .
11:    Estimate the  $SIR$  vector for all possible filter permutations according to (5.34).
12:    if  $\min(SIR) > SIR_{min}^{best}$  then
13:      Update  $\mathbf{f}_i^{best} = \mathbf{f}_i$  and  $SIR_{min}^{best} = \min(SIR)$  to save the filter shape that leads to highest minimum
       SIR for any filter permutations.
14:    end if
15:    Compute the objective function  $objective^t$  (5.36a) using normalized  $\mathbf{f}_i$ .
16:    if  $|objective^t - objective^{t-1}| < \text{tolerance}$  then
17:      break
18:    end if
19:    Save  $\mathbf{f}_i$  in  $\mathbf{f}_i^{t-1}$  for next iteration.
20:  end for
21: return  $\mathbf{f}_i^{best}$ 

```

Finally, it is worth mentioning that the filter bank design is prepared once offline to define the modulation. Thus, the computational complexity and time of the optimization algorithm is not a problem in the proposed filter IM schemes.

5.3 Results

5.3.1 Filter bank of 2 filter shapes

In this section, the FSIM scheme's performance is evaluated with the two optimized filter shapes and compared to those with the previously designed filter bank. The problem $\mathbf{P2}$ in our proposed filter design Algorithm 4 is solved using Matlab Software for Disciplined Convex Programming (CVX), a package for specifying and solving convex programs [214, 215]. The control parameters used in the filter design are the following: $L = 10, \lambda = 8, \eta = 10, \epsilon = 0.125^2, \gamma = 12$. The last two parameters are selected by the designer to have a good tradeoff between the filter properties. The optimized f_2 is obtained by initializing f_1 with the filter shape f_1 in Fig. 4.4, and f_2 is firstly initialized

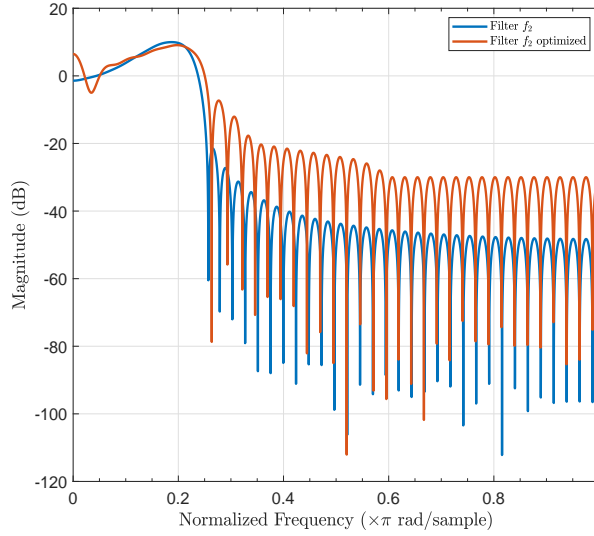


Figure 5.3 – Magnitude response of the optimized filter f_2 using the iterative ISI minimization in Algorithm 4 compared to the previously designed filter by intuition depicted in Fig. 5.4a.

by a RRC filter in \mathbf{B}_{f_2} calculation. The used magnitude response constraints are based on Fig. 5.2 with $\delta_p(dB) = 0$, $\delta_s(dB) = -20$, $\delta_{s_1}(dB) = -25$, $\delta_{s_2}(dB) = -30$ according to current sub-THz standardization activities. The magnitude response of the optimized filter f_2 is depicted in Fig. 5.3, which is clear that it matches the mentioned constraints. The impulse responses of the filter f_1 and the optimized filter f_2 are depicted in Fig. 5.4a and compared to the previously designed filter by intuition in Fig. 4.4 used in Section 4.3. Similar comparison is performed for the complete response after correct matched filtering at the receiver side in Fig. 5.4b, which highlight that the optimized filter f_2 has better zero-crossing at integer multiple of symbol period compared to the previous f_2 , and thus lower ISI. The average SIR for all possible filter permutations according to (5.34) after the optimization is 42.63 dB and the minimum SIR for the worst filter sequence permutation is 13.41 dB, while the former using the previous filters in Fig. 4.4 is 47.41 dB and the latter is 7.71 dB. This maximization of the minimum SIR is a crucial factor for better filter IM schemes' performance as shown in Figs. 5.5-5.7, because low-ISI permits to performs correct tentative decisions and more accurate ISI estimation and cancellation (lower residual ISI). Note that much higher minimum SIR can be reached using Algorithm 4 by relaxing the other constraints, and/or using different f_1 initialization.

Figures 5.5-5.7 shows the FSIM can achieve a larger performance gain compared to its equivalent scheme. For clarification, the filter design by optimization allows increasing the gain of 2-FSIM-MQAM by 0.35 dB for $M = 4$ and up to 6.5 at $\text{BER}=10^{-3}$ for $M = 64$ where the previous error floor disappears. It is clear in Figs. 5.5-5.7 that the gain increases with M , because the previous residual ISI has negligible impact on QPSK, and the minimization of ISI affects more the modulations with higher sensitivity to ISI. In addition, it is worth mentioning that 2-FSIM-MQAM for $M < 64$ using the optimized filter shapes achieves 1 bit per symbol SE enhancement with a negligible SNR increase (0.3 to 1.5 dB) compared to MQAM of lower SE. Therefore, we conclude that the proposed optimization

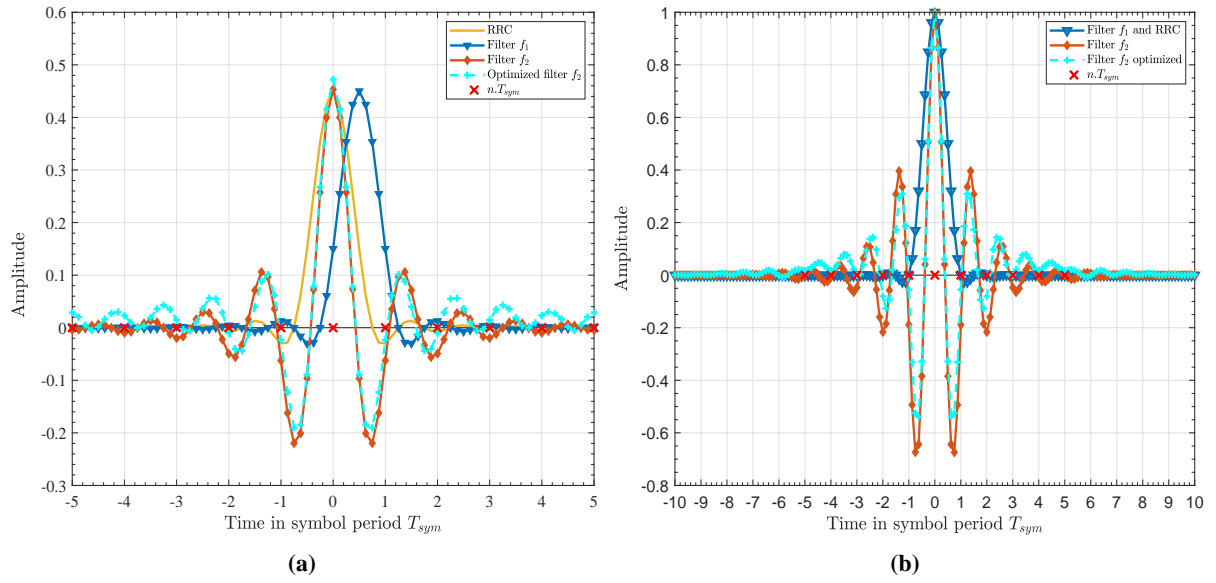


Figure 5.4 – Comparison of the previous intuitive filters and the optimized filter f_2 using the iterative ISI minimization in Algorithm 4: (a) impulse responses, (b) complete responses after correct matched filtering at the receiver side.

for filter design enhances the SE and EE gain by FSIM and IQ-FSIM, where the latter's results with the optimal filter design are directly presented in Section 4.4.5.

The average SIR achieved with all possible filter permutations $N^{2\eta+1}$ limits the M -ary modulation order that can be used without any performance degradation since FSIM/IQ-FSIM with higher-order $M > 64$ modulation schemes will face a performance degradation starting this average SIR.

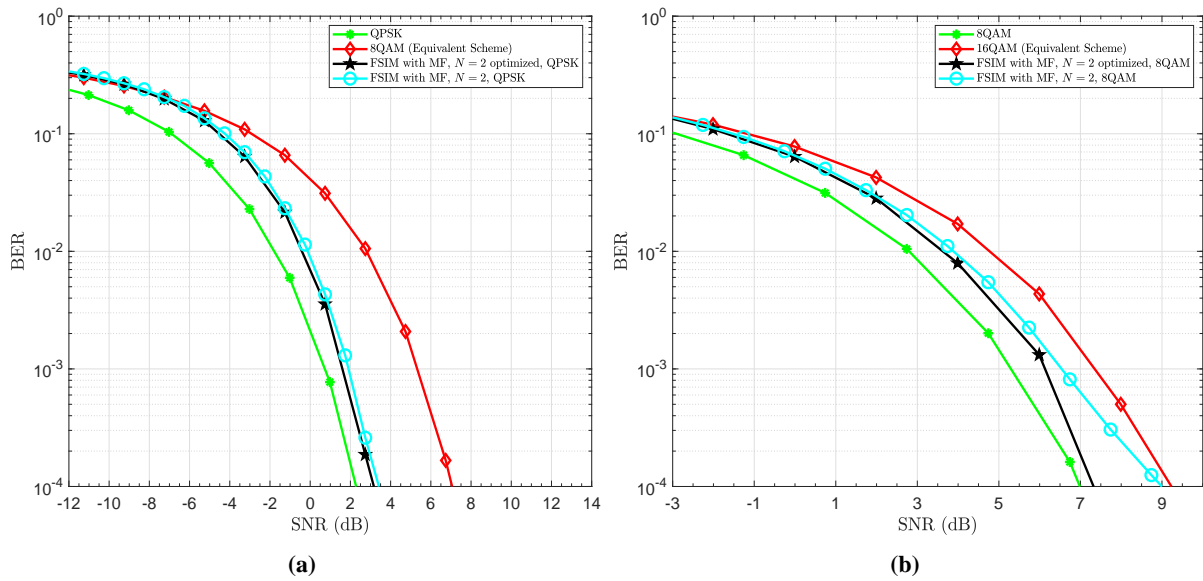


Figure 5.5 – Uncoded BER performance of 2-FSIM-MQAM with optimized filter shapes, and its equivalent scheme 2MQAM of the same SE: (a) 3 bits/symbol using $M = 4$, (b) 4 bits/symbol using $M = 8$.

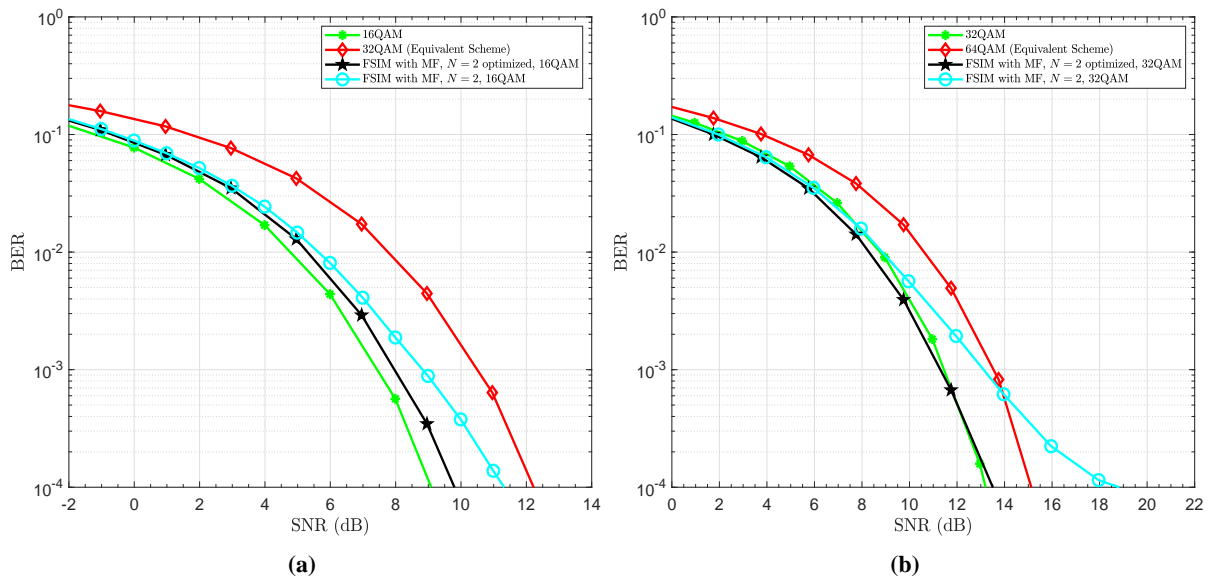


Figure 5.6 – Uncoded BER performance of 2-FSIM-MQAM with optimized filter shapes, and its equivalent scheme 2MQAM of the same SE: (a) 5 bits/symbol using $M = 16$, (b) 6 bits/symbol using $M = 32$.

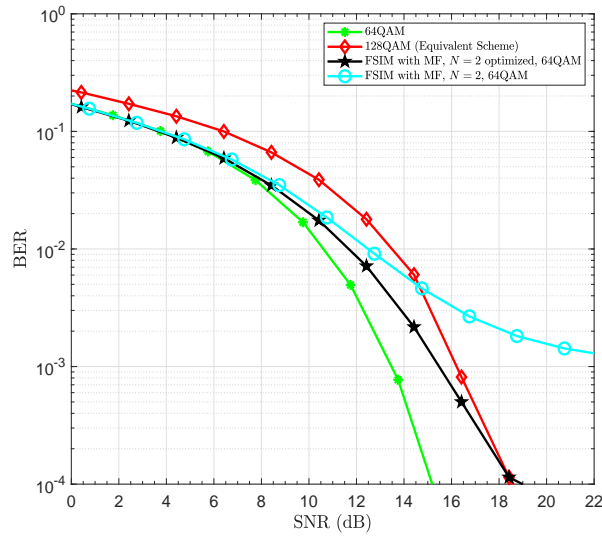


Figure 5.7 – Uncoded BER performance of 2-FSIM-64QAM with optimized filter shapes, and its equivalent scheme 128QAM of the same SE=5 bits/symbol.

5.3.2 Filter bank of N filter shapes

Recalling that the recursive filter design used for $N = 2$ in the previous section can be generalized for N filter design as discussed in Section 5.2.2, but the main limitation of the recursive $N \geq 2$ filter design is the initialization of the first filter. For instance, this initialization is critical to guarantee the feasibility and convergence of the filter bank optimization. The intuitive designed 2 filters shown in Fig. 4.4 helped to overcome the initialization issue and achieve the optimal results for $N = 2$ presented in the previous sub-section 5.3.1. However, the first filter initialization for $N \geq 2$ is not obvious and off-the-shelf filters does not permit to design larger filter bank design with the recursive method due to problem infeasibility with the strict constraints for filter IM schemes. In order to overcome this issue, we proposed in this chapter an iterative joint filter optimization according to Algorithm 5 which is used in the following. The four filter shapes are successfully designed by the Algorithm 5 with the following parameters: $L = 10$, $\lambda = 8$, $\eta = 10$, $N = 4$, $N_{iter} = 1000$, $\epsilon = 0.5$, $\epsilon_{ISI} = 0.3$, and random initialization for all filters on the first iteration. This filter bank depicted in Fig. 4.12 is used to evaluate FSIM and IQ-FSIM to achieve higher SE in Sections 4.3.5 and 4.4.5 respectively, where the results reveal that these schemes achieve significant performance gain and EE enhancement compared to their equivalent schemes. However, we acknowledge that these filter shapes can be a local optimal solution since the proposed iterative joint optimization is based on the initialization of all filters, and many relaxations are introduced in the problem formulation. Hence, a better filter bank maybe can be designed if the initialization limitation is tackled to achieve lower filters' dot-product and higher minimum SIR that leads to better system performance. This limitation of the proposed optimization framework is caused by the non-convex problem characteristics: jointly constrained multivariate optimization with non-convex multimodal objective/constraints.

5.4 Conclusion

In this chapter, the filter bank design that satisfies the requirements of the proposed FSIM and IQ-FSIM schemes in the filter IM domain is formulated as an optimization problem. The filter bank requirements highlighted in Section 4.3.3 are categorized as Magnitude response constraints, low filters' dot-product, low ISI distortion by the filter shapes to keep high SIR and avoid error propagation in the system performance, and the filter energy normalization constraints. The proposed optimization framework aims to minimize the introduced ISI distortion with a spectral mask, low filters' dot-product, and filter energy constraints to respect a predefined spectral mask and allow the filter shape detection. In contrast to conventional schemes, the FSIM and IQ-FSIM may have false match filtering if the filter index is mis-detected, and this error will propagate to ISI estimation and cancellation for the subsequent symbols that can lead to error floor in the system performance. Hence, our filter design optimization considers the joint minimization of the ISI resulting from correct and false matched filtering to limit the ISI increase in the case of inaccurate ISI estimation due to filter misdetection. The introduced ISI by the non-Nyquist filter shapes affects MF-based detection, especially the tentative detection. In addition, it is highlighted that the ISI from correct/false matched filtering naturally occurs in the tentative detection since each filter of the MF-bank is used to filter the L samples around the current symbol, and these samples correspond to the overlap of future and past symbols that results from different pulse shaping filters. After the in-depth analysis of ISI effect on system performance, the proposed optimization framework does not consider only the joint minimization of ISI resulting from correct/false matched filtering but also targets to enhance the detection of the current symbol by maximizing the minimum SIR of all possible filter permutations in the η past and η future symbols.

The fundamental multivariate optimization problem to jointly design the N filter shapes of length L is a non-convex jointly constrained problem with a multimodal quartic objective function, quadratic equality, and several multimodal quartic non-convex constraints. Such a challenging problem for N filter shapes joint design is not addressed in the literature to the best of the author's knowledge. In order to find a suitable filter bank for the proposed filter IM schemes, a problem reformulation with relaxation and restriction is proposed to approximate and solve it by convex optimization method. For instance, it is worth mentioning that this joint filter design is a jointly constrained multi-non-convex problem since even if all filters except one are fixed, the ISI resulting from correct matched filtering in the objective and the filters' energy quadratic equality constraints also lead to a non-convex problem. These constraints and a part of the ISI in the objective prevent solving our problem by multi-convex optimization methods.

Recalling that the optimization of a multimodal quartic function, in general, can only be solved by iterative approach [212], if the filter shapes initialization lies in the vicinity of its global optimum. After the study of the fundamental problem **P1** (5.31), the filter bank design with $N = 2$ is addressed firstly, then it is generalized and updated for a larger filter bank. To design the filter bank with $N = 2$, the first filter f_1 is initialized by the intuitively designed filter f_1 that provides good results in previous

chapter 4, then the algorithm 4 search iteratively for the best corresponding linear-phase FIR filter f_2 . This iterative process requires also the initialization of f_2 , and its update in each stage by the previous optimized f_2^{t-1} corresponding to a given f_1 . The former initialization (f_1) simplifies the multivariate problem to a design of a single variable filter of L samples and avoid the jointly constrained multivariate multimodal condition related to low filters' dot-product. However, the latter initialization (f_2) and its iterative update are used to solve the multimodal objective due to the ISI term resulting from correct matched filtering. Solving this relaxed optimization algorithm by convex methods leads to a better filter bank, where the 2 optimized filters enhance the FSIM scheme performance by 0.35 dB with QPSK and up to 6.5 dB with 64QAM. Hence, the proposed filter bank optimization provides a significant performance enhancement compared to the previously designed filters by intuition, and besides allows to avoid the error floor that appears in Fig. 4.10b with FSIM using high order QAM scheme ($M > 16$). Thanks to the minimization of ISI resulting from correct/false matched filtering in the proposed algorithm and its embedded maximization of the minimum SIR for all possible filter permutations that lead to these enhancements.

Moreover, a recursive approach is discussed to design N filter shapes, where the previously proposed algorithm to design the filter shape f_2 given f_1 is performed firstly, then in each recursion step, an additional filter is designed given the filters of previous stages. This approach is limited by the initialization of the first filter that pilots the overall recursive optimization. For this reason, the N filter shapes joint design is proposed to reduce the initialization of f_1 limitation in problem feasibility. Hence, the 2 filter shapes problem formulation is generalized in the proposed joint design procedure while another set of constraints is added to restrict the ISI resulting from correct matched filtering below a predefined threshold. The filter shapes' initialization is still required due to previously mentioned optimization problem characteristics. However, in contrast to the recursive approach, the proposed joint filters design initializes the N filter shapes and updates them in each step of the iterative algorithm to search for the best filter bank with the multivariate multimodal objective/constraints. The proposed algorithm allowed to design 4 filter shapes, and their results with FSIM and IQ-FSIM are presented in Chapter 4 where a significant performance gain is achieved compared to the equivalent QAM schemes of the same SE. But the results of Figs. 4.13a-4.13b for FSIM and Figs. 4.26a-4.26b for IQ-FSIM reveal that the filter bank of 4 filters could be improved to approach the lower bound of the proposed filter IM schemes. Finally, it is worth mentioning the filter shapes' initialization affects the optimization problem feasibility, the achieved minimum ISI, and filters' dot-product. Thus, a better filter bank could be designed by another filter initialization in the vicinity of the global optimum and/or by considering different problem formulation. Therefore, there is room for a potential SE and EE improvements by the filter IM schemes, where the filter bank challenging design problem plays a major role.

Chapter 6

General Conclusions and Perspectives

The work presented in this dissertation aims to provide an innovative solution for ultra-high data rates wireless communication system in sub-THz bands that satisfies B5G requirements. Wireless Tbps links will become an urgent requirement within the next 10 years. Hence, acquiring larger bands in the mmWave/sub-THz bands and employing spectral-efficient MIMO technology is necessary to deal with the ever-increasing demand and the scarce sub-GHz spectrum. For massive production and business market perspectives, low-cost electronics technology is envisioned. However, it is functioning at the edge of its operation region in sub-THz bands leading to different limitations and severe RF impairments (i.e., high PN, CFO, PA non-linearity, low transmit power, etc.), as highlighted in Chapter 1. The naive high-data-rate approach adopted by different standards in sub-GHz bands (e.g., IEEE802.11ax) is based on acquiring more spectrum, adopting MIMO techniques, using MC with high APM modulation order (up to 1024 QAM), and then working on reducing its power consumption. However, to cope with sub-THz limitations and enable low-power Tbps wireless communication systems, we proposed a new approach that insists on using wider bandwidth, adopting power-efficient SC modulation, and exploiting Index Modulation to enhance the system spectral efficiency mainly. Based on this approach, several contributions and solutions are proposed in this thesis to answer the problematic “*Can we design a low-power wireless ultra-high data rate system with low cost/complexity that survives with the severe sub-THz challenges?*”, and they are presented in the following.

6.1 Conclusion on our contributions

We started this manuscript by investigating the wireless Tbps scenarios, detailing the sub-THz channel characteristics, highlighting its technological limitations, RF impairments, and sub-THz waveform requirements. Besides, a broad survey on existing IM domains and techniques is provided to study and promote a spectral-efficient scheme like GSM in spatial IM domain, and then to add our fingerprint by proposing a novel IM domain, called Filter IM domain. In Part I, we proved the proposed approach’s

feasibility by using power-efficient CPM and low order QAM modulations accompanied by the spectral-efficient GSM scheme, firstly in a general context. The result confirmed that not only a low-power high-data-rate system can be achieved using this approach, but it pointed out that the previous approach is no more possible for sub-THz due to its high SNR requirements even with perfect conditions that cannot be reached using current electronics technology. It is also interesting to highlight that the implicit transmission of most information bits in the IM domain leads to the best performance results.

After this conclusion, the main GSM challenges of high detection complexity and performance degradation in highly correlated channels like those in sub-THz are addressed. To enhance GSM BER performance, we proposed two methods summarized as in the sequel. An efficient legitimate TACs' set selection without using instantaneous CSIT (system denoted by S-EGSM) is proposed, and it provides the near-optimal performance achieved by the adaptive GSM technique with full CSIT knowledge (system denoted by EGSM [63]). The former reduces the number of detection errors of the activated TAC that also affects APM symbols detection. This is achieved by avoiding the use of the most correlated TACs. However, our second proposed method minimizes the BER that may result from the activated TAC misdetection due to the ambiguity between the remained correlated TACs in the legitimate set. The latter proposed method, called best-effort gray spatial bit-mapping, is based on a careful TACs index-to-bit mapping based on their correlation indicators. To consider the high-detection complexity challenge in large-scale MIMO for GSM and even for conventional MIMO SMX, we proposed a low-complexity quasi-optimal detector for each system (OSICML for SMX, and O²SIC-ML for GSM). These detectors are designed mainly by a clever combination of OSIC and ML techniques to reach the ML optimal performance with a linear structure leading to a 99% complexity reduction. In addition, the proposed detectors are controllable to provide the best tradeoff complexity-performance, even with channel estimation error and large-scale MIMO. It is worth mentioning that the high GSM complexity due to its two-layer of information bits is tackled by ordering the TAC detection based on their reliability indicator and performing a linear detection followed by ML verification on a reduced set.

Moreover, we proposed DP-GSM to achieve higher SE gain and better robustness to spatial correlation than the GSM system. This multi-dimensional IM scheme activates a TAC where a single polarization per TA is used for data transmission. This permits to convey information bits by the indices of activated TAC and polarization. This technique benefits from the orthogonal polarization to reduce the overall correlation among the legitimate TACs, and it exploits this IM dimension for SE enhancement. These advantages come with antenna-array space occupancy reduction inherited from the usage of DP antennas. This point and the sub-THz short-wavelength allow the integration of large-scale MIMO even on the end-user devices. But the success of this idea at sub-THz bands is limited by the antenna array design in current technology and the hardware level interconnection. Furthermore, the different candidates (SMX, GSM, and their dual-polarized version) for low-power wireless Tbps are evaluated in a realistic sub-THz environment using channels obtained by ray-based deterministic channel modeling for sub-THz (provided by the BRAVE project partner Siradel) with

RF impairments (MIMO PN model extracted from the PN model of the BRAVE project partner CEA-Leti). These evaluations are carried at different levels, and the short-listed candidates are compared from different perspectives such as: performance, EE/SE, detection complexity, cost, link-budget, and power consumption estimation. To conclude this part, the power-efficient SC with GSM-based schemes (e.g., GSM-QPSK) shows many advantages compared to the competing SMX based systems. Note that the proposed solution for low-power ultra-high data rates can be used at any frequency bands.

In Part II, a novel IM domain called the filter IM domain is proposed to achieve better performance, higher SE/EE gain than the previous solutions. In addition, the proposed domain targets to overcome the performance degradation of the spatial IM domain that cannot be completely mitigated in the highly correlated channel, even with the best enhancement techniques. Another issue that we increased our interest to explore this novel filter IM domain is the RF-switching problem effect on any transmit spatial IM that leads to spectral regrowth, and this switching is currently unfeasible at these ultra-high symbol rate. Nevertheless, a possible solution based on using a full-RF architecture with transmit spatial IM can solve both problems but at the price of higher system cost. In this case, the spatial IM schemes sacrifice with the available spatial and RF resources to bring IM advantages. The proposed novel filter IM domain allows overcoming all these issues since it makes possible the exploitation of all available time/frequency and spatial resources while providing the advantages of IM. Moreover, the filter IM domain generalizes most of the existing SISO-IM schemes, especially those in the time/frequency IM domains. We explored two schemes (FSIM and IQ-FSIM) within our proposed domain that convey additional information bits by an index of a filter-shape changing at the symbol rate to maximize SE gain. Both schemes can transmit any APM symbols, and IQ-FSIM doubles the SE gain of FSIM by using separate indexation on I and Q components. These systems achieve even with non-optimal filters a significant performance and SE/EE gain compared to the conventional QAM and SISO-IM systems in AWGN and frequency-selective fading channels. These results are verified by their derived theoretical performances. Furthermore, we proposed MF-based detectors for both schemes to reach the optimal joint-ML performance with a tremendous complexity reduction. Also, an ISI estimation and cancellation technique is proposed to combat the injected controllable ISI by the non-Nyquist filter shapes. The zero-ISI Nyquist condition is relaxed to permits finding a filter bank with low filters' cross-correlations. Moreover, both proposed schemes (FSIM and IQ-FSIM) are compared at the same SE by using the designed filter banks and their theoretical lower bounds. We would like to highlight several interesting points based on this comparison: The lowest order APM with the maximum number of filters gives the best results as expected since IM, in general, is more power-efficient than the conventional signal domain (any APM). The theoretical lower bound confirms that FSIM can achieve better performance than IQ-FSIM of the same SE using the same APM but a lower number of filters. IQ-FSIM with the designed filter bank provides the best realistic performance compared to FSIM (which is the most competent SISO-IM scheme), and IQ-FSIM reaches its lower-bound in contrast to FSIM with 4 filters since the challenges in filter bank design increases with a higher number of filters.

After proposing this novel IM domain that achieves a significant SE/EE gain in SISO, we extended this system to MIMO to exploit the multiplexing and IM gain together. The proposed SMX-FSIM system elevates the achieved SE gain of FSIM using IM by the multiplexing order and thus permits to transmit more information bits in the IM domain. The strength of the SMX-FSIM system lies in its independent parallel indexation strategy on each transmit antenna. This permits the design of a linear receiver architecture of low-complexity based on linear equalization and parallel linear MF-based FSIM detectors suitable for the high-throughput. Furthermore, the proposed SMX-FSIM system with the decentralized VBs transmission overcomes the performance degradation of the spatial IM domain that occurs when the activated TAC in GSM is misdetects. This degradation is due to the fact that TAC detection error propagates to all APM symbols detection and thus affects all bits. These advantages are validated by the derived theoretical performance, and then a wider assessment for all candidate schemes in sub-THz environments concluded this thesis. **The conclusive study promotes SMX-FSIM as the most promising solution for low-power wireless ultra-high data rates system in sub-THz bands.** This conclusion is based on the different proved advantages in performance, SE/EE gain, cost (lower number of RF chains), link budget, power consumption, and robustness to PN (using a linear receiver at medium PN level, SMX-FSIM is the only candidate with good performance and without any error floor, while the equivalent GSM and SMX of the same SE have a high error floor).

Furthermore, to complete the study of the proposed solution, we addressed the challenging filter bank design problem by optimization. In order to solve this problem, we defined the filter bank requirements, and we highlighted that the ISI resulting from correct and false matched filtering should be jointly minimized. This ISI minimization is needed to enhance the tentative decisions for ISI estimation and cancellation in the filter IM schemes. Moreover, we discussed the importance of maximizing the SIR at the considered symbol under detection by considering all permutations of previous and future filters that contributes to its ISI. We provided an optimization framework to solve this problem and reach our goal of maximizing SE/EE gain by the proposed filter IM schemes (FSIM and IQ-FSIM). However, solving the formulated non-convex optimization problem necessitates some relaxations and restrictions to solve it using convex methods. This is imposed by the jointly constrained multivariate multimodal objective function and the different non-convex constraints (quadratic equality and jointly constrained multimodal constraint). In general, solving such a problem requires an iterative approach with initialization, and it converges to the global optimal if this initialization lies within the vicinity of this optimum. Based on this strategy, we succeeded in finding filter banks that provide a significant performance improvement for FSIM based schemes. However, we want to acknowledge that there is still room for future improvements in the challenging filter design problem, and even higher SE/EE gain are expected by the filter IM domain.

Finally, in order to verify the feasibility of the proposed filter IM domain with real hardware, we implemented using LabView communication software the proof-of-concept for FSIM transceiver with all the necessary RF impairments' mitigation techniques. Then, we performed a real-time demonstration on NI-USRP at sub-GHz frequencies at the first stage, and then we proved FSIM

robustness to sub-THz RF impairments by real-demonstration with more severe RF impairments added artificially like those in sub-THz bands (high CFO, PN, time offset,...). This wireless demonstration with over the air synchronization validated our theoretical study, and it is ready to be extended to MIMO system and tested using a sub-THz RF front-end.

6.2 Perspectives for future works

This thesis mainly tackled the transceiver and waveform design for low-power wireless ultra-high data rate system in sub-THz bands. Note that the proposed system is designed to maintain the minimum receiver complexity/cost to enable its implementation on end-user devices. However, it opens the door for potential perspectives and different directions for future works, as outlined in the following:

Exploring more IM schemes in filter IM domain

The proposed filter IM domain offers the opportunity for more exploitation of IM benefits. Even though, we proposed in Chapter 4 two novel schemes that provide different advantages, but we still can imagine different indexation techniques enabled by this domain. These techniques could enhance more the SE and/or EE, or provide much lower receiver complexity convenient for different kinds of B5G applications. Moreover, we acknowledge that more scheme(s) in the filter IM domain is(are) possible like any novel domain recently proposed.

Filter Bank design for our proposed filter IM domain

At the end of this thesis, we had limited time for solving the challenging filter bank design problem. However, more advanced techniques could provide a higher SE/EE gain for the filter IM domain when the global optimal bank is designed. The fundamental optimization problem could be reformulated to reduce the non-convexity of the objective and constraints, and thus it permits to solve it more efficiently with fewer relaxations to avoid the impact of filter initializations. However, another possible approach for the filter bank design could be based on machine learning. Therefore, we expect that tackling this challenging problem will provide more promising SE/EE gain by approaching the derived theoretical lower bound of the proposed filter IM schemes.

Specialized FSIM/IQ-FSIM receiver blocks for synchronization and RF mitigation

The FSIM and IQ-FSIM receivers have a different structure and require a specialized receiver architecture. This requirement is due to sending information bits via the selected filter shapes that will be detected at the receiver. Hence, the matched filter at the receiver side could not be performed immediately on the received signal compared to the existing conventional system. This

modification requires adapting all the existing receiver blocks for time/frequency synchronization, channel estimation, and equalization. In order to do the real-time demonstration, the receiver has been carefully designed to consider the specifications of FSIM scheme. However, a more optimized receiver specialized for filter IM domain has to be designed. Therefore, this filter IM domain also opens a research area at different levels of the receiver.

Enhanced FSIM/IQ-FSIM detection/equalization techniques

In Chapter 4, we proved that filter IM schemes with a MF-based detector reach the optimal joint ML performance while providing a very-low complexity. However, a more advanced detection/equalization technique could achieve better performance by approaching the system performance of FSIM/IQ-FSIM with perfect ISI cancellation when a high number of filters and/or modulation order are used. This thesis aims to keep the minimum receiver complexity to support Tbps applications with UE receiver like Kiosk, enhanced throughput WLAN/WPAN, etc. However, for other scenarios like Backhaul, the receiver can support a higher complexity, and we have in mind a more powerful detection/equalization technique specialized for these schemes. For instance, a joint detection-equalization method specialized for filter IM domain is a possible solution to reduce the residual ISI, and thus achieve better performance and EE gains.

Adaptive filter IM domain

The proposed filter IM domain allowed to reach higher SE and EE compared to existing IM schemes, and it also generalizes most SISO-IM schemes, especially the time/frequency IM domains. Moreover, the filter IM domain can be reconfigured to a conventional transceiver with Nyquist filter by using the same Nyquist filter in the filter bank as proved in Appendix D. In order to exploit this generalization of the filter IM domain, we can propose an adaptive scheme that changes between these schemes and/or adjusts the system SE according to channel condition, SNR, ...etc.

Study the performance of the proposed filter IM scheme in a multi-user scenario

The proposed solution for sub-THz considered a single user transmission in a single time/frequency resources, which means the multi-user (MU) scenario does not introduce more interference. However, the SDMA technique in sub-THz is interesting to allow resources re-use and maximize the cell SE. This is enabled by MIMO precoding and the small beamwidth in sub-THz bands. Thus, the theoretical study and performance assessment of the filter IM domain in a MU-MIMO setup is also required.

Effect of PA non-linearity on sub-THz candidates

After proposing different systems and comparing them in sub-THz channels with PN, it is necessary to consider the PA non-linearity on the considered IM schemes. Higher non-linearity occurs in all analog components at sub-THz frequencies, and thus considering this impairment and studying its effect on system performance is necessary.

This thesis took some steps forward towards achieving B5G requirements, and opens several directions for more improvements. Finally, we would like to mention that several points from these perspectives will be considered in the short term.

Appendix A

Excel Sheet for link budget and power consumption estimation



Different tools are prepared in Excel sheets to allow evaluating the tested systems quickly. The tools are listed in the following:

- Achievable Signal-to-Noise Ratio estimator according to scenario parameters.
- Data rate estimator with channel aggregation and/or bonding based on the system spectral efficiency at the achievable SNR.
- Link budget and power consumption estimator based on the required SNR to achieve a target performance.

The first tool is to estimate the achievable SNR based on RF properties (antenna gain, cable losses, available transmit power, etc.), environment, and channel characteristics (Tx-Rx separation distance, losses, ...). This tool can be configured to deduce the realistic achievable SNR for any scenario by updating the different parameters highlighted in Fig. [A.1](#). This inputs should consider the recent values of current technology suitable for the studied scenario.

The second tool calculates the maximum data rate according to the system spectral efficiency. Note that this spectral efficiency should consider the achievable SNR of the studied scenario and the required system performance. In addition, the data rates are deduced if channel bonding and/or aggregation is used with an assumption of negligible inter-band interference. The two different total bandwidths considered in this tool are:

- Up to 12.5 GHz by channel bonding of equal channel bands, this total bandwidth is available around the 157.75 GHz.



Achievable SNR estimation

Fill Parameters in yellow to deduce achievable SNR
NB: All parameters in grey are calculated automatically

Parameter Name	Value	Parameter symbol and equations
Carrier frequency (GHz)	145.00	fc
Distance (m)	8.00	d
Bandwidth (GHz)	1.00	BW
Transmit Power (dBm)	14.00	Pt
Transmit antenna gain (dBi)	25.00	Gt
Tx Losses	1.00	Ltx
EIRP (dB)	38.00	$EIRP = Pt + Gt - Ltx$
Free space propagation loss (dB)	93.74	$f_{spl} = 20 \log(4\pi \cdot d \cdot fc / c)$
Other losses (gas attenuation, shadowing, fading,...)	0.00	Lchannel
Total Channel losses	93.74	Lchannel_total
Rx losses	1.00	Lrx
Receive antenna gain (dBi)	0.00	Gr
Rx Signal Level (dBm)	-56.74	$RSL = EIRP - Lchannel_total - Lrx + Gr$
Thermal noise (dBm)	-83.93	Nthermal
Noise figure	7.00	NF
Noise floor	-76.93	Noise floor = NF + Nthermal
Achievable SNR (dB)	20.19	$SNR = RSL - \text{Noise floor}$

Figure A.1 – Excel Sheet for achievable SNR estimator.

- Up to 58.6 GHz by channel bonding and aggregation of different bands available between 90 GHz and 200 GHz.

**Data rate with channel bounding and aggregation
(using system spectral efficiency)**

Fill Parameters in yellow to deduce data rate

Channel Bandwidth (GHz)	2.00		
Percentage of usefull BW	0.83		
System Spectral efficiency	12.00		
Data rate per channel (Gbps/channel)	20.00	Nb of Channels	Total Aggregated BW (GHz)
Data rate with channel bounding (up to 12.5 GHz) around 157.75 GHz	120.00	6.00	12.00
Data rate with channel aggregation and bounding (up to 58.6 GHz) of equal channel bands between 90 GHz and 200 GHz	500.00	25.00	50.00

Figure A.2 – Excel Sheet for data rate estimation with channel bonding and/or aggregation.

The last tool prepared in the Excel sheet depicted in Fig. A.3 estimates the required transmit power and the resulting EIRP. This calculation is according to the link budget and the required SNR to achieve the target BER performance. Moreover, this tool allows to roughly estimate the power consumption while considering the PAPR of the transmitted waveform that affects the PA. This tool estimates these parameters simultaneously for several systems (up to 6) under the same conditions. It uses their required SNR to achieve the same performance and SE, and thus it allows the comparison of the following factors:

- System Link budget.
- Feasibility of required transmit power in current technology.
- Compliance to THz regulations, standards, and specifications (e.g., EIRP within the allowed range).

- System power consumption.

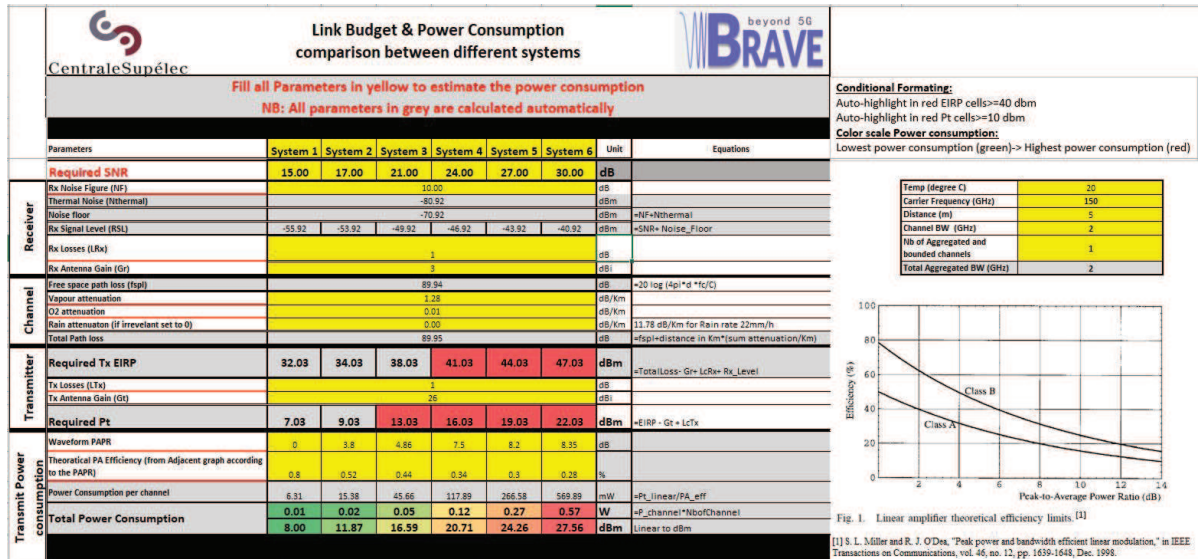


Figure A.3 – Excel Sheet for link budget and power comparison estimation.

Note that all tools require to fill the input parameters in the excel sheet (highlight in yellow in Fig. A.1-A.2) according to the considered scenario and system configuration. Then, the tool provides its output calculation accordingly. In addition, the last tool in Fig. A.3 for power consumption estimation also includes automatic conditional formatting for:

- Required Transmit Power (Pt): if it exceeds 10 dBm which is at the boundaries of current electronics technology, the cell will be highlighted in red to alert the user.
- Total Power Consumption: the colour scale from green to red is used to highlight the power consumption of the different systems from the lowest to highest.

Appendix B

PDF characteristics for PEP derivation in DP-GSM systems

The conditional PDF of the received signal is given by

$$f_{\mathbf{y}}(\mathbf{y}|\mathbf{H}, \mathbf{x}) = \prod_{i=1}^{2N_r} f_{n_i}(n_i) = \prod_{i=1}^{2N_r} \frac{1}{\pi\sigma^2} \exp\left(-\frac{|n_i|^2}{\sigma^2}\right) \quad (\text{B.1})$$

$$= \frac{1}{\pi^{2N_r} \sigma^{4N_r}} \exp\left(-\frac{\|\mathbf{v}\|_F^2}{\sigma^2}\right) \quad (\text{B.2})$$

The ML solution is given by

$$\hat{\mathbf{x}} = \arg \max_{\mathbf{x}} f_{\mathbf{y}}(\mathbf{y}|\mathbf{H}, \mathbf{x}) \quad (\text{B.3})$$

$$= \arg \max_{\mathbf{x}} \frac{1}{\pi^{2N_r} \sigma^{4N_r}} \exp\left(-\frac{1}{\sigma^2} \text{tr}[(\mathbf{y} - \mathbf{H}\mathbf{x})(\mathbf{y} - \mathbf{H}\mathbf{x})^H]\right) \quad (\text{B.4})$$

$$= \arg \min_{\mathbf{x}} \text{tr}[(\mathbf{y} - \mathbf{H}\mathbf{x})(\mathbf{y} - \mathbf{H}\mathbf{x})^H] \quad (\text{B.5})$$

Accordingly,

$$(\hat{i}, \hat{\ell}, \hat{\mathbf{s}}_{\hat{v}}) = \arg \min_{i, \ell, v} \text{tr}[(\mathbf{y} - \mathbf{H}_{i, P} \mathbf{s}_v)(\mathbf{y} - \mathbf{H}_{i, P} \mathbf{s}_v)^H] \quad (\text{B.6})$$

For erroneous detected vector symbol $(\hat{i}, \hat{\ell}, \hat{\mathbf{s}}_{\hat{v}}) \neq (i, \ell, \mathbf{s}_v)$ the following condition is satisfied

$$\text{tr}[(\mathbf{y} - \mathbf{H}_{i, P} \mathbf{s}_v)(\mathbf{y} - \mathbf{H}_{i, P} \mathbf{s}_v)^H] \geq \text{tr}[(\mathbf{y} - \mathbf{H}_{\hat{i}, \hat{P}} \hat{\mathbf{s}}_{\hat{v}})(\mathbf{y} - \mathbf{H}_{\hat{i}, \hat{P}} \hat{\mathbf{s}}_{\hat{v}})^H] \quad (\text{B.7})$$

The previous inequality can be written otherwise

$$\text{tr}[\mathbf{v}\mathbf{v}^H] \geq \text{tr}[(\mathbf{y} - \mathbf{H}_{\hat{i}, \hat{P}} \hat{\mathbf{s}}_{\hat{v}})(\mathbf{y} - \mathbf{H}_{\hat{i}, \hat{P}} \hat{\mathbf{s}}_{\hat{v}})^H] \quad (\text{B.8})$$

$$= \text{tr}[(\mathbf{H}_{\mathbb{I},P}\mathbf{s}_v - \mathbf{H}_{\hat{\mathbb{I}},\hat{P}}\mathbf{s}_{\hat{v}}) + \mathbf{v})(\mathbf{H}_{\mathbb{I},P}\mathbf{s}_v - \mathbf{H}_{\hat{\mathbb{I}},\hat{P}}\mathbf{s}_{\hat{v}}) + \mathbf{v}]^H \quad (\text{B.9})$$

$$= \text{tr}[(\mathbf{H}_{\mathbb{I},P}\mathbf{s}_v - \mathbf{H}_{\hat{\mathbb{I}},\hat{P}}\mathbf{s}_{\hat{v}})(\mathbf{H}_{\mathbb{I},P}\mathbf{s}_v - \mathbf{H}_{\hat{\mathbb{I}},\hat{P}}\mathbf{s}_{\hat{v}})^H] + \text{tr}[2\Re\{(\mathbf{H}_{\mathbb{I},P}\mathbf{s}_v - \mathbf{H}_{\hat{\mathbb{I}},\hat{P}}\mathbf{s}_{\hat{v}})\mathbf{v}^H\}] + \text{tr}[\mathbf{v}\mathbf{v}^H] \quad (\text{B.10})$$

The last inequality implies :

$$\text{tr}[-2\Re\{(\mathbf{H}_{\mathbb{I},P}\mathbf{s}_v - \mathbf{H}_{\hat{\mathbb{I}},\hat{P}}\mathbf{s}_{\hat{v}})\mathbf{v}^H\}] \geq \text{tr}[(\mathbf{H}_{\mathbb{I},P}\mathbf{s}_v - \mathbf{H}_{\hat{\mathbb{I}},\hat{P}}\mathbf{s}_{\hat{v}})(\mathbf{H}_{\mathbb{I},P}\mathbf{s}_v - \mathbf{H}_{\hat{\mathbb{I}},\hat{P}}\mathbf{s}_{\hat{v}})^H] \quad (\text{B.11})$$

$$= \|\mathbf{H}_{\mathbb{I},P}\mathbf{s}_v - \mathbf{H}_{\hat{\mathbb{I}},\hat{P}}\mathbf{s}_{\hat{v}}\|_F^2 \quad (\text{B.12})$$

Defining the scalar variable $W = \text{tr}[-2\Re\{(\mathbf{H}_{\mathbb{I},P}\mathbf{s}_v - \mathbf{H}_{\hat{\mathbb{I}},\hat{P}}\mathbf{s}_{\hat{v}})\mathbf{v}^H\}]$ and trying to find the distribution of W :

$$W = \text{tr}[-2\Re\{(\mathbf{H}_{\mathbb{I},P}\mathbf{s}_v - \mathbf{H}_{\hat{\mathbb{I}},\hat{P}}\mathbf{s}_{\hat{v}})\mathbf{v}^H\}] \quad (\text{B.13})$$

$$= \sum_{l=1}^{2N_r} -2\Re\{(\mathbf{h}_l\mathbf{s}_v - \hat{\mathbf{h}}_l\mathbf{s}_{\hat{v}})n_l\}, \quad \mathbf{h}_l, \hat{\mathbf{h}}_l \text{ are the } l\text{-th row of } \mathbf{H}_{\mathbb{I},P} \text{ and } \mathbf{H}_{\hat{\mathbb{I}},\hat{P}} \text{ respectively,} \quad (\text{B.14})$$

$$= 2 \sum_{l=1}^{2N_r} \Im\{(\mathbf{h}_l\mathbf{s}_v - \hat{\mathbf{h}}_l\mathbf{s}_{\hat{v}})\} \Im\{n_l\} - \Re\{(\mathbf{h}_l\mathbf{s}_v - \hat{\mathbf{h}}_l\mathbf{s}_{\hat{v}})\} \Re\{n_l\} \quad (\text{B.15})$$

$\Re\{n_l\}$ and $\Im\{n_l\}$ are zero-mean independent Gaussian random scalars. As consequence,

$$\Im\{\mathbf{h}_l\mathbf{s}_v - \hat{\mathbf{h}}_l\mathbf{s}_{\hat{v}}\} \Im\{n_l\} \sim \mathcal{N}(0, 1/2 \sigma^2 \Im\{\mathbf{h}_l\mathbf{s}_v - \hat{\mathbf{h}}_l\mathbf{s}_{\hat{v}}\}^2) \quad (\text{B.16})$$

$$\Re\{\mathbf{h}_l\mathbf{s}_v - \hat{\mathbf{h}}_l\mathbf{s}_{\hat{v}}\} \Re\{n_l\} \sim \mathcal{N}(0, 1/2 \sigma^2 \Re\{\mathbf{h}_l\mathbf{s}_v - \hat{\mathbf{h}}_l\mathbf{s}_{\hat{v}}\}^2) \quad (\text{B.17})$$

The combination of the previous variables is also zero-mean Gaussian random variable with variance given by $\frac{\sigma^2}{2} \Im\{\mathbf{h}_l\mathbf{s}_v - \hat{\mathbf{h}}_l\mathbf{s}_{\hat{v}}\}^2 + \frac{\sigma^2}{2} \Re\{\mathbf{h}_l\mathbf{s}_v - \hat{\mathbf{h}}_l\mathbf{s}_{\hat{v}}\}^2 = \frac{\sigma^2}{2} \|\mathbf{h}_l\mathbf{s}_v - \hat{\mathbf{h}}_l\mathbf{s}_{\hat{v}}\|^2$.

Accordingly, the variable W is the sum of zero-mean independent Gaussian random scalars. The variance of W is given by

$$\text{var}(W) = 4 \sum_{l=1}^{2N_r} \frac{\sigma^2}{2} \|\mathbf{h}_l\mathbf{s}_v - \hat{\mathbf{h}}_l\mathbf{s}_{\hat{v}}\|^2 \quad (\text{B.18})$$

$$= 2\sigma^2 \sum_{l=1}^{2N_r} (\mathbf{h}_l\mathbf{s}_v - \hat{\mathbf{h}}_l\mathbf{s}_{\hat{v}})(\mathbf{h}_l\mathbf{s}_v - \hat{\mathbf{h}}_l\mathbf{s}_{\hat{v}})^H \quad (\text{B.19})$$

$$= 2\sigma^2 \|\mathbf{H}_{\mathbb{I},P}\mathbf{s}_v - \mathbf{H}_{\hat{\mathbb{I}},\hat{P}}\mathbf{s}_{\hat{v}}\|_F^2 \quad (\text{B.20})$$

In conclusion, $W = \text{tr}[-2\Re\{(\mathbf{H}_{\mathbb{I},P}\mathbf{s}_v - \mathbf{H}_{\hat{\mathbb{I}},\hat{P}}\mathbf{s}_{\hat{v}})\mathbf{v}^H\}] = -2\Re\{\mathbf{v}^H(\mathbf{H}_{\mathbb{I},P}\mathbf{s}_v - \mathbf{H}_{\hat{\mathbb{I}},\hat{P}}\mathbf{s}_{\hat{v}})\}$ is a zero-mean Gaussian random variable with variance equal to $2\sigma^2 \|\mathbf{H}_{\mathbb{I},P}\mathbf{s}_v - \mathbf{H}_{\hat{\mathbb{I}},\hat{P}}\mathbf{s}_{\hat{v}}\|_F^2$

Appendix C

Simplification of ABEP for DP-GSM

The APEP is given by the following double integral

$$Pr(\mathbf{x} \rightarrow \hat{\mathbf{x}}) = \frac{1}{\pi} \int_0^{\pi/2} \int_{\mathbf{z}} \exp\left(-\frac{\mathbf{z}^H \mathbf{z}}{2 \sin^2 \theta}\right) f_{\mathbf{z}}(\mathbf{z}) d\mathbf{z} d\theta \quad (\text{C.1})$$

where \mathbf{z} is assumed to be proper complex Gaussian random vector with joint PDF is given by equation (3.70). By substituting the PDF of \mathbf{z} in the APEP equation, the second integral is then given by

$$A = \int_{\mathbf{z}} \frac{1}{\pi^{2Nr} |\Sigma_{\mathbf{z}}|} \exp\left(-\frac{\mathbf{z}^H \mathbf{z}}{2 \sin^2 \theta} - (\mathbf{z} - \mathbf{m}_{\mathbf{z}})^H \Sigma_{\mathbf{z}}^{-1} (\mathbf{z} - \mathbf{m}_{\mathbf{z}})\right) d\mathbf{z} \quad (\text{C.2})$$

The above equation can be re-expressed by considering the inside of the integral as multivariate scaled Gaussian distribution with mean $\mu_{\mathbf{z}}$ and variance Σ

$$-\frac{\mathbf{z}^H \mathbf{z}}{2 \sin^2 \theta} - (\mathbf{z} - \mathbf{m}_{\mathbf{z}})^H \Sigma_{\mathbf{z}}^{-1} (\mathbf{z} - \mathbf{m}_{\mathbf{z}}) = -(\mathbf{z} - \mu_{\mathbf{z}})^H \Sigma^{-1} (\mathbf{z} - \mu_{\mathbf{z}}) + \mathbf{Const} \quad (\text{C.3})$$

The left side of the previous equation can be developed as following

$$-\mathbf{z}^H \left(\Sigma_{\mathbf{z}}^{-1} + \frac{\mathbf{I}}{2 \sin^2 \theta}\right) \mathbf{z} + \mathbf{m}_{\mathbf{z}}^H \Sigma_{\mathbf{z}}^{-1} \mathbf{z} + \mathbf{z}^H \Sigma_{\mathbf{z}}^{-1} \mathbf{m}_{\mathbf{z}} - \mathbf{m}_{\mathbf{z}}^H \Sigma_{\mathbf{z}}^{-1} \mathbf{m}_{\mathbf{z}} \quad (\text{C.4})$$

and the right side can also be developed as

$$-\mathbf{z}^H \Sigma^{-1} \mathbf{z} + \mu_{\mathbf{z}}^H \Sigma^{-1} \mathbf{z} + \mathbf{z}^H \Sigma^{-1} \mu_{\mathbf{z}} - \mu_{\mathbf{z}}^H \Sigma^{-1} \mu_{\mathbf{z}} + \mathbf{Const} \quad (\text{C.5})$$

After identification we can conclude that

$$\Sigma^{-1} = \frac{\mathbf{I}}{2 \sin^2 \theta} + \Sigma_{\mathbf{z}}^{-1} \quad (\text{C.6})$$

$$\mu_{\mathbf{z}} = \Sigma \Sigma_{\mathbf{z}}^{-1} \mathbf{m}_{\mathbf{z}} \quad (\text{C.7})$$

$$\mathbf{Const} = \mathbf{m}_z^H \boldsymbol{\Sigma}_z^{-1} (\boldsymbol{\Sigma} - \boldsymbol{\Sigma}_z) \boldsymbol{\Sigma}_z^{-1} \mathbf{m}_z \quad (\text{C.8})$$

As consequence, the new expression of A is given by

$$A = \frac{1}{\pi^{2Nr} |\boldsymbol{\Sigma}_z|} \exp\left(\mathbf{m}_z^H \boldsymbol{\Sigma}_z^{-1} (\boldsymbol{\Sigma} - \boldsymbol{\Sigma}_z) \boldsymbol{\Sigma}_z^{-1} \mathbf{m}_z\right) \times \int_{\mathbf{z}} \exp\left(-(\mathbf{z} - \boldsymbol{\mu}_z)^H \boldsymbol{\Sigma}^{-1} (\mathbf{z} - \boldsymbol{\mu}_z)\right) d\mathbf{z} \quad (\text{C.9})$$

$$= \frac{1}{|\boldsymbol{\Sigma}_z \boldsymbol{\Sigma}^{-1}|} \exp\left(\mathbf{m}_z^H \boldsymbol{\Sigma}_z^{-1} (\boldsymbol{\Sigma} - \boldsymbol{\Sigma}_z) \boldsymbol{\Sigma}_z^{-1} \mathbf{m}_z\right) \quad (\text{C.10})$$

$$= \frac{1}{\left|\frac{\boldsymbol{\Sigma}_z}{2 \sin^2 \theta} + \mathbf{I}\right|} \exp\left(-\mathbf{m}_z^H (\boldsymbol{\Sigma}_z^{-1} - \boldsymbol{\Sigma}_z^{-1} \boldsymbol{\Sigma} \boldsymbol{\Sigma}_z^{-1}) \mathbf{m}_z\right) \quad (\text{C.11})$$

Using the matrix inversion lemma: $(A - CB^{-1}D)^{-1} = A^{-1} + A^{-1}C(B - DA^{-1}C)^{-1}DA^{-1}$, we can write that

$$(\boldsymbol{\Sigma}_z^{-1} - \boldsymbol{\Sigma}_z^{-1} \boldsymbol{\Sigma} \boldsymbol{\Sigma}_z^{-1}) = (\boldsymbol{\Sigma}_z + 2 \sin^2 \theta \mathbf{I})^{-1} \quad (\text{C.12})$$

Finally, the APEP $Pr(\mathbf{x} \rightarrow \hat{\mathbf{x}})$ is then given by

$$Pr(\mathbf{x} \rightarrow \hat{\mathbf{x}}) = \frac{1}{\pi} \int_0^{\pi/2} \frac{\exp\left(-\mathbf{m}_z^H (\boldsymbol{\Sigma}_z + 2 \sin^2 \theta \mathbf{I})^{-1} \mathbf{m}_z\right)}{\left|\frac{\boldsymbol{\Sigma}_z}{2 \sin^2 \theta} + \mathbf{I}\right|} d\theta \quad (\text{C.13})$$

Appendix D

Proof of the equivalency between conventional pulse shaping and the proposed filter domain schemes

The pulse shaping in conventional transmitter is a discrete convolution of $c''[m]$ the complex symbols up-sampled by λ with the finite impulse response (FIR) pulse shaping filter $f[m]$ of length L . Thus, the proposed system becomes equivalent to conventional transceiver when all filters in the bank are the same Nyquist filter f . In this case, the ISI cancellation at the receiver can be deactivated. The conventional pulse shaping can be expressed as:

$$x[m] = f[m] * c''[m] = \sum_{m=-\infty}^{\infty} f[m].c''[n-m] = \sum_{m=1}^L f[m].c''[n-m], \quad (\text{D.1})$$

where $f[m] = 0$ when m is outside the region $[1, L]$, $c''[m]$ is of length $N.\lambda$ and N is the number of APM symbols.

Using “Overlap-Add method”, the output of the filtering convolution can be divided into multiple convolutions of $f[m]$ with segments of $c''[m]$:

$$c''_n[m] = \begin{cases} c''[m+n.\lambda] & m = 1, 2, \dots, \lambda \\ 0 & \text{otherwise} \end{cases} \quad (\text{D.2})$$

Then:

$$c''[m] = \sum_n c''_n[m-n.\lambda]. \quad (\text{D.3})$$

Thus, $x[m]$ can be written as a sum of convolutions by replacing (D.3) in (D.1), we obtain:

$$x[m] = f[m] * c''[m] = f[m] * \left(\sum_n c''_n[m-n.\lambda] \right) = \left(\sum_n f[m] * c''_n[m-n.\lambda] \right) = \sum_n s_n[m-n.\lambda],$$

where $s_n[m] \triangleq f[m] * c_n''[m] = f[m] * c_n'[m]$ is zero outside the region $[1, L]$ because $c_n''[m]$ and $c_n'[m]$ contains only one non-zero element for each n .

In the proposed system, $s_n[m]$ is calculated for each APM symbol, then these outputs are overlapped and added but the filter f can be changed at each symbol period to gain in SE by indexing the selected filter.

Appendix E List of Publications

Publication related to the thesis

The contributions related to the works presented in this manuscript are listed in the following, and ordered historically from the most recent to the oldest:

Accepted Journal articles:

- [J4] N. Bouhlef, M. Saad, F. Bader, "Sub-Terahertz Wireless System using Dual-Polarized Generalized Spatial Modulation with RF Impairments," *IEEE Journal on Selected Areas in Communications*- Special issue on THz Communications and Networking, 2021, In press.
- [J3] M. Saad, N. Al Akkad, H. Hijazi, A. C. Al Ghouwayel, F. Bader and J. Palicot, "Novel MIMO Technique for Wireless Terabits Systems in sub-THz Band," *IEEE Open Journal of Vehicular Technology*, vol. 2, pp. 125-139, Jan. 2021, doi: 10.1109/OJVT.2021.3054737.
- [J2] M. Saad, J. Palicot, F. Bader, A. C. Al Ghouwayel and H. Hijazi, "A Novel Index Modulation Dimension based on Filter Domain: Filter Shapes Index Modulation," *IEEE Transactions on Communications*, *IEEE Transactions on Communications*, Nov. 2020, In press, doi: 10.1109/TCOMM.2020.3039842.
- [J1] H. Hijazi, A. Haroun, M. Saad, A. C. Al Ghouwayel and A. Dhayni, "Near-Optimal Performance with Low Complexity ML-based detector for MIMO Spatial Multiplexing," *IEEE Communications Letters*, vol. 25, no. 1, pp. 122-126, Jan. 2021, doi: 10.1109/LCOMM.2020.3024107.

Accepted International conferences

- [C7] M. Saad, J. Palicot, F. Bader, A. C. Al Ghouwayel and H. Hijazi, "Filter Shape Index Modulation," *IEEE International Conference on Communications (ICC)*, Montreal, Canada, June 2021.

- [C6] N. Bouhlef, M. Saad, F. Bader and J. Palicot “Dual-Polarized Generalized Spatial Modulation for Wireless Terabit System,” *2020 IEEE International Symposium on Personal, Indoor and Mobile Radio Communications (PIMRC)*, London, United Kingdom, Sept 2020, pp. 1-7.
- [C5] M. Saad, A. C. Al Ghouwayel, H. Hijazi, F. Bader and J. Palicot, “MIMO Techniques for Wireless Terabits Systems under sub-THz Channel with RF Impairments,” in *IEEE International Conference on Communications (ICC)*, Dublin, Ireland, June 2020, pp. 1-6.
- [C4] M. Saad, F. Bader, A. C. Al Ghouwayel, H. Hijazi, N. Bouhel and J. Palicot, “Generalized Spatial Modulation for Wireless Terabits Systems Under Sub-THz Channel With RF Impairments,” *2020 IEEE International Conference on Acoustics, Speech and Signal Processing (ICASSP)*, Barcelona, Spain, 2020, pp. 5135-5139.
- [C3] M. Saad, F. C. Lteif, A. C. Al Ghouwayel, H. Hijazi, J. Palicot and F. Bader, “Generalized Spatial Modulation in Highly Correlated Channels,” *2019 IEEE 30th International Symposium on Personal, Indoor and Mobile Radio Communications (PIMRC Workshops)*, Istanbul, Turkey, 2019, pp. 1-6.
- [C2] Y. Corre, G. Gougeon, J. Doré, S. Bicaïs, B. Miscopain, M. Saad, J. Palicot, F. Bader, “Sub-THz Spectrum as Enabler for 6G Wireless Communications up to 1 Tbit/s”, *2019 6G wireless summit*, Levi Lapland, Finland, Marc 2019.
- [C1] M. Saad, F. Bader, J. Palicot, A. Chamas Al Ghouwayel and H. Hijazi, ”Single Carrier with Index Modulation for Low Power Terabit Systems,” *2019 IEEE Wireless Communications and Networking Conference (WCNC)*, Marrakech, Morocco, Apr. 2019, pp. 1–7.

French National Conference

- [NC1] M. Saad, F. Bader, J. Palicot, A. C. Al Ghouwayel and H. Hijazi, “Nouvelle Approche pour les Systèmes Térabit à Faible Puissance,” *XXVIIème Colloque francophone de traitement du signal et des images-GRETSI*, Lille, France, Aug. 2019.

Poster

- [P1] M. Saad, “Back to single carrier for beyond 5G communications above 90GHz”, IETR PhD student Day, University of South Brittany (UBS)- Campus Tohannic, Vannes, France, June 2018.

Technical deliverable of the French funded project-ANR-17-CE25-0013 BRAVE

- [TR2] M. Saad, F. Bader, J. Palicot, Y. Corre, G. Gougeon, J-B Doré, “Beyond-5G wireless Tbps Scenarios and Requirements,” French funded project-ANR-17-CE25-0013 BRAVE,

Tech. Report BRAVE D1.0, 2018. [Online]. Available: <https://hal.archives-ouvertes.fr/hal-01947363/document>.

- [TR1] M. Saad, N. Bouhlef, F. Bader, S. Bicaïs, J-B Doré, Y. Corre, M. Z. Aslam, “Propagation channel model and RF impairments definition and waveform design,” French funded project-ANR-17-CE25-0013 BRAVE, Tech. Report BRAVE D2.1, 2020.

Talks without proceedings

- [T1] M. Saad, “New Methodology for Low Power Terabit Systems/ Nouvelle Méthodologie pour les Systèmes Térabit à Faible Puissance”, IETR/CentraleSupélec seminar, Rennes, France, 21th Feb. 2019.

Publications indirectly related to this thesis

During my earlier research in PhD, I have had the opportunity to work on broader research aspects indirectly related to this dissertation, in the fields of 5G waveform candidates and the transceiver complexity reduction. The relevant published works are listed here.

International conferences

- [C9] M. Saad, A. Al-Ghouwayel and H. Hijazi, “UFMC Transceiver Complexity Reduction,” *2018 25th IEEE International Conference on Telecommunications (ICT)*, St. Malo, Jun. 2018, pp. 295-301.
- [C8] M. Saad, M. Alawieh, A. C. Al Ghouwayel, H. Hijazi and S. Omar, “On the Hardware Implementation of a Reduced Complexity UFMC Chain,” *2018 IEEE International Conference on Computer and Applications (ICCA)*, Beirut, Aug. 2018, pp. 162-167.

R&D ANR Project Involvement

BRAVE

BRAVE (**B**ack to single-ca**R**rier for beyond-5G communications **A**bo**V**E 90GHz) is a collaborative research project funded by the French Research Agency ANR started in January 2018 and ends in September 2021. BRAVE aims at creating new physical-layer (PHY) techniques devoted to beyond-5G wireless communications. The partners (Siradel, CentraleSupélec, CEA-Leti and ANFR) are designing new high-data-rate and energy-efficient waveforms that operate in frequencies above 90 GHz. Application to scenarios such as kiosks, backhauling, hotspots are assessed to evaluate the benefit of the proposed technology [8].

The consortium is combining skills from an industry (SIRADEL), an academic laboratory (Centrale-Supélec), a research institute (CEA-Leti) and a regulator (ANFR), which are all familiar with collaborative research and recognized in the field of wireless innovation. The partners bring complementary skills to efficiently tackle the project's different challenges: regulation, signal processing, realistic modeling of the PHY-layer, and software-based evaluation.

My role as a member of CentraleSupélec in this project has been related mainly to ultra-high data rates scenarios' definition, waveform design, and its performance assessment in sub-THz bands with RF impairments. Almost all the publications related to this thesis contribute to this project.

Others

- Participating in the organizing committee of the 2018 25th IEEE International Conference on Telecommunication (ICT) held at Saint-Malo, France, June 2018.
- Earning a mobility grant for research collaboration between IETR-CentralSupélec and University of Patras-Greece from the French National Centre for Scientific Research (CNRS) jointly with “Le Groupement de Recherche Information, Signal, Images et ViSion” (GdR-ISIS) organization in 2019.

Bibliography

- [1] M. Latva-aho and K. Leppänen, “Key drivers and research challenges for 6G ubiquitous wireless intelligence,” in *6G Research Visions 1, 6G summit*, Oulu, Finland, Sep. 2019.
- [2] IEEE 802.15.3d Standard Association, *IEEE 802.15.3d TG3d Technical Requirements Document*, Mar. 2016, [Online]. Available: <https://mentor.ieee.org/802.15/dcn/14/15-14-0309-20-003d-technical-requirements-document.docx>.
- [3] IEEE 802.15.3d Standard Association, *IEEE 802.15.3d TG3d Applications Requirements Document (ARD)*, May 2015, [Online]. Available: <https://mentor.ieee.org/802.15/dcn/14/15-14-0304-16-003d-applications-requirement-document-ard.docx>.
- [4] M. Saad, F. Bader, J. Palicot, Y. Corre, G. Gougeon, and J.-B. Doré, “Beyond-5G wireless Tbps scenarios and requirements,” French funded project-ANR-17-CE25-0013 (BRAVE), Tech. Report D1.0, 2018, [Online]. Available: <https://hal.archives-ouvertes.fr/hal-01947363/document>.
- [5] N. Rajatheva, I. Atzeni, E. Bjornson, A. Bourdoux, S. Buzzi, J.-B. Dore, S. Erkucuk, M. Fuentes, K. Guan, Y. Hu, others Nandana Rajatheva, I. Atzeni, E. Björnson, A. Bourdoux, S. Buzzi, J.-B. Doré⁵, S. Erkucuk, M. Fuentes, K. Guan, Y. Hu, X. Huang, J. Hulkkonen, J. M. Jornet, M. Katz, R. Nilsson, E. Panayirci, K. Rabie, N. Rajapaksha, M. Salehi, H. Sardeddeen, S. Shahabuddin, T. Svensson, O. Tervo, A. Tölli, Q. Wu, and W. Xu, “White paper on broadband connectivity in 6G,” (*6G Research Visions, No. 10*). *University of Oulu*, Jun. 2020, [Online]. Available: <http://urn.fi/urn:isbn:9789526226798>.
- [6] T. S. Rappaport, Y. Xing, O. Kanhere, S. Ju, A. Madanayake, S. Mandal, A. Alkhateeb, and G. C. Trichopoulos, “Wireless communications and applications above 100 GHz: opportunities and challenges for 6G and beyond,” *IEEE Access*, vol. 7, pp. 78 729–78 757, Jun. 2019.
- [7] L. Cailloce, “Numérique : Le grand gâchis énergétique ;,” *CNRS, le journal*, May 2018, CNRS, le journal. [Online]. Available: <https://lejournel.cnrs.fr/articles/numerique-le-grand-gachis-energetique>.

- [8] French funded project-ANR-17-CE25-0013, “Back to single-carrier for beyond-5G communications above 90 GHz-(BRAVE),” [Online]. Available: <http://www.brave-beyond5g.com>.
- [9] J. Palicot and F. Bader, “Backing to single carrier in Tera Hertz communications for green considerations,” in *2017 XXXIInd General Assembly and Scientific Symposium of the International Union of Radio Science (URSI GASS)*, Montreal, QC, Canada, Aug. 2017, pp. 1–4.
- [10] M. Saad, F. Bader, J. Palicot, A. C. Al Ghouwayel, and H. Hijazi, “Nouvelle approche pour les systèmes Térabit à faible puissance,” in *XXVIIème Colloque francophone de traitement du signal et des images-GRETSI*, Lille, France, Aug. 2019.
- [11] S. Bicais and J.-B. Doré, “Phase noise model selection for sub-THz communications,” in *2019 IEEE Global Communications Conference (GLOBECOM)*, Waikoloa, HI, USA, Dec. 2019, pp. 1–6.
- [12] J. Wells, “Faster than fiber: The future of multi-g/s wireless,” *IEEE Microwave Magazine*, vol. 10, no. 3, pp. 104–112, May 2009.
- [13] T. S. Rappaport, J. N. Murdock, and F. Gutierrez, “State of the art in 60-ghz integrated circuits and systems for wireless communications,” *Proceedings of the IEEE*, vol. 99, no. 8, pp. 1390–1436, Aug. 2011.
- [14] M. Saad, F. Bader, J. Palicot, A. C. Al Ghouwayel, and H. Hijazi, “Single carrier with index modulation for low power terabit systems,” in *2019 IEEE Wireless Communications and Networking Conference (WCNC)*, Marrakech, Morocco, Apr. 2019, pp. 1–7.
- [15] M. Saad, F. C. Lteif, A. C. Al Ghouwayel, H. Hijazi, J. Palicot, and F. Bader, “Generalized spatial modulation in highly correlated channels,” in *2019 IEEE 30th International Symposium on Personal, Indoor and Mobile Radio Communications (PIMRC Workshops)*, Istanbul, Turkey, Sep. 2019, pp. 1–6.
- [16] M. Saad, F. Bader, A. C. Al Ghouwayel, H. Hijazi, N. Bouhel, and J. Palicot, “Generalized spatial modulation for wireless Terabits systems under sub-THz channel with RF impairments,” in *ICASSP 2020 - 2020 IEEE International Conference on Acoustics, Speech and Signal Processing (ICASSP)*, Barcelona, Spain, May 2020, pp. 5135–5139.
- [17] M. Saad, A. C. Al Ghouwayel, H. Hijazi, F. Bader, and J. Palicot, “MIMO techniques for wireless Terabits systems under sub-THz channel with RF impairments,” in *IEEE International Conference on Communications (ICC)*, Dublin, Ireland, Jun. 2020, pp. 1–6.

-
- [18] M. Saad, H. Hijazi, A. C. Al Ghouwayel, F. Bader, and J. Palicot, "Low Complexity Quasi-Optimal Detector for Generalized Spatial Modulation," *IEEE Communications Letters*, 2020, (Submitted).
- [19] H. Hijazi, A. Haroun, M. Saad, A. C. Al Ghouwayel, and A. Dhayni, "Near-optimal performance with low complexity ML-based detector for MIMO spatial multiplexing," *IEEE Communications Letters*, vol. 25, no. 1, pp. 122–126, Jan. 2021.
- [20] N. Bouhleb, M. Saad, F. Bader, and J. Palicot, "Dual-polarized generalized spatial modulation for wireless terabit system," in *31st IEEE International Symposium on Personal, Indoor and Mobile Radio Communications (PIMRC'2020)*, London, United Kingdom, Sep. 2020, pp. 1–7.
- [21] N. Bouhleb, M. Saad, and F. Bader, "Sub-Terahertz wireless system using dual-polarized generalized spatial modulation with RF impairments," *IEEE Journal on Selected Areas in Communications - Special Issue on THz Communications and Networking*, 2020, (In press.).
- [22] M. Saad, J. Palicot, F. Bader, A. C. Al Ghouwayel, and H. Hijazi, "A Novel Index Modulation Dimension based on Filter Domain: Filter Shapes Index Modulation," *IEEE Transactions on Communications*, 2020, In Press.
- [23] M. Saad, J. Palicot, F. Bader, A. C. Al Ghouwayel, and H. Hijazi, "Filter Shapes Index Modulation," in *2021 IEEE International Conference on Communications (ICC)*, Montreal, Canada, Jun. 2021, in press.
- [24] M. Saad, H. Hijazi, A. C. Al Ghouwayel, F. Bader, and J. Palicot, "Quadrature Filter Shapes Index Modulation," *IEEE Transactions on Communications*, 2021, (Submitted).
- [25] M. Saad, N. Al Akkad, H. Hijazi, A. C. Al Ghouwayel, F. Bader, and J. Palicot, "Novel MIMO Technique for Wireless Terabits Systems in sub-THz Band," *IEEE Open Journal of Vehicular Technology*, vol. 2, pp. 125–139, Jan. 2020.
- [26] J.-B. Doré, Y. Corre, S. Bicaïs, J. Palicot, E. Faussurier, D. Ktenas, and F. Bader, "Above-90GHz spectrum and single-carrier waveform as enablers for efficient Tbit/s wireless communications," in *2018 25th International Conference on Telecommunications (ICT)*, St. Malo, France, Jun. 2018, pp. 274–278.
- [27] "TS 38.101-2: NR; User Equipment (UE) radio transmission and reception; Part 2: Range 2 Standalone", 3GPP Std., Oct. 2020, [Online]. Available: https://www.3gpp.org/ftp/Specs/archive/38_series/38.101-2/38101-2-g50.zip.
- [28] IEEE Std 802.15.3e-2017 (Amendment to IEEE Std 802.15.3-2016), *IEEE Standard for High Data Rate Wireless Multi-Media Networks—Amendment 1: High-Rate Close Proximity Point-to-Point Communications*, Jun. 2017.

- [29] IEEE Std 802.15.3d-2017 (Amendment to IEEE Std 802.15.3-2016 as amended by IEEE Std 802.15.3e-2017), *IEEE Standard for High Data Rate Wireless Multi-Media Networks—Amendment 2: 100 Gb/s Wireless Switched Point-to-Point Physical Layer*, Oct. 2017.
- [30] I. F. Akyildiz, J. M. Jornet, and C. Han, “Terahertz band: Next frontier for wireless communications,” *Physical Communication (Elsevier) Journal*, vol. 12, pp. 16–32, Sep. 2014.
- [31] Y. Corre, G. Gougeon, J.-B. Doré, S. Bicaïs, B. Miscopein, E. Faussurier, M. Saad, J. Palicot, and F. Bader, “Sub-THz spectrum as enabler for 6G wireless communications up to 1 Tbit/s,” in *6G Wireless Summit*, Levi Lapland, Finland, Mar. 2019.
- [32] “FCC opens spectrum horizons for new services & technologies,” Mar. 2019, [Online]. Available: https://docs.fcc.gov/public/attachments/FCC-19-19A1_Rcd.pdf.
- [33] ISO/IEC/IEEE 8802-11:2012/Amd.3:2014(E), *ISO/IEC/IEEE International Standard for Information technology—Telecommunications and information exchange between systems—Local and metropolitan area networks—Specific requirements—Part 11: Wireless LAN Medium Access Control (MAC) and Physical Layer (PHY) Specifications Amendment 3: Enhancements for Very High Throughput in the 60 GHz Band (adoption of IEEE Std 802.11ad-2012)*, 2014.
- [34] H. Elayan, R. M. Shubair, J. M. Jornet, and P. Johari, “Terahertz channel model and link budget analysis for intrabody nanoscale communication,” *IEEE Transactions on NanoBioscience*, vol. 16, no. 6, pp. 491–503, Sep. 2017.
- [35] Y. Xing and T. S. Rappaport, “Propagation measurement system and approach at 140 ghz-moving to 6g and above 100 ghz,” in *2018 IEEE Global Communications Conference (GLOBECOM)*, Abu Dhabi, United Arab Emirates, Dec. 2018, pp. 1–6.
- [36] G. Gougeon, Y. Corre, and M. Z. Aslam, “Ray-based deterministic channel modelling for sub-THz band,” in *2019 IEEE 30th International Symposium on Personal, Indoor and Mobile Radio Communications (PIMRC Workshops)*, Istanbul, Turkey, Sep. 2019, pp. 1–6.
- [37] Hua Wang and Fei Wang and Sensen Li and Tzu-Yuan Huang and Amr S. Ahmed and Naga Sasikanth Mannem and Jeongseok Lee and Edgar Garay and David Munzer and Christopher Snyder and Sanghoon Lee and Huy Thong Nguyen and Michael Edward Duffy Smith, “Power Amplifiers Performance Survey 2000-Present,” [Online]. Available: https://gems.ece.gatech.edu/PA_survey.html.
- [38] G. Chattopadhyay, “Technology, capabilities, and performance of low power terahertz sources,” *IEEE Transactions on Terahertz Science and Technology*, vol. 1, no. 1, pp. 33–53, Sep. 2011.
- [39] B. Murmann, “ADC performance survey 1997-2020,” 2020, [Online]. Available: <http://web.stanford.edu/~murmman/adcsurvey.html>.

-
- [40] “Radio frequency channel/block arrangements for Fixed Service systems operating in the bands 130-134 GHz, 141-148.5 GHz, 151.5-164 GHz and 167-174.8 GHz,” ECC Recommendation (18)01 of 27 April 2018, Tech. Report 18(01), 2018, [Online]. Available: <https://www.ecodocdb.dk/download/a5533f97-5a92/Rec1801.pdf>.
- [41] S. Weithoffer, C. A. Nour, N. Wehn, C. Douillard, and C. Berrou, “25 years of turbo codes: From mb/s to beyond 100 gb/s,” in *2018 IEEE 10th International Symposium on Turbo Codes & Iterative Information Processing (ISTC)*. Hong Kong, China: IEEE, Dec. 2018, pp. 1–6.
- [42] S. Weithoffer, R. Klaimi, C. A. Nour, N. Wehn, and C. Douillard, “Fully pipelined iteration unrolled decoders the road to TB/s turbo decoding,” in *ICASSP 2020 - 2020 IEEE International Conference on Acoustics, Speech and Signal Processing (ICASSP)*, Barcelona, Spain, May 2020, pp. 5115–5119.
- [43] G. Fettweis, F. Guderian, and S. Krone, “Entering the path towards terabit/s wireless links,” in *2011 Design, Automation Test in Europe*, Grenoble, France, Mar. 2011, pp. 1–6.
- [44] J. M. Jornet and I. F. Akyildiz, “Graphene-based plasmonic nano-transceiver for terahertz band communication,” in *The 8th European Conference on Antennas and Propagation (EuCAP 2014)*, The Hague, Netherlands, Apr. 2014, pp. 492–496.
- [45] J. M. Jornet and I. F. Akyildiz, “Graphene-based plasmonic nano-antenna for terahertz band communication in nanonetworks,” *IEEE Journal on Selected Areas in Communications*, vol. 31, no. 12, pp. 685–694, Dec. 2013.
- [46] P. K. Singh, G. Aizin, N. Thawdar, M. Medley, and J. M. Jornet, “Graphene-based plasmonic phase modulator for terahertz-band communication,” in *2016 10th European Conference on Antennas and Propagation (EuCAP)*, Davos, Switzerland, Apr. 2016, pp. 1–5.
- [47] L. Zakrajsek, E. Einarsson, N. Thawdar, M. Medley, and J. M. Jornet, “Lithographically defined plasmonic Graphene antennas for terahertz-band communication,” *IEEE Antennas and Wireless Propagation Letters*, vol. 15, pp. 1553–1556, Feb. 2016.
- [48] A. Singh, M. Andreello, N. Thawdar, and J. M. Jornet, “Design and operation of a Graphene-based plasmonic nano-antenna array for communication in the terahertz band,” *IEEE Journal on Selected Areas in Communications*, vol. 38, no. 9, pp. 2104–2117, sep 2020.
- [49] J. Andrews, *Fundamentals of WiMAX : understanding broadband wireless networking*. Upper Saddle River, NJ: Prentice Hall, 2007.
- [50] H. Yang, P. F. Smulders, and E. R. Fledderus, “Comparison of single- and multi-carrier block transmissions under the effect of nonlinear HPA,” in *2007 14th IEEE Symposium on Communications and Vehicular Technology in the Benelux*, Delft, Netherlands, Nov. 2007, pp. 1–7.

- [51] “LoRa™ modulation basics,” Semtech Corporation, techreport AN1200.22, May 2015.
- [52] T. Schenk, *RF imperfections in high-rate wireless systems: Impact and digital compensation*, 1st ed. Springer Netherlands, 2008.
- [53] T. Pollet, M. V. Bladel, and M. Moeneclaey, “BER sensitivity of OFDM systems to carrier frequency offset and Wiener phase noise,” *IEEE Transactions on Communications*, vol. 43, no. 2/3/4, pp. 191–193, Feb. 1995.
- [54] J. Tubbax, L. V. der Perre, M. Engels, H. D. Man, and M. Moonen, “OFDM versus single carrier: A realistic multi-antenna comparison,” *EURASIP Journal on Advances in Signal Processing*, vol. 2004, no. 9, aug 2004.
- [55] J. Dohl, S. Krone, and G. Fettweis, “On the impact of non-linear amplifiers in single-carrier systems: an analytical approach,” in *2010 IEEE 71st Vehicular Technology Conference*. IEEE, 2010.
- [56] A. A. Zaidi, J. Luo, R. Gerzaguët, H. Wang, X. Chen, Y. Qi, N. Cassiau, A. Wolfgang, J. Vihriala, A. Kakkavas, T. Svensson, J. Mohammadi, R. J. Weiler, M. Dieudonne, H. Halbauer, V. Moles-Cases, and H. Miao, “Evaluation of waveforms for mobile radio communications above 6 GHz,” in *2016 IEEE Globecom Workshops (GC Wkshps)*, Washington, DC, USA, Dec. 2016, pp. 1–6.
- [57] J. M. Jornet and I. F. Akyildiz, “Channel modeling and capacity analysis for electromagnetic wireless nanonetworks in the terahertz band,” *IEEE Transactions on Wireless Communications*, vol. 10, no. 10, pp. 3211–3221, Oct. 2011.
- [58] J. M. Jornet and I. F. Akyildiz, “Femtosecond-long pulse-based modulation for terahertz band communication in nanonetworks,” *IEEE Transactions on Communications*, vol. 62, no. 5, pp. 1742–1754, May 2014.
- [59] I. F. Akyildiz and J. M. Jornet, “The internet of nano-things,” *IEEE Wireless Communications*, vol. 17, no. 6, pp. 58–63, Dec. 2010.
- [60] K. Yang, D. Bi, Y. Deng, R. Zhang, M. M. U. Rahman, N. A. Ali, M. A. Imran, J. M. Jornet, Q. H. Abbasi, and A. Alomainy, “A comprehensive survey on hybrid communication in context of molecular communication and terahertz communication for body-centric nanonetworks,” *IEEE Transactions on Molecular, Biological and Multi-Scale Communications*, vol. 6, no. 2, pp. 107–133, Nov. 2020.
- [61] I. Llatser, A. Cabellos-Aparicio, E. Alarcon, J. M. Jornet, A. Mestres, H. Lee, and J. Sole-Pareta, “Scalability of the channel capacity in Graphene-enabled wireless communications to the nanoscale,” *IEEE Transactions on Communications*, vol. 63, no. 1, pp. 1–1, Dec. 2014.
- [62] I. F. Akyildiz and J. M. Jornet, “Realizing ultra-massive MIMO(1024×1024)communication in the (0.06–10) Terahertz band,” *Nano Communication Networks*, vol. 8, pp. 46–54, Jun. 2016.

-
- [63] L. Xiao, P. Xiao, Y. Xiao, C. Wu, H. V. Nguyen, I. A. Hemadeh, and L. Hanzo, "Transmit antenna combination optimization for generalized spatial modulation systems," *IEEE Access*, vol. 6, pp. 41 866–41 882, Jul. 2018.
- [64] J. Pierce, "Optical channels: Practical limits with photon counting," *IEEE Transactions on Communications*, vol. 26, no. 12, pp. 1819–1821, Dec. 1978.
- [65] X. Liu, T. H. Wood, R. W. Tkach, and S. Chandrasekhar, "Demonstration of record sensitivity in an optically pre-amplified receiver by combining PDM-QPSK and 16-PPM with pilot-assisted digital coherent detection," in *Optical Fiber Communication Conference and the National Fiber Optic Engineers Conference*, Los Angeles, CA, USA, Mar. 2011, pp. 1–3.
- [66] M. Nakao, T. Ishihara, and S. Sugiura, "Single-carrier frequency domain equalization with index modulation," *IEEE Communications Letters*, vol. 21, no. 2, pp. 298–301, Feb. 2017.
- [67] E. Basar, U. Aygolu, E. Panayirci, and H. V. Poor, "Orthogonal frequency division multiplexing with index modulation," *IEEE Transactions on Signal Processing*, vol. 61, no. 22, pp. 5536–5549, Nov. 2013.
- [68] D. Tsonev, S. Sinanovic, and H. Haas, "Enhanced subcarrier index modulation (SIM) OFDM," in *2011 IEEE GLOBECOM Workshops (GC Wkshps)*, Houston, TX, USA, Dec. 2011, pp. 728–732.
- [69] E. Ozturk, E. Basar, and H. A. Cirpan, "Generalized frequency division multiplexing with flexible index modulation numerology," *IEEE Signal Processing Letters*, vol. 25, no. 10, pp. 1480–1484, Oct. 2018.
- [70] G. Cheng, L. Wang, W. Xu, and G. Chen, "Carrier index differential chaos shift keying modulation," *IEEE Transactions on Circuits and Systems II: Express Briefs*, vol. 64, no. 8, pp. 907–911, Aug. 2017.
- [71] A. M. Jaradat, J. M. Hamamreh, and H. Arslan, "OFDM with subcarrier number modulation," *IEEE Wireless Communications Letters*, vol. 7, no. 6, pp. 914–917, Dec. 2018.
- [72] S. Dang, G. Ma, B. Shihada, and M. Alouini, "Enhanced orthogonal frequency-division multiplexing with subcarrier number modulation," *IEEE Internet of Things Journal*, vol. 6, no. 5, pp. 7907–7920, Oct. 2019.
- [73] S. Althunibat, R. Mesleh, and T. F. Rahman, "A novel uplink multiple access technique based on index-modulation concept," *IEEE Transactions on Communications*, vol. 67, no. 7, pp. 4848–4855, Jul. 2019.
- [74] S. Althunibat, R. Mesleh, and K. A. Qaraqe, "IM-OFDMA: A novel spectral efficient uplink multiple access based on index modulation," *IEEE Transactions on Vehicular Technology*, vol. 68, no. 10, pp. 10 315–10 319, Oct. 2019.

- [75] S. Althunibat, R. Mesleh, and K. Qaraqe, "Quadrature index modulation based multiple access scheme for 5g and beyond," *IEEE Communications Letters*, vol. 23, no. 12, pp. 2257–2261, dec 2019.
- [76] R. Fan, Y. J. Yu, and Y. L. Guan, "Generalization of orthogonal frequency division multiplexing with index modulation," *IEEE Transactions on Wireless Communications*, vol. 14, no. 10, pp. 5350–5359, Oct. 2015.
- [77] M. Wen, B. Ye, E. Basar, Q. Li, and F. Ji, "Enhanced orthogonal frequency division multiplexing with index modulation," *IEEE Transactions on Wireless Communications*, vol. 16, no. 7, pp. 4786–4801, Jul. 2017.
- [78] J. Li, S. Dang, M. Wen, X.-Q. Jiang, Y. Peng, and H. Hai, "Layered orthogonal frequency division multiplexing with index modulation," *IEEE Systems Journal*, vol. 13, no. 4, pp. 3793–3802, dec 2019.
- [79] M. Nakao and S. Sugiura, "Dual-mode time-domain single-carrier index modulation with frequency-domain equalization," in *2017 IEEE 86th Vehicular Technology Conference (VTC-Fall)*, Toronto, ON, Canada, Sep. 2017, pp. 1–5.
- [80] M. Nakao, T. Ishihara, and S. Sugiura, "Dual-mode time-domain index modulation for nyquist-criterion and faster-than-nyquist single-carrier transmissions," *IEEE Access*, vol. 5, pp. 27 659–27 667, Nov. 2017.
- [81] T. Mao, Z. Wang, Q. Wang, S. Chen, and L. Hanzo, "Dual-mode index modulation aided OFDM," *IEEE Access*, vol. 5, pp. 50–60, Aug. 2017.
- [82] T. Mao, Q. Wang, and Z. Wang, "Generalized dual-mode index modulation aided OFDM," *IEEE Communications Letters*, vol. 21, no. 4, pp. 761–764, Apr. 2017.
- [83] M. Wen, E. Basar, Q. Li, B. Zheng, and M. Zhang, "Multiple-mode orthogonal frequency division multiplexing with index modulation," *IEEE Transactions on Communications*, vol. 65, no. 9, pp. 3892–3906, Sep. 2017.
- [84] M. Wen, Q. Li, E. Basar, and W. Zhang, "Generalized multiple-mode OFDM with index modulation," *IEEE Transactions on Wireless Communications*, vol. 17, no. 10, pp. 6531–6543, Oct. 2018.
- [85] M. Chafii, F. Bader, and J. Palicot, "SC-FDMA with index modulation for M2M and IoT uplink applications," in *2018 IEEE Wireless Communications and Networking Conference (WCNC)*, Barcelona, Spain, Apr. 2018, pp. 1–5.
- [86] T. Ishihara and S. Sugiura, "Faster-than-nyquist signaling with index modulation," *IEEE Wireless Communications Letters*, vol. 6, no. 5, pp. 630–633, Oct. 2017.

-
- [87] M. Nakao and S. Sugiura, "Spectrally efficient frequency division multiplexing with index-modulated non-orthogonal subcarriers," *IEEE Wireless Communications Letters*, vol. 8, no. 1, pp. 233–236, Feb. 2019.
- [88] E. Basar, "Multiple-input multiple-output OFDM with index modulation," *IEEE Signal Processing Letters*, vol. 22, no. 12, pp. 2259–2263, Dec. 2015.
- [89] G. Kaddoum, M. F. A. Ahmed, and Y. Nijsure, "Code index modulation: A high data rate and energy efficient communication system," *IEEE Communications Letters*, vol. 19, no. 2, pp. 175–178, Feb. 2015.
- [90] G. Kaddoum, Y. Nijsure, and H. Tran, "Generalized code index modulation technique for high-data-rate communication systems," *IEEE Transactions on Vehicular Technology*, vol. 65, no. 9, pp. 7000–7009, Sep. 2016.
- [91] W. Xu and L. Wang, "CIM-DCSK: A differential chaos shift keying scheme with code-index modulation," in *2016 16th International Symposium on Communications and Information Technologies (ISCIT)*, Qingdao, China, Sep. 2016, pp. 100–104.
- [92] S. Alamouti, "A simple transmit diversity technique for wireless communications," *IEEE Journal on Selected Areas in Communications*, vol. 16, no. 8, pp. 1451–1458, Oct. 1998.
- [93] J. Proakis, *Digital signal processing: principles algorithms and applications*. Prentice Hall, 2001.
- [94] L. Zheng and D. Tse, "Diversity and multiplexing: a fundamental tradeoff in multiple-antenna channels," *IEEE Transactions on Information Theory*, vol. 49, no. 5, pp. 1073–1096, May 2003.
- [95] G. J. Foschini, "Layered Space-Time Architecture for wireless communication in a fading environment when using multi-element antennas," *Bell Labs Technical Journal*: 41–59., Tech. Rep., Oct. 1996.
- [96] P. Wolniansky, G. Foschini, G. Golden, and R. Valenzuela, "V-BLAST: an architecture for realizing very high data rates over the rich-scattering wireless channel," in *1998 URSI International Symposium on Signals, Systems, and Electronics. Conference Proceedings (Cat. No.98EX167)*, Pisa, Italy, Oct. 1998, pp. 295–300.
- [97] R. Mesleh, H. Haas, C. W. Ahn, and S. Yun, "Spatial Modulation - A new low complexity spectral efficiency enhancing technique," in *2006 First International Conference on Communications and Networking in China*, Beijing, Oct. 2006, pp. 1–5.
- [98] R. Y. Mesleh, H. Haas, S. Sinanovic, C. W. Ahn, and S. Yun, "Spatial modulation," *IEEE Transactions on Vehicular Technology*, vol. 57, no. 4, pp. 2228–2241, Jul. 2008.

- [99] N. Serafimovski, M. Di Renzo, S. Sinanovic, R. Y. Mesleh, and H. Haas, "Fractional bit encoded spatial modulation (FBE-SM)," *IEEE Communications Letters*, vol. 14, no. 5, pp. 429–431, May 2010.
- [100] L. Xiao, Y. Xiao, L. You, P. Yang, S. Li, and L. Hanzo, "Single-RF and twin-RF spatial modulation for an arbitrary number of transmit antennas," *IEEE Transactions on Vehicular Technology*, vol. 67, no. 7, pp. 6311–6324, Jul. 2018.
- [101] Y. Yang and S. Aissa, "Information guided channel hopping with an arbitrary number of transmit antennas," *IEEE Communications Letters*, vol. 16, no. 10, pp. 1552–1555, Oct. 2012.
- [102] J. Jeganathan, A. Ghrayeb, L. Szczecinski, and A. Ceron, "Space shift keying modulation for MIMO channels," *IEEE Transactions on Wireless Communications*, vol. 8, no. 7, pp. 3692–3703, Jul. 2009.
- [103] J. Jeganathan, A. Ghrayeb, and L. Szczecinski, "Generalized space shift keying modulation for MIMO channels," in *2008 IEEE 19th International Symposium on Personal, Indoor and Mobile Radio Communications*, Cannes, France, Sep. 2008, pp. 1–5.
- [104] A. Younis, N. Serafimovski, R. Mesleh, and H. Haas, "Generalised spatial modulation," in *2010 Conference Record of the Forty Fourth Asilomar Conference on Signals, Systems and Computers*, Pacific Grove, CA, Nov. 2010, pp. 1498–1502.
- [105] J. T. Wang, S. Y. Jia, and J. Song, "Generalised spatial modulation system with multiple active transmit antennas and low complexity detection scheme," *IEEE Transactions on Wireless Communications*, vol. 11, no. 4, pp. 1605–1615, Apr. 2012.
- [106] M. Di Renzo and H. Haas, "Bit error probability of space-shift keying MIMO over multiple-access independent fading channels," *IEEE Transactions on Vehicular Technology*, vol. 60, no. 8, pp. 3694–3711, Oct. 2011.
- [107] H.-W. Liang, R. Y. Chang, W.-H. Chung, H. Zhang, and S.-Y. Kuo, "Bi-space shift keying modulation for MIMO systems," *IEEE Communications Letters*, vol. 16, no. 8, pp. 1161–1164, Aug. 2012.
- [108] R. Mesleh, S. S. Ikki, and H. M. Aggoune, "Quadrature spatial modulation," *IEEE Transactions on Vehicular Technology*, vol. 64, no. 6, pp. 2738–2742, Jun. 2015.
- [109] L. Xiao, P. Xiao, Y. Xiao, H. Haas, A. Mohamed, and L. Hanzo, "Compressive sensing assisted generalized quadrature spatial modulation for massive MIMO systems," *IEEE Transactions on Communications*, vol. 67, no. 7, pp. 4795–4810, Jul. 2019.
- [110] E. Basar, U. Aygolu, E. Panayirci, and H. V. Poor, "Space-Time block coded spatial modulation," *IEEE Transactions on Communications*, vol. 59, no. 3, pp. 823–832, Mar. 2011.

-
- [111] Z. Yigit and E. Basar, "Space-time quadrature spatial modulation," in *2017 IEEE International Black Sea Conference on Communications and Networking (BlackSeaCom)*, Istanbul, Turkey, Jun. 2017, pp. 1–5.
- [112] L. He, J. Wang, C. Pan, and J. Song, "Extended space shift keying scheme for MIMO channels," in *2014 IEEE International Symposium on Broadband Multimedia Systems and Broadcasting*, Beijing, China, Jun. 2014, pp. 1–4.
- [113] A. Mokh, M. Helard, and M. Crussiere, "Space Shift Keying Modulations for Low Complexity Internet-of-Things Devices," in *GLOBECOM 2017 - 2017 IEEE Global Communications Conference*, Singapore, Dec. 2017, pp. 1–7.
- [114] L. He, J. Wang, and J. Song, "Extended spatial modulation scheme with low complexity detection algorithms," in *2014 International Wireless Communications and Mobile Computing Conference (IWCMC)*, Nicosia, Cyprus, Aug. 2014, pp. 582–587.
- [115] P. Liu, M. Di Renzo, and A. Springer, "Variable- N_u generalized spatial modulation for indoor LOS mmWave communication: Performance optimization and novel switching structure," *IEEE Transactions on Communications*, vol. 65, no. 6, pp. 2625–2640, Jun. 2017.
- [116] Y. Bian, X. Cheng, M. Wen, L. Yang, H. V. Poor, and B. Jiao, "Differential spatial modulation," *IEEE Transactions on Vehicular Technology*, vol. 64, no. 7, pp. 3262–3268, Jul. 2015.
- [117] N. Ishikawa and S. Sugiura, "Unified differential spatial modulation," *IEEE Wireless Communications Letters*, vol. 3, no. 4, pp. 337–340, Aug. 2014.
- [118] R. Mesleh, S. Althunibat, and A. Younis, "Differential quadrature spatial modulation," *IEEE Transactions on Communications*, vol. 65, no. 9, pp. 3810–3817, Sep. 2017.
- [119] M. Wen, Z. Ding, X. Cheng, Y. Bian, H. V. Poor, and B. Jiao, "Performance analysis of differential spatial modulation with two transmit antennas," *IEEE Communications Letters*, vol. 18, no. 3, pp. 475–478, Mar. 2014.
- [120] W. Zhang, Q. Yin, and H. Deng, "Differential full diversity spatial modulation and its performance analysis with two transmit antennas," *IEEE Communications Letters*, vol. 19, no. 4, pp. 677–680, Apr. 2015.
- [121] L. Yang, "Transmitter preprocessing aided spatial modulation for multiple-input multiple-output systems," in *2011 IEEE 73rd Vehicular Technology Conference (VTC Spring)*, Yokohama, Japan, May 2011, pp. 1–5.
- [122] R. Zhang, L.-L. Yang, and L. Hanzo, "Generalised pre-coding aided spatial modulation," *IEEE Transactions on Wireless Communications*, vol. 12, no. 11, pp. 5434–5443, Nov. 2013.

- [123] J. Li, M. Wen, X. Cheng, Y. Yan, S. Song, and M. H. Lee, "Generalized precoding-aided quadrature spatial modulation," *IEEE Transactions on Vehicular Technology*, vol. 66, no. 2, pp. 1881–1886, Feb. 2017.
- [124] D.-T. Phan-Huy and M. Helard, "Receive antenna shift keying for time reversal wireless communications," in *2012 IEEE International Conference on Communications (ICC)*, Ottawa, ON, Canada, Jun. 2012, pp. 4852–4856.
- [125] A. Mokh, M. Helard, and M. Crussiere, "Extended receive antenna shift keying," in *2017 24th International Conference on Telecommunications (ICT)*, Limassol, Cyprus, May 2017, pp. 1–6.
- [126] A. Mokh, M. Helard, and M. Crussiere, "Extended receive spatial modulation MIMO scheme for higher spectral efficiency," in *2018 IEEE 87th Vehicular Technology Conference (VTC Spring)*, Porto, Portugal, Jun. 2018, pp. 1–6.
- [127] M. Zhang, M. Wen, X. Cheng, and L. Yang, "Pre-coding aided differential spatial modulation," in *2015 IEEE Global Communications Conference (GLOBECOM)*, San Diego, CA, USA, Dec. 2015, pp. 1–6.
- [128] P. Cheng, Z. Chen, J. A. Zhang, Y. Li, and B. Vucetic, "A unified precoding scheme for generalized spatial modulation," *IEEE Transactions on Communications*, vol. 66, no. 6, pp. 2502–2514, Jun. 2018.
- [129] M. Koca and H. Sari, "Precoding for spatial modulation against correlated fading channels," *IEEE Transactions on Wireless Communications*, vol. 17, no. 9, pp. 5857–5870, Sep. 2018.
- [130] N. Ishikawa, R. Rajashekar, S. Sugiura, and L. Hanzo, "Generalized spatial modulation based reduced-RF-chain millimeter-wave communications," *IEEE Transactions on Vehicular Technology*, vol. 66, no. 1, pp. 879–883, Jan. 2017.
- [131] C. Liu, L.-L. Yang, W. Wang, and F. Wang, "Joint transmitter–receiver spatial modulation," *IEEE Access*, vol. 6, pp. 6411–6423, Jan. 2018.
- [132] D. N. Viet, M. Di Renzo, V. Basavarajappa, B. B. Exposito, J. Basterrechea, and D.-T. Phan-Huy, "Spatial modulation based on reconfigurable antennas: performance evaluation by using the prototype of a reconfigurable antenna," *EURASIP Journal on Wireless Communications and Networking 2019*, vol. 149, Jun. 2019.
- [133] Z. Boudia, H. El-Sallabi, A. Ghrayeb, and K. A. Qaraqe, "Reconfigurable antenna-based space-shift keying (SSK) for MIMO Rician channels," *IEEE Transactions on Wireless Communications*, vol. 15, no. 1, pp. 446–457, Jan. 2016.
- [134] B. Zuo, K. Zhao, W. Li, and N. Zhang, "Polarized modulation scheme for mobile satellite MIMO broadcasting," in *2015 IEEE International Wireless Symposium IWS*, Shenzhen, China, Mar. 2015, pp. 1–4.

-
- [135] Y. Ding, K. J. Kim, T. Koike-Akino, M. Pajovic, P. Wang, and P. Orlik, "Spatial scattering modulation for uplink millimeter-wave systems," *IEEE Communications Letters*, vol. 21, no. 7, pp. 1493–1496, Jul. 2017.
- [136] Y. Ding, V. Fusco, A. Shitvov, Y. Xiao, and H. Li, "Beam index modulation wireless communication with analog beamforming," *IEEE Transactions on Vehicular Technology*, vol. 67, no. 7, pp. 6340–6354, Jul. 2018.
- [137] S. Guo, H. Zhang, P. Zhang, P. Zhao, L. Wang, and M.-S. Alouini, "Generalized beamspace modulation using multiplexing: A breakthrough in mmWave MIMO," *IEEE Journal on Selected Areas in Communications*, vol. 37, no. 9, pp. 2014–2028, Sep. 2019.
- [138] A. K. Khandani, "Media-based modulation: A new approach to wireless transmission," in *IEEE International Symposium on Information Theory*, Istanbul, Turkey, Jul. 2013, pp. 3050–3054.
- [139] Y. Naresh and A. Chockalingam, "On media-based modulation using RF mirrors," *IEEE Transactions on Vehicular Technology*, vol. 66, no. 6, pp. 4967–4983, Jun. 2017.
- [140] E. Basar, "Media-Based Modulation for Future Wireless Systems: A Tutorial," *IEEE Wireless Communications*, vol. 26, no. 5, pp. 160–166, Oct. 2019.
- [141] Y. Naresh and A. Chockalingam, "A low-complexity maximum-likelihood detector for differential media-based modulation," *IEEE Communications Letters*, vol. 21, no. 10, pp. 2158–2161, Oct. 2017.
- [142] E. Seifi, M. Atamanesh, and A. K. Khandani, "Media-based MIMO: A new frontier in wireless communication," Oct. 2015, [Online]. Available: <https://arxiv.org/abs/1507.07516>.
- [143] E. Basar and I. Altunbas, "Space-Time channel modulation," *IEEE Transactions on Vehicular Technology*, vol. 66, no. 8, pp. 7609–7614, Aug. 2017.
- [144] S. Dogan-Tusha, A. Tusha, E. Basar, and H. Arslan, "Multidimensional index modulation for 5g and beyond wireless networks," *Archive pre-print*, 2020.
- [145] J. Zhu, P. Yang, Y. Xiao, M. Di Renzo, and S. Li, "Dual polarized spatial modulation for land mobile satellite communications," in *2018 IEEE Globecom Workshops (GC Wkshps)*, Abu Dhabi, United Arab Emirates, Dec. 2018, pp. 1–6.
- [146] G. Zafari, M. Koca, and H. Sari, "Dual-polarized spatial modulation over correlated fading channels," *IEEE Transactions on Communications*, vol. 65, no. 3, pp. 1336–1352, Mar. 2017.
- [147] K. Zhang, X.-Q. Jiang, M. Wen, R. Qiu, and H. Ge, "Precoding-aided spatial modulation with dual-polarized antennas over correlated channels," *IEEE Communications Letters*, vol. 24, no. 3, pp. 676–680, Mar. 2020.

- [148] B. Shamasundar, S. Bhat, S. Jacob, and A. Chockalingam, "Multidimensional index modulation in wireless communications," *IEEE Access*, vol. 6, pp. 589–604, Nov. 2018.
- [149] X. Chen, M. Wen, Q. Li, Y.-C. Wu, and T. A. Tsiftsis, "Dual-polarized spatial media-based modulation," *IEEE Journal of Selected Topics in Signal Processing*, vol. 13, no. 6, pp. 1258–1269, Oct. 2019.
- [150] C.-C. Cheng, H. Sari, S. Sezginer, and Y. T. Su, "Enhanced spatial modulation with multiple signal constellations," *IEEE Transactions on Communications*, vol. 63, no. 6, pp. 2237–2248, Jun. 2015.
- [151] C.-C. Cheng, H. Sari, S. Sezginer, and Y. T. Su, "New signal designs for enhanced spatial modulation," *IEEE Transactions on Wireless Communications*, vol. 15, no. 11, pp. 7766–7777, Nov. 2016.
- [152] M. Wei, S. Sezginer, G. Gui, and H. Sari, "Bridging spatial modulation with spatial multiplexing: frequency-domain ESM," *IEEE Journal of Selected Topics in Signal Processing*, vol. 13, no. 6, pp. 1326–1335, Oct. 2019.
- [153] T. Datta, H. S. Eshwaraiah, and A. Chockalingam, "Generalized space-and-frequency index modulation," *IEEE Transactions on Vehicular Technology*, vol. 65, no. 7, pp. 4911–4924, Jul. 2016.
- [154] S. Jacob, T. L. Narasimhan, and A. Chockalingam, "Space-Time index modulation," in *2017 IEEE Wireless Communications and Networking Conference (WCNC)*, San Francisco, CA, USA, Mar. 2017, pp. 1–6.
- [155] S. Sugiura, S. Chen, and L. Hanzo, "Coherent and differential space-time shift keying: A dispersion matrix approach," *IEEE Transactions on Communications*, vol. 58, no. 11, pp. 3219–3230, Nov. 2010.
- [156] S. Sugiura, C. Xu, S. X. Ng, and L. Hanzo, "Reduced-complexity coherent versus non-coherent QAM-aided space-time shift keying," *IEEE Transactions on Communications*, vol. 59, no. 11, pp. 3090–3101, Nov. 2011.
- [157] S. Sugiura, S. Chen, and L. Hanzo, "Generalized space-time shift keying designed for flexible diversity-, multiplexing- and complexity-tradeoffs," *IEEE Transactions on Wireless Communications*, vol. 10, no. 4, pp. 1144–1153, Apr. 2011.
- [158] M. I. Kadir, S. Sugiura, J. Zhang, S. Chen, and L. Hanzo, "OFDMA/SC-FDMA aided space-time shift keying for dispersive multiuser scenarios," *IEEE Transactions on Vehicular Technology*, vol. 62, no. 1, pp. 408–414, Jan. 2013.
- [159] I. A. Hemadeh, M. El-Hajjar, S. Won, and L. Hanzo, "Multi-set space-time shift-keying with reduced detection complexity," *IEEE Access*, vol. 4, pp. 4234–4246, Jun. 2016.

-
- [160] H. A. Ngo, C. Xu, S. Sugiura, and L. Hanzo, "Space-time-frequency shift keying for dispersive channels," *IEEE Signal Processing Letters*, vol. 18, no. 3, pp. 177–180, Mar. 2011.
- [161] W. O. Popoola, E. Poves, and H. Haas, "Error performance of generalised space shift keying for indoor visible light communications," *IEEE Transactions on Communications*, vol. 61, no. 5, pp. 1968–1976, May 2013.
- [162] L. He, J. Wang, and J. Song, "On generalized spatial modulation aided millimeter wave MIMO: Spectral efficiency analysis and hybrid precoder design," *IEEE Transactions on Wireless Communications*, vol. 16, no. 11, pp. 7658–7671, Nov. 2017.
- [163] P. Liu, J. Blumenstein, N. S. Perovic, M. Di Renzo, and A. Springer, "Performance of generalized spatial modulation MIMO over measured 60ghz indoor channels," *IEEE Transactions on Communications*, vol. 66, no. 1, pp. 133–148, Jan. 2018.
- [164] T. Mao, Q. Wang, Z. Wang, and S. Chen, "Novel Index Modulation Techniques: A Survey," *IEEE Communications Surveys and Tutorials*, vol. 21, no. 1, pp. 315–348, FirstQuarter 2019.
- [165] Y. Xiao, Z. Yang, L. Dan, P. Yang, L. Yin, and W. Xiang, "Low-complexity signal detection for generalized spatial modulation," *IEEE Communications Letters*, vol. 18, no. 3, pp. 403–406, Mar. 2014.
- [166] Y. Chau and S.-H. Yu, "Space modulation on wireless fading channels," in *IEEE 54th Vehicular Technology Conference. VTC Fall 2001. Proceedings (Cat. No.01CH37211)*, vol. 3, Atlantic City, NJ, USA, Oct. 2001, pp. 1668–1671.
- [167] A. Paulraj, R. Nabar, and D. Gore, *Introduction to space-time wireless communications*. Cambridge University Press, 2003.
- [168] S. Loyka, "Channel capacity of MIMO architecture using the exponential correlation matrix," *IEEE Communications Letters*, vol. 5, no. 9, pp. 369–371, Sep. 2001.
- [169] A. Chatterjee, S. Chatterjee, and S. S. Das, "Evaluation of spatial correlation and its effect on channel capacity of uniform planar antenna array," in *2017 Twenty-third National Conference on Communications (NCC)*, Chennai, India, Mar. 2017, pp. 1–6.
- [170] M. Koca and H. Sari, "Generalized spatial modulation over correlated fading channels: Performance analysis and optimization," in *2013 20th International Conference on Telecommunications (ICT)*, Casablanca, Morocco, May 2013, pp. 1–5.
- [171] A. Ç. Ulusoy and H. Schumacher, "Multi-Gb/s analog synchronous QPSK demodulator with phase-noise suppression," *IEEE Transactions on Microwave Theory and Techniques*, vol. 60, no. 11, pp. 3591–3598, Nov. 2012.

- [172] S. Sugiura and L. Hanzo, "Single-RF spatial modulation requires single-carrier transmission: Frequency-domain turbo equalization for dispersive channels," *IEEE Transactions on Vehicular Technology*, vol. 64, no. 10, pp. 4870–4875, Oct. 2015.
- [173] P. Yang, Y. Xiao, Y. L. Guan, K. V. S. Hari, A. Chockalingam, S. Sugiura, H. Haas, M. Di Renzo, C. Masouros, Z. Liu, L. Xiao, S. Li, and L. Hanzo, "Single-carrier SM-MIMO: A promising design for broadband large-scale antenna systems," *IEEE Communications Surveys and Tutorials*, vol. 18, no. 3, pp. 1687–1716, ThirdQuarter 2016.
- [174] K. Ishibashi and S. Sugiura, "Effects of antenna switching on band-limited spatial modulation," *IEEE Wireless Communications Letters*, vol. 3, no. 4, pp. 345–348, Aug. 2014.
- [175] E. Soujeri and G. Kaddoum, "The impact of antenna switching time on spatial modulation," *IEEE Wireless Communications Letters*, vol. 5, no. 3, pp. 256–259, Jun. 2016.
- [176] S. Fang, K. Zheng, Y. Xiao, Y. Yang, X. Zeng, and M. Xiao, "Offset spatial modulation and offset space shift keying: efficient designs for single-RF MIMO systems," *IEEE Transactions on Communications*, vol. 67, no. 8, pp. 5434–5444, Aug. 2019.
- [177] G. D. G. Simha, S. Koila, N. Neha, M. A. N. S. Raghavendra, and U. Sripathi, "Redesigned spatial modulation for spatially correlated fading channels," *Wireless Personal Communications*, vol. 97, no. 4, pp. 5003–5030, Aug. 2017.
- [178] M. F. Ozkoc, M. Koca, and H. Sari, "Combating transmit antenna and channel correlations in spatial modulation using signature constellations," in *2019 IEEE 89th Vehicular Technology Conference (VTC2019-Spring)*, Kuala Lumpur, Malaysia, Apr. 2019, pp. 1–5.
- [179] M. R. Khanzadi, D. Kuylenstierna, A. Panahi, T. Eriksson, and H. Zirath, "Calculation of the performance of communication systems from measured oscillator phase noise," *IEEE Transactions on Circuits and Systems I: Regular Papers*, vol. 61, no. 5, pp. 1553–1565, May 2014.
- [180] A. Ugolini, A. Piemontese, and T. Eriksson, "Spiral constellations for phase noise channels," *IEEE Transactions on Communications*, vol. 67, no. 11, pp. 7799–7810, Nov. 2019.
- [181] A. Haroun, C. A. Nour, M. Arzel, and C. Jego, "Low-complexity soft detection of QAM demapper for a MIMO system," *IEEE Communications Letters*, vol. 20, no. 4, pp. 732–735, Apr. 2016.
- [182] E. Viterbo and J. Bours, "A universal lattice code decoder for fading channels," *IEEE Transactions on Information Theory*, vol. 45, no. 5, pp. 1639–1642, Jul. 1999.
- [183] B. Hochwald and S. ten Brink, "Achieving near-capacity on a multiple-antenna channel," *IEEE Transactions on Communications*, vol. 51, no. 3, pp. 389–399, Mar. 2003.

-
- [184] M. Damen, H. E. Gamal, and G. Caire, "On maximum-likelihood detection and the search for the closest lattice point," *IEEE Transactions on Information Theory*, vol. 49, no. 10, pp. 2389–2402, Oct. 2003.
- [185] T. Cui and C. Tellambura, "Joint data detection and channel estimation for OFDM systems," *IEEE Transactions on Communications*, vol. 54, no. 4, pp. 670–679, Apr. 2006.
- [186] J. Jalden and B. Ottersten, "On the complexity of sphere decoding in digital communications," *IEEE Transactions on Signal Processing*, vol. 53, no. 4, pp. 1474–1484, Apr. 2005.
- [187] D. A. Basnayaka, P. J. Smith, and P. A. Martin, "Performance analysis of macrodiversity MIMO systems with MMSE and ZF receivers in flat Rayleigh fading," *IEEE Transactions on Wireless Communications*, vol. 12, no. 5, pp. 2240–2251, May 2013.
- [188] A. Dhayni and H. Hijazi, "Low complexity maximum-likelihood-based method for estimating emitted symbols in a SM-MIMO receiver," U.S. Patent 20 150 030 107, May 16, 2017, ST-Ericsson Invention Disclosure.
- [189] M. Saad, A. Al-Ghouwayel, and H. Hijazi, "UFMC transceiver complexity reduction," in *2018 25th International Conference on Telecommunications (ICT)*, St. Malo, France, Jun. 2018, pp. 295–301.
- [190] Z. Guo and P. Nilsson, "Algorithm and implementation of the k-best sphere decoding for MIMO detection," *IEEE Journal on Selected Areas in Communications*, vol. 24, no. 3, pp. 491–503, mar 2006.
- [191] C.-E. Chen, C.-H. Li, and Y.-H. Huang, "An improved Ordered-Block MMSE detector for generalized spatial modulation," *IEEE Communications Letters*, vol. 19, no. 5, pp. 707–710, May 2015.
- [192] A. Younis, S. Sinanovic, M. D. Renzo, R. Mesleh, and H. Haas, "Generalised sphere decoding for spatial modulation," *IEEE Transactions on Communications*, vol. 61, no. 7, pp. 2805–2815, Jul. 2013.
- [193] Y. Jiang, Y. Lan, S. He, J. Li, and Z. jiang, "Improved low-complexity sphere decoding for generalised spatial modulation," *IEEE Communications Letters*, vol. 22, no. 6, pp. 1164–1167, Jun. 2018.
- [194] I. Al-Nahhal, O. A. Dobre, and S. S. Ikki, "Quadrature spatial modulation decoding complexity: Study and reduction," *IEEE Wireless Communications Letters*, vol. 6, no. 3, pp. 378–381, Jun. 2017.
- [195] Yeqiu Lan, "T-SD/P-SD," 2017, Yeqiu Lan, "T-SD/P-SD ", IEEE Dataport, 2017. [Online]. Available: <http://dx.doi.org/10.21227/H2F93M>.

- [196] J. A. Cal-Braz and R. Sampaio-Neto, "Low-complexity sphere decoding detector for generalized spatial modulation systems," *IEEE communications letters*, vol. 18, no. 6, pp. 949–952, 2014.
- [197] T. Q. Tran, S. Sugiura, and K. Lee, "Ordering-and partitioning-aided sphere decoding for generalized spatial modulation," *IEEE Transactions on Vehicular Technology*, vol. 67, no. 10, pp. 10 087–10 091, 2018.
- [198] T.-H. Liu, C.-E. Chen, and C.-H. Liu, "Fast maximum likelihood detection of the generalized spatially modulated signals using successive sphere decoding algorithms," *IEEE Communications Letters*, vol. 23, no. 4, pp. 656–659, 2019.
- [199] K. P. Liolis, J. Gomez-Vilardebo, E. Casini, and A. I. Perez-Neira, "Statistical modeling of dual-polarized MIMO land mobile satellite channels," *IEEE Transactions on Communications*, vol. 58, no. 11, pp. 3077–3083, Nov. 2010.
- [200] C. Oestges, B. Clerckx, M. Guillaud, and M. Debbah, "Dual-polarized wireless communications: from propagation models to system performance evaluation," *IEEE Transactions on Wireless Communications*, vol. 7, no. 10, pp. 4019–4031, Oct. 2008.
- [201] H. Asplund, J.-E. Berg, F. Harrysson, J. Medbo, and M. Riback, "Propagation characteristics of polarized radio waves in cellular communications," in *2007 IEEE 66th Vehicular Technology Conference*, Baltimore, MD, USA, Sep. 2007, pp. 839–843.
- [202] B. Kumbhani and R. S. Kshetrimayum, *MIMO wireless communications over generalized fading channels*. Boca Raton, FL: CRC Press, 2017.
- [203] J. Proakis and M. Salehi, *Digital communications*. Boston, MA: McGraw-Hill, 2008.
- [204] F. Neeser and J. Massey, "Proper complex random processes with applications to information theory," *IEEE Transactions on Information Theory*, vol. 39, no. 4, pp. 1293–1302, Jul. 1993.
- [205] V. Veeravalli, "On performance analysis for signaling on correlated fading channels," *IEEE Transactions on Communications*, vol. 49, no. 11, pp. 1879–1883, Nov. 2001.
- [206] F. Pancaldi, G. M. Vitetta, R. Kalbasi, N. Al-Dhahir, M. Uysal, and H. Mheidat, "Single-carrier frequency domain equalization," *IEEE Signal Processing Magazine*, vol. 25, no. 5, pp. 37–56, 2008.
- [207] K. Berberidis and P. Karaivazoglou, "A block adaptive DFE in the frequency domain based on tentative decisions," in *9th European Signal Processing Conference (EUSPICO 1998)*, Rhodes, Greece, Sep. 1998, pp. 1–4.
- [208] K. Berberidis and P. Karaivazoglou, "An efficient block adaptive decision feedback equalizer implemented in the frequency domain," *IEEE Transactions on Signal Processing*, vol. 50, no. 9, pp. 2273–2285, Sep. Sept. 2002.

- [209] J. Xu, X. Tao, and P. Zhang, “Analytical SER performance bound of M-QAM MIMO system with ZF-SIC receiver,” in *2008 IEEE International Conference on Communications*, Beijing, China, 2008, pp. 5103–5107.
- [210] S. Bicaïs and J. Doré, “Design of digital communications for strong phase noise channels,” *IEEE Open Journal of Vehicular Technology*, vol. 1, pp. 227–243, 2020.
- [211] T. Davidson, “Enriching the art of FIR filter design via convex optimization,” *IEEE Signal Processing Magazine*, vol. 27, no. 3, pp. 89–101, May 2010.
- [212] B. Farhang-Boroujeny, “A square-root Nyquist (M) filter design for digital communication systems,” *IEEE Transactions on Signal Processing*, vol. 56, no. 5, pp. 2127–2132, May 2008.
- [213] S. Boyd and L. Vandenberghe, *Convex optimization*, C. U. Press, Ed. Cambridge University Press, 2016.
- [214] M. Grant and S. Boyd, “CVX: Matlab software for disciplined convex programming, version 2.1,” <http://cvxr.com/cvx>, Mar. 2014, [Online]. Available: <http://cvxr.com/cvx>.
- [215] M. Grant and S. Boyd, “Graph implementations for nonsmooth convex programs,” in *Recent Advances in Learning and Control*, ser. Lecture Notes in Control and Information Sciences, V. Blondel, S. Boyd, and H. Kimura, Eds. Springer-Verlag Limited, 2008, pp. 95–110, [Online]. Available: http://stanford.edu/~boyd/graph_dcp.html.

Titre : Retour vers Les Monoporteuses pour les Communications de l'après 5G

Mots clés : Terabits, Terahertz, millimeter wave, index modulation, MIMO, filter index modulation domain.

Résumé : Pour les futures applications de l'après 5G, qui seront très gourmandes en données, des communications sans fils de l'ordre du Terabits/s sont envisagées. Pour atteindre ce niveau de débit, il faudra disposer d'une grande largeur de bande. Comme le spectre est déjà saturé autour de 6 GHz, il est envisagé d'utiliser la bande sous-THz (90-200GHz). Les formes d'ondes doivent être étudiées en prenant en compte les caractéristiques des canaux à ces fréquences, les limitations technologiques, la sensibilité aux défauts RF (bruit de phase, par exemple). Nous avons donc proposé d'étudier une modulation monoporteuse très efficace énergétiquement, puis d'accroître son efficacité spectrale par des techniques d'indexation et des techniques MIMO.

Dans un premier temps les techniques MIMO multiplex spatial et spatial Index Modulation (GSM) sont étudiées. En particulier des détecteurs réduisant la complexité de 99% sont proposés. La très forte corrélation spatiale du GSM est aussi étudiée et des solutions pour en diminuer l'effet sont proposées. Une modulation d'index dans

Le domaine de la polarisation est aussi proposé pour augmenter l'efficacité spectrale.

Dans un second temps, nous proposons un nouveau domaine pour l'indexation : le domaine filtre. Ce domaine généralise la plupart des schémas de modulation d'Index existants. Dans ce domaine filtre, nous avons proposé deux nouvelles modulations d'index : la modulation d'index de filtre de mise en forme (FSIM) et sa version en phase et en quadrature (I/Q-FSIM). Une version MIMO de ces modulations est aussi proposée. Différents détecteurs sont proposés, ainsi que des techniques d'égalisation. Les performances théoriques de ces modulations sont développées et validées par des simulations. Ces modulations nécessitent de définir des bancs de filtres avec de fortes contraintes. Deux solutions sont proposées pour résoudre ce challenge, qui font partie des perspectives de cette thèse. Tous nos résultats confirment que la modulation FSIM MIMO offre un gain considérable par rapport aux modulations de l'état de l'art et permet d'atteindre le Terabits/s dans les canaux sous-THz.

Title : Back to Single-Carrier for Beyond-5G Communications above 90GHz

Keywords : Terabits, Terahertz, millimeter wave, index modulation, MIMO, filter index modulation domain.

Abstract : Wireless Terabits per second (Tbps) link is needed for the new emerging data-hungry applications in Beyond 5G (B5G) (e.g., high capacity broadband, enhanced hotspot, 3D extended reality, etc.). Besides, the sub-THz/THz bands are the next frontier for B5G due to scarce sub-GHz spectrum, and insufficient bandwidth for wireless Tbps link in 5G millimeter wave bands. Even though a wider bandwidth and large-scale MIMO are envisioned at sub-THz bands, but the system and waveform design should consider the channel characteristics, technological limitations, and high RF impairments. Based on these challenges, we proposed to use an energy-efficient low order single carrier modulation accompanied by spectral-efficient Index Modulation (IM) with MIMO. Firstly, MIMO Spatial Multiplexing (SMX) and spatial IM domain (e.g. Generalized Spatial Modulation (GSM)) are explored, where we reduced their optimal detection complexity by 99% and the high-spatial correlation effect on GSM. Besides, we proposed dual-polarized (DP)-GSM that provides higher spectral efficiency (SE) via multi-dimensional IM and helps with the latter problem. We derived the theoretical performance of DP-GSM,

and all these potential candidates are assessed in sub-THz environment. We also proposed a novel IM domain, called filter IM domain, that generalizes most existing SISO IM schemes. In the filter IM domain, we proposed two novel schemes: Filter Shapes IM (FSIM) and Quadrature FSIM (IQ-FSIM) to enhance system SE and energy efficiency (EE) through indexation of the filters in the bank. In addition, their optimal low complexity detectors and their specialized equalization techniques are designed. Striving for further SE and EE improvement, this filter IM domain is exploited in MIMO. Besides, we theoretically characterized the performance of FSIM, IQ-FSIM, and SMX-FSIM systems. To conclude, the proposed SMX-FSIM is compared in sub-THz environment to the previously considered candidates. The results confirm that SMX-FSIM is the most promising solution for low-power wireless Tbps B5G system due to its high SE/EE, robustness to RF impairments, low power consumption, and low complexity/cost with a simple linear receiver. Finally, the challenging filter bank design problem imposed by the filter IM domain is tackled by optimization to achieve better results.